Electrochemical and Photoelectrochemical Water Splitting to generate Hydrogen

A Thesis Submitted for the Degree of

Doctor of Philosophy

By

Manjeet Chhetri

New Chemistry Unit

Jawaharlal Nehru Centre for Advanced Scientific Research

(*A Deemed University*)

Bangalore, India.

November 2018

Dedicated to all my Teachers

Declaration

I hereby declare that the matter embodied in this thesis entitled ***"Electrochemical and Photoelectrochemical Water Splitting to Generate Hydrogen"*** *is the result of investigations carried out by me under the supervision of Prof. C. N. R. Rao, FRS at the New Chemistry Unit, Jawaharlal Nehru Centre for Advanced Scientific Research, Bangalore, India and that it has not been submitted elsewhere for the award of any degree or diploma.*

In keeping with the general practice in reporting scientific observations, due acknowledgement has been made whenever the work described is based on the findings of other investigators.

_____

(Manjeet Chhetri)

Certificate

I hereby certify that the matter embodied in this thesis entitled ***"Electrochemical and Photoelectrochemical Water Splitting to Generate Hydrogen"*** *has been carried out by Manjeet Chhetri at the New Chemistry Unit, Jawaharlal Nehru Centre for Advanced Scientific Research, Bangalore, India under my supervision and it has not been submitted elsewhere for the award of any degree or diploma.*

(Prof. C. N. R. Rao)

(*Research Supervisor****)***

Acknowledgements

It is my extreme joy to be able to get an opportunity to express my gratitude to my research supervisor, **Prof. C. N. R. Rao, FRS,** for giving me chance to work under him and guiding me throughout. I consider myself privileged to have worked under his supervision, guidance and mentorship. The value he has inculcated in me over the course of time has helped me become more informed and positive towards science and life at large. His unending source of motivation has encouraged me to value the importance of hard work. His "no substitute for hard work" philosophy will remain ingrained in me and will be followed throughout my life. His unique methodology to manage his students and bring out the best of them has indeed helped me in my PhD works to learn more and improve myself. He has always encouraged me to pursue good science, to have an innovative outlook while solving challenging problems and be able to think unique. I am grateful to him for introducing me to the fascinating field of water splitting. Not only has he been a great teacher, but also a valuable moral support on the personal front. It has been a fulfilling experience, a lifetime opportunity for me to work under his full spirited guidance.

I am extremely fortunate to have Prof. U. V. Waghmare (JNCASR) and Prof. Reshef Tenne (Weizmann Institute of Sciences) and Dr. Ujjal K. Gautam as my collaborators and for their invaluable discussions and timely guidance.

The contribution from my co-workers has been indispensable and without them most of the works would have been incomplete. The assistance of Dr. Pramoda K., Dr. Uttam Gupta and Dr. Sunita Dey has been immense in completing my PhD work.

During my PhD works, lab was the place where probability of finding myself was maximum (however unpredictable be that function with respect to time and event may be). So the time spent with my lab mates is precious. I am thankful and shall remain ever indebted to all my past and present lab mates especially Dr. Sunita Dey, Dr. Pramoda K., Dr. Uttam Gupta, Dr. Kaur, Dr. Gopalakrishnan, Dr. Srinivas, Dr. Sreedhara, Anand, Dr.Vishnoi, Dr. Manjunath, Mohnis, Manaswee, Navin, Reetender, Rohit, Amit, Swaraj for their help in various occasions and for always keeping an amicable and enjoyable atmosphere in lab. It is always joyful and uplifting to be able to spend time with my

juniors. I have been very fortunate to have experienced always supporting nature from my juniors in lab.

The courses offered by Prof. S. Balasubramanium, Prof. T. K. Maji, Dr. R. Viswanatha, Dr. T. Govindaraju, Dr. S. C. Peter, Prof. A. Sundaresan has been a learning curve to initiate my research career. I am indebted to them for the same.

The contributions from Dr. Ujjal K. Gautam and Dr. Moumita Rana for introducing me to research field and teaching me the research methodology during my initial days of research has been instrumental. I will ever be indebted to them. The patience with which Dr. Moumita taught me the essence of PhD work will always be remembered.

I am thankful to chairmen of NCU for allowing me to use the various departmental facilities.

PhD work depends heavily on the helps from technical and instrumental fronts. I thank Ms. N. R. Selvi, Mrs. T. Usha, Dr. J. Ghatak, Mr. Anil, Mr Mahesh, Mr. A. Srinivas and Mr. Nandkishor for various helps. I thank Mrs.Shashi, Mrs.Sudha, Mr.Gowda and Mr. Victor for their help in various ways.

I thank UGC and Sheik Saqr laboratory for providing fellowships. I thank JNCASR and IISc for research facilities. The hostel, admin staff, academic staff, complab staff and Dhanvantari for all their help during my stay in JNCASR.

My deepest thanks to Mrs.Indumati Rao and Mr. Sanjay for their love, affection and hospitality extended to me during the course of my association with them. I can never forget those wonderful dinners at Prof. Rao's house every now and then. This would be cherished throughout my life.

Thanks to all my PhD. batch mates with whom I started my life at this centre and whose cheerful company made these years of life so memorable. Special thanks to Pawan, Anand, Rafi, Kollur, Rajaji, KD. I have had an opportunity to meet people like Dr. Chandan Mishra, Shashikiran Reddy whose outlook towards life and people made me rethink and improve myself. They have been very much involved in changing my thought process in life.

The time spent with the Achal, Adma, Raaghesh with various outings, treks, visiting places and long drives has been amongst the most cherished moments in JNCASR. There were some crazy moments hidden in those moments.

I am thankful to all the colleagues and friends for bearing with me. I know all the times were not the same. Special thanks to my friends who held and understood my

circumstances during my ups and down. I consider myself blessed to have received all the care, affection, suggestions and advice from two of my buddies from IISc., Dev Kumar Thapa and Sukanta Nandi. They have been no less than family members to me.

I express my deep gratitude to all my teachers from Caesar School, Siliguri College and University of North Bengal. Their contributions to my completion of PhD have been enormous. Special thanks to Dr. J. Dasgupta, Prof. S. K. Saha, Prof. M. N. Roy for limitless advices and helps.

This thesis is a humble offering to all my Teachers from kindergarten to PhD.

It would not be possible for me to continue my studies without the help of Late. Rev. John Robert Thwaytes, the founder director of Caesar School where I completed 14 years of schooling. I also thank many of my childhood friends from Boys Town where I spent my initial 16 years.

I consider myself very lucky to have my childhood friend Ruchi beside me in all my times of joys and sorrows, to support me and be my strength, to believe in me more than I believe myself. I wish this friendship never ends. I thank my childhood friend Rajiv who has always been there for me in every aspects of life.

I would like to thank my family, my two elder brothers and my niece Rachel. Their understanding and supportive nature for things I do in life has helped me to withstand any adversaries arisen.

Above all, the Almighty has been very kind to me. I am very thankful to the Almighty for whatever he has bestowed on me.

If you want to have good ideas you must have many ideas. Most of them will be wrong and what you have to learn is which ones to throw away.

- Linus Carl Pauling

- *As quoted by Francis Crick in his presentation "The impact of Linus Pauling on Molecular Biology" (1995)*

Prologue

Generation of Hydrogen as clean and green fuel by splitting water is one of the important aspects of mitigating the overuse of non-renewabale sources of energy and its associated environmental degredation. Since the time when water was predictably forseen as the coal of future there has been many scientific efforts to reduce water and produce hydrogen which is struggingly uphill task in comparison to the other alternatives like steam reforming process (presently holding 96% of the world's hydrogen production). These efforts include using sunlight as the major energy source: Photochemical, Photoelectrochemical and PV-Electrolyzers. All these methods utilize energy from sun to generate charge carriers which if prevented from recombination results in successful utilization in redox reaction to produce hydrogen and oxygen from water or generating required elecytrical enerrgy for electrolysis. For this to achieve in an economical way, inexpensive novel materials which can reduce/oxidize water is required.

We present the noteworthy contributions and important results in hydrogen generation using water splitting by electrochemical and photoelectrochemical methods. This thesis comprises of six chapters. The first chapter discusses a brief overview of water splitting process. Each of the rest chapters discusses the step wise improvements in catalytic systems towards fuel production by various methods keeping in mind the basic understanding of electrochemical and photoelectrochemical processess and the cost of the catalysts.

Chapter-1 presents the basic understanding of electrochemical and photoelectrochemical water splitting processes. This entails the discussions of catalysts selection criteria and the various instrumental techniques used to estimate the activity of the catalysts. One of the most important aspects of electrochemical processes, that is the formation of electrode-electrolyte interface and its consequences in electrocatalysis and photoelectrocatalysis is discussed.

In **chapter-2**, we first investigated the electrocatalytic properties of Pt nanostructures. Pt has been the standard catalyst system for electrochemical processes including water splitting [hydrogen evolution reaction (HER)], fuel cell applications

[oxygen reduction reactions (ORR), alcohol oxidation reaction (AOR)]. Thus understanding of the various electrochemical processes and electrochemical instrumentation systems using Pt as the catalyst was attempted by us initailly.

Considering the cost of precious metal and its limited availability, it is imperative to think of inexpensive active materials that are readily available. However the bottleneck to this approach is the compromise with the electrocatalytic activity. Hence the search for low cost efficient electrocatalyst is addressed in **chapters-3, 4 and 5**. In **chapter-3**, one of the most active 2D materials- MoS_2 have been obtained in inorganic fullerene (IF) morphology which exposes the active edge sites for electrochemical HER process. A systematic study of deleberate doping to tune the activity in the wide pH range of electrolyte has been discussed which involves Re and Nb as p-type and n-type dopants respectively. In **chapter-4**, we report for the first time the HER activity of metal-free, low-cost borocarbonitrides ($B_xC_yN_z$). Since $B_xC_yN_z$ is amongsts the few metal-free elecytrocatalysts high high activity, we performed first principles calculations to investigate the origin of its activity and the role of specific composition and configurations in electrochemical water splitting. In **chapter-5** we have explore the use of graphite rod to fabricate $Ni/Ni(OH)_2$ and used it as an efficient electrode for hydrogen generation.

However one of the limitations of electrochemical water splitting process electrochemical HER is that the large input energy has to be provided in the form of voltage or current unless used in combination with photovoltaics. In order to reduce the input energy, coupling solar energy with electrical energy has been attempted in **chapter-6**. In this chapter we explored the photoelectrochemical water splitting using inexpensive oxide based semiconductors as photoelectrodes. A new strategy to deposit active co-catalyst by employing pulse plating electrodeposition technique has been reported. Application of amorphous mixed metal hydroxides of Co and La and band edge energetics in Cu_2O based photoelectrodes results in enhnaced PEC activity with higher photocurrent and charge separation efficiency. In part C these two electrodes have been used in two electrode configuration to split sea water. A comparative study shows that these electrodes can succesfully split sea water (inspite of the involvement of various ions affecting the water splitting redox reaction) taking into account the abundancy of sea water (75% earth) and the limited fresh water availability.

Table of Contents

Chapter-1

Hydrogen Generation by Splitting Water: A Brief Overview

Hydrogen Generation by Splitting Water: A Brief Overview

1. Introduction:

All round development has been driven by Fossil fuel reserves till present times but sustainable economical growth has forced limitations on the drilling operations of fossil fuel reserve. Not only depletion of fossil fuel but also the accompanied environmental problems have compelled us, albeit belatedly, to think of alternate energy sources. Solar energy can be utilized in photo-splitting of water to store hydrogen gas as an eco-friendly fuel. Hydrogen as a fuel can serve as a potential solution to both renewable energy crisis as well as the threat caused to environment due to excessive use of non renewable sources of energy. Hydrogen has highest calorific value amongst all the sources of energy used today. On the commercial scale production of hydrogen, there are four major sources: natural gas (48%), oil (30%), coal (18%), and electrolysis (4%) with the percentages representing world's hydrogen production by those means. Thus steam reforming which uses non renewable sources of energy accounts for ~96% of hydrogen production where as electrolysis only accounts for 4% in industry scale hydrogen generation.[1]

It is scientifically most desirable to move towards hydrogen production using renewable sources of energy and using abundant natural energy of sunlight. In doing so five possible methods can be envisioned which can be powered by the abundant energy input from the sun: Photochemical, Thermochemical, Electrochemical, Photoelectrochemical and PV-Electrolyzers. The source of hydrogen is water which is plenty (75% of earth). Hence water splitting to generate hydrogen as a clean and green energy is potentially the "holy grail" of energy and environmental problems faced by us today. The five methods are briefly discussed in **Figure 1.1**.

2. Water splitting to produce hydrogen using sunlight:

2.1. Photochemical method:

The process of hydrogen generation by splitting water using the sunlight as the only input energy source is photochemical water splitting. In an effort to mimic the natural

photosynthesis, artificial water splitting using solar energy can be driven by three important steps: absorption of light with band gap greater than 1.23 eV (thermodynamic requirement), efficient separation of the photogenerated charges (electrons and holes) and redox reaction at catalyst/water interface.[2-4] The photocatalysts used for water splitting must conform to these requirements to be efficient catalyst. In contrast to the hydrogen generation (2 electron process) the counter reaction i.e. the oxygen evolution is 4 electrons process and hence is the rate determining factor (due to its kinetic sluggishness). So sometimes sacrificial agents (Na_2S-Na_2SO_3 redox couple) are used to accept holes and promote water splitting at the counter reaction. Similarly acceptor sacrificial agents ($AgNO_3$, $Na_2S_2O_8$ etc.) are used to accept electrons and promote the counter reactions.[5]

$$2H_2O + 2e_{CB}^- \rightarrow H_2 + 2OH^- \quad (eq.1.1)$$

$$2H_2O + 4h_{VB}^+ \rightarrow O_2 + 4H^+ \quad (eq.1.2)$$

where e_{CB}^- and h_{VB}^+ are the photogenerated electron and hole pairs and the symbols have their usual meaning in chemical equation.

2.2. Thermochemical water splitting:

Thermochemical water splitting to H_2 is a strategy that is sometime coupled with reduction of CO_2 to CO. The solar to hydrogen conversion efficiency achieved by thermochemical water splitting can be high since this process utilizes the entire solar energy. Due to the limitation posed by input energy (T~1500 K), direct conversion of water to hydrogen and oxygen is not practical. Apart from this there is an added risk of obtaining explosive mixture of H_2 and O_2 in the same reaction compartment. Thus, a two or multistep process is successfully employed which split water at reasonable temperatures.[6-9] As a catalyst material, redox active metal-oxides are used. The schematic of the process is shown in **Figure 1.1**. The two step process can be represented in simple equation form which is given below.

$$MO_x \rightarrow MO_{x-y} + \frac{y}{2}O_2 \quad (eq.1.3)$$

$$MO_{x-y} + yH_2O \rightarrow MO_y + yH_2 \quad (eq.1.4)$$

2.3. Electrochemical water splitting:

Water splitting through electrolysis can also be achieved via electrochemical reduction of hydronium and hydroxide ions in H_2O.[10-14] For the evolution of H_2 the source of hydrogen depends on the acidic or alkaline medium used.

$$2H^+(aq) + 2e^- \rightarrow H_2(gas)\ (acidic) \quad (eq.1.5)$$

$$2H_2O + 2e^- \rightarrow 2OH^-(aq) + H_2(gas)\ \ (alkaline)\ \ (eq.1.6)$$

Unlike the previous two methods, in case of electrochemical water splitting, an input energy in the form of electricity (applied voltage or current) is needed. However if the input energy comes from the solar powered photovoltaic cells then electrolysis can be rendered very cheap and hydrogen production in large scale is possible. Hence, Electrolyzers and PV-Electrolyzer technology are put together as the method for hydrogen generation from water splitting using solar energy (**Figure 1.1**).

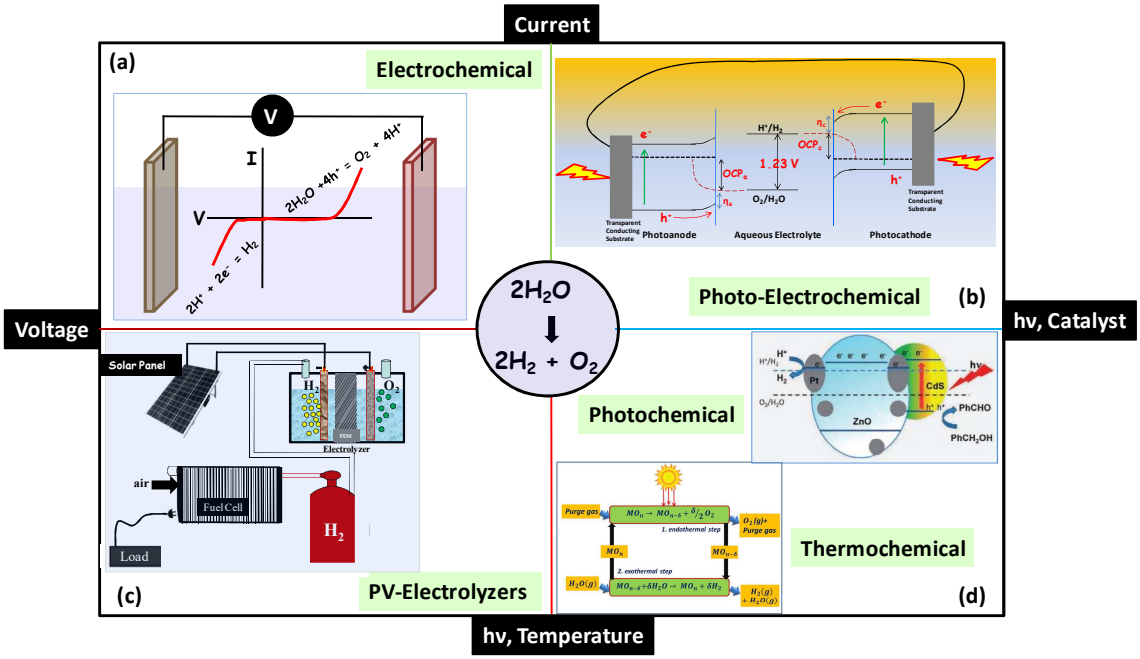

Figure 1.1: The representative description of possible ways to achieve hydrogen is shown in figure. (a) Electrochemical water splitting. The input energy is provided by electricity which can be generated by renewable sources of energy like sun, wind, hydel power energy. (b) Photoelectrochemical water splitting showing the direct coupling of electrolysis and solar energy. The photoanode and photocathode is represented in left and right side respectively along with its band structure with respect to water redox potential. The dotted lines represent the fermi level. OCP stands for open circuit potential and η is overpotential required for the process. (c) PV-Electrolyzers: PEM fuel cells for power generation completing the energy cycle. (d) Photochemical and Thermochemical water splitting. Reproduced with permission [15], copyright 2013 Royal Society of Chemistry. Reproduced with permission [16], copyright 2017 National Academy of Sciences.

2.4. Photo-Electrochemical water splitting:

One of the most practical feasible ways to reduce the cost of hydrogen production is to couple electrochemical and photochemical techniques in water splitting- photoelectrochemical (PEC) water splitting.[17-21] This is a long-term technology goal for energy related issues, with the prospects of zero emission of greenhouse gases. The detailed mechanism is discussed in next sections. The schematic representation of all these methods is show in **Figure 1.1**.

3. Electrochemistry of water splitting reaction:

Water splitting reaction is conceptually simple yet obtaining its constituents- oxygen and hydrogen is difficult task in practice. The Gibbs free energy associated with water splitting is ΔG^o = +237 kJ/mol. This corresponds to the redox potential of ΔE^o = 1.23 V [$\Delta G^o = -nF\Delta E^o$]. The half reactions at cathode and anode can be represented as,

In acidic medium,

$$2H^+ + 2e^- \rightarrow H_2 \qquad E^0 = 0.000\,V \qquad vs\ NHE \qquad (eq.1.7)$$

$$O_2 + 4H^+ + 4e^- \rightarrow 2H_2O \qquad E^0 = 1.229\,V \qquad vs\ NHE \qquad (eq.1.8)$$

In alkaline medium,

$$4H_2O + 4e^- \rightarrow 2H_2 + 4OH^- \qquad E^0 = -0.828\,V \qquad vs\ NHE\ (eq.1.9)$$

$$2H_2O\ +\ O_2 + 4e^-\ \rightarrow 4OH^- \qquad E^0 = +0.401\,V \qquad vs\ NHE\ (eq.1.10)$$

The cathodic half-reaction to produce hydrogen involves a 2-electron transfer process whereas the anodic half reaction proceeds via 4-electron transfer reaction for the oxidation of water to form oxygen. The overall water splitting reaction is as follows:

$$2H_2O \rightarrow 2H_2 + O_2 \quad \Delta G^0 = 237\ kJmol^{-1} \qquad (eq.1.11)$$

In an experimental set-up when electrodes are submerged in conductive water (aqueous electrolyte), upon application of required voltage (equal to or more than 1.23 V vs

RHE), hydrogen and oxygen are produced at the respective electrodes. Considering the Nernst equations for the two half cells (in acidic medium, equations 1 and 2),

$$E = E^0_{red} + \frac{0.059}{2} log[H^+]^2 \ = 0 - 0.059pH \ (eq.1.12)$$

$$E = E^0_{ox} + \frac{0.059}{4} log[H^+]^4 \ = 1.23 - 0.059pH \ (eq.1.13)$$

Subtracting *(eq.1.13)-(eq.1.12)* and putting the values of E^0_{ox} and E^0_{red}, theoretically in order to split water we would only need a voltage difference of 1.23 V between the anode and the cathode, but in practice we find it is necessary to apply a larger voltage due to the internal resistances accompanying the cell as well as the need to surpass kinetic barriers at each electrode. This difference in the required voltage more than the thermodynamically determined voltage is called as the overpotential (η).

$$\eta_{required} = 1.23 + \eta_{cathod} \ + \eta_{anode} + iR_{internal\ resistance} \ (eq.1.14)$$

Where $\eta_{catho} \quad and \quad \eta_{anode}$ are the kinetic activation barriers imposed at the surface of electrode to the electron transfer reactions at cathode and anode respectively. This extra voltage can be minimized by the rational optimization of many parameters like appropriate catalysts, cell design. The overall target is to reduce the overpotential as low as zero.

Referring to the earlier equations, it may appear that the pH terms cancel each other in a two electrode configuration electrolyzers, however the pH of the electrolyte does matter when we study the activity of one of the two half cell electrodes with a potentiostat. So the required potential for that particular half cell reaction is applied depending on the pH as dictated by the Nernst equation. In which case, the observed potential is reported with respect to reversible hydrogen electrode (RHE) allowing us to directly compare the positions of redox event with respect to standard reduction potential of hydrogen (0 V vs RHE) regardless of pH.

$$E_{RHE} = E_{NHE} + 0.059 \times pH \ (eq.1.15)$$

In all the chapters, few essential concepts and a number of parameters and terms are used to access and infer the activity of the catalyst. Hence, in the following pages these terms are explained along with their significance and application within the context of water splitting. Before that, a brief explanation of electrochemical techniques used is discussed.

4. Electrode-Electrolyte Interface:

The interface of electrode and electrolyte induces rearrangement of the solvent dipoles and charged species where the electrode can be thought of to be a giant central ion. The electro-neutrality is broken at this interface (compared to bulk of an electrolyte) and the electrode-electrolyte surface becomes electrified interface. At this interface the charges are separated and a potential difference develops (electrical double layer). Although the potential developed across this interface is not large, due to the extremely small dimensions of the double layer interface region, the field strength i.e. the potential gradient is as high as 10^7 V/cm. It is because of this enormous field gradient that the electrode-electrolyte interface is in fact the essence of any electrochemical reactions or electrochemistry at large. The importance of the double layer arises from the fact that the electric field in this region can either accelerate or decelerate an ionic species involved in a half cell reaction.

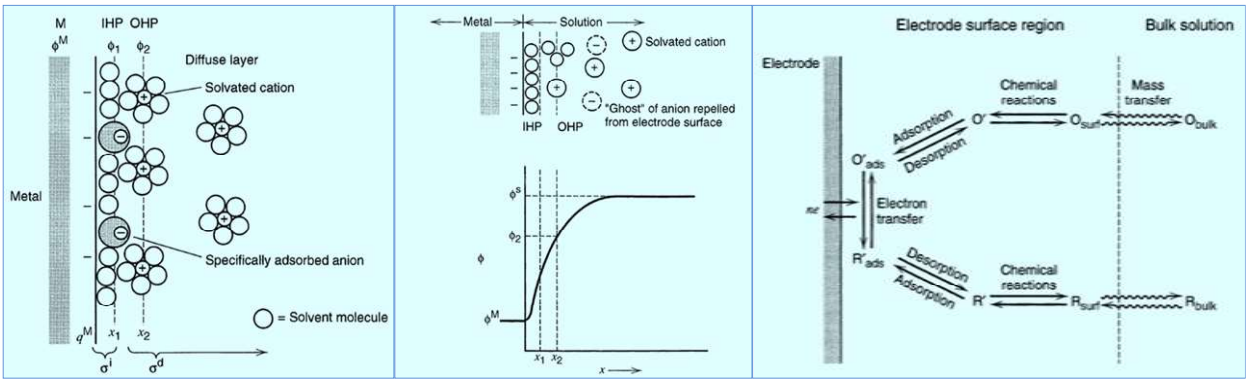

Figure 1.2: (left) representative proposed model of the electrochemical double layer (where anions are specifically adsorbed). (Centre) Variation of potential along the doublel layer. (right) Various electrochemical events occurring at the electrode-electrolyte interface for reactant to product conversion. In the figure, IHP is the inner Helmholtz potential, OHP is the outer Helmholtz potential, ϕ is representation of potential. Reproduced with permission [22], copyright 2002, John Wiley & Sons, Inc.

A more precise and useful information in electrocatalysis can be gained if the understanding of double layer structure can be attained based on the nature of electrode and the properties of electrolyte. For example, double layer is formed as a consequence of unequal distributions of ionic species at the interface as compared to bulk. If the number of positive ions is more than those of negative ions at the lamina of this interface, evidently there is accumulation of positive ions at the interfacial boundary relative to bulk of an electrolyte (**Figure 1.2**). This would mean that the electrode surface is capable of preferentially collecting/accumulating positive ions (*this is termed as an **active site** in following chapters*). This is essentially the adsorption phenomenon which is one of the most important parameters in electrocatalytic reactions like water splitting. The knowledge of electrical double layer helps in estimating the electrochemically active surface area (ECSA) [discussed in chapter-3] and consequently its activity towards the specific electrochemical reaction depending on the feasibility and nature of ionic adsorption [discussed in all the subsequent chapters]. This of course depends on the nature of electrode surface and the electrolyte used.

5. Factors affecting electrocatalysis:

Assuming a simple electrochemical reaction,

$$[Oxidized\ form] + ne^- \rightleftharpoons [Reduced\ form]$$

Broadly speaking considering all the parameters, the current obtained as a function of voltage (or the electrode reaction rate) is dependent on following factors –

- Electron transfer rate
- Mass diffusion rate at the interface
- Adsorption/Desorption kinetics
- Kinetics of chemical reaction after the electron transfer.

In the steady state condition, the magnitude of current is controlled by the most sluggish reaction step (for a multistep reaction) called as the rate determining step. The value of current density (*j*) obtained is controlled by a certain overpotential which is in turn the collective sum of all the above four factors (impedance in essence).

$$\eta_{total} = \eta_{charge\ transfer} + \eta_{mass\ transfer} + \eta_{internal\ resistance} \qquad (eq.\ 1.16)$$

The overall aim of an efficient catalysts (or electrode material) is to reduce the η_{total} to maximize the product formation (in the context of present discussion, hydrogen). The information of efficiency of an electrocatalyst can be obtained by studying the changes in the characteristics of the electrode upon application of an electrical perturbation (voltage). Thus, to study these individual overpotential terms (*eq. 1.14 and 1.16*), some electrochemical techniques/methods are used which are discussed below.

6. Cyclic Voltametry (CV) and Linear Sweep Voltametry (LSV):

In the study of current vs voltage (*I-V*) relationship usually two techniques are involved. If the potential is linearly swept at a constant rate (v, mV/sec) from voltage V_1 to a V_2, it is called as linear sweep voltametry (LSV). If the scan is continued at this point in a reverse direction back to V_1 keeping the scan rate same, it completes a whole cycle which is called cyclic voltammetry (CV) (**Figure 1.3**). In the context of water splitting (hydrogen evolution or oxygen evolution reaction), both the techniques are used to study the efficiency and activity of a catalyst. The schematic representation of these two techniques is shown in **Figure 1.3**. In the water splitting reaction, LSV is employed to determine the onset potential, overpotential at specific current density (10mA/cm^2) and to obtain tafel slopes. These are useful parameters and are discussed in following sections. CV is used to study the redox behavior of catalysts, electrodeposition and stability tests (change in oxidation states, morphology etc after various cycles). Multiple cycling (> 5000 cycles) is used to evaluate the stability of a catalyst, although other techniques like chronoamperometric and chronopotentiometric tests are applied along with CV. In a chronoamperometric the potential of the working electrode is stepped to a fixed value (ca. 500 mV from onset potential) and the resulting current from faradic process (electron transfer process) is plotted as a function of time. Similarly, in a chronopotentiometric technique, current is ramped to fixed value (10 or 50 mA/cm^2) and the resulting overpotential required sustaining this current is monitored as a function of time. Both these techniques help in evaluating the long term stability of electrocatalysts.

7. Overpotential and Onset potential:

For the electrocatalysts activity comparison purpose, the terms- overpotential and onset overpotential is used throughout the thesis. While overpotential required to achieve a current density usually of 10 $mAcm^{-2}$ for water splitting (both hydrogen evolution and oxygen evolution) is used, onset overpotential or simply onset potential (vs RHE) is used to describe the potential at which the redox reaction of study (HER or OER) starts. The value is usually compared with that of the thermodynamically determined value (theoretical redox potential) and extra amount of energy needed to initiate the process is calculated.

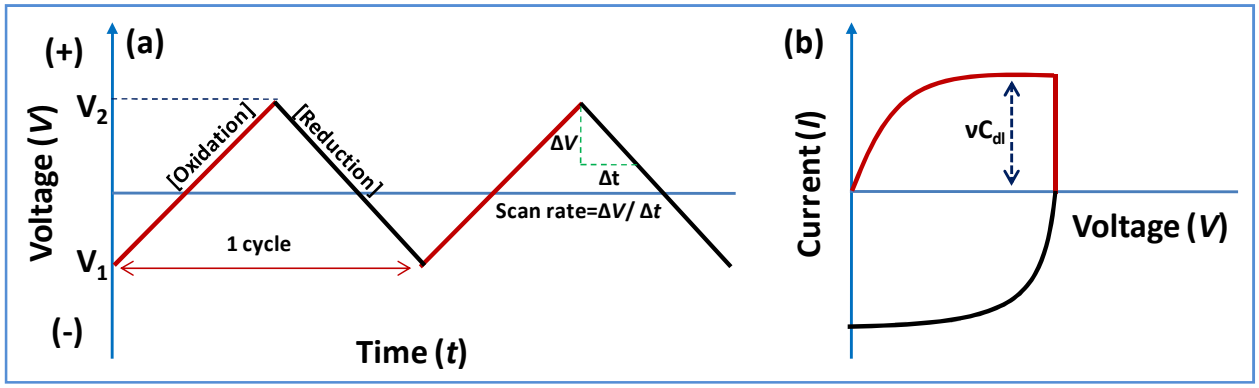

Figure 1.3: Schematic representation of potential sweep for cyclic voltametry and linear sweep voltametry. (a) V-t relation showing the oxidation and reduction cycles as red and black lines respectively. (b) Shows the corresponding *I-V* characteristics of an ideally polarizable electrode consisting of an RC circuit element in series. (R and C stands for resistor and capacitor respectively). Here no faradic process takes place and this particular relationship for non faradic process is used for estimation of electrochemical surface area discussed in chapter-3. v is the scan rate and C_{dl} represents double layer capacitance.

However the onset potential for the half-reaction under study is not a very useful term unless accompanied with a value of the current density, since there is no clear consensus in what exactly is considered the "onset". Some researchers assume the potential corresponding to $1mA/cm^2$ as the onset potential whereas some assume the onset potential by drawing the tangent to the cathodic/anodic curve and the initial non-faradic curve; the point of intersection of these two is the onset potential. Depending on the nature of *I-V* curve these two methods are interchangeably used[13-14,18,23,25-26].

8. Electrochemical techniques for electrocatalysts' characterizations:

8.1. Tafel Analysis:

Butler–Volmer equation is the basic foundation for the study of electrochemical kinetics describing the relation between current as a function of overpotential. The most simplified expression of Butler-Volmer equation is given below,

$$I = I_0 \left[e^{\frac{(1-\alpha)ne\eta}{k_B T}} - e^{\frac{-\alpha n}{k_B T}} \right] \quad (eq.1.17)$$

Where $I_0 = neA(k_c C_O)^{1-\alpha}(k_a C_R)^{\alpha}$ is the exchange current density. 'O' and 'R' stands for oxidation and reduction whereas 'a' and 'c' stands for anode and cathode. C is the concentration and η is overpotential. 'α' is the electron transfer coefficient. 'k' is the rate of reaction, 'k_B' and T are the Boltzman constant and temperature respectively.

If we consider the limiting conditions of the equation,

1) For small overpotential, $\eta \ll \frac{k_B T}{ne}$, Butler-Volmer equation can be linearized. This leads to the approximation within which the current is linearly related to overpotential.

$$I \sim I_0 \frac{ne\eta}{k_B T} \quad (eq.1.18)$$

Thus there is a constant activation resistance (>0) of the Faradaic reaction. Activation overpotential is positive for anode and negative for cathode in a galvanic cell (*I>0*) and electrons flows from anode to cathode.

2) Similarly, if we look at the tafel response of Butler-Volmer equation,

For large overpotentials, $\eta \gg \frac{k_B T}{ne}$,

$I \sim I_0 e^{\frac{(1-\alpha)ne\eta}{k_B T}}$ or $I \sim I_0 e^{\frac{-\alpha ne\eta}{k_B T}}$ $(eq.1.19)$, depending on the anodic or cathodic reaction nature.

Thus, Butler-Volmer equation predicts an asymptotic linear dependence for large overpotentials, where the slope is related to the transfer coefficient and the y-intercept gives the exchange current. So *equation 1.19* can be represented as tafel equation given below,

$$\eta = a + b\ log(j) \quad (eq. 1.20)$$

where a and b are constants. If current density given by electrocatalyst at different values of potential is plotted as logarithm of the current density vs the overpotential, we should find a linear graph (**Figure 1.4**). This is used in all the chapters to evaluate the electrocatalytic performance of the material under examination. Empirically, the smaller the Tafel slope the better the catalyst, since it means that it requires smaller increments of overpotential to give increased current densities. Although the Tafel equation is extensively applied to basically any kind of heterogeneous electrocatalysts, *equation 1.20* was originally developed for metallic electrodes (Platinum), and so its applicability to non-metal electrodes should be carefully considered (This discussion is included in chapters -3 and 4). This is because, since the electrons in a metal follow the Fermi statistics while molecular/organic species follow the Boltzmann statistics, the expression for the electrochemical potential of molecular species should include a term proportional to the logarithm of their concentration, while the same is not true for metallic systems.[23] In this line of explanation, the electrocatalysts used in the subsequent chapters are metal-free electrocatalysts or oxides and sulfides of metals. So the tafel analysis is not a complete analysis because of the lack of complete theories available for such systems. Since most of the electrochemical community seems to accept the validity of tafel equation for all heterogeneous electrocatalysts, we have followed the lead and explained the mechanistic information based on the extractable inferences from the tafel plot. The details of these analyses are discussed in chapter 3 (section 3.10.). The Tafel plot of log(current) versus overpotential for the same is represented below,

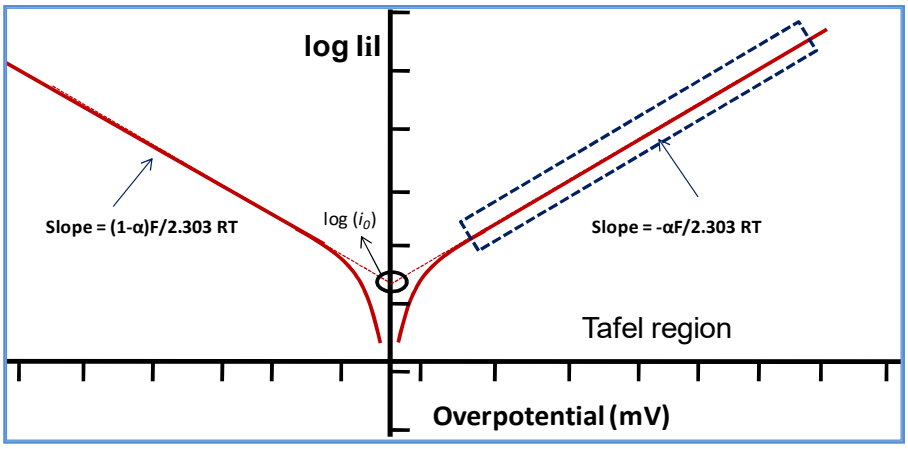

Figure 1.4: Tafel plots for anodic and cathodic branches of the current-overpotential curve with α=0.5 for the reaction: [Oxidized form] + e ↔ [Reduced form].

8.2. Electrochemical Impedance Spectroscopy (EIS):

An electrode system consisting of catalyst coated onto the substrate and the electrode-electrolyte interface has many components to be investigated in order to decipher the resistance involved in the successful transfer of charges for a redox reaction under study. For example, if we assume an electrocatalyst consisting of 'A' and 'B' components (say MoS_2@rGO for HER). In order to study the overall activity of the catalyst for cathodic hydrogen evolution, one has to estimate the resistance involved in transfer of e^- to H^+ ions at the electrode-electrolyte interface (charge transfer resistance) along with the resistances involved in the electron transfer within the catalyst and at the interface of catalysts and substrate. To find all these component resistances electrochemical impedance spectroscopy (EIS) is employed. It is a non-destructive experimental technique that can be used to separate and quantify the sources of overpotential (ohmic, kinetic or mass transfer overpotentials). So the electrical properties of the individual components of the electrode can be estimated. In this technique, at a certain voltage (usually open circuit voltage) and amplitude of ca. 5 mV, AC source is passed within the frequency range depending on the system under study (10^5 Hz to 0.1 Hz) and the impedance (Z) is estimated.[24-25]

An AC input and output signal can be represented by a sine or cosine wave function of amplitude and phase. For example,

$Input$: $V = V_0 cos(\omega t)$, $angular\ frequency, \omega = 2\pi f\ rad\ s^{-1}\ and\ f\ is\ frequency$

$Output$: $I = I_0 cos(\omega t + \phi)$ $the\ input\ and\ output\ has\ a\ phase\ difference\ of\ \phi$

For ease in analysis, they can be represented in complex exponentials,

$$Input: \quad V = V_0\ .\ e^{j\omega t} \qquad (eq.1.21)$$

$$Output: \quad I = I_0\ .\ e^{j(\omega t+\phi)} \qquad (eq.1.22)$$

Impedance (*Z*) is given by, $Z = \frac{V}{I} = \frac{V_0}{I_0}.e^{-j\phi} = |Z|.e^{j\theta} = |Z|cos\theta + j.|Z|sin\theta = Z_{real} + Z_{img.}$

So, the total impedance can be represented as the sum of its real and imaginary components as a function of phase angle. For a pure resistor (R), the impedance, Z'=R (same phase) and for pure capacitor (C), the impedance, Z''=$\frac{-j}{\omega C}$.

In an experiment, we take the plot of Z'' vs Z' at a particular frequency range with OCP as the AC input with an amplitude of 5 mV. The plot is called as Nyquist plot. However, for detailed analysis, sometimes Bode plot is invoked [(Frequency vs total impedance) and (Frequency vs phase)]. It can be mathematically shown that for a RC circuit (parallel configuration), Z'' vs Z' plot is a semicircular. This is important because RC is actually similar to the electrode system in electrocatalyst where 'C' is represented by the porous system (double layer) and 'R' is the ohmic resistance on catalyst surface. The actual information regarding the electrode system can be gained by modeling an equivalent circuit and trying to fit it with the raw data of Nyquist plot. The equivalent circuit depends on the electrode system of study and fitting is done by inbuilt software in electrochemical systems or external software like ZView. The pictorial representation of the EIS analysis is given in **Figure 1.5**.

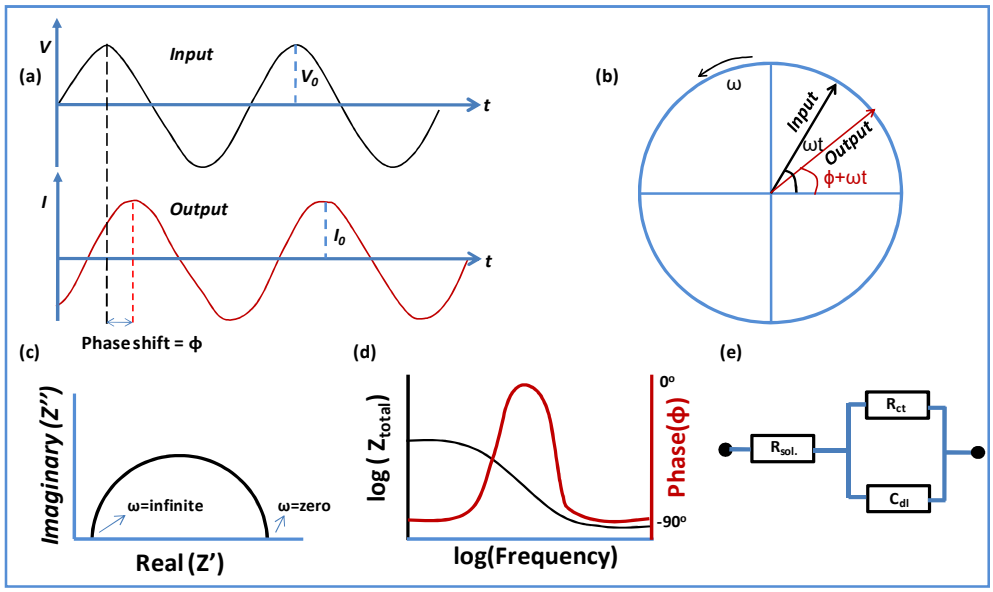

Figure 1.5: Representation of Electrochemical Impedance spectroscopy (EIS) study: (a) phase difference in input (V) and output (I) signal. (b) Representation of input and output signals in complex plane. (c) Nyquist plot and (d) Bode plot of simple Randles' circuit represented in (e).

8.3. Mott-Schottky Analysis:

The importance of electrode-electrolyte interface has already been discussed previously. In the electrochemical and photoelectrochemical experiments, we have to deal with two kinds of interfaces on the electrode surface-:semiconductor/metal interface and semiconductor/electrolyte interface. These interfaces act as Schottky barriers which results into the formation of electrostatic depletion layer. There are many electrochemical information that can be extracted from this region like- carrier density (acceptor or donor) of semiconductors, band edges (conduction band minima and valence band maxima), life time of minority charge carriers and diffusion lengths and Flat band potential (V_{fb}). These are mainly important parameters in photoelectrochemical studies discussed in next section. The analysis involves invoking Mott-Schottky equation which is the relation between the capacitance of the space charge region and the applied voltage. The simplified form is expressed in equation-17.

$$\frac{1}{C^2} = \frac{2}{\varepsilon\varepsilon_0 A^2 e N_d}\left(V - V_{fb} - \frac{k_B T}{e}\right) \qquad (eq.\,1.23)$$

where '*e*' is the electronic charge and 'ϵ' and 'ε_0' are the dielectric constant of semiconductor and absolute permittivity of free space respectively. '*C*' and '*A*' are the interfacial capacitance and area, respectively. Donor density is represented by 'N_d' and 'V' is the applied voltage in the experiment. Boltzman constant and absolute temperature are denoted by k_B and *T* respectively. If we plot $1/C^2$ vs applied voltage (V) we should get a straight line whose intercept can be used to determine V_{fb} and from the slope we can determine donor density. In the most photoelectrochemical experiments, determination of flat band potential helps in estimating the onset potential of photocurrent and the band edges.[26-27] Furthermore the carrier densities can be compared between various photoelecrocatalysts under study.

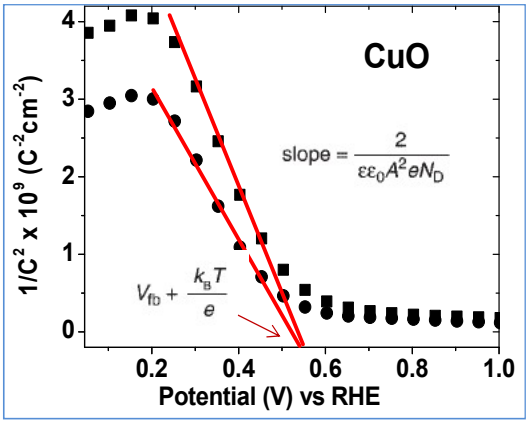

Figure 1.6: Mott–Schottky (MS) plot of CuO measured in 0.5 M Na_2SO_4 (pH 7) at different AC frequencies (circle: 50 kHz, square: 75 Hz).

Example of Mott-Schottky (MS) plot for p-type semiconductor in shown in **Figure 1.6**. In an experimental process, the $1/C^2$ term is calculated from the EIS analysis as explained earlier. In some of the electrochemical workstations, Mott-Schottky analysis technique is pre-installed and one can select the potential window over which the analysis is to be carried out and the particular frequency of investigation. However, in most of the cases, the $1/C^2$ term is calculated from the EIS measurement by performing impedance analysis at different voltages of interest and then fitting the Nyquist plot to obtain the capacitance value for the electrode at that voltage. MS analysis is very important tool in understanding photoelectrochemistry of the catalyst especially for PEC water splitting.

9. Photo-Electrochemistry of Water Splitting:

Similar to electrochemical water splitting to produce its products: oxygen and hydrogen, the principle of photoelectrochemical (PEC) water splitting involves redox reactions at electrode/electrolyte interface. Here coupling of electrolysis and photolysis takes place utilizing the abundant sunlight as the major energy source and minimum bias (sometimes zero bias) as the driving force for accelerating the rate of charge transfer (electro/hole) reactions. In PEC system, the photoelectrode (semiconductor) absorbs sunlight and generates excited electrons (e_{CB}^-) and holes (h_{VB}^+) in conduction band and valence band respectively. These two participate in water splitting and thus minimizes the input energy (usually in terms of applied bias) required for hydrogen production. The PEC reaction is shown below,

$$Photocathode: \quad 4H^+ + 4e_{CB}^- = 2H_2 \qquad (eq.1.24)$$

$$Photoanode: \quad 2H_2O + 4h_{VB}^+ = O_2 + 4H^+ \qquad (eq.1.25)$$

$$Overall: \quad 2H_2O + 4h\nu\ (e_{CB}^- + h_{VB}^+) = H_2 + O_2 \qquad (eq.1.26)$$

The energy requirement for the materials to be used as photoelectrode and the thermodynamics at the semiconductor/electrolyte interface is shown in **Figure 1.7**.

In a PEC water splitting experiment, the photoelectrode (photocathode or photoanode), is immersed in the electrolyte. As explained in earlier section, the semiconductor-electrolyte interface is formed. Here based on the relative positions of Fermi level of semiconductor and the electrolyte redox potential, charge transfer reaction starts until the steady state electrochemical equilibrium is achieved. This is shown in **Figure 1.7** taking an example of n-type semiconductor as a photoanode. When the photoanode is in contact with aqueous electrolyte, a space charge region is developed as shown in **Figure 1.7a,b**, the rearrangement of the band edge positions of photoanode with respect to redox potential of electrolyte occurs. This leads to band bending (pinning of band edge positions) and a development of space charge region similar to the schottky barrier. Electrons are transferred from the n-type semiconductor to the electrolyte, until it reaches equilibrium. This is when the Fermi level of the semiconductor is at the same level as the redox level of the electrolyte (**Figure 1.7c**). As result, an upward bending of the bands is created, and there is a region near the surface of the semiconductor where the

concentration of electrons is depleted. This region is called depletion layer or space charge layer.

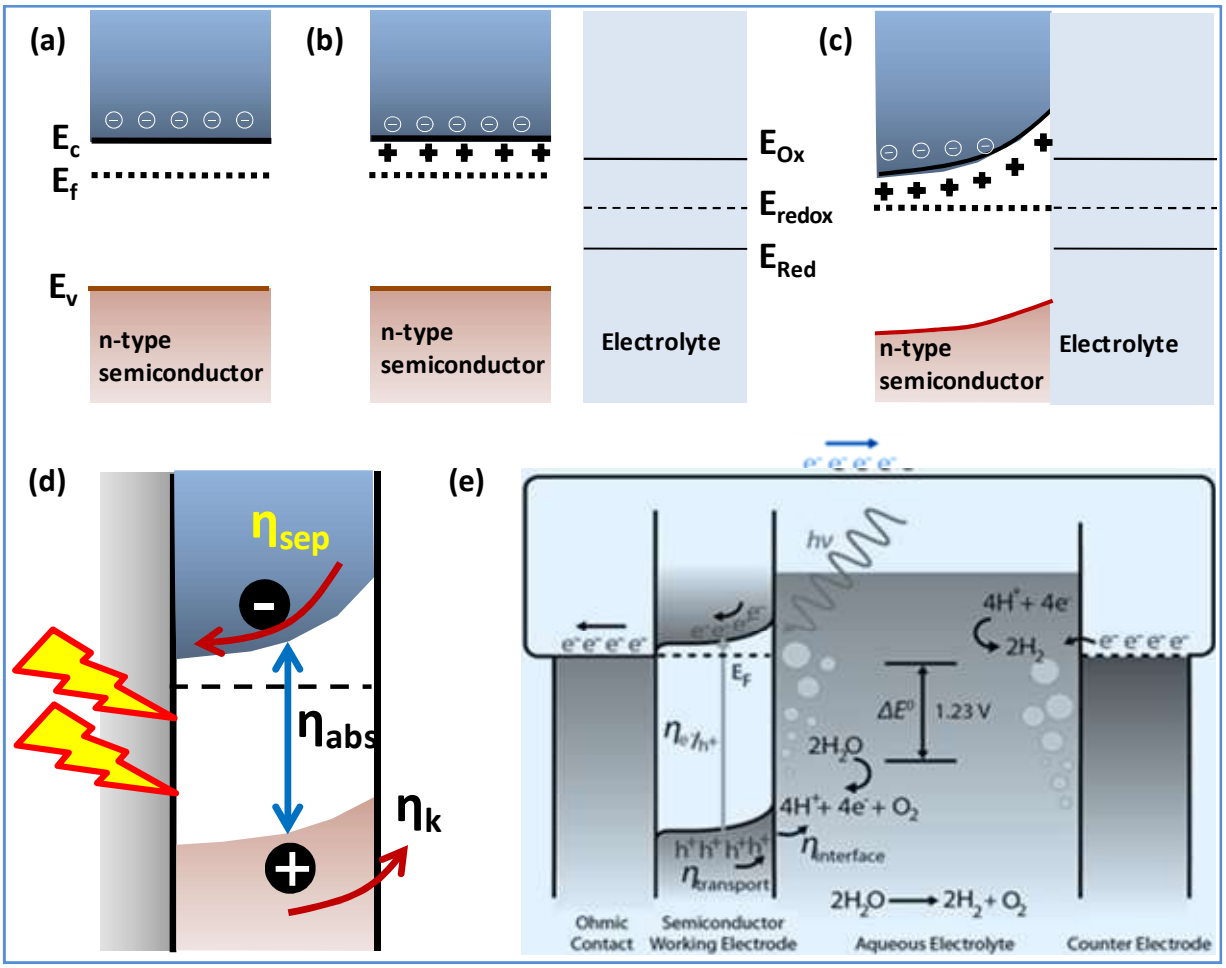

Figure 7: The formation of space charge layer in n-type semiconductor/electrolyte interface :(a) represents the isolated band diagram of the semiconductor, (b) when it is immersed in the electrolyte, (c) represents the equilibrated band diagram. E_{ox} ,E_{red} and E_{redox} are the representative band positions of electrolyte redox process. E_c, E_f and E_v are the band edge positions of conduction band, fermi level and valence band respectively for n-type semiconductor. (d) The PEC event processes occurring in the semiconductor upon illumination of sunlight. (e) Band structure of an n-type photoanode water splitting device illustrating the various processes of photon irradiation, electron–hole pair formation, charge transport, and interfacial reactions. Reproduced with permission [28], 2013 Springer Nature Switzerland AG. Here 'η' terms represent the overpotential for absorbance, charge separation and kinetics as represented as η_{abs}, η_{sep}, η_k respectively.

The space charge region is also termed as the depletion layer since this region corresponds to the depletion of majority carrier at the interface. Due to this, a potential gradient is developed (also discussed in earlier section) which actually helps in the separation of photogenerated electrons and holes.

Under the light illuminated condition, the semiconductor electrode absorbs the photon energy (light source with energy larger than its bandgap) and generates electron-hole pair (**Figure 1.7d**). The aim is to use them for the respective redox reactions of interest without allowing them to recombine. These photogenerated charges can be separated by two mechanism-drift and diffusion. While diffusion is related to the intrinsic nature of semiconductor (the local charge particles concentration gradient), drift is provided by the applied electrical bias. For example, in n-type semiconductor (**Figure 1.7e**), the photogenerated electrons are driven towards semiconductor/conducting substrate interface and photogenerated holes are driven towards the semiconductor-electrolyte interface (depletion layer). Now based on the relative mobility of these two charge carriers, the recombination of electron and hole may occur. The ratio of concentration of photogenerated charges reaching the respective interfaces and the photogenerated charges recombined is called as the separation efficiency (η_{sep}). Among the various processes happening at the interface upon light illumination (**Figure 1.7e**), charge transfer efficiency is the concentration of photogenerated charges (holes in case of n-type semiconductor) undergoing water oxidation to yield oxygen. The ratio of the holes undergoing water oxidation to all the holes reaching as semiconductor-electrolyte interface is the catalytic efficiency (η_k). On the other hand, the electrons are transported by an external circuit to the metal counter electrode (usually platinum), where they undergo the water reduction reaction to complete the redox reaction of water. The same processes occur for PEC water splitting using a p-type semiconductor, except that water is reduced on its surface and oxidized at the counter electrode. Based on the half-reactions at the surface, an n-type semiconductor in PEC water splitting is called a photoanode (oxidation) and a p-type semiconductor is called a photocathode (reduction).

To evaluate the efficiency of the photoelectrode for PEC water splitting, there are two efficiency definitions depending on the mode of PEC study. One is the benchmark efficiency definition: solar to hydrogen conversion efficiency (STH)[28]. This is the true efficiency of a PEC device operating in two electrode configuration where no applied bias is applied.

$$STH = \left[\frac{(mmol\ H_2\ \ s^{-1}) \times (237\ kJmol^{-1})}{P_{total}(mWcm^{-2}) \times Area(cm^2)}\right] \qquad (eq.1.27)$$

$$or, \qquad STH = \left[\frac{J(mAcm^{-2}) \times (1.23\ V) \times (faradic\ efficiency)}{P_{total}(mWcm^{-2})}\right] \quad (eq.1.28)$$

Where, P_{total} is the total integrated power input density and *J* is the current density obtained in PEC device.

STH is the chemical energy produced as the function of solar energy absorbed. Since the measurement of STH involves exposing PEC device to broadband solar Air Mass 1.5 Global (AM 1.5 G) under zero bias condition, it is the most important of all efficiency measurements. The other efficiency definition includes diagnostic efficiencies (where an applied bias is provided to carry out water splitting). This helps in understanding the photoelectrode material characterizations prior to be used in PEC device. The most frequently used diagnostic efficiency is the applied bias photon to current efficiency (ABPE) and Incident photon to current efficiency (IPCE).

$$ABPE = \left[\frac{j(mAcm^{-2}) \times (1.23 - \ appl.)(V)}{P_{total}(mWcm^{-2})}\right] \quad (eq.1.29)$$

$$IPCE = \eta_{sep.} \times \eta_{trans.} \times \eta_{interface} = \left[\frac{j(mAcm^{-2}) \times 1239.8(V \cdot nm)}{P_{mono}(mWcm^{-2}) \times \lambda(nm)}\right] \quad (eq.1.30)$$

where *j* is the photocurrent density in an applied bias $V_{appl.}$. The η terms stands for efficiency of photogenerated charge separation (sep.), charge transport (trans.) and the kinetic efficiency for charge transfer reaction (interface) respectively as shown in **Figure 6e**. λ is the wavelength at which the photoelectrode is monochromatically illuminated with a power (P_{mono}).

Any prospective material to be used in PEC water splitting as a photoelectrode must be a good absorber of sunlight. The theoretical values of STH or any efficiency is governed by the bandgap of material. For example small bandgap materials (E_g<1.9eV) can have higher STH whereas, more band gap materials have decreased maximal theoretical STH. On the other hand, an additional effect of kinetic overpotential also contributes to the overall efficiency since wider band gap materials are more likely to convert absorbed photons to current.

10. Experimental Methods and Instrumentation:

The instruments used for the electrochemical water splitting and PEC water splitting experiments are shown in **Figure 1.8**. The method used for Photoelectrode preparation in the

subsequent works is electrodeposition and conventional catalyst ink drop-drying method. The substrates used for the electrochemical and PEC experiments are glassy carbon electrode (GCE) and flourine dope tin oxide (FTO) respectively. The Solar simulator for the calibrated 1.5 AM G is also shown in **Figure 1.8**. Hydrogen and Oxygen detections were done with the help of gas chromatographer and fluorescence based oxygen sensor (Neofox) as shown in **Figure 1.8**. The step wise characterizations of the materials for its evaluation in PEC activity test is depicted in **Figure 1.9** as flow chart which was employed in the subsequent works discussed in following chapters.

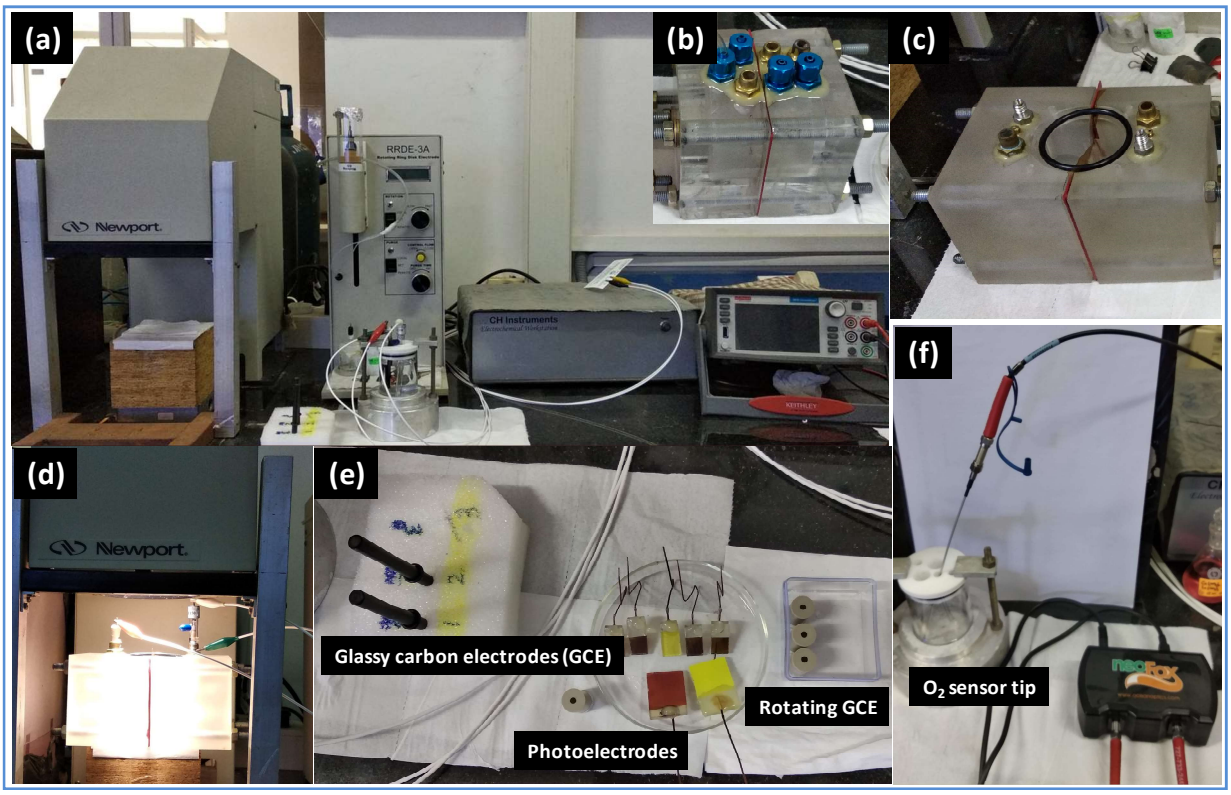

Figure 1.8: Electrochemical workstation used for Electrochemical and Photoelectrochemical (PEC) water splitting. (a) CHI electrochemical work station showing the electrochemical reaction in a three electrode configuration. Left side shows the light source used for PEC water splitting- solar simulator AM 1.5 G with a calibrated intensity of 100 mW/cm^2. (b) and (c) are the customized electrochemical and PEC cells for collection of gases for the measurement of faradic efficiency. (d) PEC water splitting process under 1 sun light illumination. (e) Various kinds of electrodes used in this work- glassy carbon electrode used in electrochemical hydrogen evolution reaction (HER), photocatalyst coated fluorine doped tin oxide substrate electrodes for PEC water splitting. For the study of HER and oxygen reduction reaction, rotating disk electrode (RDE) is used which is also shown. The RDE consists of disk of glassy carbon electrode which was obtained from CHI Instruments and Sigma Aldrich. (f) For the quantification of gases- hydrogen and oxygen, gas chromatographer and fluorescence based oxygen sensor were used. The neofox kit for oxygen sensing in electrochemical and PEC cell is shown in (f).

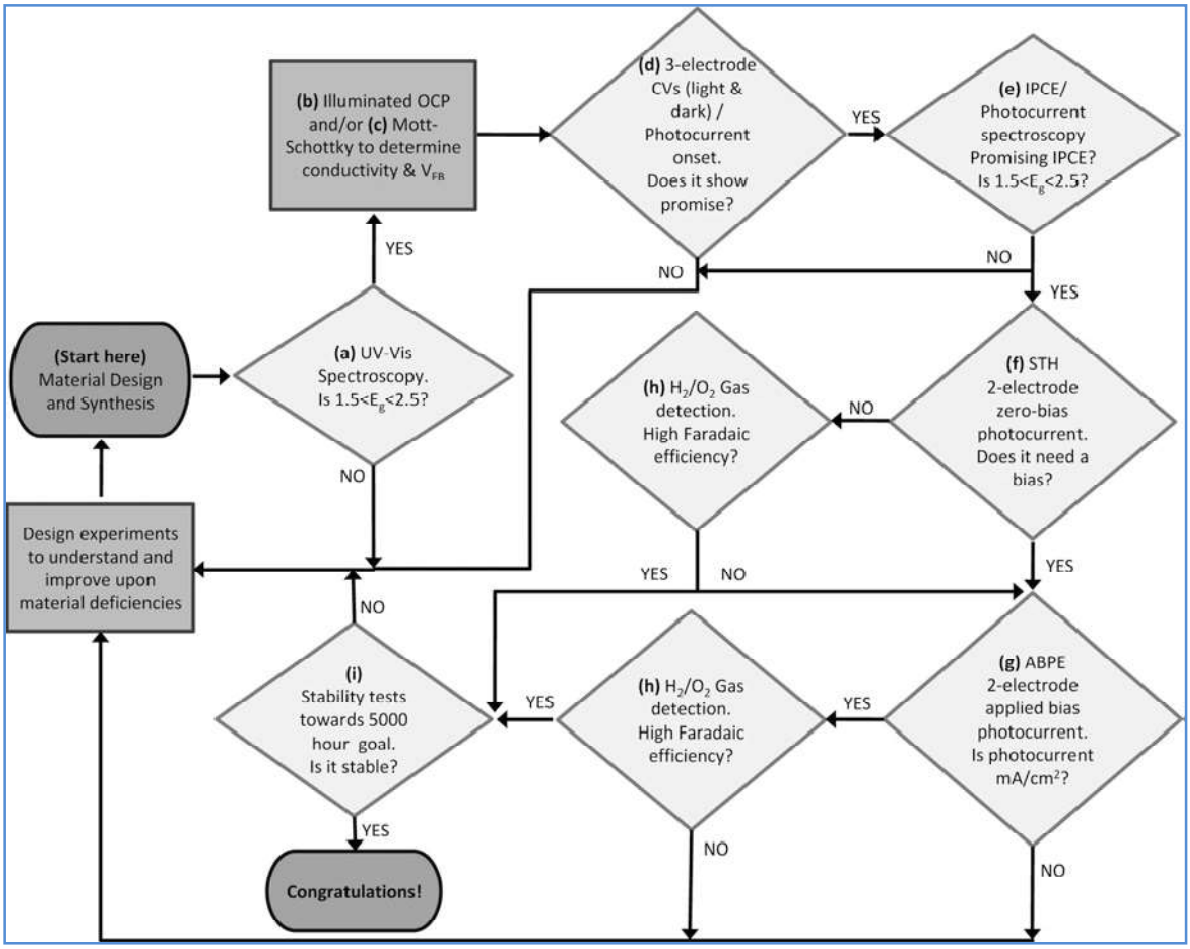

Figure 1.9: PEC characterization steps for single absorber material as suggested by ref [29]. Reproduced with permission [29], copyright 2010 Cambridge University Press.

11. Selection of materials for water splitting:

In electrocatalysis, the concept of a catalyst is introduced as a substance that can alter the rate/velocity of redox reaction without undergoing any chemical change. Thus during a faradic process, an electrocatalyst interacts with the redox species and gives rise to heterogeneous catalysis. Since the electrode materials are usually solid and the reacting species are in ionic state, heterogeneous catalysis involves dynamic adsorption/desorption steps on the surface of an electrocatalyst. Now in order to compare the activity of the catalysts, a current density at constant overpotential (or vice versa) is measured. A qualitative approach to theoretically evaluate the efficacy of a material as an electrocatalyst is provided by sebatier principle.

In order to compare the catalytic activity of different electrode materials, one can compare the current density at a constant overpotential, or measure the overpotential at a constant current density. A good electrocatalyst should show high current density at low overpotential. To understand the activity The Sebatier's principle is used. The principle states that for high catalytic activity, the reactants-catalysts interaction should neither be too strong nor too weak. If the case of too weak interaction, there will be no reaction on the surface (because it is difficult for catalyst surface to bind the reactants) and in the case of too strong interaction reaction, the reaction species is difficult to get desorbed from catalyst surface ultimately lowering the activity. Thus if one plots some adsorption property (ΔG^0_{ad}) [for instance, in case of hydrogen evolution reaction, hydrogen binding energy (HBE) is used] of the prospective electrocatalysts as a function of obtainable exchange current density or reaction rate, one can get a volcano shaped plot. This helps in identifying the catalysts with best possible activity. For example the one occupying the top of volcano plot is the best catalyst for that particular redox reaction (**Figure 1.10**). For the subsequent works done, the information from volcano plot has been invoked and an appropriate catalyst was selected based on the electrochemical process of interest (hydrogen evolution, oxygen evolution, oxygen reduction, methanol oxidation etc). The already reported works (as discussed in the introduction of each chapter) and the knowledge of volcano pot served as the basis of catalysts selection in this work.

In the case of photoelectrochemical water splitting experiments, the selection of catalyst is based on two criteria: (a) optical function and (b) catalytic function. This means that for a semiconductor to be considered as a good material for PEC water splitting, it needs to absorb maximum sunlight (visible light) and efficiently use the energy absorbed from sun to induce the redox reaction at the elecrode/electrolyte interface. The minimum energy needed to thermodynamically split water into its constituents; photons with at least energy of 1.23 eV are useful. This is equivalent to λ_{max}~1000 nm. In addition to this, there is an added restriction put forward by the thermodynamic losses and the overpotentials required for sufficiently fast reaction kinetics which dictates the minimum bandgap to be 1.9 eV.[30-32] This corresponds to λ_{max}~600 nm. For practical purpose in PEC technology minimum current density should be ca.

8 mA/cm^2 which would give STH of ca. 10%. This would mean a maximum bandgap ca. 2.4 eV. Thus an ideal band gap of a material should be in the range of 1.9-2.4 eV.

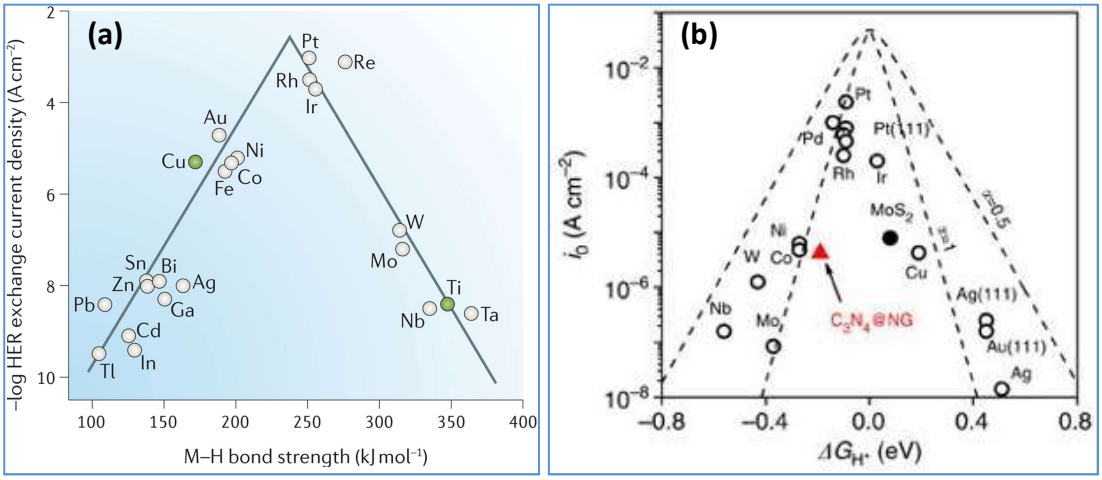

Figure 1.10: Selection of electrocatalyst: (a) Trasatti's volcano plot for transition metal electrocatalysts showing exchange current density (y-axis) and metal-hydrogen bond strength (x-axis). Reproduced with permission [33], copyright 2017, Springer Nature Ltd (b) Extended volcano plot for hydrogen evolution reaction evaluation with introduction of new catalysts- 2D materials (MoS_2) and metal-free catalyst (NG@C_3N_4). Reproduced with permission [13], copyright 2014, Springer Nature Ltd.

The next requirement is that for a single material to split water, its band edges should be suitably positioned with respect to water redox potential. The conduction band minima and valence band maxima should straddle the redox potential of water. Thus, the photo-generated charges (electrons and holes) can have required thermodynamic potential to perform water spitting. The intrinsic characteristics of the semiconductor material then comes into play to determine its charge carrier diffusion length, charge density and mobility, presence of defect states (which acts as recombination sites) and the ability to efficiently transport the charge at the interface to carry out the redox reaction. For example, the photogenerated holes should have enough η_{trans} at the interface to avoid electron-hole recombination.

One of the most vital characteristics of the prospective semiconductor material to be used as a photoelectrode is its stability under light illuminated condition. This means that some semiconductors are susceptible to self photoredox reactions; they decompose instead of participating in water spitting when illuminated. This happens if the redox potential of semiconductor is not appropriately aligned. The oxidation potential of n-type semiconductor is higher than water oxidation potential and the reduction potential of p-type semiconductor is

lower than the water reduction potential. In order to render them stable, the band edge positions should be reversed with respect to water redox potential. One of the ways to make them stable is by introduction of a thin passivating layer of stable semiconductor (eg. TiO_2). Other method includes modifying the band edge energetics in order to render a directional flow of photogenerated charges in the opposite sides (towards interface and substrate). This has been done in case of Cu_2O in chapter-5.

In the recent years there have been many reports of PEC activity tests using materials like WO_3, TaON, Fe_2O_3 etc. which are mostly oxides, sulfides, nitrides and oxyhalides. However the two most desirable candidates for PEC water splitting activity are $BiVO_4$ and Cu_2O for water oxidation and reduction respectively. In this thesis they have been used as photoelectrode material. The details of $BiVO_4$ and Cu_2O, motivations for using them and previous works based on these materials have been discussed in the introduction of chapter-5.

12. Studies reported in the thesis:

In the following works discussed, two methods of hydrogen generation has been investigated- Electrochemical and Photoelectrochemical water splitting. Apart from this, the essential component of renewable energy source-fuel cell is discussed in chapter-2.The main aim of the work is to reduce the cost of electrocatalyst by using metal-free or precious metal free catalysts as discussed in chapters-3,4 and 5. In chapter-6, the photoelectrochemical method to split water is investigated using two low cost materials- $BiVO_4$ and Cu_2O as photoanode and photocathode respectively. The objectives being – (a) develop experimental methods for the quantitative understanding of processes during photoelectrochemical oxygen evolution and hydrogen generation and (b) a better understanding of the effects introduced by the type of co-catalyst. The issue of photodegredation for oxide photoelectrode has been addressed. In this chapter the introduction to hydrogen generation using water and sunlight as the sources is discussed. The basic electrochemistry and photoelectrochemistry of water splitting reaction is discussed in details. The techniques used for the efficiency study of the selected

catalysts and the efficiency terms used to benchmark the catalysts have also been discussed. The criteria of catalysts selection and the major characteristics of the materials to be used as a catalyst are included in discussions.

13. References:

[1] Press, Roman J.; Santhanam, K. S. V.; Miri, Massoud J.; Bailey, Alla V.; Takacs, Gerald A. (2008). *Introduction to hydrogen Technology*. John Wiley & Sons

[2] A. J. Bard, M. A. Fox, Acc. Chem. Res. 1995, 28, 141.

[3] C. N. R. Rao, S. R. Lingampalli, Small 2016, 12, 16.

[4] A. Kudo, Y. Miseki, Chem. Soc. Rev. 2009, 38, 253.

[5] C. N. R. Rao, S. R. Lingampalli, S. Dey, A. Roy, Phil. Trans. R. Soc. A 2016, 374.

[6] J. E. Miller, A. H. McDaniel, M. D. Allendorf, Adv. Energ. Mater. 2014, 4, 1300469.

[7] J. R. Scheffe, A. Steinfeld, Mater. Today 2014, 17, 341.

[8] S. Abanades, P. Charvin, G. Flamant, P. Neveu, Energy 2006, 31, 2805.

[9] M. Roeb, M. Neises, N. Monnerie, F. Call, H. Simon, C. Sattler, M. Schmücker, R. Pitz-Paal, Materials 2012, 5, 2015.

[10] R. Subbaraman, D. Tripkovic, D. Strmcnik, K.-C. Chang, M. Uchimura, A. P. Paulikas, V. Stamenkovic, N. M. Markovic, Science 2011, 334, 1256.

[11] R. Subbaraman, D. Tripkovic, K.-C. Chang, D. Strmcnik, A. P. Paulikas, P. Hirunsit, M. Chan, J. Greeley, V. Stamenkovic, N. M. Markovic, Nat. Mater. 2012, 11, 550.

[12] E. J. Popczun, J. R. McKone, C. G. Read, A. J. Biacchi, A. M. Wiltrout, N. S. Lewis, R. E. Schaak, J. Am. Chem. Soc. 2013, 135, 9267.

[13] Y. Zheng, Y. Jiao, Y. Zhu, L. H. Li, Y. Han, Y. Chen, A. Du, M. Jaroniec, S. Z. Qiao, Nat. Commun. 2014, 5, 3783.

[14] E. J. Popczun, C. G. Read, C. W. Roske, N. S. Lewis, R. E. Schaak, Angew. Chem. Int. Ed. 2014, 53, 5427.

[15] S. R. Lingampalli, U. K. Gautam, C. N. R. Rao, Ener. Environ. Sci. 2013, 6, 3589.

[16] C. N. R. Rao, S. Dey, Proc. Natl. Acad. Sci. 2017, 114, 13385.

[17] T. W. Kim, K.-S. Choi, Science 2014, 343, 990.

[18] R. D. L. Smith, M. S. Prévot, R. D. Fagan, Z. Zhang, P. A. Sedach, M. K. J. Siu, S. Trudel, C. P. Berlinguette, Science 2013, 340, 60.

[19] W. Kim, T. Tachikawa, D. Monllor-Satoca, H.-i. Kim, T. Majima, W. Choi, Ener. Environ. Sci. 2013, 6, 3732.

[20] H. Dotan, K. Sivula, M. Grätzel, A. Rothschild, S. C. Warren, Ener. Environ. Sci. 2011, 4, 958.

[21] C. G. Morales-Guio, S. D. Tilley, H. Vrubel, M. Grätzel, X. Hu, Nat. Commun. 2014, 5, 3059.

[22] Allen J bard, Larry Faulkner, Fundamentals of Electrochemistry- Methods and Applications. 2nd edition, Wiley, 2000.

[23] R. Guidelli, G. Compton Richard, M. Feliu Juan, E. Gileadi, J. Lipkowski, W. Schmickler, S. Trasatti, in *Pure Appl. Chem.*, Vol. 86, 2014, 245.

[24] S. Fletcher, V. J. Black, I. Kirkpatrick, J. Solid State Electrochem. 2014, 18, 1377.

[25] J. T. S. Irvine, D. C. Sinclair, A. R. West, Adv. Mater. 1990, 2, 132.

[26] K. Gelderman, L. Lee, S. W. Donne, J. Chem. Ed. 2007, 84, 685.

[27] A. S. Bondarenko, G. A. Ragoisha, J. Solid State Electrochem. 2005, 9, 845.
[28] Z. Chen, T. G. Deutsch, H. N. Dinh, K. Domen, K. Emery, A. J. Forman, N. Gaillard, R. Garland, C. Heske, T. F. Jaramillo, A. Kleiman-Shwarsctein, E. Miller, K. Takanabe, J. Turner, in *Photoelectrochemical Water Splitting: Standards, Experimental Methods, and Protocols*, Springer New York, New York, NY 2013, 7.
[29] Z. Chen, T. F. Jaramillo, T. G. Deutsch, A. Kleiman-Shwarsctein, A. J. Forman, N. Gaillard, R. Garland, K. Takanabe, C. Heske, M. Sunkara, E. W. McFarland, K. Domen, E. L. Miller, J. A. Turner, H. N. Dinh, J. Mater. Res. 2010, 25, 3.
[30] M. F. Weber, M. J. Dignam, Int. J. Hydrog. Energy 1986, 11, 225.
[31] J. R. Bolton, S. J. Strickler, J. S. Connolly, Nature 1985, 316, 495.
[32] A. B. Murphy, P. R. F. Barnes, L. K. Randeniya, I. C. Plumb, I. E. Grey, M. D. Horne, J. A. Glasscock, Int. J. Hydrog. Energy 2006, 31, 1999.
[33] I. Roger, M. A. Shipman, M. D. Symes, Nat. Rev. Chem. 2017, 1, 0003.

Chapter-2

Electrocatalytic Properties of Platinum Nanostructures

Electrocatalytic Properties of Platinum Nanostructures

Summary *

In contrast to other shapes, tetrahedral Pt nanocrystals (Pt-NTd), with the highest number of Pt(111) surface atoms and possessing catalytic activity toward the electron transfer reactions, pose a synthetic challenge due to their thermodynamic instability. We show that, by inducing their nucleation on functionalized carbon, Pt NTds can be obtained with tunable sizes and high yields. The carbon support anchors the nanocrystals early and prevents their oriented attachment leading to nanowire formation. The in-situ generated amine is crucial for stabilization of Pt-NTds, which can later be removed to expose the Pt(111) facets for higher catalytic efficiency. Also another morphology, robust 26 nm thick free standing Pt nanosheets, an extremely rare morphology for metal nanostructures, are obtained by employing fluid induced shearing force of the order of 1.8 N and differential shear-stress of 0.5 kPa across the diameter of Te nanorod template undergoing galvanic displacement by Pt^{4+}. The bare nanocrystals and nanosheets exhibit much improved stability and electrocatalytic activity characteristic of Pt(111) toward oxygen reduction reaction (ORR) and methanol and formic acid oxidation reactions. ~90% of their activity was retained after continuous cycling.

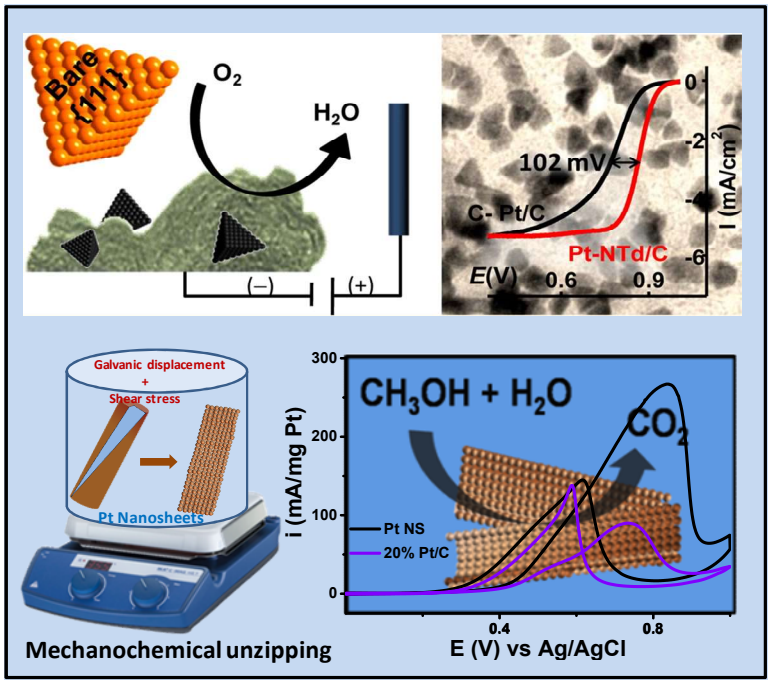

*Papers based on this work have been published in ***ACS Appl. Mater. Interfaces (2015)*** and ***Adv. Mater. (2015).***

1. Introduction:

A fuel cell (FC) is an electrochemical system that can convert chemical energy directly into electricity and thermal energy.[1,2] Owing to the advantage of not having to pass through mechanical energy conversion systems as that in case of other energy generation prototypes, fuel cells are most efficient systems for power productions.[3] As in any electrochemical cells, fuel cell consists of two electrodes (an anode and a cathode) and an electrolyte. H_2 as fuel (or small molecules like methanol, ethanol or formic acid) is provided to the anode, where it is oxidized and catalytically split into electrons and protons. The generated electrons travel through an external circuit. On the other side, the cathode, O_2 is provided to the cell where it is reduced using electrons from the external circuit. Ions combine within the electrolyte to balance the flow of electron to produce byproduct and heat (**Figure 2.1**). In case of H_2 and O_2 being used as fuel, heat and water is produced as by-products, thus making it an environmental friendly energy generation system. The direct current (DC) produced from flow of electrons from anode to cathode is continuous until the fuels lasts. Fuel cells can be installed near the place of usage and are portable. This system modular so can be built depending on the power requirements, from hundreds of watts to megawatt size.

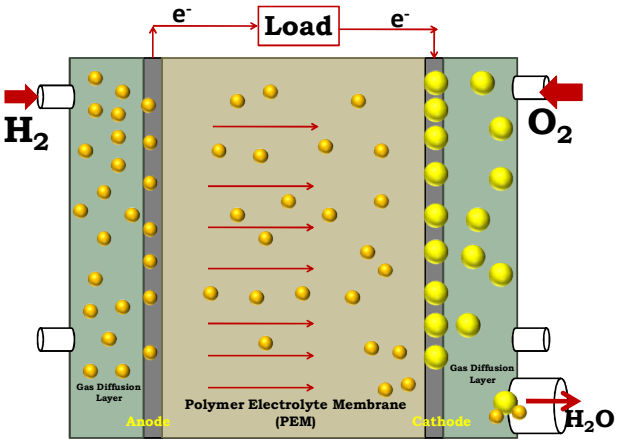

Figure 2.1: Schematic representation of fuel Cell Device [adapted from ref. 4]

1.1. Types of Fuel cells and the corresponding electrode reactions:

Depending on the kind of electrolyte they utilize, fuel cells can be classified into various categories. This classification determines the kind of catalysts required and kind of the electro-chemical reactions that take place in the cell, the temperature range in which the cell operates and the fuel required.

Table 1: Types of fuel cell and their comparison (adapted from ref. 4 and NREL website)

Fuel Cell Type	Common Electrolyte	Operating Temperature	Typical Stack Size	Electrical Efficiency (LHV)	Applications	Advantages	Challenges
Polymer Electrolyte Mebrane (PEM)	Perfluorosulfonic acid	<120°C	<1 kW - 100 kW	60% direct H_2	Backup power, Portable power, Distributed generation, Transportation Specialty vehicles	Less corrosion & electrolyte management problems Low temperature Quick start-up and load following.	Expensive catalysts Sensitive to fuel impurities.
Alkaline (AFC)	KOHin a porous matrix, or alkaline polymer membrane.	<100°C	1 - 100 kW	60%	Military, Space Backup, power Transportation.	Stable materials, lower cost components Low temperature, Quick start-up.	Sensitive to CO_2 in fuel and air. Electrolyte management.
Phosphoric Acid (AFC)	H_3PO_4 in porous matrix or imbibed in a polymer membrane.	150 - 200°C	5 - 400 kW, 100 kW .	40%	Distributed generation.	Suitable for CHP Increased tolerance to fuel impurities.	Expensive catalysts Long start-up time Sulfur sensitivity.
Molten Carbonate (MCFC).	Molten lithium, sodium, and/or potassium carbonates, soaked in a porous matrix.	600 - 700°C	300 kW - 3 MW, 300 kW module.	50%	Electric utility Distributed generation.	High efficiency Fuel flexibility Suitable for CHP Hybrid/gas turbine cycle.	High temperature corrosion and breakdown of cell components Long start-up time
Solid Oxide (SOFC)	Yttria stabilized zirconia .	500 - 1000°C	1 kW - 2 MW	60%	Auxiliary power Electric utility Distributed generation.	High efficiency Fuel flexibility Solid electrolyte Suitable for CHP Hybrid/gas turbine cycle.	High temperature corrosion and breakdown of cell components Long start-up time Limited shutdowns.

Hence the specific application of the fuel cells depends on its characteristics for which these cells are most suitable. There are several types of fuel cells currently undergoing research and development, each with its own potential applications, advantages and limitations as given in **Table 1**.

In the present chapter the reaction kinetics of two important types of fuel cells and the development in the catalysts requirements have been discussed- Polymer electrolyte membrane (PEM) fuel cells and Direct Alcohol Fuel cells (DAFC). PEM fuel cells utilizes solid proton conducting polymer as an electrolyte and porous carbon electrodes containing a platinum group elements as catalysts. They are fueled with pure hydrogen and oxygen from air. The major rate limiting step here is the cathode reaction i.e. Oxygen Reduction Reaction (ORR). The advantage of PEM is that they can operate at relatively low temperatures (80°C) and hence are durable. The applications of PEM fuel cells include stationary power generations and transportations like passenger vehicles. Another important type of fuel cell includes small molecules like methanol, ethanol or formic acid as fuel for anode and oxygen for anode. They are direct alcohol fuel cells (DAFCs). They do not have fuel storage problems because methanol has a higher energy density than hydrogen. Methanol is also easier to transport and supply to

the public using our current infrastructure because it is a liquid.[4,5] DMFCs can be used for powering portable devices like cell phones or laptop, computers etc. The fuel cell reaction is:

Cathode: $2H_2 \rightarrow 4H^+ + 4e^-$ (or Alcohol oxidation); ***Anode:*** $O_2 + 4H^+ + 4e^- \rightarrow 2H_2O$

Net Reaction: $2H_2 + O_2 \rightarrow 2H_2O$

1.2. Mechanism of Oxygen Reduction Reaction (ORR) and Methanol Oxidation Reaction (MOR):

ORR in aqueous solutions occurs mainly by two pathways: the direct 4-electron reduction pathway from O_2 to H_2O, and the 2-electron reduction pathway from O_2 to H_2O_2. In non-aqueous aprotic solvents and/or in alkaline solutions, the 1-electron reduction pathway from O_2 to superoxide (O_2^-) can also occur. In PEM fuel cells and DMFCs, ORR occurs at the cathode. Due to involvement of 4 electrons, the ORR kinetics is very slow in comparison to anode reaction kinetics (PEM fuel cell).[6]

$$O_2 + 4H^+ + 4e^- \rightarrow H_2O \ \ (E^0 = 1.229\,V) - (i)$$
$$O_2 + 2H^+ + 2e^- \rightarrow H_2O_2 \ \ (E^0 = 0.7\,V) - (ii)a$$
$$H_2O_2 + 2H^+ + 2e^- \rightarrow 2H_2O \ \ (E^0 = 1.76\,V) - \ (ii)b$$

The above equations shows the thermodynamic electrode potentials of electrochemical O_2 reduction in acid medium undergoing 4 electron pathway (equation *i*) and (2+2) electron pathway (equation *ii*) reduction to environmentally benign water as by-product. Similarly, in alkaline medium O_2 undergoes following 4 electron (equation *iii*) and (2+2) electron reduction (equation *iv*) reactions.

$$O_2 + H_2O + 4e^- \rightarrow 4OH^- \ \ (E^0 = 0.401\,V) - \ (iii)$$
$$O_2 + H_2O + 2e^- \rightarrow HO_2^- + OH^- \ \ (E^0 = -0.065\,V) - \ (iv)a$$
$$HO_2^- + H_2O + 2e^- \rightarrow 3OH^- \ \ (E^0 = 0.867\,V) - \ (iv)b$$

Ideally in a fuel cell, the 4-electron pathway is preferred. The (2+2) electron reduction pathway is used in industry for H_2O_2 production. The 1-electron reduction pathway is of importance in the exploration of the ORR mechanism. ORR is a multistep electrochemical reactions involving complex oxygen-containing species: O, OH, O_2^-, HO_2^-.[7] Due to the lower overpotential (η) and fast kinetics, ORR in alkaline medium is favorable for practical purposes. To understand ORR

mechanism it is imperative to use rotating disk electrode (RDE), the reason for the same is demonstrated below:

An electrochemical reaction on the surface of electrode can occur by two limiting mechanisms: kinetically controlled and diffusion controlled reactions of species. If kinetics of reaction are extremely fast, the electrochemical reaction is diffusion controlled (mass transport of the species that enters or leaves the electrode surface). On the other hand if the diffusion of the species is infinitely fast, the reaction is kinetically controlled. In ORR both the limiting steps are possible. So in order to discern the mechanism of ORR by electrocatalysts, i.e. to calculate the number of electron involved in ORR, we must negate the diffusion controlled part of reaction. This has been modeled by Veniamin Grigorievich Levich using Butler-Volmer equation in Levich equation (equation *v*) by which the rotation of RDE makes the reaction diffusion independent.

$$I_L = (0.620)nFAD^{\frac{2}{3}}\omega^{\frac{1}{2}}v^{\frac{-1}{6}}C \quad (equation - v)$$

And modified by Koutecky in Koutecky-Levich equation (K-L) (equation *vi*) as,

$$\frac{1}{I} = \frac{1}{I_L} + \frac{1}{I_K} \; (equation - vi)$$

where $I_K = nFAK_{O2}C_{O2}S_{cat.}$; *n*=number of electrons; F= faraday constant; *A*= electron area; K_{O2}= electron transfer constant; C_{O2}=concentration of dissolved oxygen and $S_{cat.}$ is the electrochemical surface area of catalyst. *D*=diffusion coefficient of O_2, v is the kinematic viscosity of electrolyte and ω is the rotation rate. Equation vi can be rewritten as,

$$\frac{1}{I} = \frac{1}{B\omega^{\frac{1}{2}}} + \frac{1}{I_K}$$

where $B = (0.620)nFAD^{\frac{2}{3}}v^{\frac{-1}{6}}C$. Hence at different rotation rate gives different saturation current (**Figure 2.2)**. Also for RDE data analysis, three non-electrochemical kinetic parameters, such as the diffusion coefficient of O_2, the kinematic viscosity of the electrolyte solution and the solubility of O_2 must be known accurately.

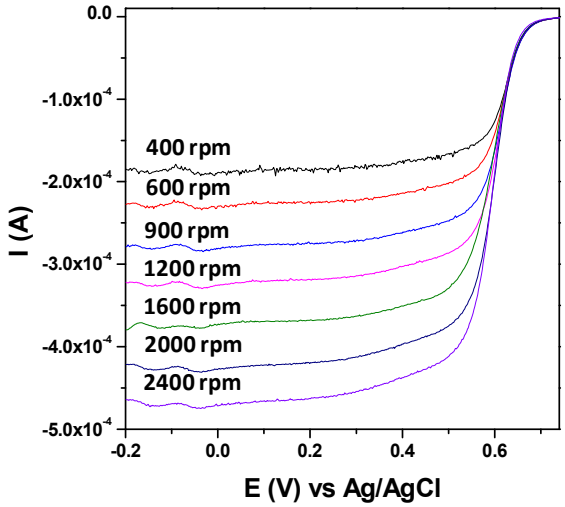

Figure 2.2: Example of variation of ORR current density as a function of rotation rate for Pt Nanowires.

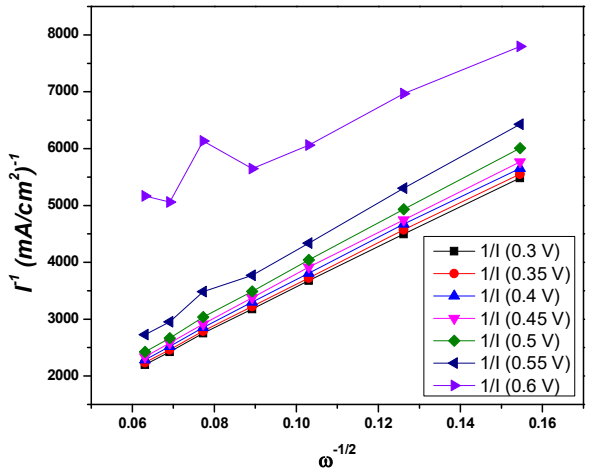

Figure 2.3: Example of inverse of total current measured at 1600 rpm for Pt Nanowires.

From an experimental data set where the current is measured at different rotation rates, it is possible to extract the kinetic current from a K-L plot. In K-L plot the inverse measured current is plotted versus the inverse square root of the rotation rate (**Figure 2.3**). This gives a linear plot from which data set and the inverse of the kinetic current can be obtained by extrapolating the line. The slope can be used to calculate number of electrons involved in ORR. Similarly, for alcohol oxidation which is the cathodic part of fuel cell following reactions takes place:

$$\boldsymbol{Anode}: CH_3CH_2OH + 12OH^- \rightarrow 2CO_2 + 9H_2O + 12e^-$$

$$\boldsymbol{Cathode}: 3O_2 + 6H_2O + 12e^- \rightarrow 12OH^-$$

While ORR is diffusion driven, electrooxidation of liquid fuel like alcohol is catalytically driven process. Since more number of electron is involved in this reaction, the mechanism is very complex and the reaction can proceed through series of intermediates. A complete reaction ($12e^-$) process should yield CO_2 and water as by-products (**Figure 2.4**).

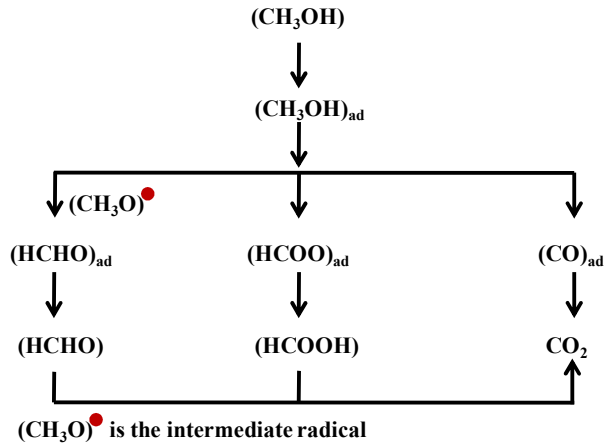

Figure 2.4: Mechanism of the electro-oxidation of methanol on Pt to form CO_2. The possible paths which lead to the formation of formaldehyde, carbon monooxide and formic acid are shown.

The oxidation of methanol or any small molecule may proceed through dual pathway, either incomplete reduction forming corresponding acid or aldehyde or forming carbon dioxide after complete reduction.

1.3. Role of Nanostructured Catalyst in fuel cell technology:

In this chapter the discussion is devided into two parts on two different types of Pt nanostructures and their effects in electrocatalytic properties. Thus, the motivation related to them is discussed separately as two parts: A and B.

1.3.1. Part-A: Pt Nanotetrahedra: Nanostructuring of active catalysts significantly improve the efficiency of low temperature fuel cells in terms of cost, performance and durability. Platinum as a catalyst for fuel cell technology still remains unbeaten. However the limited availability and cost factor dictates either Pt to be replaced by less cost catalysts like its alloys or transition metal or carbon based catalysts or improve the activity of Pt by Shape controlled nanocrystal synthesis. This would provide more active surface as well as higher mass and specific activity and hence lead to low cost energy production. The efficiency of nanocrystals

(NCs) of Pt is dependent on their shapes, as different shapes are enclosed with different crystallographic facets.[8,9] Those shapes include cubes ({100} planes), octahedra ({111} planes), icosahedra ({111} planes), octapods ({411} planes), and others.[10,11] (**Figure 2.5**)

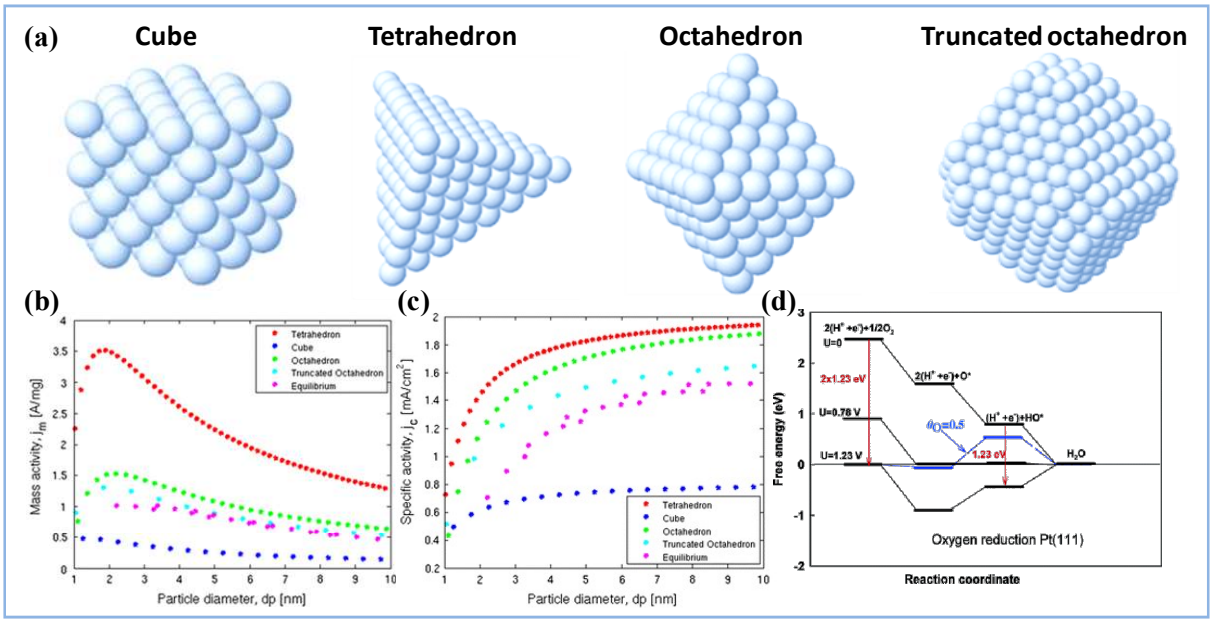

Figure 2.5: (a) Illustrations of different shapes (b and c) Dependence of the mass activities, j_m and specific activities, j_c, on the particle size of different shapes. Reprinted with permission[12], Copyright 2014, Springer. (d) Free-energy diagram for oxygen reduction over Pt(111) at zero cell potential (U = 0), at the equilibrium potential (U = 1.23 V), and at the highest potential (U = 0.78 V) where all reaction steps are exothermic. Reprinted with permission[13] Copyright 2004, American Chemical Society.

Amidst much progress, however, one aspect has triggered scientific curiosity. As many have observed, Pt NCs with tetrahedral morphology, covered entirely with {111} planes and having the highest number of closed-pack surface atoms, are extremely difficult to prepare. This is particularly the case when the size is less than 20 nm, and instead, thermodynamically more stable Pt octahedral nanocrystals are formed under the experimental conditions.[14,15] Octahedral NCs also have all {111} surfaces but are more stable than the of tetrahedral Pt nanocrystals (Pt-NTd) due to their smaller surface/edge and the surface/volume ratios. A Pt(111) facet possesses a higher atomic packing density than any other crystal-plane, resulting in lower electron affinity of the exposed Pt atoms. This led to the favorable adsorption of different chemical species, making Pt(111) facet catalytically more efficient than the other ones.[16,17] Besides, these also exhibit the highest stability against leaching and surface corrosion due to the strong cohesive energy (defined as the sum of all bond energies associated with a

single atom) of the surface Pt atoms.[17,18] Due to these factors, Pt(111) is the most desirable catalyst facet for many commercially as well as fundamentally important chemical transformations (**Figure 2.5**). For instance, recent theoretical investigations have shown that the Pt(111) plane is superior for the oxygen reduction reaction (ORR) due to a greater number of active sites for oxygen adsorption which leads to higher onset potential for O/OH adsorption and less surface poisoning.[12,13,19] (**Figure 2.5d**). In addition to single crystalline planes, the 111/111 edges having the highest coordination to the neighboring surface atoms also contribute to the ORR activities when compared with other edges.[16] This is because a higher coordination number leads to broadening of d-band and higher d-band filling which in turn causes a weaker Pt−O bond at these sites.[20] Therefore, due to the largest number of exposed (111) atoms, Pt-NTds are preferred model systems for many industrial processes. To the best of our knowledge, till 2015 however, there were only two methods to synthesize Pt-NTds in high-yield. El-Sayed and co-workers,[21,22] in an early pioneering work, established the synthesis of ~70% Pt-NTds using PVP and H_2. Chiu et al.[22] showed that a suitable amino acid sequence can be designed to prepare ~57% Pt-NTds. Occasionally, however, mixtures of octahedral nanocrystals mixed with a smaller fraction of tetrahedral ones can be obtained.[23,24] Since the high yield methods use long surface stabilizing agents, their presence is expected to lead to deteriorated catalytic performance by interfering with the approach of the chemicals to the nanocrystal surface or by modifying the interactions of catalysts with its support, and therefore, additional surface treatment may be required to remove them.

1.3.2. Part-B: Pt Nanosheets: Nanosheets (NSs) and nanoribbons of a variety of inorganic compounds have unique properties, electronic structures as well as diverse potential applications including energy harvesting and energy storage, catalysis, biological sensing, and electronic devices. Metal nanostructures on the other hand, usually form spherical or faceted nanocrystals (NCs), elongated nanorods (NRs), and occasionally even longer nanowires in template-assisted wet chemical processes.[25] The interesting properties of the metallic nanostructures are directly associated with their shape anisotropy, providing a way to enhance their efficiencies in many applications simply by tailoring their synthetic conditions.[26] Such possibility has led to a tremendous progress in shape controlled synthesis of 0D and 1D metallic

nanostructures. However, unlike those inorganic compounds that are intrinsically layered in structure and easily form stable nanosheets, 2D metal nanostructures are considerably more difficult to obtain due to lack of means to induce such a growth, marking their preparation as an important synthetic challenge. And only in the last couple of years, researchers have been able to develop a few strategies for the synthesis of nanosheets of certain metals and examine their properties. These also include assembling lower dimensional nanocrystals in a confined 2D space.[27] Graphene oxide has been used as a template to obtain gold nanosheets with an unusual hexagonally close-packed crystal-lattice. Small adsorbate molecules such as CO have also been shown to induce growth of palladium nanosheets.[28] More recently, lamellar bilayer membranes of surfactants have been used as soft templates for producing Au nanosheets with unique plasmonic properties.[29] Nonetheless, some of these successes may merely be accidental and a detail understanding of 2D growth of metallic nanocrystals is yet to arise. Platinum, for example, can be considered as the most important catalyst among all metals used in industrial processes and therefore it will be of great importance to explore possibility of obtaining freestanding Pt nanosheets. Thickness of a nanosheet can be regulated by examining its growth and tuning the synthesis parameters, although controlling their lateral dimensions is more difficult and usually leads to large size dispersions. Recently, 1D nanotubes of inorganic compounds have been used as templates to obtain nanosheets in an interesting approach, wherein vertical unzipping of the nanotubes results in sheets and ribbon-like structures with predictable widths as well as thicknesses.[30] For instance, treating multiwall carbon nanotubes with strong acids and oxidizing agents or Ar-plasma produces nanoribbons having few graphene layers[31] (**Figure 2.6**). Even simple mechanical forces from hypervelocity impact have been shown to induce defects and atom evaporation in the nanotubes, leading to their unzipping. A similar approach for nanosheets is difficult to envision in the case of metal nanotubes as they do not form by a rolling up mechanism.

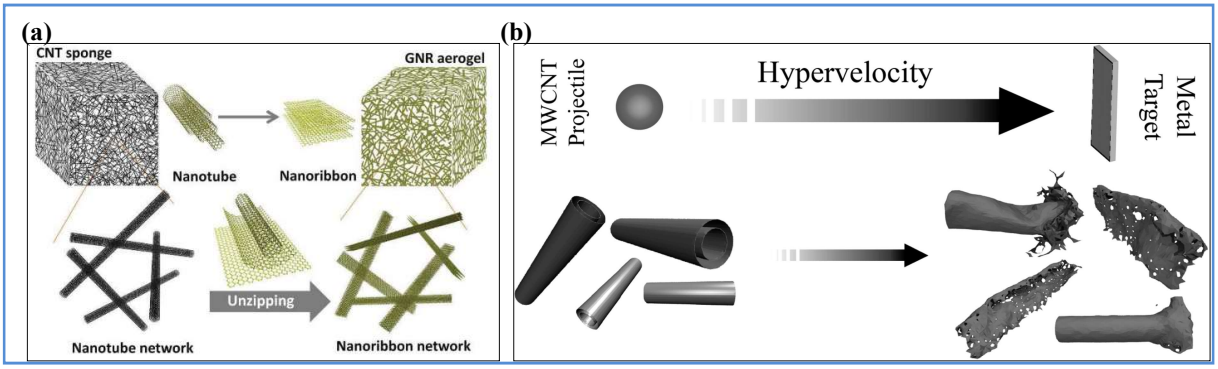

Figure 2.6: (a) Illustration of the process in which a CNT sponge is directly converted into a GNR aerogel by unzipping multi-walled nanotubes into multi-layer graphene nanoribbons, while maintaining the original three-dimensional network. Reprinted with permission[31] Copyright, 2014 WILEY-VCH Verlag GmbH&Co. KGaA, Weinheim. (b) Scheme for experimental approach used in current work showing randomly aligned carbon nanotubes subjected to high velocity and the resulting structure after process. Reprinted with permission[32] Copyright 2014, American Chemical Society.

2. Scope of the Investigations

The presence of capping agents on the electrocatalysts surface hinders its activity by blocking the active sites. Hence a simple one-step and high-yield method to synthesize sub-10 nm Pt tetrahedral NCs, loaded onto a conducting carbon support (Pt-NTd/C) has been obtained for electrocatalytic applications. No external reagent was used for controlling the selective growth of NC facets. Instead, a secondary amine species having a high affinity toward the closest-packed Pt(111) facets was generated in situ in the reaction. Dimethylamine so generated can be washed away from the catalyst surface, leading to bare Pt-NTd surfaces. External addition of secondary amine stabilizers results in much lower yields of Pt-NTds. The presence of carbon support in the reaction medium is crucial as it anchors the Pt nanoclusters generated at an early stage of the reaction and lets them evolve into shapes. The absence of carbon support encourages the association of NCs and formation of 1D nanowires by an oriented attachment mechanism. Due to the bare {111} facets, Pt-NTd/C exhibit excellent efficiency and stability toward the oxygen reduction reaction. We further report on the electrocatalytic oxidation efficiency of small renewable fuel molecules such as methanol and formic acid on the bare surfaces. Also in the subsequent section, robust, 26 nm thick free-standing platinum nanosheets, an extremely rare morphology for metal nanostructures, are obtained by employing fluid induced shearing force of the order of 1.8 N and differential

shear-stress of 0.5 kPa across the diameter of a Te template nanorod undergoing galvanic displacement by Pt^{4+}. Corrugation leads to their large surface area and much improved electrocatalytic properties when compared with conventional Pt catalysts. These electrocatalysts exhibit excellent activity towards practically important reactions like ORR, MOR and FAO. The activities are better than commercially available Pt electrocatalysts.

3. Experimental Section

3.1. Materials

Chloroplatinic acid hexahydrate ($H_2PtCl_6.6H_2O$, Sigma-Aldrich, ACS Reagent, 37.5% Pt basis), ethylene glycol (EG, 99%, SDFCL), N,N- dimethylformamide (DMF, 99.9%, Merck), Amorphous carbon (Vulcan XC72) ,Water (Millipore, 18.2 Ω), Ethanol, Nafion (5%, Sigma-Aldrich), Sodium tellurite (Na_2TeO_3, Sigma-Aldrich), poly(vinyl pyrrolidone) (PVP10-100G, Sigma-Aldrich, Avg. mol wt 10,000), hydrazine hydrate ($H_4N_2.H_2O$, SDFCL, 99%, AR), aqueous ammonia solution (NH_3, SDFCL, 30%, AR) and were used without further purification were used as received without further purification.

3.2. Synthesis

3.2.1. Synthesis of Pt nanotetrahedra nanocrystals (called as Pt-NTd/C): Pt nanotetrahedra were prepared by solvothermal method as briefed. 50 mg of H_2PtCl_6 (37% Pt basis, Sigma) was taken in a 25 mL round bottom flask. 6 mL DMF and 4 mL EG was added to dissolve the Pt precursor. 500 mg KOH was put to the mixture and was stirred overnight at 27 ˚C. To the clear yellow colored solution so obtained, 14.2 mg of acid treated Vulcan-X72 carbon (see below) was added. The mixture was sonicated for 15 minutes and then was transferred into a 25 mL teflon lined stainless steel autoclave. The autoclave was maintained at 170^{o}C for 8 hours and then cooled to room temperature (it takes about 1.5 hour for natural cooling). The black product so obtained was washed several times with water and ethanol and centrifuged at 10,000 rpm. The final product was then dispersed in ethanol and allowed to dry overnight at 70 ^{o}C in vacuum and used for various characterizations. To investigate the effect of various

experimental parameters, control reactions were carried out with different amount of solvents as well as using other relevant chemicals, as described in preceding sections.

3.2.2. Acid treatment on carbon support: 1 g carbon powder (Vulcan-X72) was exposed to 100 mL of 5 M HCl at 50 °C for 12 hours with continuous stirring. This material (C_t) was washed with water and ethanol several times to remove excess HCl and dried at 60 °C in vacuum overnight.

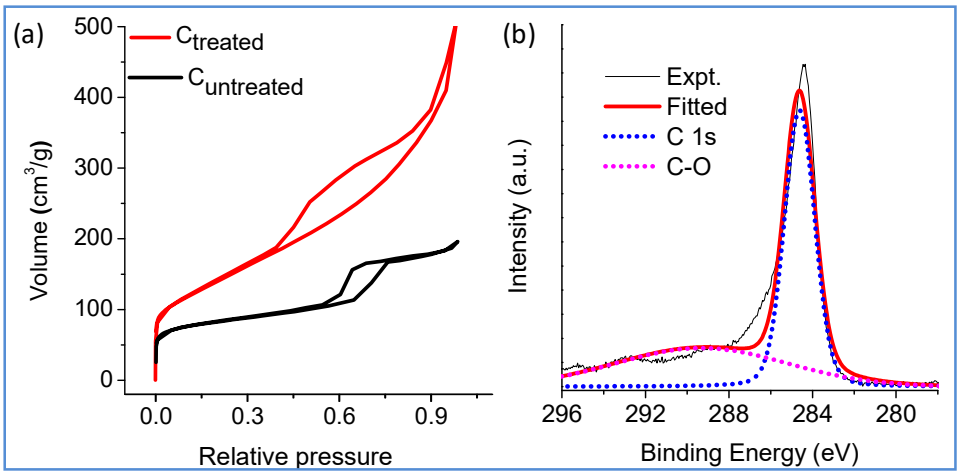

Figure 2.7: Brunauer–Emmett–Teller (BET) plot of treated and untreated carbon for N2 adsorption at 77 K. The surface area in treated carbon (497.76 m²/g) was found to be increased compared to the pristine amorphous carbon (265.52 m²/g).

This treatment makes their dispersion extremely stable in polar solvents such as water (up to several hours). In addition, this treatment introduces surface functional groups, which is responsible for improved adsorption of metal salts[33]. This also leads to a high surface area of 497.76 m²/g compared to 265.52 m²/g for the untreated sample. (**Figure 2.7**)

3.2.3. Control Experiments: In order to investigate *the effect of reaction time* on the evolution of desired shape, reactions were carried out by varying the time of solvothermal treatment (1h, 2h, 4h and 12h) and keeping all the other reaction conditions same. In order to investigate the effect of solvent on shape of the NCs, reactions were performed by changing the relative ratios of DMF/EG systematically. For this, different amounts of DMF and EG were employed in the initial step of the reaction procedure. The various ratios of DMF/EG used were 0:10, 2:8, 4:6, 6:4, 8:2 and 10:0. In order to confirm the role secondary amine species in shape control, a

reaction was carried out by replacing DMF with diethylamine and using EG as the only reducing agent.

3.2.4. Synthesis of Te nanorods (NR): Te NRs were prepared by using previously reported hydrothermal method.[34] In a typical synthesis, 1 g PVP and 0.0922 g Na_2TeO_3 (0.416 mmol) were dissolved in 25 mL of DI water under vigorous magnetic stirring at room temperature to form a homogenous solution. Next, 1.65 mL of hydrazine hydrate (85%, w/w %) and 3.35 mL of aqueous ammonia solution were added to it. This mixture was then transferred to a Teflon lined stainless steel autoclave (50 mL) and placed in a preheated oven at 180^{o}C for 4 hour. The sample was then allowed to cool to room temperature under ambient atmospheric conditions. Te NRs were precipitated by adding 90 ml acetone to the reaction mixture and collected by centrifugation (10,000 rpm, 10 min). The Te NRs were washed several times with double-distilled water and absolute ethanol before further characterization.

3.2.5. Synthesis of Pt nanosheets (Pt NS): Te nanorods 12.76 mg (0.1 mmol) was dispersed in 20 mL of EG with vigorous magnetic stirring at room temperature and then 63.26 mg $H_2PtCl_6.6H_2O$ (0.12mmol Pt) was added to it. The mixed solution was then magnetically stirred at 900 rpm for 15 h at 50^{0}C. The products were collected by centrifugation (10,000 rpm, 15 min) and washed several times with double-distilled water and absolute ethanol. Additional control experiments were carried out where (i) the amount of Pt precursor was reduced and (ii) reaction intermediates were collected at 2 h intervals during the Pt NS growth and (iii) by varying the stirring rate at 0, 300, 600, 900, 1200 and 1500 rpm). This helped in studying the mechanism of Pt NS growth and the effect of various reaction parameters.

3.3. Characterizations:

Powder X-ray diffraction data (PXRD) of all Pt-NTd/C catalysts were recorded using a Bruker AXS D8 Discover diffractometer attached with Cu Kα radiation). Field-emission scanning electron microscopy studies were carried out using FEI Quanta FESEM equipped with energy-dispersive X-ray spectroscopy (EDX), under 10 kV accelerating voltage and 10 microsecond accumulation time. Transmission electron microscopy (TEM, Technai F30 UHR, 200 kV and FEI Titan 80–300 kV, aberration-corrected) were used to study the morphology and crystallinity of the Pt-NTd/C

nanocrystals and Pt NS. Inductively coupled plasma mass spectrometry (ICP-OES, Perkin Elmer Optima, 7000DV) was used to determine the atomic ratios of Te and Pt in various reaction products and the percentages of Pt loading on the carbon support. X-ray photoelectron spectroscopy (XPS, VG Scientific ESCA LAB V) was employed to study the surface properties. The ^{1}H nuclear magnetic resonance (NMR) measurements were carried out with NMR (Bruker AV-400) using 10 µL of aliquot in 0.5 mL $CDCl_3$.

3.4. Electrochemical Characterization:

3.4.1. Electrochemical activity of Pt nanostructures towards ORR and small molecule oxidation: The electrocatalytic activities of Pt-NTd/C and the commercial 40% Pt/C (Pt on graphitized carbon, Sigma Aldrich) and Pt NS towards oxygen reduction reaction (ORR), methanol oxidation reaction (MOR) and formic acid oxidation (FAO) were studied by cyclic voltammetry (CV) and linear sweep voltammetry (LSV) techniques. The measurements were done on electrochemical workstation (CHI760E and RRDE-3A) using three electrode system – a glassy carbon (GCE) electrode (3 mm in diameter) as substrate for working electrode, Ag/AgCl (3 M NaCl) as the reference electrode and a platinum coil as the counter electrode. Prior to use, the GC electrode was well polished using alumina powders (particle sizes 1µm, 0.3µm and 0.05µm on nylon cloths) until mirror shiny surface was obtained. Catalyst ink for the working electrode was prepared by dispersing 1.6 mg of Pt-NTd/C catalyst in 300 µL of nafion solution (5 wt% nafion:isopropanol:water = 0.05:1:4 (v/v/v)). The optimization of this ink composition was done based on the quality of film formed on GCE after many control experiments. This composition optimizes the viscosity and drying time of ink to form smooth continuous film of catalysts on GCE. 10 µL of this ink was drop-casted on the polished GC and allowed to dry overnight. Pt loading on the GC was calculated accordingly (based on ICP data) and was estimated to be 0.028 mg/cm^2 or as mentioned in proceeding sections. CV was recorded in Ar saturated 0.1 M $HClO_4$ (aq. solution) in the potential window of -0.25 V to 0.9 V at a scan rate of 50 mV/s. LSV was performed in O_2 saturated 0.1 M $HClO_4$ in the potential range of -0.25 V to 0.9 V and scan rate of 5 mV/s. The stability tests were done by performing accelerated CV cycles. For MOR and FAO study, CV profiles were recorded at the scan rate of 20 mV/s in Ar saturated 0.1 M $HClO_4$ + 1 M CH_3OH and 0.1 M $HClO_4$ + 1 M HCOOH respectively. For MOR

and FAO, stability was checked by chronoamperometry measurements (recorded at a voltage corresponding to peak forward current, I_f). For Pt NS, CV was recorded in 0.5 M H_2SO_4 (aqueous), saturated with UHP Ar gas (99.99%, Chemix specialty gasses and equipments, Bangalore, India) purged for 15 minutes and in the potential range of -0.25 V to 1 V at the scan rate of 50 mV/s. For MOR and FAO study, CV profiles were recorded at the scan rate of 20 mV/s in Ar saturated 0.5 M H_2SO_4 + 1 M CH_3OH and 0.5 M H_2SO_4 + 1 M HCOOH respectively. The accelerated stability test of catalyst was checked by the CVs recorded between 0.4-0.9 V, scan rate of 0.1 V/s.

3.4.2. Calculations: The Electrochemical active surface area (ECSA) of the Pt NS was calculated by the following relationship:

$$ECSA = \frac{Q_H}{q_H \times (mg\ Pt)}$$

Where q_H is the charge deposited per unit surface area of polycrystalline Pt electrode surface due to underpotentially deposited monolayer of hydrogen atom on the Pt surface. q_H on 0.5 M H_2SO_4 is equal to 230 μC/cm^2. Q_H is the charge associated with the hydrogen adsorption calculated from the recorded CV of the PtNS in Ar saturated 0.5 M H_2SO_4 in the potential range of -0.25 V – 0.18 V vs Ag/AgCl.

4. Results and Discussion

The two advantageous morphology of Platinum obtained by us have been individually studied for the respective cathode and anode part of fuel cell components. While Pt nanotetrahedra is discussed with respect to its activity towards oxygen reduction reaction (ORR), Pt nanosheets have been studied for its activity towards methanol and other small molecule oxidation (MOR). ORR is a cathode and MOR is anode of fuel cell reaction. The rationale of synthetic protocol, corresponding mechanism and the enhancement in activity towards these electrocatalytic reactions along with appropriate inferences from the study is discussed in two parts A and B as follows:

Part-A:

High-Yield Synthesis of Sub-10 nm Pt Nanotetrahedra with Bare ‹111› Facets for Efficient Electrocatalytic Applications

The Pt NTd nanocrystals supported on activated carbon (Pt-NTd/C) obtained after 8 hours of reaction were investigated by electron microscopy. **Figure 2.8a, b** show overview transmission electron microscope (TEM) images of Pt-NTd/C. The NCs are uniform, with an average size of 7.1±0.9 nm and well dispersed on the carbon support (**Figure 2.8a and 2.9**).

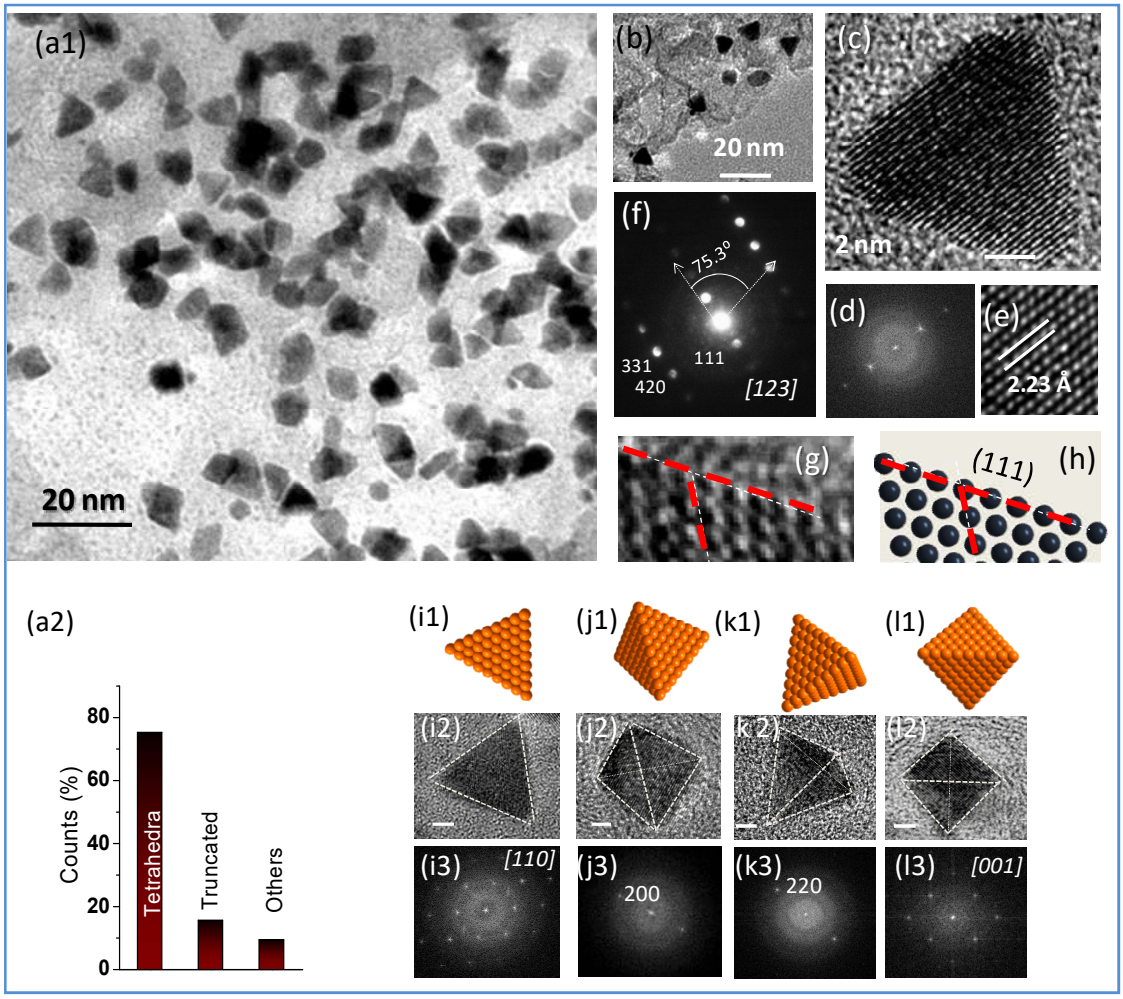

Figure 2.8: (a, b) TEM images of Pt-NTd/C obtained after 8 h using an EG/DMF ratio of 4:6. (a2) Shape distribution of the NCs. (c, d, e) HRTEM image and the corresponnding FT pattern of a Pt particle. (f) SAED pattern of the particle viewed along the [123] zone axis. (g) HRTEM image of an edge of a particle and (h) the corresponding model showing the atomic arrangement (i–l): (1) Atomic model, (2) TEM images, and (3) corresponding FFT patterns of various Pt-tetrahedron nanocrystals from different projections. The scale bars in the (i–l) TEM images denote 2 nm.

A careful analysis of the images suggests that about 75% of the NCs are tetrahedra, the rest consists of other shapes (**Figure 2.8a**). The powder X-ray diffraction pattern of the Pt-NTd/C confirms that the as-prepared sample is exclusively composed of face-centered cubic Pt (JCPDS no. 65-2868, a = 3.706(1) Å) (**Figure 2.10**). Single-crystalline nature of Pt NTds is observed from

the high resolution TEM image and its corresponding fourier transform (FFT) pattern are shown in **Figure 2.8c,d**. Pt(111) planes corresponds to the lattice fringes of 2.23 Å parallel to the edge which indicates that the facets at the surface consists of {111} planes (**Figure 2.8e and 2.9**). The electron microscopy reveals the triangular appearance of Pt NTds. This triangular appearance can arise because of plate-like triangular Pt NCs also, covered with {111} and {100} facets, in which case the particle should be associated with stacking fault along the {111}[35].

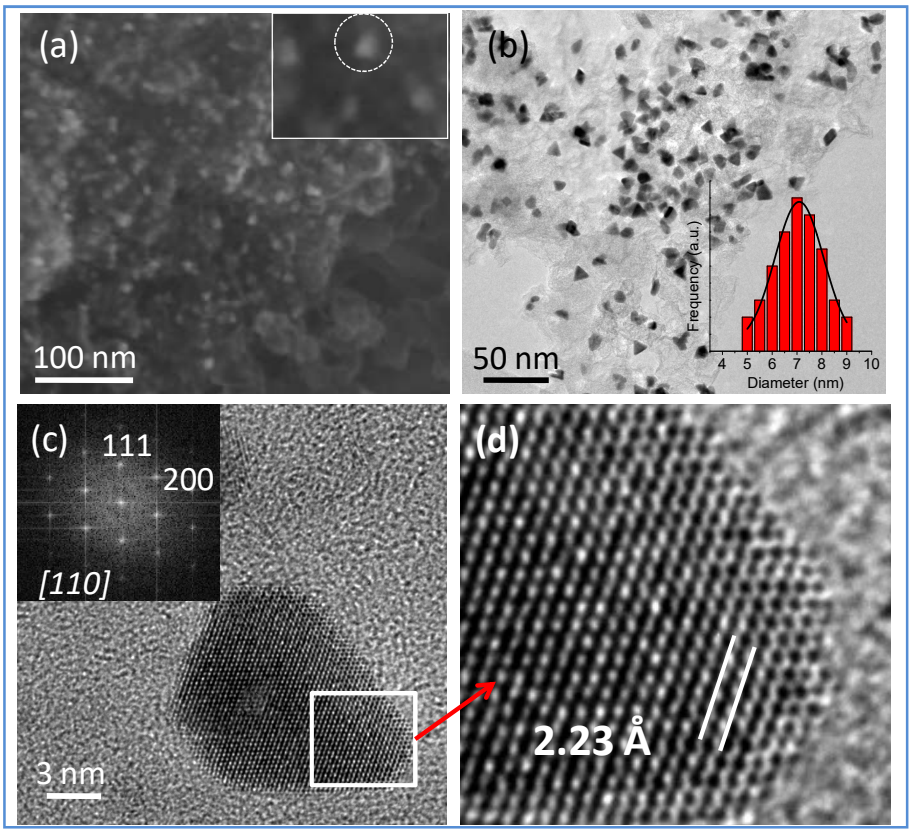

Figure 9: (a) FESEM and (b) TEM images of Pt-NTd/C samples prepared using DMF/EG ratio of 6:4 at 170 ^{o}C for 8 hours, showing homogeneous distribution of the nanocrystals. Inset in (a) shows the tetrahderal shape of Pt nanoparticles visible in FESEM. (c, d) HRTEM image of a truncated Pt-NTd and its FFT pattern (inset) along [110] zone axis.

We therefore recorded electron diffraction (SAED) pattern from a number of triangular particles (**Figure 2.8d,f,g,i-l**). The forbidden 1/3{422} reflection due to the stacking fault was absent in all, confirming tetrahedron shape of the Pt NCs. Some particles were oriented close to [110] zone axis enabling direct visualization of the Pt atoms along (111) closely matching the atomic model as given alongside the image (**Figure 2.8h**).

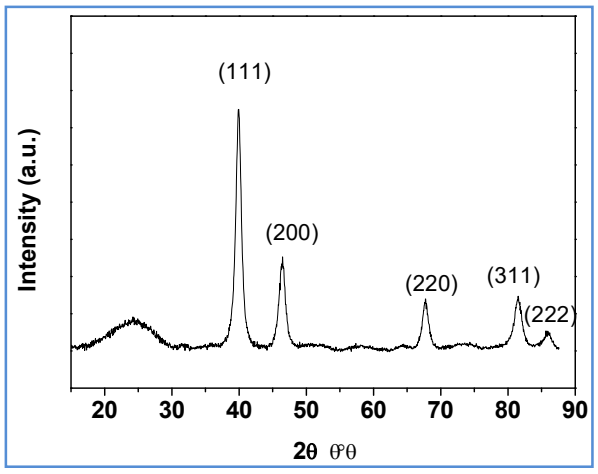

Figure 2.10: Powder XRD pattern of Pt-NTd/C obtained at 170°C (8h) using a EG, DMF ratio of 4:6. The broad peak at 24° correspond to the carbon support.

To examine the shape of non- triangular particles, various tilting experiments were carried out during TEM imaging. **Figure 2.8i-l** and **Figure 2.11** depicts a single particle in different tilting direction, showing gradual changes in appearance. Models of Pt-NTds in different projections along with HRTEM images and FT pattern are seen in **Figure 2.8 and 2.11**, confirming their shape. Thus the clear differentiation between triangular Pt nanosheets and Pt NTds could be established.

Examination of the chemical nature of Pt-NTds by X-ray photoelectron spectroscopy (XPS, **Figure 2.12**) revealed presence of both Pt(0) and Pt(II) species. The strong doublet at 74.4 and 71.1 eV appears due to the $4f_{5/2}$ and $4f_{7/2}$ states of Pt(0), corresponding to ~80 mass% obtained by comparing the areas of both the species in core level XPS. The peaks centered at 78 and 72 eV suggests the presence of Pt(II), possibly originating from surface Pt-O species or interaction of Pt NCs with the functional groups of the support. The Pt(0)/Pt(II) ratio was much higher than commercial Pt/C and other Pt NCs with {111} facets.[36]

We performed several control-experiments to gain insight into the growth mechanism. The Pt-NTds appear as early as 1 h (**Figure 2.13a**). In addition, the carbon support contained 2-4 nm Pt clusters initially, which disappeared after 4 h. The Pt loading on the carbon support significantly increased in the early stage of the reaction, before slowing down (**Figure 2.13**). The Pt contents on carbon support were estimated to be 9.7, 23, 28 and 30 wt%, after 2, 4, 8 and 12 h of reaction time respectively.

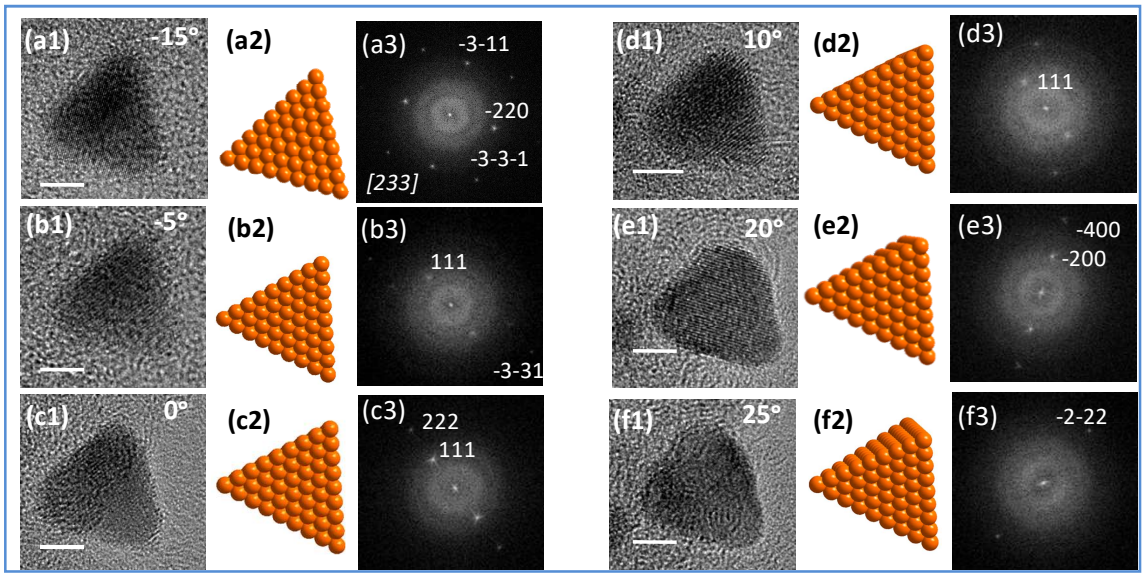

Figure 2.11: HRTEM images (1), representative atomic models (2) and FFT patterns (3) of a single crystalline Pt-NTd showing the systematic change in the appearance and corresponding diffraction pattern with change in α tilting of (a) -15°, (b) –5°, (c) 0°, (d) 10°, (e) 20°, (f) 25°. The HRTEM images were recorded by tilting the particle across [233] zone axis. Scale bars in each image correspond to 2 nm.

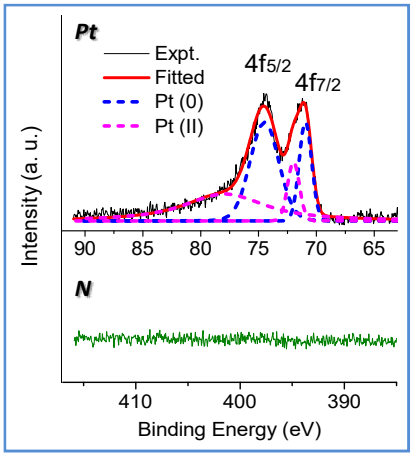

Figure 2.12: XPS spectra of Pt-NTd/C corresponding to Pt and N.

4.1. Investigation of the Reaction Mechanism:

We performed several control experiments to gain insight into the growth mechanism. The reaction proceeds with progressively slow kinetics until completion in 12 h. Pt contents on carbon support were estimated to be 9.7, 23, 28, and 30 wt % after 2, 4, 8, and 12 h of reaction time, respectively (**Figure 13a**). The Pt-NTds appear as early as 1 h (**Figures 2.13b and 2.14a**). In addition, the carbon support contained a large number of 2–4 nm Pt clusters initially (**Figure 2.13c,d**), which disappeared after 4 h along with an increase in the number of NCs with

tetrahedral morphology (**Figure 2.14b**). With increasing reaction time, the Pt on the carbon support significantly increased in the early stage of the reaction, before slowing down.

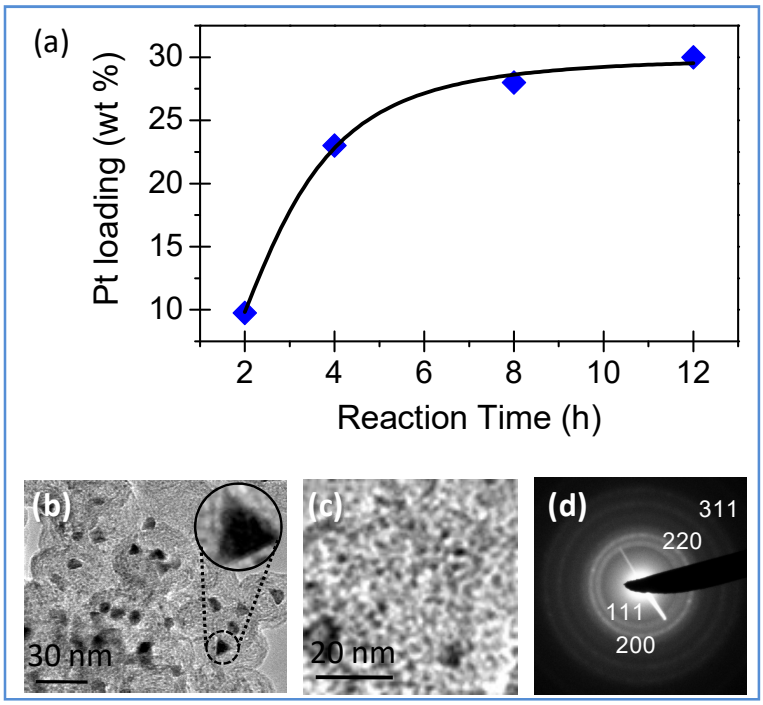

Figure 2.13: (a) A plot depicting increase in Pt loading on carbon support with increasing reaction time. TEM images of a Pt-NTd obtained at 170 °C by using a DMF/EG ratio of 6:4 after (b,c) 1 hour reaction time showing full and truncated tetrahedra. (c) Formation of small Pt clusters (2-4 nm). (d) SAED pattern recorded on the 2-4 nm Pt clusters, which can be indexed on pure Pt.

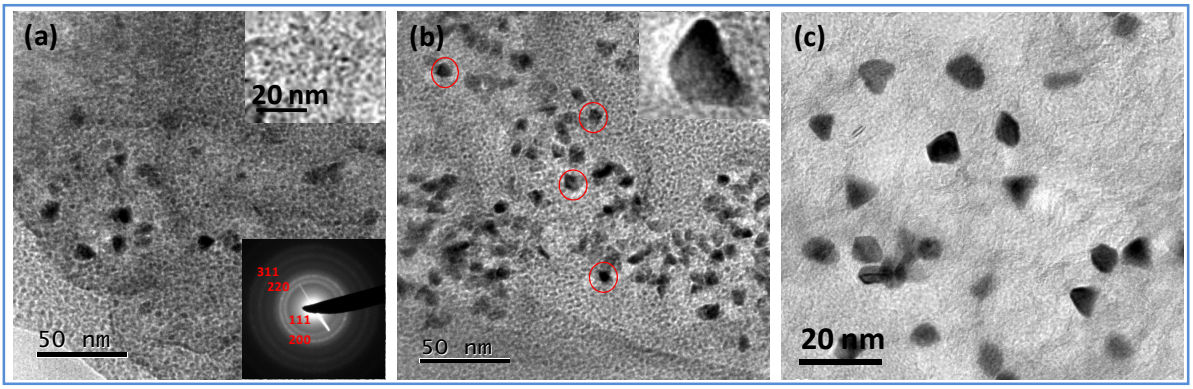

Figure 2.14: HRTEM images of a Pt-NTd obtained at 170 °C by using a DMF:EG ratio of 6:4. (a, b) 1 hour and (c) 4 hours reaction time. The insets in (a) and (b) shows formation of small Pt clusters (2-3 nm), its SAED (bottom inset) and incomplete Pt tetrahedron after 1 hour reaction time.

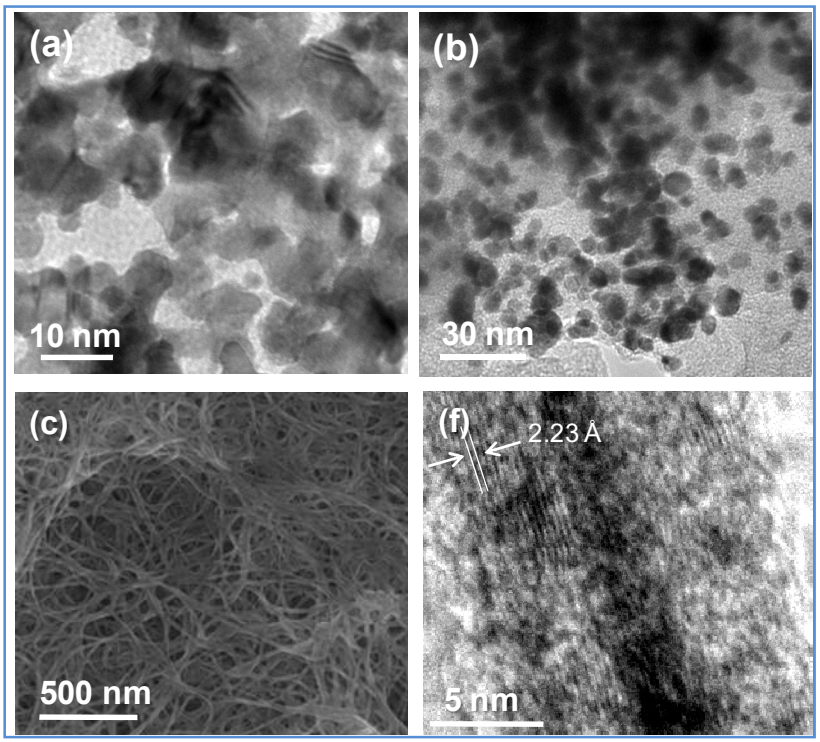

Figure 2.15: TEM images of NCs obtained using only (a) DMF or (b) EG at 170 °C. (c) FESEM image of the product obtained in the absence of carbon support in a similar experimental condition. (f) HRTEM image of a single nanowire.

In order to obtain the Pt-NTds, two factors were found to be crucial: *(i)* use of EG and DMF simultaneously in the reaction and *(ii)* the carbon support. When the synthesis is carried out in EG or in DMF alone, the NCs develop irregular shapes (**Figure 2.15, b** and **Figure 2.16**).

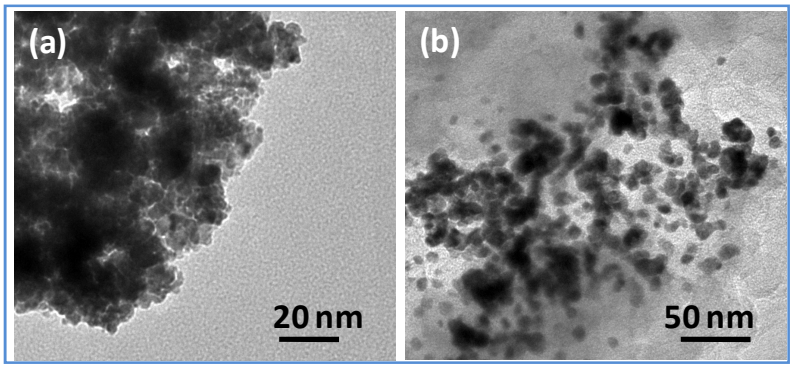

Figure 2.16: TEM images of the Pt NCs obtained at 170 ^{o}C after 8 h using (a) only DMF and (b) only EG respectively.

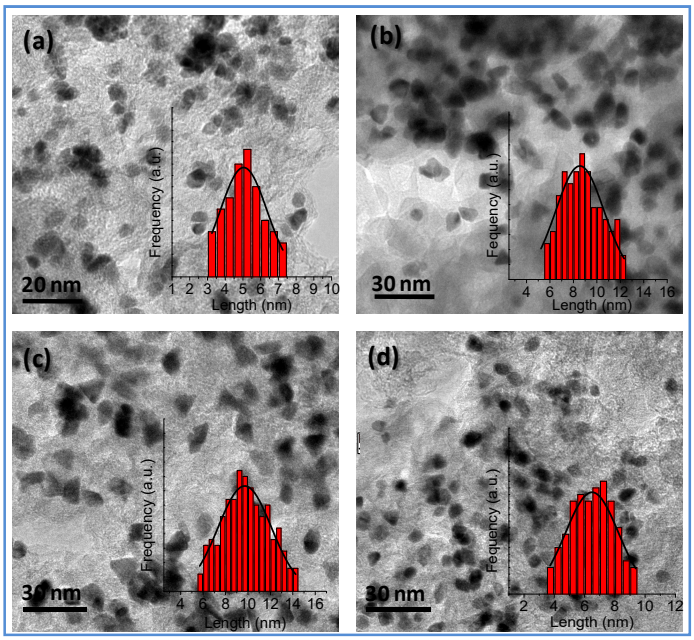

Figure 2.17: TEM images of the Pt-NTd/C obtained at 170 ^{o}C after 8 h reaction using DMF/EG volume ratios of (a) 8:2, (b) 5:5, (c) 4:6 and (d) 2:8. The histograms for the size distribution of Pt NTds are shown in the inset.

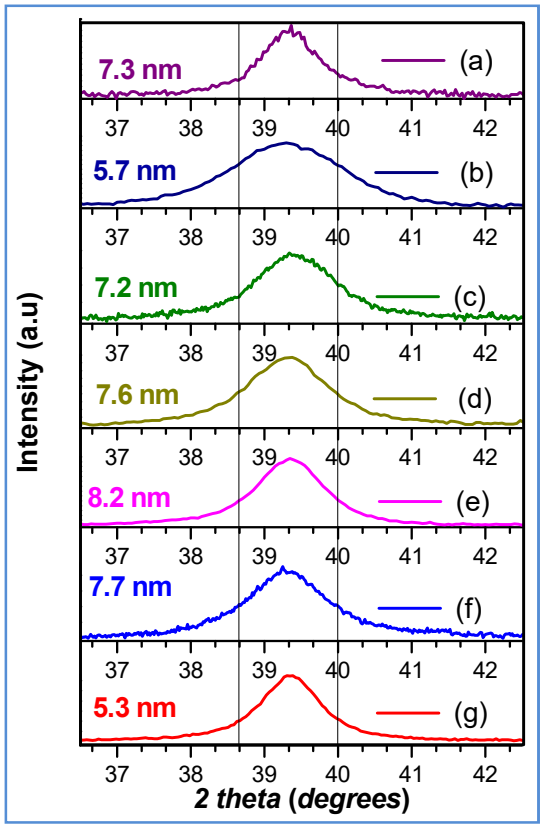

Figure 2.18: Powder XRD patterns of different Pt nanocrystals obtained at 170 ^{o}C after 8 h using DMF/EG ratios of 10:0 (a), 8:2 (b), 6:4 (c), 5:5 (d), 4:6 (e), 2:8 (f) and 0:10 (g). All patterns represent pure Pt samples. The peak centred at ~39.4^{o} corresponding to Pt(111) plane represents the changes in the particle size with changing solvent ratios. The calculated particle sizes from FWHM using Scherrer formula are mentioned in each plot, showing that the largest Pt-NTds are obtained with a solvent ratio of 4:6.

On the other hand, using a mixture of DMF and EG in different proportions invariably led to Pt-NTd/C. With increasing DMF fraction, the average size of the Pt-NTds increases initially reaching ~9.7 nm, before reducing again (**Figure 2.17**), also supported by XRD data (**Figure 18**). For examining the role of carbon support, the synthesis was carried out without it, keeping the other parameters unaltered. This led to the formation of crystalline Pt nanowire bundles only (**Figure 15c**), and no particulates were found even in small numbers. **Figure 2.15f** is a high resolution TEM image of such a nanowire showing the lattice fringes of Pt(111) parallel to the nanowire wall. Similar results were observed in other studies as well.[25] On the basis of these observations, clearly, the DMF and EG mixture in the presence of KOH stabilizes the {111} planes of Pt. Usually, Pt(111) stabilization is achieved by using specific reagents such as PVP or peptide or by forming alloys.[21,22,37] Such stabilization depends not only upon the interaction strength of individual functional groups with the Pt surface but also on their packing efficiency on the Pt surface. This is probably the reason that different amine species were found to stabilize the {111} sub facets, Pt(X11), X = 3, 4, or 5 planes.[38] Theoretical investigations on the nature of interactions have shown that the stability of -NH species is more on Pt(111) and that of $-NH_2$ on Pt(100)[39]

In our solvothermal conditions, a secondary amine is generated from the oxidation of DMF, as described below:

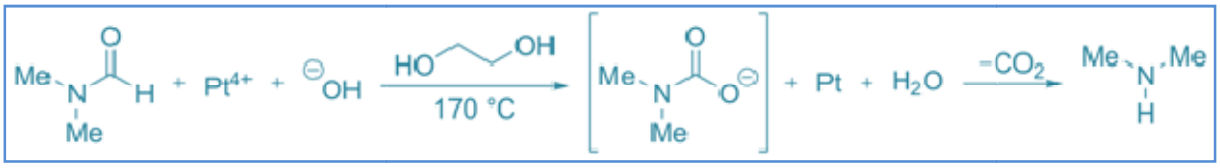

This was observed earlier in the case of reduction of Ag^+ salt.[40] Reduction of Pt^{4+} by DMF in the presence of KOH led to the formation of the carbamic acid intermediate which in the presence of protic solvent degrades to dimethylamine and CO_2 at high temperatures. Examination of our reaction mixture, which has strong ammonia like pungent odor, was performed by nuclear magnetic resonance (NMR) spectroscopy (**Figure 2.19a**). A singlet peak at 2.23 ppm for two methyl ($-CH_3$) groups and multiplet at 0.843 ppm for N−H proton (the ratio of peak areas

corresponding to the two methyl (−CH_3) groups to that for the N−H proton, I_{CH3}/I_{NH} = 5.908/1.056 = 5.6, ~6) correspond to dimethylamine[41].

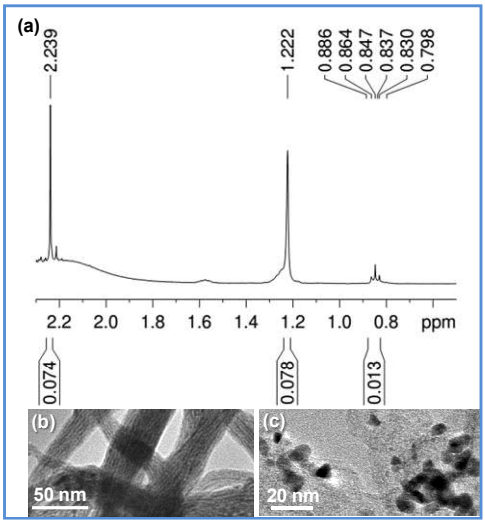

Figure 2.19: (a) NMR spectrum of the reaction mixture after an 8 h solvothermal treatment at 170 °C. (b, c) TEM images of products obtained from control experiments using only ethylene glycol as reducing agent in the presence of diethylamine. The formation of nanowire bundles along with tetrahedral morphology supports the stabilization of the Pt ⟨111⟩ plane by secondary amine species.

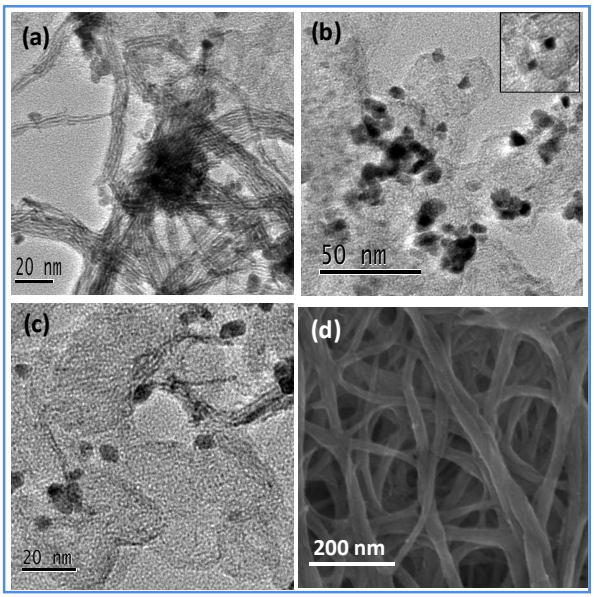

Figure 2.20: (a-c) TEM images of products obtained in presence of diethylamine, using EG as the only reducing agent at 170 ^{o}C after 8 h reaction time. The presence of nanowire bundles as well as tetrahedra nanocrystals (c inset) confirms stabilization of Pt (111) facet by secondary-amine species. (d) FESEM image of entangled Pt nanowires obtained in absence of carbon support at 170 ^{o}C after 8 h using DMF/EG ratio of 6:4.

To be conclusive, we performed a control synthesis in the absence of carbon support and the presence of dielthylamine (DEA) using EG as solvent separately (**Figure 2.20**). The reaction product contained Pt- NTds anchored on carbon support as well as free-standing nanowires that arise due to solution phase nucleation and oriented attachment of NCs (**Figures 2.19b,c and 2.20**).

These observations confirm the role of amine and also point to the fact that in situ generation of amine is necessary for high yield generation of NTds. The activated carbon contains a high surface area and a large number of surface functional groups (**Figure 2.7**). This increases the adsorption of Pt precursor and provides a large number of nucleation sites for growth of Pt- NTds. We observed that, throughout the TEM grid, all Pt- NTds are attached to the carbon indicating that the NCs grew only on the support. We believe that, unlike the free-floating NCs solution, these anchored Pt-NTds cannot migrate and attach with each other to form nanowires by the oriented attachment mechanism.[42]

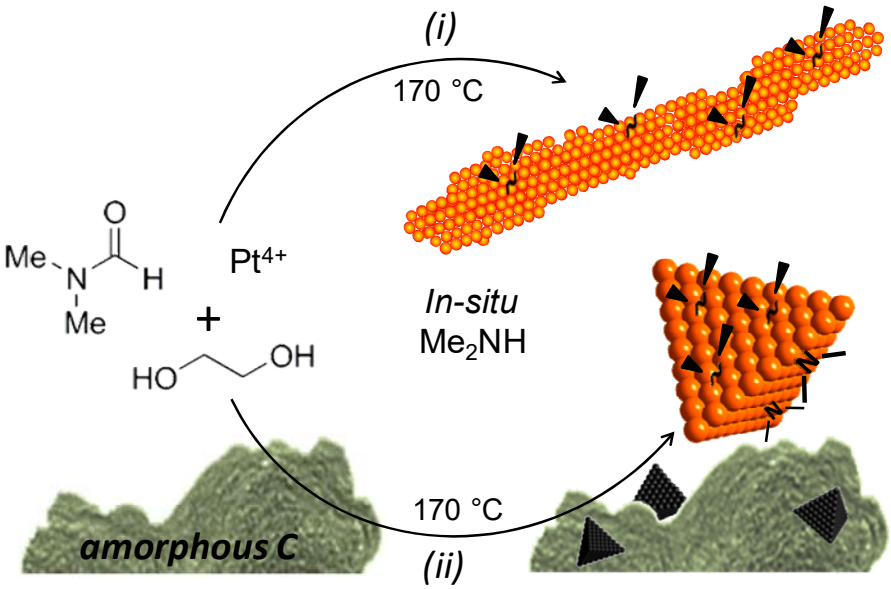

Figure 2.21: Schematic Illustration of Synthesis of Pt-NTd/C.

On the basis of these observations, we propose a growth mechanism for the Pt-NTd/C (**Figure 2.21**). Nucleation of the Pt-NTds first takes place in the carbon support. The in situ generated DMA stabilizes the Pt(111) facet, leading to formation of Pt tetrahedra NCs. Importantly, we found that the amine molecules can be easily removed from the Pt sample by

repeated washing with a water/ethanol mixture (absence of nitrogen is seen in XPS spectra in **Figure 2.12**). Since DMA is the most strongly interacting molecule with Pt-NTds in the reaction mixture, its removal suggests that Pt(111) facets are free and exposed.

4.2. Electrocatalytic Performance of Bare Pt-NTds

The presence of strongly attached surface stabilizing agent may suppress the catalytic activity of nanoparticles of a noble metal, whose efficiencies are otherwise good.[43,44] Since, in our case, the surface stabilizing agents for the formation of Pt-NTd can be easily removed, the catalytic performance is expected to be high and true to the particular crystal-facet for electron transfer reactions. We have therefore examined the stability and activity of the Pt-NTds toward fuel cell reduction as well as oxidation reactions such as ORR, MOR, and FAO. We investigated the long-term stability and electrocatalytic efficiency of the Pt-NTds using a three electrode system with Ag/AgCl (3 M NaCl) as reference electrode. Cyclic voltammograms (CV) were recorded with a sweep rate of 50 mV/s at 27 °C. For comparison, the performances of commercial carbon supported Pt NCs (C−Pt/C) were evaluated under identical conditions.

Figure 2.22 shows CV plots for the Pt-NTd/C before and after recycling for 1000, 3000, and 5000 cycles. It nearly maintained the distinct hydrogen adsorption/desorption peaks (0.05 < V < 0.4 V vs RHE) even after 5000 cycles, accompanied by a minimal decrease in the peak current. It is important to note that the distinct butterfly like shape of the CV is characteristic to the Pt(111) surface and further establishes our TEM observations.32 C−Pt/C was distinctly different, as these peaks diminished quickly, exhibiting a gradual decrease in peak current (**Figure 22b**). The initial electrochemically active surface area (ECSA) for the Pt-NTd/C and C−Pt/C was comparable (19.22 and 17.62 m^2/g Pt, respectively). The ECSA for the Pt- NTd/C is maintained at ~90% even after 5000 cycles. On the other hand, ECSA of the C−Pt/C reduced to 49.5% after 5000 cycles (**Figure 22c**). Their high durability, compared to many other shapes,[25,45,46] is due to structural stability due to higher cohesive energy of surface Pt atoms on {111} planes. Moreover, due to strong attachment to the carbon support, these NCs might avoid gradual agglomeration and Ostwald ripening. The ORR activities of the Pt-NTd/C were investigated by recording polarization curves and calculating the kinetic current densities

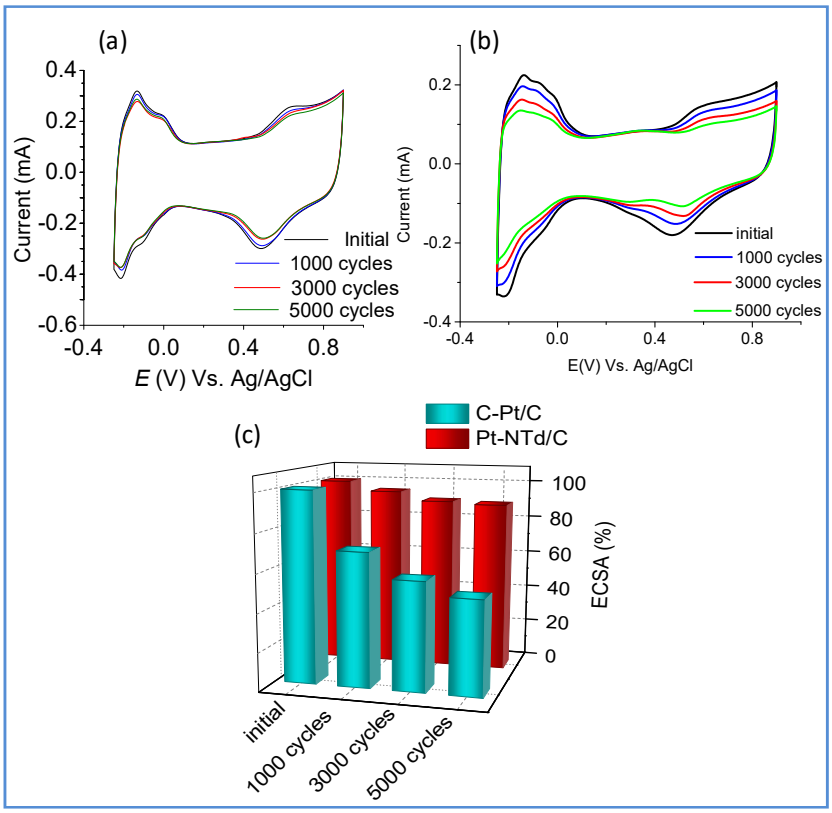

Figure 2.22: CV of (a) Pt-NTd/C and (b) commercial Pt/C before and after the stability test (in Ar saturated 0.1 M $HClO_4$ solution with 50 mV/s scan rate). (c) Surface areas of Pt-NTd/C (red) and C−Pt/C (cyan).

using the Koutecký−Levich equation (**Figures 2.23 and 2.24**).

$$\frac{1}{I} = \frac{1}{I_k} + \frac{1}{I_d}$$

Here I, I_k, and I_d are measured, kinetic, and diffusion limited currents, respectively.

The Pt-NTd/C exhibited a good onset potential of +1.011 V (vs RHE) as compared to +0.951 V recorded for the commercial catalyst. The corresponding halfwave potentials ($E_{1/2}$) show a significant positive shift of 102 mV (0.873 and 0.771 V for Pt-NTd/C and C−Pt/C, respectively) indicating much improved ORR kinetics. We also compared the ORR activities of the Pt nanowires obtained in absence of the carbon support. The nanowires exhibited an ORR onset and half-wave potential of +0.968 and +0.796 V, respectively (**Figure 2.25)**. Such superior ORR activity of Pt-NTd/C can be attributed to the presence of bare Pt ⟨111⟩ facets and 111/111 edges which allow easy electron transfer from catalyst to adsorbed oxygen28 whereas in the case of Pt NW, along with exposure of Pt ⟨111⟩ facets in certain places, the oriented attachment

mechanism may give rise to many defect sites giving rise to comparatively sluggish reduction kinetics. Furthermore, we compared the stability of the Pt-NTds with that for C–Pt/C. After 5000 cycles, the Pt-NTd/C showed nearly the same onset potential and a minimal 47 mV decrease in E1/2. In comparison, C–Pt/C recorded a substantial decrease on onset and $E_{1/2}$ values by 130 mV, respectively (**inset in Figure 23a**). Mass activity of the Pt- NTd/C at 0.9 V (and at 0.85 V) is 22.8 A/g (104.6 A/g), which is 6.76 times higher than the C–Pt/C (**Figures 2.23b and 2.24c**). Mass activity of the Pt-nanowires at 0.85 V was estimated to be 24.5 A/g (**see Figure 2.25d,** for comparison of mass activities of all samples). The $E_{1/2}$ values recorded for these Pt-NTd/C are comparable to or better than most state of the art Pt electrocatalysts reported recently (**Tables 2 and 3**).

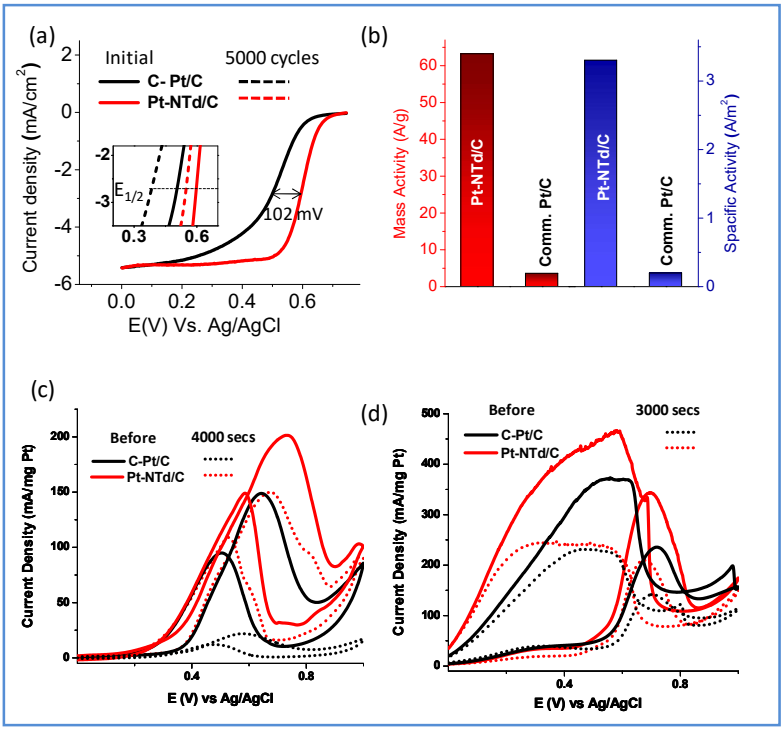

Figure 2.23: (a) LSV of Pt-NTd/C (red) and commercial Pt/C (black) in O2 saturated 0.1 M HClO4 with a scan rate 5 mV/s. Inset shows the change in E1/2 after 5000 potential cycles for both the catalysts. (b) Comparison of mass and specific activitiesof Pt-NTd/C and the commercial one at 0.9 V. CV of Pt-NTd/C and commercial Pt/C before and after stability test for (c) MOR recorded in 0.1 M HClO4 + 1 M CH_3OH and (d) FAO recorded in 0.1 M $HClO_4$ + 1 M HCOOH at scan rate 20 mV/s.

We have further studied the electrochemical oxidation of small organic fuel molecules such as methanol and formic acid (MOR and FAO, respectively). The CV (**Figure 2.23c**) shows

two distinct anodic current peaks typical of methanol oxidation in the forward and backward sweeps in the cyclic voltammogram.

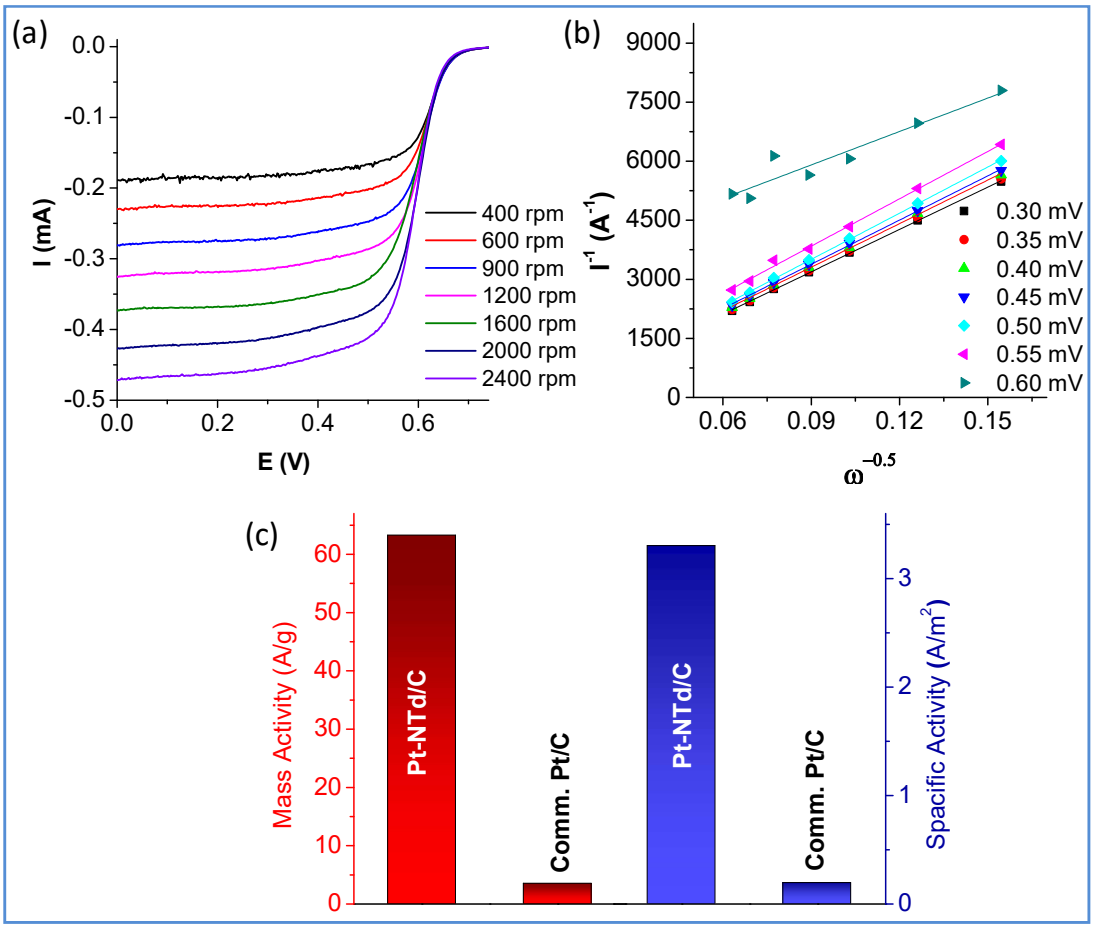

Figure 2.24: (a) Linear Sweep voltammograms of Pt-NTd/C at different rotation speed performed using RDE in O2 saturated 0.1 M HClO4 solution with scan rate 5 mV/s. (b) Koutecky-Levich plot for Pt-NTd/C giving rise to electron transfer number of 3.7 for ORR. (c) Comparison of mass and specific activity for Pt-NTd/C with commercial Pt/C at 0.85V (Vs. RHE).

The corresponding mass and specific activities are compared with those of C–Pt/C in **Figure 2.26a,b**. Initially, the mass and specific activities of Pt- NTd/C for MOR were 201.35 A/g and 23.56 A/m2, respectively, much higher than 148.68 A/g and 8.38 A/m2, respectively, recorded for C–Pt/C and comparable to most state of the art catalyst systems (**Tables 3 and 4**). The ratio of the forward and backward peak current (I_f/I_b) measured 1.39 indicating high relative oxidation of fuel molecules in the forward scan as compared to many recently developed catalytic particles. A study by Tong and co-workers pointed out that oxidation of

methanol takes place in both forward and reverse scans, contrary to a belief that the reverse peak is due to oxidation

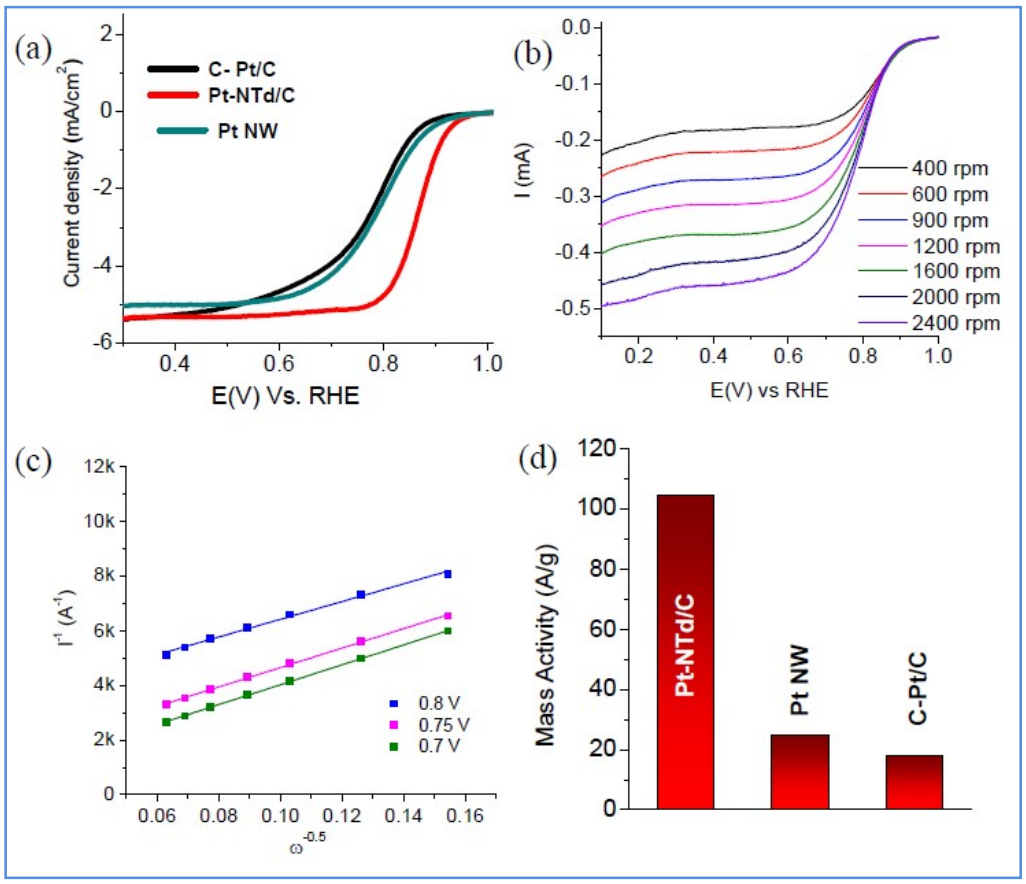

Figure 2.25: (a) Comparison of linear sweep voltametry (LSV) of Pt NW with Pt-NTd/C and C-Pt/C, performed in O_2 saturated 0.1 M $HClO_4$ solution at 5 mV/sec scan rate. (b) LSV of Pt-NW recorded at different rotation speed performed using RDE in similar condition. (c) Koutecky-Levich plot for Pt NW. (d) Comparison of mass activity for Pt-NTd/C with commercial Pt/C at 0.85V (*vs.* RHE).

of residual carbon species.[47] We further examined the catalytic performance of these particles after 4000s by employing chronoamperometry. Pt-NTd/C retained 52% of the initial activity, while the deactivation of C–Pt/C was far rapid. Interestingly, in the case of FAO too, as during MOR, the I_f/I_b ratio for Pt-NTd/C was found to be very small (0.73) as compared to most other efficient Pt nanocrystals reported earlier[23,48,49] (**Figure 2.23d**). Pt-NTd/C has shown mass and specific activities of 312.65 A/g and 17.59 A/m^2, respectively, which decreased by 31% after 3000 s, whereas the corresponding activity loss for the C–Pt/C was recorded as 54% (**Figure 2.26**). In both cases, the high stability of Pt-NTd/C during the electrochemical process can be attributed to the highest cohesive energy of surface atoms on exposed Pt ⟨111⟩ planes giving

rise to the lowest electrochemical leaching probability. The ORR, MOR and FAO studies clearly how that the Pt-NTds/C exhibit not only impressive electrocatalytic efficiency but also high stability under corrosive conditions.(**Figures 2.27 and 2.28**)

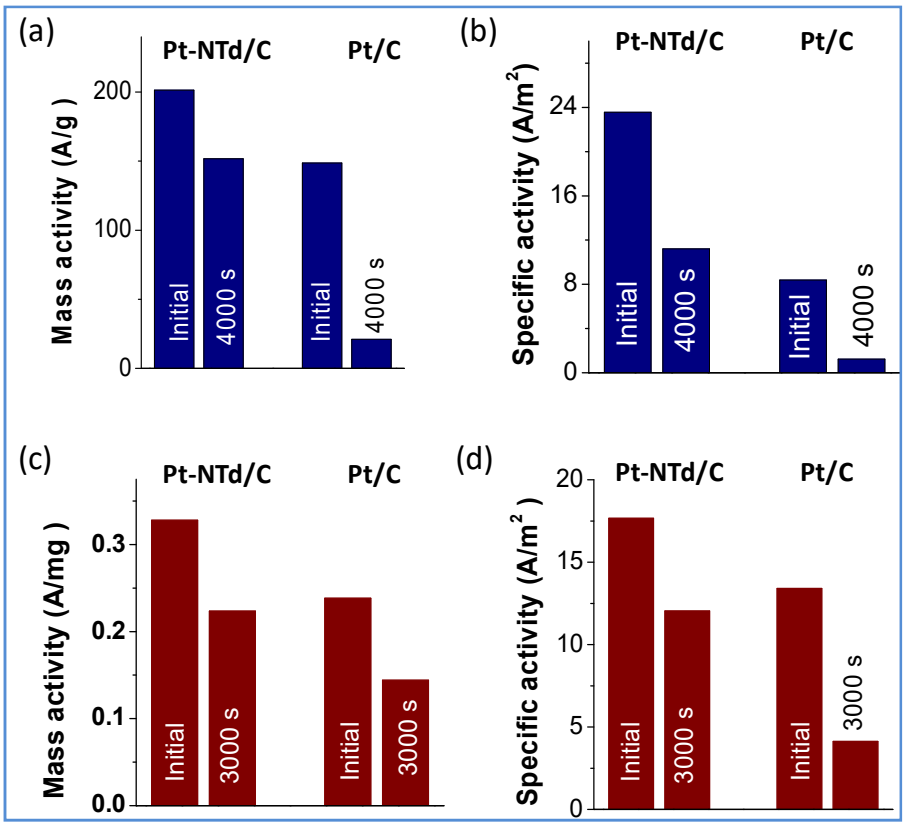

Figure 2.26: Comparison of (a,c) mass activities and (b,d) specific activities between Pt-NTd/C and commercial Pt/C for (a,b) MOR and (c,d) FAO respectively before and after chronoamperometric stability test.

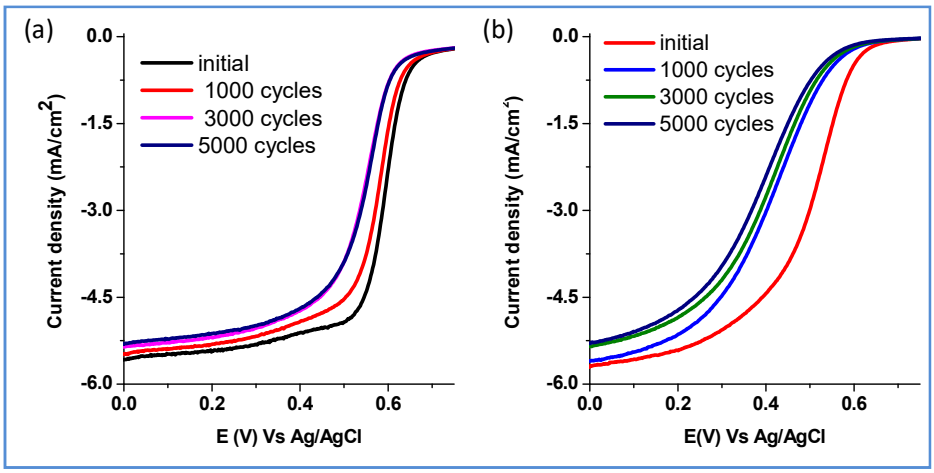

Figure 2.27: Linear sweep voltammograms of (a) Pt-NTd/C and (b) commercial Pt/C before and after stability tests, performed in O_2 saturated 0.1 M $HClO_4$ solution at 5 mV/sec scan rate.

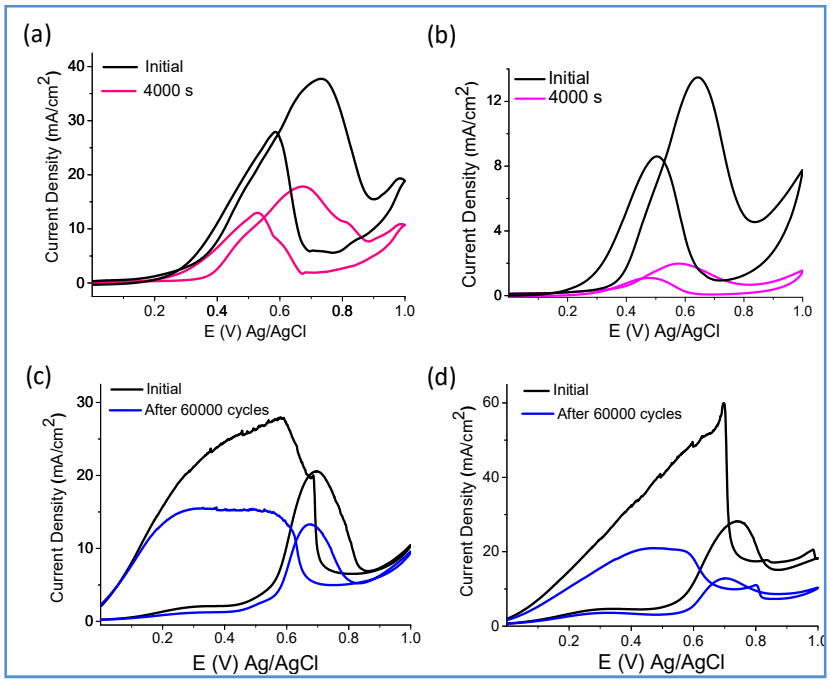

Figure 2.28: Cyclic voltammetry (CV) profiles of (a,c) Pt-NTd/C and (b,d) commercial Pt/C for (a,b) methanol oxidation recorded in 0.1 M $HClO_4$ + 1 M CH_3OH and (c,d) formic acid oxidation recorded in 0.1 M $HClO_4$ + 1 M HCOOH at scan rate 20 mV/sec.

Table 2: Comparison of half-wave potentials (in V *vs.* RHE) recorded for different state-ofthe-art Pt electrocatalysts and Pt-NTds from this study.

Pt Morphology	Exposed facet	$E_{1/2}$	Mass Activity (A/g)	Pt loading(mg/cm^2)	Reference
Tetrahedra	(111)	0.873	22.8 (0.9V)	0.28	This work
Nanoframe	(740)	0.834	13.1 (0.8V)	02	[50]
Nanocube	(100)	0.816	10.74 (0.8V)	0.2	[50]
Nanocube	(100)	0.810	13.9 (0.8V)	0.2	[51]
Nanowire	unknown	0.840	17 (0.85V)	0.2	[52]
Nanowire	unknown	0.802	-	0.2	[25]
Nanoparticle	unknown	0.820	0.2 mA/µg (0.85V)	0.007	[53]
Mesoporous film	Unknown	0.840	0.3A/mg (0.9V)	0.014	[54]
Multioctahedra	(111), (100)	0.843	0.3 mA/µg (0.85V)	0.015	[55]
Nanoparticle	U=unknown	0.830	0.317 mA/µg (0.9V)	0.0113	[56]
Nanowire	(111)	0.848	0.135 mA/µg (0.9V)	0.006	[45]

Table 3: Comparison of onset potential, E1/2, electron no and mass activity at 0.85 V for Pt-NTd/C, Pt NW and C-Pt/C.

Material	Onset (V)	$E_{1/2}$	Electron number	Mass activity@0.85 (V)
Pt –NTd/C	1.011	0.873	3.74	104.6 A/g
Pt-NW	0.968	0.796	3.62	24.5 A/g
Commercial Pt/C	0.951	0.771	3.46	17.1 A/g

Table 4: Comparison table of mass activity for methanol oxidation

Material	Mass Activity (A/g))	Pt loading (mg/cm^2)	Reference
Pt –NTd/C	201	0.28	This work
Spiny Porous Pt NT	260	0.042	[57]
Pt NWs	500	0.2	[25]
Pt Nancubes	500	0.2	[51]
Mesoporous Pt-Nanorod	209	-	[58]

Table 5: Comparison table of mass activity for formic acid oxidation

Material	Mass Activity (A/g))	Pt loading (mg/cm^2)	Reference
Pt –NTd/C	312.65	0.28	This work
Spiny Porous Pt NT	375	0.2	[51]
Pt NWs	670	0.2	[51]
Pt Nancubes	450	0.009	[59]
Mesoporous Pt-Nanorod	354	0.04	[47]

Part-B:

Mechanochemical Synthesis of Free-Standing Platinum Nanosheets and Their Electrocatalytic Properties.

For the first time the synthesis of 2D free-standing platinum nanosheets (PtNS) by inducing mechanochemical transformation of Te template nanorods under the influence of external deforming forces exerted by magnetic stirring has been reported. The PtNS are ≈27 nm in thickness, elongated in morphology, polycrystalline in nature and unlike the nanosheets of layered materials, contain rough surfaces that exhibit high surface area and excellent electrochemical activity when compared with commercial or even many state-of-the-art carbon supported Pt catalysts. In general, mechanical force has rarely been used for controlling growth of nanostructures, even though a greater potential can be envisioned for them.[60] In a typical synthesis of nanocrystal in solution, stirring is routinely used for homogenizing the reaction mixture. Therein, mechanical forces and shear stress exerted by the reaction medium on the nanostructure can critically influence the final morphology which are seldom neglected or not noticed upon. During initial stages of synthesis in particular, as demonstrated by El-Sayed and co-workers,[7,21] mechanical forces can break the growth symmetry of nanostructures.[61] Using experimental tools and theory, they demonstrated that high speed stirring of the solution mixture during the reaction has a profound effect in ion transport and therefore in shaping of the seed clusters that later govern the asymmetric shape of nanoparticles. If a viscous fluid is subjected to a vortex motion by stirring, a shear stress is developed which varies linearly with the rate of stirring and the viscosity of the fluid. Furthermore, the rotation of the solution mixture also creates a centripetal force which tends to keep the nanosolute particles in the solution aligned. These effects have been elegantly utilized recently to obtain highly elongated TiO_2 nanotubes that are difficult to synthesize otherwise.[62] In order to reduce shear stress, shorter TiO_2 nanotubes undergo 'end to end' attachments leading to the formation of elongated tubes. We have adopted galvanic displacement (GD) method in this work to obtain Pt nanostructures using Te NRs as sacrificial templates. This method has remarkable advantages because Te nanostructures can be easily obtained in a controlled manner, forming a variety of unique morphologies in sub-micrometer size-range that are not natural to Pt. Te has a lower reduction potential than Pt and therefore in presence of a Pt salt, Te oxidizes and begin to leach out of the nanostructures as its oxide, accompanied by the deposition of metallic Pt. At the end of the displacement, the Te nanostructure transforms in to a Pt-based nanostructure nearly

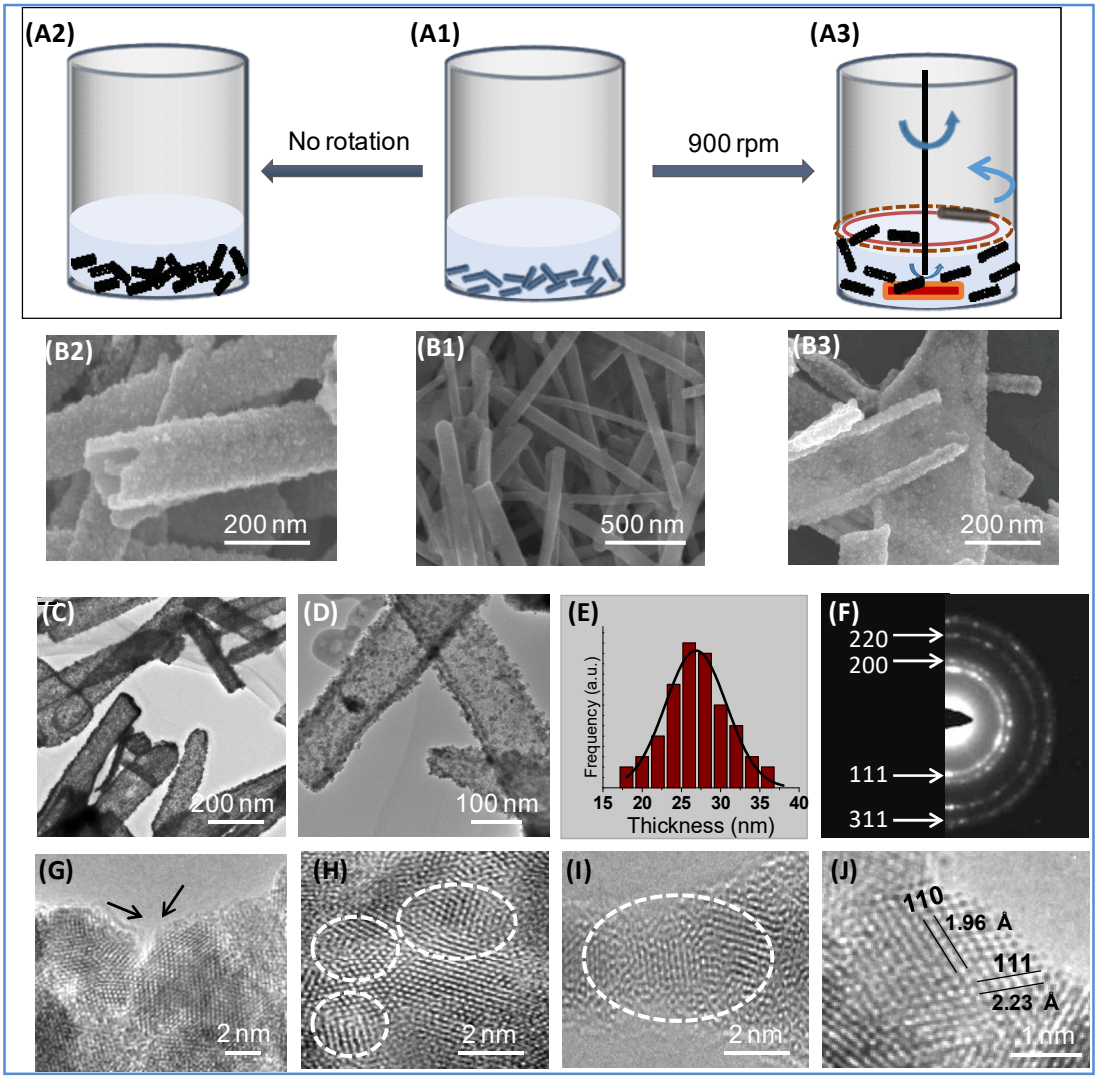

Figure 2.28: (A) Schematic depiction of the mechanochemical transformation of Te nanorods subjected to shear stress, when Te is being galvanically displaced by Pt. (B) FESEM images of various nanostructures associated with the different stages shown in Schematic (A): precursor Te nanorods, nanotubular Pt obtained at 0 rpm and the Pt nanosheets obtained at 900 rpm. (C,D) Low magnifi cation TEM images of PtNS. (E) Average thickness of the nanosheets. (F) Indexed SAED pattern acquired from single PtNS. (G–J) Typical lattice resolved TEM images of Pt nanosheets showing the association of its constituting nanocrystals with the neighboring ones. It can be seen that at times, the nanocrystals have different orientations and distinct crystal boundaries while in other instances, the same set of lattice planes run though more than one nanocrystal, indicating an oriented attachment.

maintaining original morphology. Due to the smaller atomic size of Pt (lower molar volume) and effect of surface diffusion, a NR of Te usually converts to form a Pt nanotube (NT), somewhat similar to Kirkendall effect.[63]

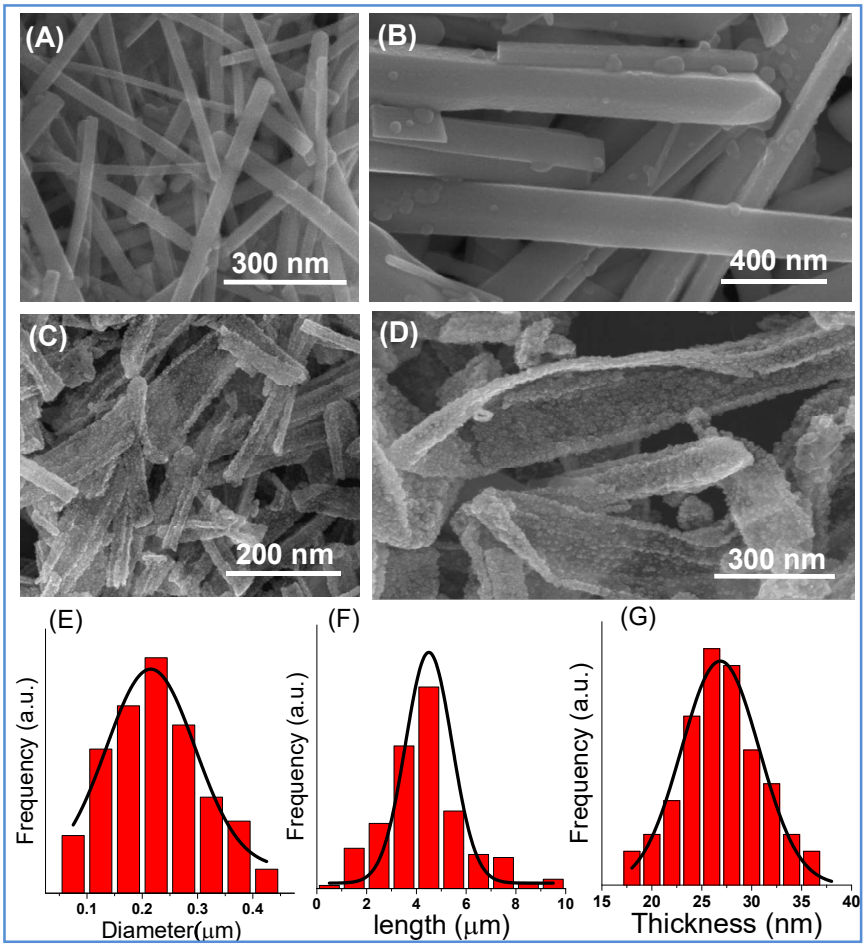

Figure 2.29: FESEM images of (A), (B) Te NRs showing the smooth surface and (C), (D) Pt nanosheets showing rough surfaces. Histograms showing the mean diameter of Te NRs (E), mean length of Te NRs (F) and the mean thickness of the Pt nanosheets.

In this study, we have chosen Te nanorods having an average diameter of ≈220 nm and length of 4 μm as templates (**Figure 2.28 A1,B1, and Figures 2.29A,B and Figure 2.30**). These nanorods were synthesized by a hydrothermal method at 180 °C using Na_2TeO_3 as the Te precursor and hydrazine hydrate as reducing agent.[34] The Te NRs were further used for galvanic displacement using H_2PtCl_6 as Pt precursor in ethylene glycol medium. The displacement was performed at 50°C for 15 h. When we kept the reaction mixture undisturbed, we obtained 1D Pt nanostructures containing mostly nanotubes as the reaction product (**Figure 2.28 A2,B2**). However when the reaction mixture was subjected to constant stirring at different rates, we observed that the morphology of the product began to change gradually, opening up the tube-like structures. In a typical synthesis, when the stirring rate was adjusted to 900

rotations per minute (rpm) for for 15 h, the reaction product mainly consisted of free-standing PtNS (**Figure 2.28 A3,B3 and Figure 2.29C,D, XRD in Figure 2.30**).

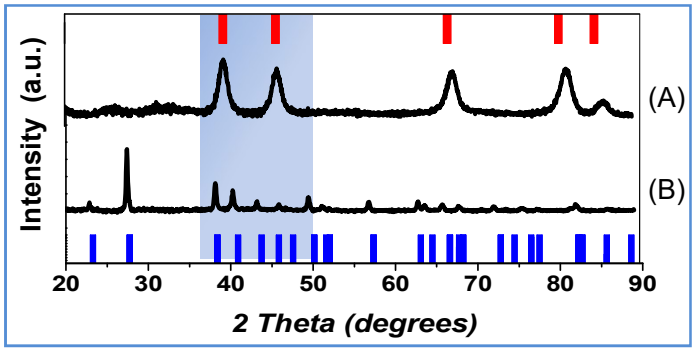

Figure 2.30: XRD pattern of (A) Pt nanosheets (red bar shows Pt, 41525-ICSD) and (B) Te nanorods (blue bar shows Te, 23058-ICSD).

4.3. Morphology analysis:

These nanosheets appear flat, about 4–10 times longer than their width and semitransparent in TEM suggesting their small thickness (**Figure 2.28 C,D**). From the analysis of a large number of scanning electron microscopy (SEM) and transmission electron microscope (TEM) images, we measured the mean thickness of the sheets to be 26.8 $\pm$ 4 nm (**Figure 2.28 E**). Their length varies between 1 and 3.5 µm. The smaller length of the nanosheets suggests that some of the nanorods not only open up during galvanic displacement, but also undergo breakage to yield short nanostructures. The ring SAED patterns acquired on these films indicated that the nanosheets are polycrystalline in nature (**Figure 2.28F**). We did not observe any diffraction spot corresponding to Te suggesting complete replacement of Te by Pt in those nanostructures. A high resolution TEM examination of the sample shows that the nanosheets are made of 4–10 nm Pt nanocrystals. Each of these nanoparticles is attached to few others surrounding it (**Figure 2.28 G–J**) forming a network of nanocrystals that stabilizes the nanosheet. There are usually two types of neighboring nanocrystals: ones that are attached to it without any crystallographic orientation, while the others that contain at least one set of crystal planes that are common to both nanocrystals, akin to the ones observed in oriented attachment mechanism.[34] It may be presumed that the second type of nanocrystals lend extra stability to the nanosheets (**Figure 2.28 H–J and Figure 2.31**). Interestingly, the PtNS do not

have as smooth surface as that of precursor Te NRs, which results in a larger surface area than expected (**Figure 2.32A,B**). According to the Brunauer–Emmett–Teller (BET) surface area measurement (**Figure 2.32C**), the PtNS has a surface area of 15.8 m^2g^{-1}.

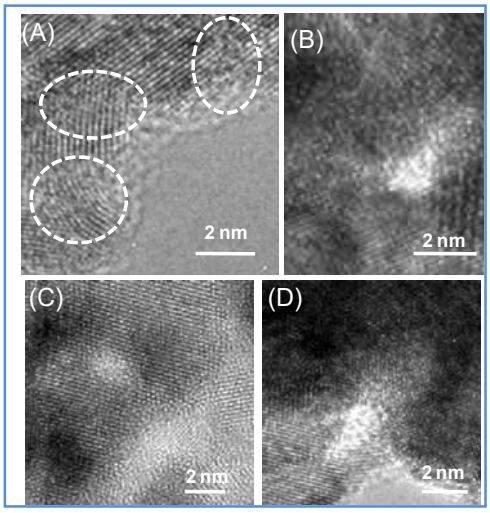

Figure 2.31: HRTEM images of PtNS showing the Pt lattice planes in different nanocrystals and attachment to neighboring ones.

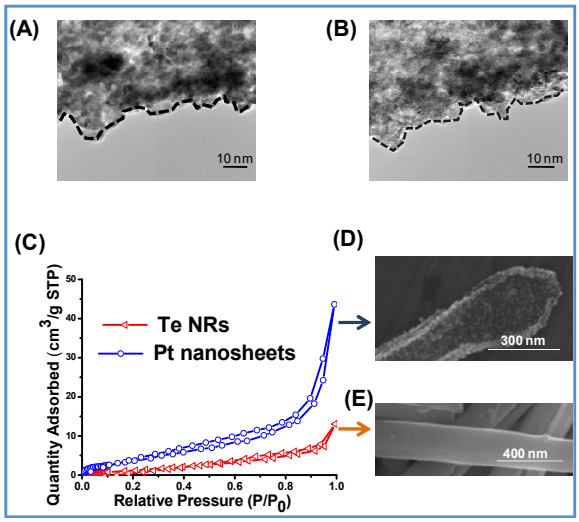

Figure 2.32: (A) and (B) TEM images of Pt NS surface highlighting their roughness. (C) BET adsorption isotherms of Te NRs and PtNS. The corresponding FESEM image of rough PtNS surface (D) and smooth Te NR surface (E).

This corresponds to a 4.23 times increase in surface area, if one considers that on an average, each Te NR with a diameter of 220 nm opens up to produce a 27 nm thick PtNS (**as below Figure 2.33**).

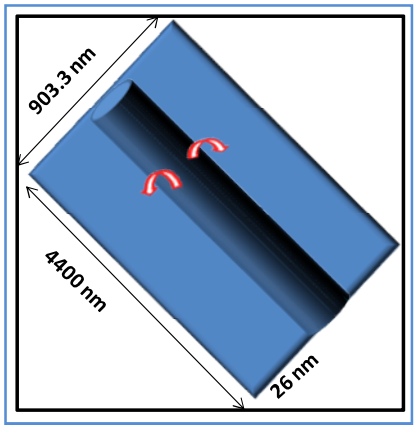

Figure 2.33: Schematic of conversion of a nanorod to a nanosheet with a diameter comparable to the PtNS obtained experimentally.

The expected surface area for this nanosheet with a smooth surface is calculated as follows:

Surface area of one PtNS = 2[(4400*903.92) + (903.92*26) + (4400*26)]

$= 8230317.84\ nm^2 = 8.23 * 10^{-12}\ m^2.$

Volume of one PtNS = $4400*903.92*26\ nm^3 = 1.03 * 10^{-19}\ m^3$

$$Mass = \rho * V$$

Mass = $21400 * 1.03 * 10^{-19} = 2.2042 * 10^{-15}$ kg

Surface area/g = $(8.23 / 2.2042) * 10^{-12} * 10^{15} * 10^{-3}$

$= 3.373\ m^2/g$

The BET surface area of the PtNS is 15.58 m^2/g. This value is 4.23 times of that of as calculated. This indicates that after the GD reaction, PtNS develops surface roughness and thereby increment in surface area.

As will be discussed later, a larger and rough surface is beneficial in many applications since otherwise, stacking of sheets with smooth surfaces when deposited on a working platform leads to enormous loss of exposed surface area.[64] Careful analysis of elemental composition of the reaction products at intermediate stages as well as at the end of the reaction showed that a tiny fraction of the Te precursor remains unreacted, despite diffraction studies suggesting otherwise.

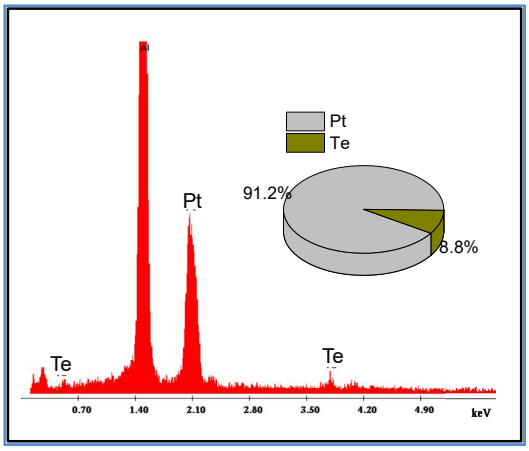

Figure 34: EDAX pattern recorded on a Pt nanosheet

The composition of these NS was examined by ICP and EDAX measurements (**Figure 2.34 and inset of Figure 2.35**). The PtNS obtained after 15 h of reaction was found to compose of about 93 ± 0.8% Pt and rest amount of unreacted Te, which must be amorphous in nature as it could not be detected by XRD or SAED.

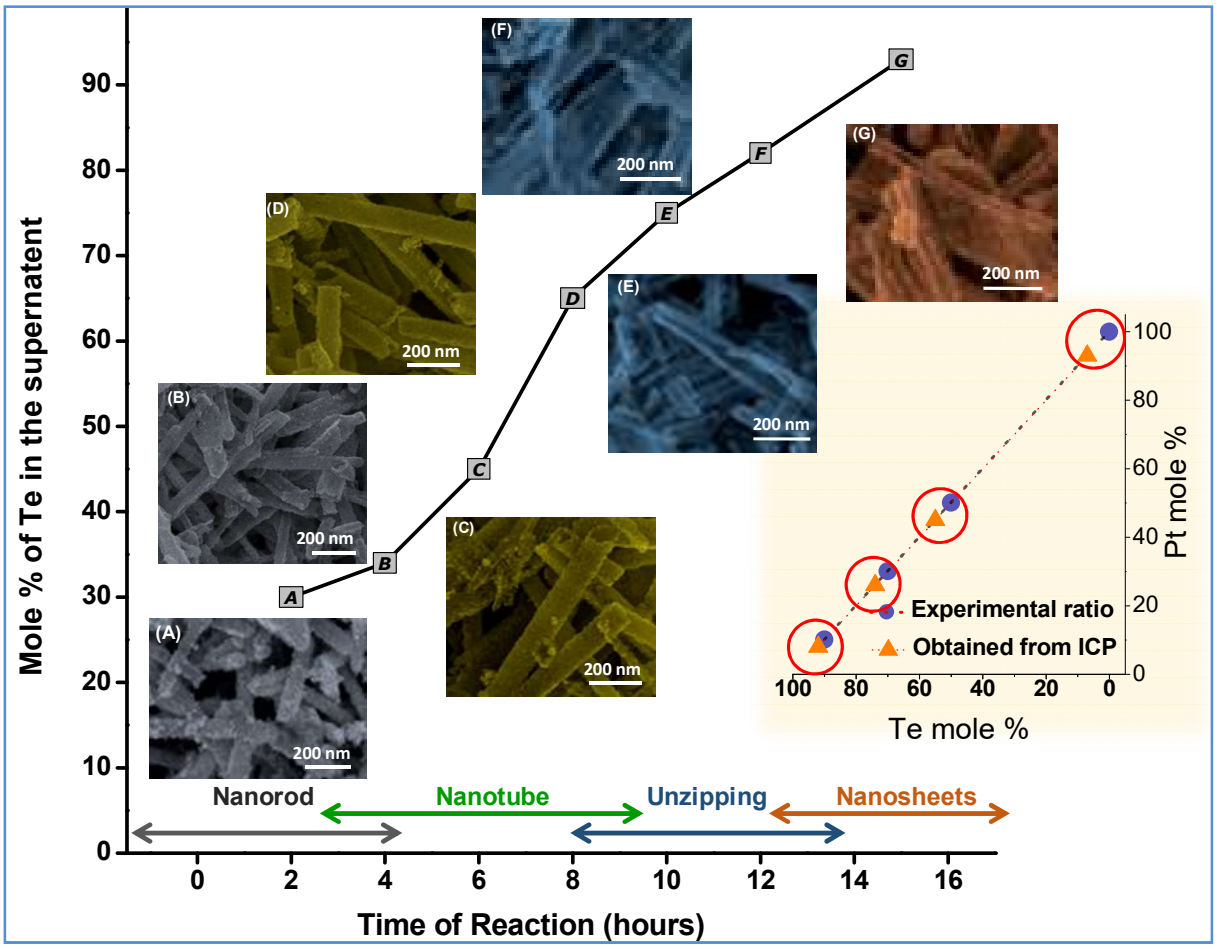

Figure 2.35: Kinetic study of the GD reaction during PtNS formation at 900 rpm: gradual change in the Te content with time (at 2 h intervals). FESEM images corresponding to each fraction of the reaction intermediate is also seen, representing the gradual transformation of nanostructure morphology. Inset is a plot showing expected and obtained composition of the reaction product, when different fractions of Te was galvanically displaced with Pt.

A similar trend was observed for other samples too, where the amount of Pt in the reaction product was found to be slightly less (estimated to be 45%, 26%, and 8%) than the intended ones (for 50%, 30%, and 10% substitution, respectively) (**inset in Figure 2.35**). This is probably caused by the decrease in the driving force of GD process with progress of reaction either due to alloying of Pt and Te atoms in the template or extremely slow reaction kinetics

due to lower concentration of the Pt precursor.[65] In order to monitor the progress of the reaction and evolution of nanosheet morphology, we collected reaction products at different time intervals and studied by FESEM and ICP (**Figure 2.35**). It was found that after 2h of reaction, surface of the nanorods (**Figure 2.35A**) were partially replaced (≈30%) by Pt particles. At 4 and 6h of reaction time, products consisting of increasing number of nanotubes of PtTe (34:66 and 45:55 in Te:Pt composition, respectively) were obtained (**Figure 2.35 B,C**). At these stages, the dimensions of the nanostructures do not appear to be very different from the parent nanorods, while slight increase in the diameter is expected. These nanotubes then begin to open up in 8–10h of reaction (**Figure 2.35 D,E**), when more than 50% of Te has been displaced. Their transformation to PtNS take place in 12–15h (**Figure 2.35 F,G)** and the extent of nanotube opening slowly increases with time. After 15h, the reaction completely stops as indicated by the ICP study. The product collected at 24h had the same composition (Pt:Te = 93:7) as that of the final product obtained after 15 h. Having observed the unmistakably distinct morphologies of the nanostructures under the influence of mechanical forces, we have carried out controlled experiments to get an insight into the mechanism of nanosheet formation. First, we observed that it is important to ensure that the deforming forces act upon the nanostructures when they are being transformed from Te to a Pt-based one by galvanic displacement process. Keeping the reaction medium still or using incubator shaker during the GD process leads to only 1D structures of Pt and not to nanosheets. On the other hand, when we took preformed Pt nanotubes and subjected to stirring, it did not lead to any change in morphology even after prolonged treatment, confirming that 1D structures are forced open only when the GD reaction is in progress. This is very similar to the observations of El-Sayed and co-workers that mechanical forces promote evolution of strikingly different nanocrystal-morphologies only when applied during their growth.[61] It may here be pointed out that even though mechanical forces were not considered before, the combination of GD with other processes has already been shown to impact morphology of nanostructures.[66,67] In order to discern the events associated with the nanosheet formation, we first have to consider the influence of one process on the other. The efficacy of the GD process is dependent upon several parameters[68-70] including: (a) stress or presence of defects in the Te nanorods and (b) the

rates of ionic diffusion to the nanorod surface which may undergo changes due to external factors. Diffusion of ions, or instance, is affected by viscosity of medium or mechanical turbulences, such as stirring or

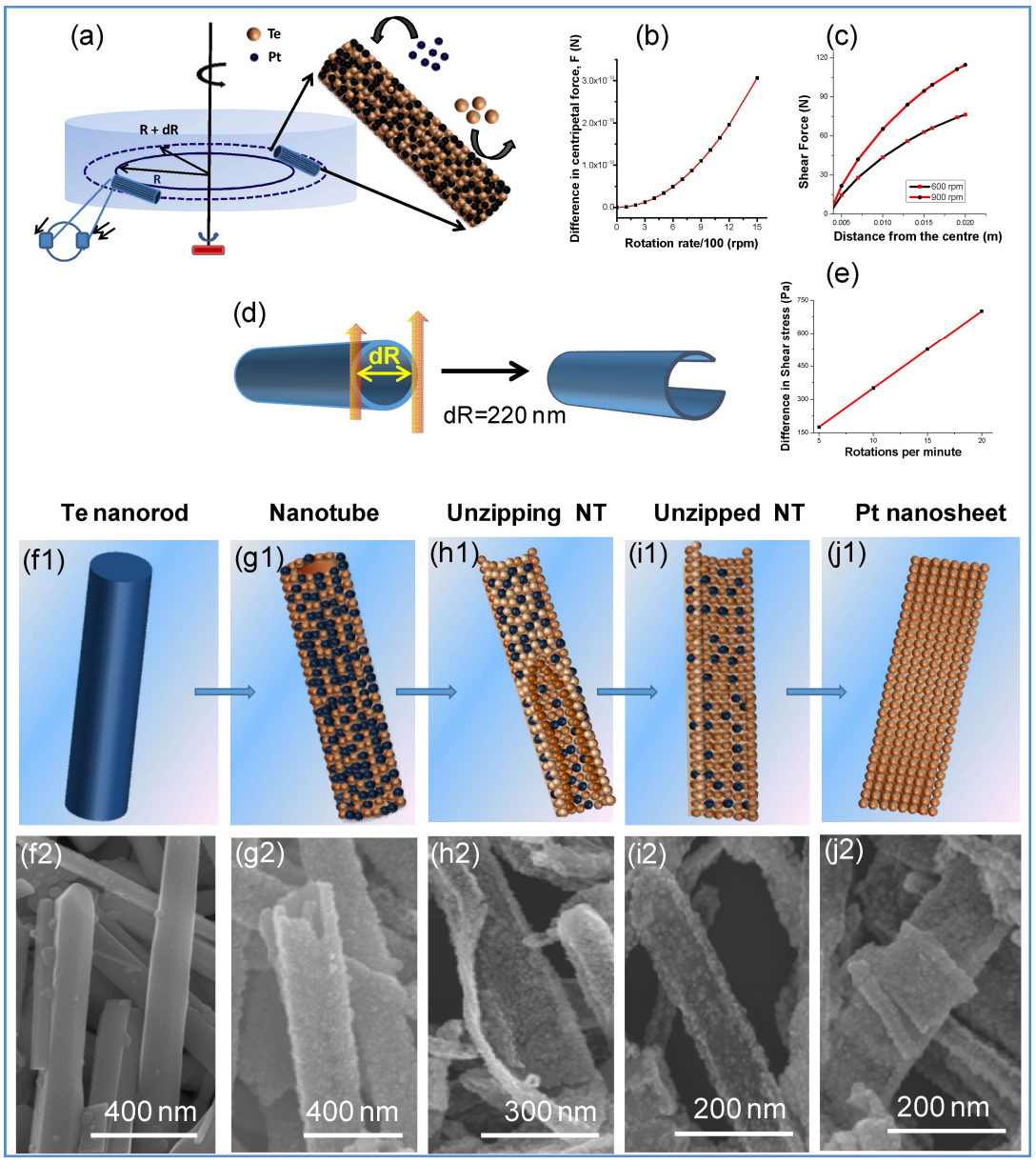

Figure 2.36: (a) Schematic of a Te nanorod in a solution with a circular motion due to stirring, undergoing a galvanic displacement reaction with Pt simultaneously. (b) The difference of centripetal force across a Te nanorod at different rotation speed and (c) shear forces experienced by it at various distances from the rotation center under our experimental conditions. (d) Schematic of the proposed opening mechanism to form a nanosheet due to difference in shear stress across the nanotube. Estimated delta-gamma during PtNS synthesis at 900 rpm is depicted in (e). (f–j) various model structures and the respective SEM images showing the possible stages of formation of a Pt nanosheet.

shaking that changes convective transport of ions and other reacting species. Here, we have invoked a simple model mimicking our experiments to understand the effect of magnetic stirring and estimate typical forces working on a Te nanorod under GD (**Figure 2.36a**).

Stirring imparts a continuous rotational motion to the nanorod solution leading to the generation of centripetal forces (F_c) and shear stress (τ). Influence of these factors in our experimental condition is discussed in details as follows.

4.4. Forces involved in the nanosheet formation: The simultaneous action of galvanic displacement and shear forces induced by magnetic stirring changes the morphology of our reaction products from that of the template itself. Herein, we have observed that for formation of Pt nanosheets, there must be sufficient shear stress. A nanostructure under stirring, in a fluid, experiences a centripetal force, which keeps it moving in a circular path. It also experiences shear stress arising out of velocity gradient the fluid experiences as the distance from the rotation centre increases. The factors responsible for creating this deforming stress in the nanotube are discussed below.

4.4.1. Centripetal force:

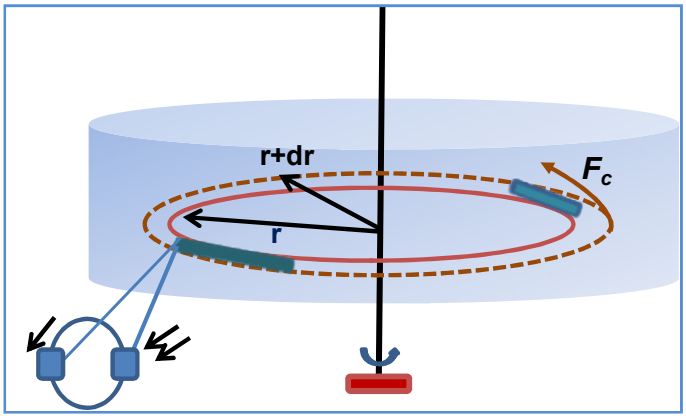

Figure 2.37: Schematic illustration showing the cenripetal force acting on an imaginary area of rotating fluid.

The rotating motion of the reaction solution creates centripetal force on a nanostructure.

Force on any mass ‘m’ and moving with an acceleration of ‘a’ is equal to,

$$F = ma$$

If a body is subjected to a circular motion with an angular acceleration of 'a_r' where $a_r = \omega^2 r$ r = radius of circular motion and ω = angular velocity. In that case, the resulting centripetal force is given by,

$$F = m\omega^2 r$$

Or, $F = mr4\pi^2 n^2$ *ω = 2πn, n = stirring rate (rotations per second)*

Hence the centripetal force varies as a square of the rate of rotation (per second) at a definite distance away from the axis of the rotating fluid. It is independent of the fluid used and the chemical interactions. So at distance of r and r+dr from the axis of rotation the centripetal force would be,

$F_1 = m_1 r4\pi^2 n^2$ and $F_2 = m_2(r + dr)4\pi^2 n^2$

In case of an object with diameter *dr*, the object will experience different centripetal force near and away from the axis or rotation. The difference in centripetal force,

$$= F_2 - F_1 = m4\pi^2 n^2 dr$$

While the centripetal force induces circular motion, this difference in force on either side of the object forces it to maintain a steady orientation with respect to the rotation centre. For an individual Te nanorods with 200 nm diameter, (considering mass of 1 unit cell of Pt = 6.64 * 10^{-24}g)

$dr = 200nm$ $m = \rho \times V$ $m = \rho \times (\pi r^2 L)$

$$= 6.24 \times 2 \times 3.14 \times 100 \times 100 \times 4410\ gcm^{-3}nm^{-3}$$

$$= 6.3 \times 10^{-16} kg$$

Thus difference in centripetal force is,

$$\Delta F_c = 6.3 \times 10^{-16} \times 4 \times 3.14 \times 3.14 \times 200 \times 10^{-9} \times n^2(N)$$

$= 4.9 \times 10^{-21} \times n^2(N)$

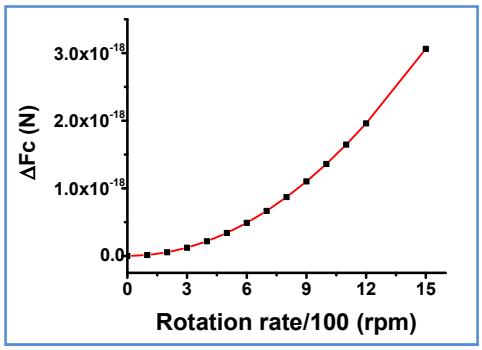

Figure 38: Plot showing the difference in centripetal force across the diameter of a 200 nm Te nanorod (dispersed in a liquid) rotating in a beaker at various speeds (rotations per minute = rpm).

From **Figure 2.38**, it can be noticed that ΔF_c is of the order of attoN (10^{-18} N), independent of the distance from the rotation centre, but increases significantly as the rotation speed increases. This increase is significant because at higher rotational speed, external turbulences cannot easily deflect the nanorods from circular path and hence the (reactive) environment around it remains same.

4.4.2. Forces acting on a continuously rotating viscous fluid

Velocity gradient in a real fluid subjected to stirring

When an infinite viscous fluid is subjected to a vortex flow, velocity of the fluid layers follows the following equation.

v $\propto$ r, for $(r \leq c)$ $\propto \frac{1}{r}$, $(r > c)$, r is the distance from the central axis rotation, c is a critical distance

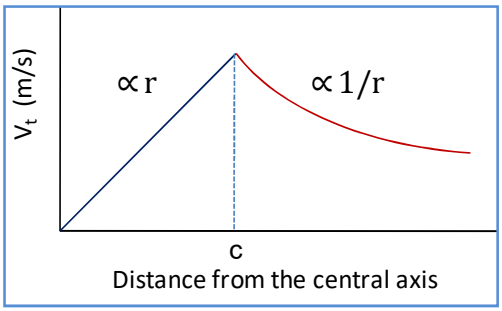

Figure 2.39: Variation of velocity as a function of 'r' in a fluid subjected to vortex motion.

However in a beaker, the situation is more complex as the vortex flow is contained within walls, and a near understanding of the fluid flow can be achieved by estimating a fluid flow model as shown in **Figure 2.40 and 2.41**.

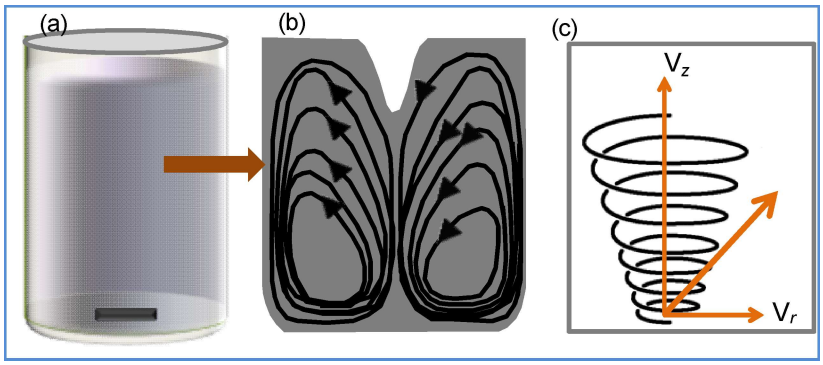

Figure 2.40: (a) Rotating fluid in beaker. (b) A cross-sectional view of the fluid flow showing the direction of motion of fluid during the vortex motion. (c) Three components of fluid velocity in the above mention model of fluid flow.

The fluid has three velocity components- tangential (v_t), axial (v_r) and vertical (v_z). At a particular rotation rate of the fluid in a container the three components are

$$v_r = \frac{2\eta}{c^2} r \quad -(1) \qquad v_t = \frac{C}{r}\left(1 - e^{-r^2/c^2}\right) \quad -(2) \qquad v_z = \frac{4\eta}{c^2} z \quad -(3)$$

And $V_{total} = v_t + v_r + v_z$ - (4)

V_{total} varies at different positions within a beaker, and at a particular position, V_{total} varies with the rate of rotation of the fluid.

$$V \propto rpm(\omega).$$

'C' in v_t (Eq (2)) is the vortex strength and is given by, $C = A\omega$ where A is a constant and ~1 for the present system and ω $(in\ rps)$ is the rotation rate. Among the various components, v_t has the strongest contribution (**Figure 2.42c**: for instance, for each complete rotation w.r.t v_t, the displacement along v_r and v_z is much smaller. Moreover not only the magnitude of v_z and v_r are small, v_z changes its sign and v_r becomes zero near the wall and at the beaker centre). Therefore consideration of v_t alone will provide a good approximation for the force arising out of fluid motion.

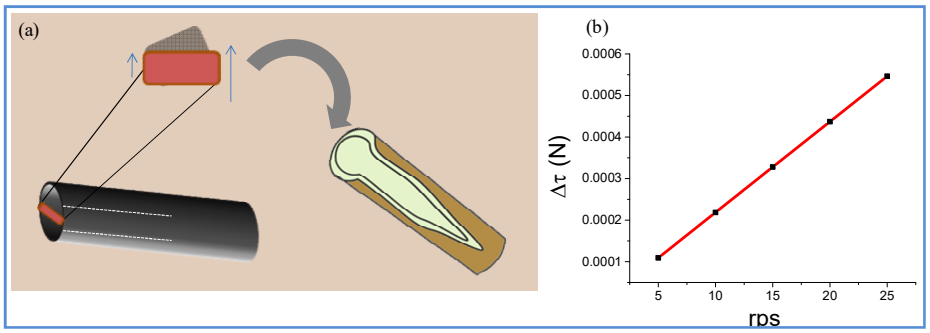

Figure 2.41: (a) Shear stress generated in the nanotube due to rotation of the fluid. (b) Difference in Shear force at the two diametrically opposite ends of the nanorod as a function of rotation rate.

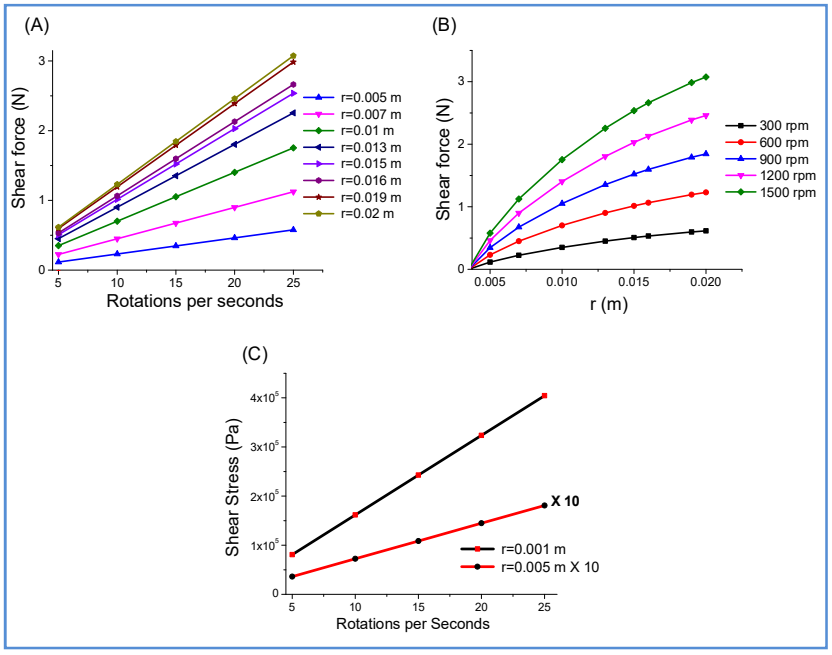

Figure 2.42: (A) Plot of Shear force at different rotation rates (B) at different distances from the central axis of rotation and (C) Shear stress at 0.1 cm and 0.5 cm as a function of rotation rate. The length of the magnetic stirring bar is 1.52 cm.

In our experiments, we have used a beaker with a diameter of 4.02 cm. So V_t changes at various distances from the centre of the beaker and at different values of rps.

4.5. Shear forces generated in our experiments

Magnetically stirring will give rise to a velocity gradient depicted in **Figure 2.40**. Considering a non-newtonian viscous fluid, the force exerted by the magnetic stirrer is not transferred to the nanorods by mechanical means alone, and chemical interactions (effective viscosity) also plays

a crucial role in determining shear forces generated in the fluid due to rotation. The shear stress on long thin cylinder suspended in a continuously rotating viscous fluid is given by,

$\tau = \mu \frac{dv_t}{dr}$ $\tau =$ Shear stress, μ = Dynamic viscosity of the fluid and v_t = Tangential velocity of the fluid element.

The shear force, on the other hand, acting on the imaginary cylindrical portion of the fluid column is given by,

$$F = \int \tau\,(2\pi r)dr$$

$$= 2\pi\mu\omega\left[\int r\left\{-\frac{1}{r^2} + \frac{2e^{-r^2/c^2}}{r^2} + \frac{\left(e^{-r^2/c^2}\right)}{r^2}\right\}dr\right]$$

$$= 2\pi\mu\omega\left[\frac{Ei\left(\frac{-r^2}{c^2}\right)}{2} - e^{-r^2/c^2} - \log(r)\right]$$

In our experiments, the viscosity of the reaction mixture was estimated to be 0.0161 Ns/m^2. **Figure 2.41 and 2.42** shows how shear forces within the beaker in our experimental conditions. So to sum up, A Te nanorod subjected to stirring will experience centripetal force that increases proportionally with the distance and varies as the square of the rotation rate (**Figure 2.36B**). Our estimation from the above calculations indicates that regular bench-top stirring leads to a difference in F_c across the nanorod, which of the order of 1 *a*N (on two Pt unit cells located across the diameter of a 220 nm thick nanorod rotating at 900 rpm. The rod is considered in a lying down position as depicted in the schematic, **Figure 2.37**). This keeps the nanorods floating, prevents large-scale agglomeration and drives their flow in a circular path about the rotation centre allowing the τ and GD to act upon simultaneously and uniformly. Nanorods experience more shear force when positioned away from the rotation axis (**Figure 2.36C,D**). During our PtNS synthesis at 900 rpm, shear force and τ reach up to ≈1.8 N and ≈2.4 × 10 4 Pa, respectively (**Figure 2.42**), comparable to the ones during shear induced protein agglomeration and TiO_2 nanotube fusion.[60-62,71] The importance of shear force on chemical deformation was first demonstrated in 1935.[72] Strain generated by shear forces leads to the

elongation of chemical bonds and often rupture them.[73,74] We believe that contribution of shear force is crucial for the synthesis of PtNS too. During the GD process, small Pt nanoparticles deposit on the Te NR initially. On the other hand, the template becomes increasingly fragile as more and more of Te leaches out. When nearly 50%–60% of Te is displaced, and the cohesive energy between neighboring Pt NCs are not yet sufficiently strong, the nanosheets begin to appear (**Figure 2.35**). In such an instance, a larger shear stress on one side of the fragile Te–Pt structure than the other (**Figure 2.36 D,E**) leads to its opening, gradual unzipping and finally to the formation of nanosheet. The various possible intermediates formed during the generation of a nanosheet are shown in (**Figure 2.36 F–I**). Therefore, as stated earlier, when we subjected to stirring a preformed Pt nanostructure where the Pt NCs had been already strongly attached to each other, we did not observe any change in morphology.

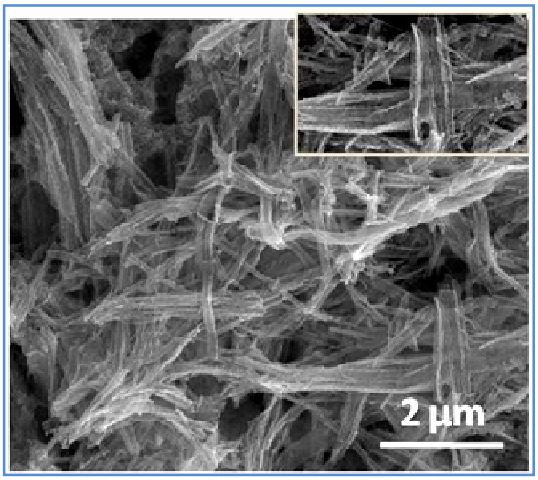

Figure 2.43: FESEM images of the Pt nanostructures obtained at 600 rpm, where the 1D structures are fused and do not appear to be free-standing.

To further understand the effect of mechanical stirring, we systematically varied the rotation rate of the reaction mixture keeping other conditions identical. Absence of stirring leads to the formation of only Pt nanotubes. At 300 and 600 rpm, the nanostructures begin to open gradually, though they still look like 1D nanostructures or their agglomerate, and not like the free-standing sheets obtained at 900 rpm (**Figure 2.43**). Increasing in rotation rate beyond 900 does not affect the morphology any more. Since the nanosheets do not form at 600 rpm, probably a shear force greater than 1N is a necessity. From **Figure 42B**, it can be estimated that nearly 60%–70% of nanostructures will be exposed to such force at 900 rpm. The fraction of

such nanostructures will be larger at higher rotation speed. Next, we altered the viscosity of the reaction mixture by introducing water into the medium, expecting that lower viscosity would lead to enhanced ionic diffusion and accelerated GD kinetics. We found that as the proportion of EG decreased, the reaction finished faster and instead of a uniform distribution, cluster of Pt nanoparticles formed surrounding the Te nanorod (**Figure 2.44**).

This observation led us to believe that the GD process should be slow enough so that shear forces can act upon for a sufficiently long time to yield the nanosheets. Due to many possible advantages associated with the Pt nanosheets, we explored their catalytic efficiencies toward methanol and formic acid oxidation reaction (MOR and FAO, respectively). Even though the sheets consist of nanocrystals without any predominant crystal facet, their free-standing nature should provide much higher electrochemically active surface area (ECSA) and better effi ciency for the following reasons.

(1) Usually catalyst nanocrystals are anchored onto conducting supports such as graphene, RGO or amorphous carbon in order to reduce their agglomeration and increase conductivity.[75] Otherwise, the loosely bound nanocrystals within agglomerates behave as Schottky contacts leading to higher reaction overpotential. Such effects would be minimal in the nanosheets as the constituent nanocrystals are crystallographically attached to some of the neighboring nanocrystals.

(2) On the other hand, employing catalyst support also induces large loss of effective surface area. The supports, during the preparation of the working electrode, can deposit as layers one on top of others and sandwich many nanocrystals.[76]

This situation may be avoided or minimized in the nanosheets, as we have observed during SEM examination of numerous drop-casted samples. Deposition of the nanosheets do not lead to their stacking and instead, they intertwine leaving enough space for electrolyte and fuel percolation (kinematic diameter for small fuel molecules is ≈0.38–0.54 nm,[77] much smaller that the nanosheet dimensions). Therefore almost entire nanosheet-surface would be able to participate in catalysis reaction.

4.5. Electrochemical activity of Pt NS:

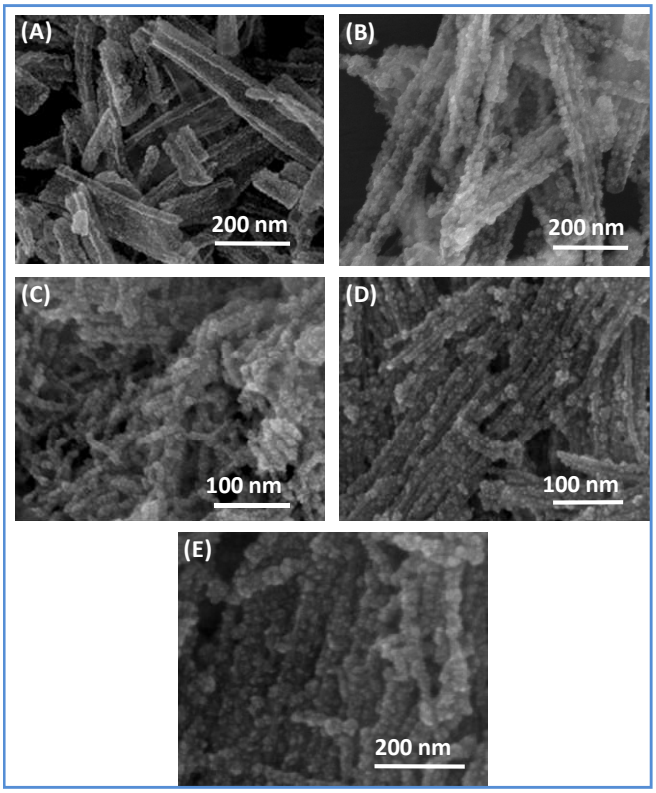

Figure 2.44: FESEM images of the products obtained by introducing H_2O into the reaction mixture. (A) 0 ml, (B) 3 ml, (C) 5 ml, (D) 10 ml, (E) 20 ml. the total volume of the reaction mixture was always kept 20 ml.

We first evaluated the ECSA and stability of the Pt nanosheets using Ag/AgCl (3 M NaCl) as the reference electrode and compared the performances with a commercial carbon supported Pt NCs (C–Pt/C) catalyst. The cyclic voltamograms (CVs) were recorded at 27 °C in Ar saturated 0.5 M H_2SO_4 at a scan rate of 50 mVs^{-1}. ECSA values were calculated by estimating the charge transferred during hydrogen adsorption on the electrode surface using double layer corrected CV plots. Charge transfer across Pt electrode due to underpotentially deposited monolayer of hydrogen atom corresponds to 230 μCcm^{-2}. The ECSA value for Pt nanosheets was calculated to be 47.37 m^2g^{-1} which is ≈200% higher that of C–Pt/C (23.70 m^2g^{-1}, **Figure 2.45A**) indicating highly exposed facets of the nanosheets. In addition, their CV plots also exhibit two distinct hydrogen adsorption peaks characteristic of relatively more stable low index Pt facets.[16,30] The stability of the nanosheets in absence of conducting carbon support is comparable to the commercial catalyst. ECSA for the PtNS remained high with continued use

and was found to be 2.09 times higher than that of C–Pt/C after 5000 catalysts' cycles (**Figure 2.45B**).

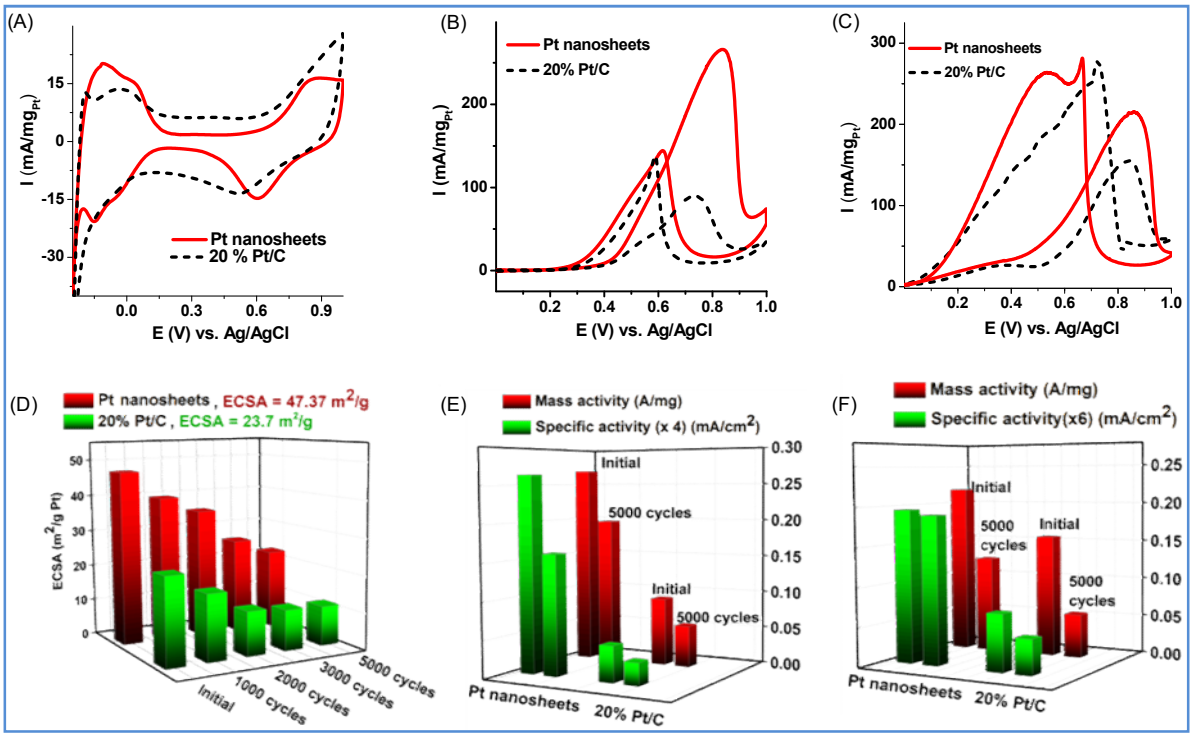

Figure 2.45: (A) CV corresponding to PtNS and commercial Pt/Ct (in Ar saturated 0.5 M H_2SO_4 solution with 50 mV s −1 scan rate). (B) Gradual change of ECSA recorded for PtNS (red) and C-Pt/C (green). (C) MOR recorded in 0.5 M H_2SO_4 + 1 M CH_3OH (scan rate 20 mVs^{-1}) and (D) corresponding mass and specific activity recorded initially and after 5000 cycles. (E) FAO recorded in 0.5 M H_2SO_4 + 1 M HCOOH at scan rate 20 mVs^{-1} and(F) corresponding mass and specific activity recorded initially and after 5000 cycles.

As a result of the above observations, and since electrolyte desorption from low index facets is relatively facile,[23] the nanosheets were expected to exhibit superior catalytic effi ciency for fuel oxidation reactions. We evaluated the MOR and FAO activities of the Pt nanosheets using Ar saturated 0.5 M H_2SO_4 + 1 M MeOH and 0.5 M H_2SO_4 + 1 M HCOOH solutions, respectively. **Figure 2.45C** is the MOR CV plots of Pt nanosheets (scan rate of 20 mVs^{-1}) showing a peak current density of 269.6 mA mg^{-1}. This represents a remarkably facile oxidation reaction, yielding 2.93 times higher anodic current than that for C–Pt/C (91.6 mA mg^{-1}) (**Figure 45D**, **Figure 46**). The rate of methanol oxidation on the nanosheets is even higher than that expected on the basis of the ECSA values, suggesting that all surface sites of the commercial catalysts may not be available for methanol oxidation due to its larger molecular size as compared to hydrogen.

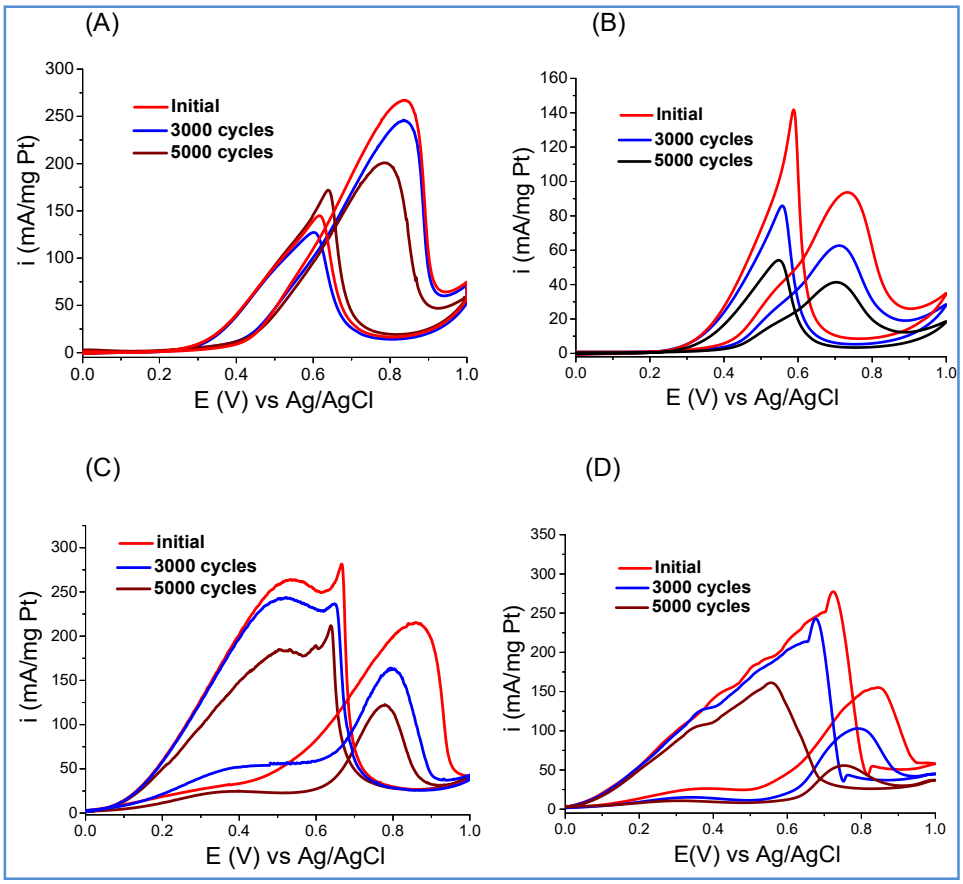

Figure 2.46: CV of Pt nanosheets (A) and 20% Pt/C (B) in 0.5 M H_2SO_4 + 1 M MeOH and CV of Pt nanosheets (C) and C-Pt/C (D) in 0.5 M H_2SO_4 and 1 M HCOOH.

Additionally, the nanosheets also exhibit superior resistance to catalyst poisoning by carbonaceous reaction intermediates, indicated by the ratio of the cathodic peak to anodic peak current density (I_f/I_b).[58,78,79] The (I_f/I_b) ratio was recorded as 1.91 for the Pt nanosheets, which is not only better than that of C-Pt/C (0.67), but also superior to many state-of-the-art Pt catalysts (**Table 6**). **Figure 2.45E**, **Figure 2.46**, shows the CV plots corresponding to FAO with the Pt nanosheets and C–Pt/C. The mass current density of Pt nanosheets is 1.4 times that of the commercial catalyst. The mass activity and the specific activity of the two catalysts for MOR and FAO are listed in **Figure 2.45D,F**, **Figure 2.46**. In addition, even after 5000 catalytic cycles in the case of MOR, the loss in the mass activity of PtNS is only 26.4% as compared to 38.5% for C–Pt/C.

Enhanced estimated ECSA, larger mass activity and greater poisoning tolerance of PtNS can be attributed to their easily accessible surfaces due to unique 2D morphology and absence of carbon-based catalyst supports that can contribute toward poisoning. We also point out that the influence of the tiny amount of Te present in the nanostructure is perhaps worth investigating, since its influence in electrochemical properties of Pt, unlike other metals, is not well established.

Table 6: Comparison of I_f/I_b of the recent Pt based 1D and 2D catalyst for methanol oxidation reaction

S. No.	Catalyst	I_f/i_b	Reference
1	Pt-HNS	1.12	[80]
2	Porous Pt NT	1.03	[81]
3	PtNP@PPy NF	1.75	[82]
4	Pt/OMC-WO_3	1.69	[83]
5	TePt Nanonetwork	1.25	[84]
6	Au/CuPt	1.62	[85]
7	Au@Pt/C	1.42	[86]
8	Pt/PEG1000	1.18	[87]
9	Te/Pt NW hybrid	2.1	[88]
10	Pt-Au-Graphene	1.53	[89]
11	UT Pt NWs	1.87	[90]
12	Pt/OMCS	1.64	[91]
12	Pt/TiC	1.4	[92]
13	C-PtPd/rGO	1.31	[93]
14	Pt nanopetals/SiNC	1.39	[94]
15	**Pt nanosheets**	**1.9**	**This work**

5. Conclusions

In summary, we have been able obtain sub-10 nm Pt tetrahedral NCs by a facile hydrothermal method, in absence of any external stabilizing agents. We establish that amine species generated *in-situ* from the reaction of EG and DMF in presence of KOH and the nucleation induced by the carbon support is responsible for generating such shape. Dimethyl amine can be easily removed from the NC surface, possibly leaving its surface entirely exposed. These Pt-NTd/C samples exhibit excellent stability and high electrocatalytic efficiency towards fuel cell oxidation and reduction reactions.

In the next part, we have demonstrated the successful synthesis of free-standing Pt nanosheets for the first time, which would be an important addition to just a few recently realized noble metal nanosheets. This was achieved by adopting a simple mechanical force driven morphology control approach wherein stirring induced shear force was employed to deform an incipient Pt nanostructure which otherwise would be form a nanotube. The nanosheets have a thickness of ≈27 nm and uneven surfaces giving rise to high catalytically active surface area. In addition, its constituent nanoparticles are crystallographically attached to their neighbors, lending further structural stability. It may be noted that even though crystallinity is not extended throughout the sheet as in convensional nanosheets, further improvement in the synthesis procedure may lead to single-crystalline sheets due to the oriented attachment of the nanocrystals. We show that these nanosheets exhibit remarkable efficiency toward electrocatalytic oxidation of small fuel molecules when compared with commercial Pt catalysts. Our results demonstrate that mechanical forces generated in simple experimental set up can be effectively used to tailor morphology of nanomaterials at a length-scale far beyond what is experimentally demonstrated so far, particularly when they are used during transformation of one material to another.

6. References:

[1] A. Kazim, Energy Convers. Manag. 2001, 42, 763.
[2] M. W. Ellis, M. R. V. Spakovsky, D. J. Nelson, Proc. IEEE 2001, 89, 1808.
[3] K. V. Kordesch, G. R. Simader, Chem. Rev. 1995, 95, 191.
[4] https://www.energy.gov/eere/fuelcells/types-fuel-cells

[5] https://www.energy.gov/eere/fuelcells/fuel-cells
[6] C. Song, J. Zhang, in *PEM Fuel Cell Electrocatalysts and Catalyst Layers: Fundamentals and Applications*, (Ed: J. Zhang), Springer London, London 2008, 89.
[7] M. A. Mahmoud, R. Narayanan, M. A. El-Sayed, Acc. Chem. Res. 2013, 46, 1795.
[8] Y. Kang, M. Li, Y. Cai, M. Cargnello, R. E. Diaz, T. R. Gordon, N. L. Wieder, R. R. Adzic, R. J. Gorte, E. A. Stach, C. B. Murray, J. Am. Chem. Soc. 2013, 135, 2741.
[9] Y. Kang, J. B. Pyo, X. Ye, T. R. Gordon, C. B. Murray, ACS Nano 2012, 6, 5642.
[10] C. Koenigsmann, M. E. Scofield, H. Liu, S. S. Wong, J. Phys. Chem. Lett. 2012, 3, 3385.
[11] V. Tripković, I. Cerri, T. Bligaard, J. Rossmeisl, Catal. Lett. 2014, 144, 380.
[12] J. K. Nørskov, J. Rossmeisl, A. Logadottir, L. Lindqvist, J. R. Kitchin, T. Bligaard, H. Jónsson, J. Phys. Chem. B 2004, 108, 17886.
[13] Y. Wang, S. Xie, J. Liu, J. Park, C. Z. Huang, Y. Xia, Nano Lett. 2013, 13, 2276.
[14] X. Younan, X. Yujie, L. Byungkwon, S. S. E., Angew. Chem. Int. Ed. 2009, 48, 60.
[15] M. Shao, A. Peles, K. Shoemaker, Nano Lett. 2011, 11, 3714.
[16] H. M. Lu, X. K. Meng, J. Phys. Chem. C 2010, 114, 1534.
[17] Q. Jiang, J. C. Li, B. Q. Chi, Chem. Phys. Lett. 2002, 366, 551.
[18] C. Koenigsmann, W.-p. Zhou, R. R. Adzic, E. Sutter, S. S. Wong, Nano Lett. 2010, 10, 2806.
[19] B. Hammer, J. K. Nørskov, Surf. Sci. 1995, 343, 211.
[20] C.-Y. Chiu, Y. Li, L. Ruan, X. Ye, C. B. Murray, Y. Huang, Nat. Chem. 2011, 3, 393.
[21] T. S. Ahmadi, Z. L. Wang, T. C. Green, A. Henglein, M. A. El-Sayed, Science 1996, 272, 1924.
[22] J. Solla-Gullon, F. J. Vidal-Iglesias, A. Lopez-Cudero, E. Garnier, J. M. Feliu, A. Aldaz, Phys. Chem. Chem. Phys. 2008, 10, 3689.
[23] H. Song, F. Kim, S. Connor, G. A. Somorjai, P. Yang, J. Phys. Chem. B 2005, 109, 188.
[24] B. Y. Xia, H. B. Wu, Y. Yan, X. W. Lou, X. Wang, J. Am. Chem. Soc. 2013, 135, 9480.
[25] P. K. Jain, X. Huang, I. H. El-Sayed, M. A. El-Sayed, Acc. Chem. Res. 2008, 41, 1578.
[26] X. Hong, C. Tan, J. Liu, J. Yang, X.-J. Wu, Z. Fan, Z. Luo, J. Chen, X. Zhang, B. Chen, H. Zhang, J. Am. Chem. Soc. 2015, 137, 1444.
[27] X. Huang, S. Tang, X. Mu, Y. Dai, G. Chen, Z. Zhou, F. Ruan, Z. Yang, N. Zheng, Nat. Nanotechnol. 2010, 6, 28.
[28] H. Duan, N. Yan, R. Yu, C.-R. Chang, G. Zhou, H.-S. Hu, H. Rong, Z. Niu, J. Mao, H. Asakura, T. Tanaka, P. J. Dyson, J. Li, Y. Li, Nat. Commun. 2014, 5, 3093.
[29] I. Lee, F. Delbecq, R. Morales, M. A. Albiter, F. Zaera, Nat. Mater. 2009, 8, 132.
[30] P. Qingyu, L. Yibin, H. Xiaodong, G. Xuchun, S. Yuanyuan, W. Chunhui, W. Chao, Z. Wenqi, D. Shanyi, S. Enzheng, L. Peixu, W. Dehai, C. Anyuan, Adv. Mater. 2014, 26, 3241.
[31] S. Ozden, P. A. S. Autreto, C. S. Tiwary, S. Khatiwada, L. Machado, D. S. Galvao, R. Vajtai, E. V. Barrera, P. M. Ajayan, Nano Lett. 2014, 14, 4131.
[32] L. Jiao, L. Zhang, X. Wang, G. Diankov, H. Dai, Nature 2009, 458, 877.
[33] J. Ye, J. Liu, Y. Zhou, Z. Zou, J. Gu, T. Yu, J. Power Sources 2009, 194, 683.
[34] H.-S. Qian, S.-H. Yu, J.-Y. Gong, L.-B. Luo, L.-f. Fei, Langmuir 2006, 22, 3830.
[35] Z. L. Wang, J. Phys. Chem. B 2000, 104, 1153.
[36] Z. Q. Tian, S. P. Jiang, Y. M. Liang, P. K. Shen, J. Phys. Chem. B 2006, 110, 5343.
[37] C. Mei, W. Binghui, Y. Jing, Z. Nanfeng, Adv. Mater. 2012, 24, 862.
[38] X. Huang, Z. Zhao, J. Fan, Y. Tan, N. Zheng, J. Am. Chem. Soc. 2011, 133, 4718.
[39] G. Novell-Leruth, A. Valcárcel, A. Clotet, J. M. Ricart, J. Pérez-Ramírez, J. Phys. Chem. B 2005, 109, 18061.
[40] I. Pastoriza-Santos, M. Liz-Marzán Luis, in Pure Appl. Chem., 2000, 72, 83.

[41] A. R. J., B. J. J., G. Lee, P. Manuel, Magn. Reson. Chem. 2006, 44, 491.
[42] P. Kundu, C. Nethravathi, P. A. Deshpande, M. Rajamathi, G. Madras, N. Ravishankar, Chem. Mater. 2011, 23, 2772.
[43] K. Gong, M. B. Vukmirovic, C. Ma, Y. Zhu, R. R. Adzic, J. Electroanal. Chem. 2011, 662, 213.
[44] M. Lei, C. Liang, Q. Huan, K. Miyabayashi, M. Miyake, T. Yang, Acta Mater. 2014, 63, 202.
[45] S. Shuhui, Z. Gaixia, G. Dongsheng, C. Yougui, L. Ruying, C. Mei, S. Xueliang, Angew. Chem. Int. Ed. 2011, 50, 422.
[46] B. Narayanamoorthy, K. K. R. Datta, M. Eswaramoorthy, S. Balaji, ACS Appl. Mater. Interfaces 2012, 4, 3620.
[47] A. M. Hofstead-Duffy, D.-J. Chen, S.-G. Sun, Y. J. Tong, J. Mater. Chem. 2012, 22, 5205.
[48] Y. Kim, H. J. Kim, Y. S. Kim, S. M. Choi, M. H. Seo, W. B. Kim, J. Phys. Chem. C 2012, 116, 18093.
[49] D. A. McCurry, M. Kamundi, M. Fayette, F. Wafula, N. Dimitrov, ACS Appl. Mater. Interfaces 2011, 3, 4459.
[50] X. B. Yu, W. H. Bin, W. Xin, L. X. Wen, Angew. Chem. Int. Ed. 2013, 52, 12337.
[51] X. B. Yu, W. H. Bin, Y. Ya, W. H. Bo, W. Xin, Small 2014, 10, 2336.
[52] L. Hai-Wei, C. Xiang, Z. Fei, C. Chun-Hua, Z. Wen-Jun, Y. Shu-Hong, Adv. Mater. 2011, 23, 1467.
[53] K. W. Kim, S. M. Kim, S. Choi, J. Kim, I. S. Lee, ACS Nano 2012, 6, 5122.
[54] J. Kibsgaard, Y. Gorlin, Z. Chen, T. F. Jaramillo, J. Am. Chem. Soc. 2012, 134, 7758.
[55] B. Lim, X. Lu, M. Jiang, P. H. C. Camargo, E. C. Cho, E. P. Lee, Y. Xia, Nano Lett. 2008, 8, 4043.
[56] J. N. Tiwari, K. Nath, S. Kumar, R. N. Tiwari, K. C. Kemp, N. H. Le, D. H. Youn, J. S. Lee, K. S. Kim, Nat. Commun. 2013, 4, 2221.
[57] Y. Zuo, K. Cai, L. Wu, T. Li, Z. Lv, J. Liu, K. Shao, H. Han, J. Mater. Chem. A 2015, 3, 1388.
[58] L. Cuiling, S. Takaaki, Y. Yusuke, Angew. Chem. Int. Ed. 2013, 52, 8050.
[59] L. Ma, C. Wang, M. Gong, L. Liao, R. Long, J. Wang, D. Wu, W. Zhong, M. J. Kim, Y. Chen, Y. Xie, Y. Xiong, ACS Nano 2012, 6, 9797.
[60] I.-Y. Jeon, Y.-R. Shin, G.-J. Sohn, H.-J. Choi, S.-Y. Bae, J. Mahmood, S.-M. Jung, J.-M. Seo, M.-J. Kim, D. Wook Chang, L. Dai, J.-B. Baek, Proc. Natl. Acad. Sci. 2012, 109, 5588.
[61] M. A. Mahmoud, M. A. El-Sayed, J. Gao, U. Landman, Nano Lett. 2013, 13, 4739.
[62] T. Yuxin, Z. Yanyan, D. Jiyang, W. Jiaqi, T. H. Le, C. B. Kallupalathinkal, D. Zhili, C. Zhong, C. Xiaodong, Adv. Mater. 2014, 26, 6111.
[63] G. U. K., B. Y., Z. J., C. P. M. F. J., F. X. S., G. D., Adv. Mater. 2008, 20, 810.
[64] C. Yu, S. Bohang, T. Xiaosheng, L. Li, X. Junmin, Small 2014, 10, 1536.
[65] X. Xiaohu, W. Yi, R. Aleksey, X. Younan, Adv. Mater. 2013, 25, 6313.
[66] W. Wang, M. Dahl, Y. Yin, Chem. Mater. 2013, 25, 1179.
[67] W. Wang, J. Goebl, L. He, S. Aloni, Y. Hu, L. Zhen, Y. Yin, J. Am. Chem. Soc. 2010, 132, 17316.
[68] X. Xia, S. Xie, M. Liu, H.-C. Peng, N. Lu, J. Wang, M. J. Kim, Y. Xia, Proc. Natl. Acad. Sci. 2013, 110, 6669.
[69] Z. L. Wang, T. S. Ahmad, M. A. El-Sayed, Surf. Sci. 1997, 380, 302.
[70] X. Lu, H.-Y. Tuan, J. Chen, Z.-Y. Li, B. A. Korgel, Y. Xia, J. Am. Chem. Soc. 2007, 129, 1733.
[71] Y. T. Z., O. C. F. G., K. S. T., K. Sameeran, S. J. N., B. W. A., P. K. M., O. T. J., I. Mariam, R. C. L., W. G. A., ChemBioChem 2015, 16, 393.
[72] P. W. Bridgman, Phys. Rev. 1935, 48, 825.
[73] S. R. Jezowski, L. Zhu, Y. Wang, A. P. Rice, G. W. Scott, C. J. Bardeen, E. L. Chronister, J. Am. Chem. Soc. 2012, 134, 7459.
[74] M. M. Caruso, D. A. Davis, Q. Shen, S. A. Odom, N. R. Sottos, S. R. White, J. S. Moore, Chem. Rev. 2009, 109, 5755.
[75] B. Narayanamoorthy, K. K. R. Datta, M. Eswaramoorthy, S. Balaji, ACS Catal. 2014, 4, 3621.
[76] Á. Kriston, T. Xie, D. Gamliel, P. Ganesan, B. N. Popov, J. Power Sources 2013, 243, 958.

[77] J. E. ten Elshof, C. R. Abadal, J. Sekulić, S. R. Chowdhury, D. H. A. Blank, Micropor. Mesopor. Mater. 2003, 65, 197.
[78] C.-H. Cui, H.-H. Li, S.-H. Yu, Chem. Sci. 2011, 2, 1611.
[79] X. Ge, R. Wang, P. Liu, Y. Ding, Chem. Mater. 2007, 19, 5827.
[80] M. Yang, Q. Cai, C. Liu, R. Wu, D. Sun, Y. Chen, Y. Tang, T. Lu, J. Mater. Chem. A 2014, 2, 13738.
[81] A. S. M., Z. Gang, K. David, L. Dongsheng, G. Shuang, J. Kurt, Y. Yushan, Adv. Funct. Mater. 2010, 20, 3742.
[82] Y. Liu, N. Lu, S. Poyraz, X. Wang, Y. Yu, J. Scott, J. Smith, M. J. Kim, X. Zhang, Nanoscale 2013, 5, 3872.
[83] J. Zeng, C. Francia, C. Gerbaldi, V. Baglio, S. Specchia, A. S. Aricò, P. Spinelli, Electrochim. Acta 2013, 94, 80.
[84] Y. Jian, L. Lagae, Nanotechnology 2014, 25, 275303.
[85] X. Sun, D. Li, Y. Ding, W. Zhu, S. Guo, Z. L. Wang, S. Sun, J. Am. Chem. Soc. 2014, 136, 5745.
[86] J. Zeng, J. Yang, J. Y. Lee, W. Zhou, J. Phys. Chem. B 2006, 110, 24606.
[87] F. Ye, L. Chen, J. Li, J. Li, X. Wang, Electrochem. Commun. 2008, 10, 476.
[88] S. Guo, S. Dong, E. Wang, J. Phys. Chem. C 2010, 114, 4797.
[89] Y. Hu, H. Zhang, P. Wu, H. Zhang, B. Zhou, C. Cai, Phys. Chem. Chem. Phys. 2011, 13, 4083.
[90] L. Zhang, N. Li, F. Gao, L. Hou, Z. Xu, J. Am. Chem. Soc. 2012, 134, 11326.
[91] C. Zhang, L. Xu, N. Shan, T. Sun, J. Chen, Y. Yan, ACS Catal. 2014, 4, 1926.
[92] Z. Qiu, H. Huang, J. Du, X. Tao, Y. Xia, T. Feng, Y. Gan, W. Zhang, J. Mater. Chem. A 2014, 2, 8003.
[93] Y. Lu, Y. Jiang, W. Chen, Nanoscale 2014, 6, 3309.
[94] J. N. Tiwari, R. N. Tiwari, K.-L. Lin, ACS Appl. Mater. Interfaces 2010, 2, 2231.

Chapter-3

Doping MoS_2 Inorganic Fullerenes (IF-MoS_2) for Electrochemical Hydrogen Production

Doping MoS_2 Inorganic Fullerenes (IF-MoS_2) for Electrochemical Hydrogen Production

Summary*

Current chapter illustrate a previously unstudied effects of p- and n- type doping of the inorganic fullerene (IF) MoS_2 on the efficiency of the hydrogen evolution reaction (HER). IF morphology gives rise to active edge site MoS_2, which eventually promotes efficient HER. Further improvements have been done by strategically introducing Nb (p-type) and Re (n-type) dopants (below 500 ppm), to enable facile HER over a range of pH values. Experimental results suggest that although Nb-doping on IF-MoS_2 leads to better electrocatalytic HER activity in an alkaline medium with an onset potential difference of 80 mV, Re-doping gives excellent activity in an acidic medium. The present work presents a systematic study of HER activity by finely tuning the activity in different electrolyte media with varied pH values through deliberate doping of the parent catalyst with p- and n- type materials. Doping results in higher current density, lower onset potential and lower charge transfer resistance compared to few-layer MoS_2 and undoped IF-MoS_2. Our study at different pH values suggests the prospect of using dopants to tune the hydrogen binding energy.

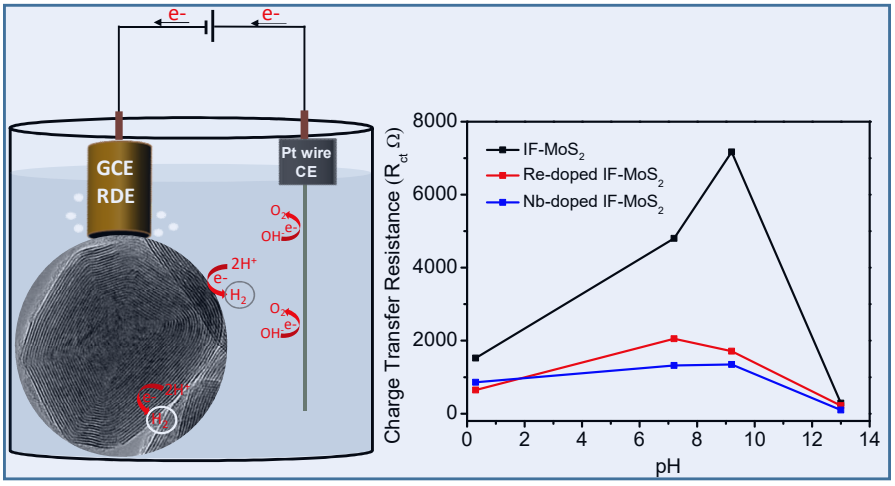

* Paper based on this chapter has appeared in ***Dalton Transactions (2015),ChemElectroChem (2016).***

1. Introduction:

The successful utilization of the concept of metal-free electrocatalyst for efficient hydrogen generation from water via electrochemical reduction has been demonstrated in literature. Mitigating the problem of energy crisis by using green fuel, in this case, H_2, is the prime focus. Hence, the search for various alternative electrocatlayst as a replacement of Pt or Pt group elements has grown exponentially over last decade. Efforts have, therefore, been made to develop inexpensive and environmentally-safe electrocatalysts based on metal alloys[1], metal oxides[2], metal dichalcogenides[3], nitrides[4], carbides[5], phosphides[6], borides[7], enzymes[8] and bioinspired electrocatalysts[9]. Through our extensive literature survey, we found that among all the electrocatalysts for HER, the one which meets the criteria of low cost, easily synthesizable, highly efficient according to Sebatier plot, MoS_2 competes appreciably in comparison to Pt group metals. It has favorable Gibbs free energy for hydrogen adsorption (ΔG_H*) and hydrogen binding energy (HBE).

After the initial report of probable HER activity of MoS_2 by Tributsch and Bennett in 1977[10] there have been many experimental and computational studies to identify its electrochemically active sites for HER. MoS_2 is a 2D hexagonal layered structure with covalently linked S-Mo-S interlayers held together by weak van der Waals forces. It is now confirmed that the edges of S-Mo-S in the MoS_2 are active for H adsorption and the basal plane are electrocatalytically inert. From the HER free-energy diagram it appears that the [1010] Mo edges brings the ΔG_H^o very close to zero as observed for Pt and it shows better activity than other transition metals (**Figure 3.1)** which has been verified by theoretical conclusions drawn from electrochemical measurements and scanning tunneling microscopy (STM) imaging [j_0 measured on MoS_2 nanoplatelets supported on Au (111) is proportional to the length of the edge sites (obtained from the observation by STM), but irrelative to the whole exposed area of MoS_2 nanoplatelets] (**Figure 3.1c**).

By appropriate synthetic modifications, MoS_2 could emerge as a competitive candidate for electrochemical hydrogen production. There have been efforts to optimize MoS_2-based electrocatalysts involving nanoparticles[13], nanowires[14], thin films[15], mesopores[16], amorphous and doped MoS_2[17] and with chemically-exfoliated sheets[18]. However, MoS_2 has a

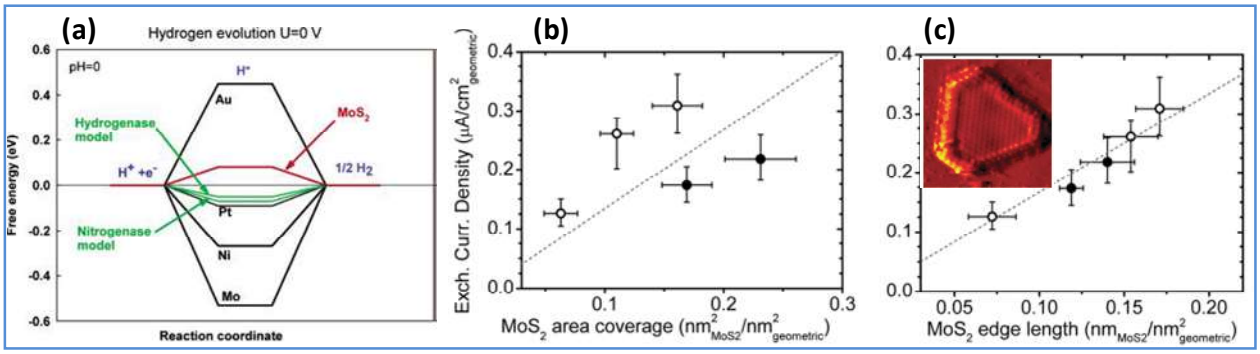

Figure 3.1: (a) Calculated free energy diagram for hydrogen evolution at a potential *U*=0 relative to the standard hydrogen electrode at pH=0 for the comparison of different elemental metals and MoS_2 and other compounds. Reprinted with permission[11], Copyright 2005, American Chemical Society. Comparison of j_o for (b) MoS_2 area coverage and (c) MoS_2 edge length. The exchange current density does not correlate with the area coverage of MoS_2, whereas it shows a linear dependence on the MoS_2 edge length. The edge length was measured on all imaged particles and normalized by the imaged area. The inset in (c) shows the atomically resolved STEM image of MoS_2 particle. Reprinted with permission[12], Copyright 2007, American Association for advancement of Science.

poor conductivity between adjacent S–Mo–S layers, which can be as low as 2200 times lower as that along the basal plane[19]. This is an inherent bottleneck for MoS_2 to be effectively used as an electrocatalyst, and implies that single-layer MoS_2 would be an optimal morphology for valuable electrochemical applications. The general strategy to improve the electrocatalytic activity of MoS_2 is to increase the proportion of edges per mole of MoS_2. For instance, MoS_2 layers with precisely one to four layers (having constant basal plane size of 5 nm) has been studied by combined experimental HER activity and the DFT calculations. With decreased layer numbers, the turnover frequency (TOF) of MoS_2 NPs increases in a quasi-linear manner (**Figure 3.2**). This insight into the nanoscale size-dependent HER activity has triggered further research into increasing the active sites by modifications in morphology and band structure tuning. Thus vertically-aligned[15] (**Figure 3.3**) or fullerene-like MoS_2 have been grown to maximise the exposure of edges[20].

An increase in the number of active sites can also be achieved by increasing the intrinsic activity of the catalyst by doping it with an atom which optimises the H^+ ion adsorption/desorption process, thereby reducing the ΔG_H*. For example, doping of MoS_2 with Re atoms at 10–100 ppm can increase the free charge carriers by 10^{16}–10^{17} cm^{-3} in the conduction band. These charge carriers lie on the surface of inorganic fullerenes (IF) or nanotubes of MoS_2, and increase the n-type character and conductivity of the pristine IF-MoS_2 and of rhenium doped analogues[21-22].

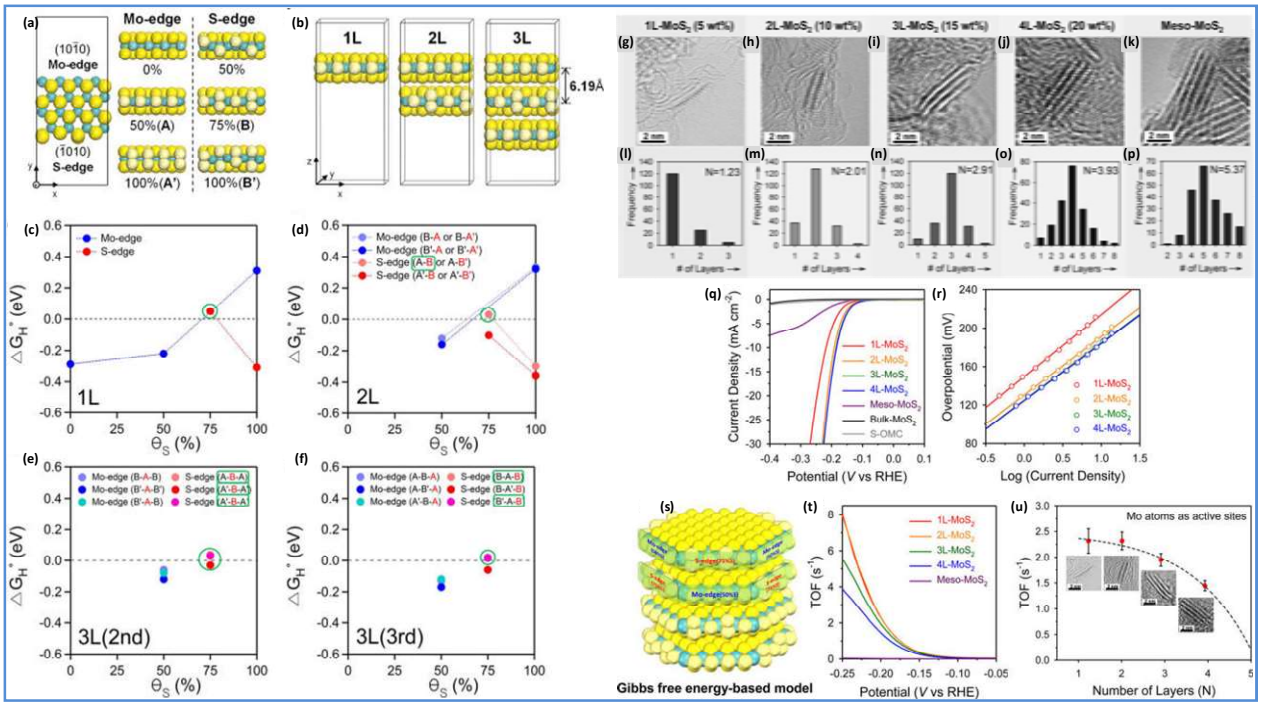

Figure 3.2: DFT calculations of the Gibbs free energy for H adsorption on the MoS_2 structures. (a) Top and side views of the semi-infinite slab models of Mo- and S-edge sites in MoS_2 with different degree of sulfur coverage. The S atoms along the edge and at terrace sites are represented by light and dark yellow spheres, respectively, and Mo atoms are presented as blue-green spheres. The terms, A, A_0, B, and B_0 represent Mo-edge (50% S), Mo-edge (100% S), S-edge (75% S), and S-edge (100% S) structures, respectively. (b) Representative layer models for 1L, 2L, and 3L MoS_2. (c-f) The Gibbs free energy (ΔG_0H) for hydrogen adsorption on the (c) 1L, (d) 2L, (e) 3L (2nd), and (f) 3L (3rd) MoS_2 models with varying degree of sulfur coverage (θ_S). Atomic resolution TEM images of (g) 1L (h) 2L (i) 3L (j) 4L -MoS_2@OMC and (k) Meso-MoS_2. (l-p) Histograms for layer number distribution. HER activity and TOF calculations. (q) LSV curves of the samples for the HER. (r) Tafel plots of LSV curves for MoS_2@OMC nanostructures. (s) MoS_2 structural model most suitable for the HER based on DFT calculations of the Gibbs free energy of hydrogen adsorption on MoS_2. (t and u) TOF calculations on MoS_2@OMC and Meso-MoS_2 nanostructures using the model shown in (s) and assuming Mo atoms at the Mo-edge as active sites: (t) TOFs with respect to potential and (u) TOFs at 200 mV (vs RHE) with respect to the number of layers (inset: Atomic resolution TEM images of corresponding MoS_2 nanoparticles in MoS_2@OMC nanostructures). Reprinted with permission[23], Copyright 2015, American Chemical Society.

Similarly, Niobium is located to the left of molybdenum in the periodic table and would therefore induce p-type doping. In mixed Mo1@xNb_xS_2 (x<1 wt%) systems, the bottom of the valence band corresponds to S-3p and Mo(Nb)-4d hybrid states and the upper part of the Mo(Nb)$4d_z^2$ states[24-26]. The number of valence electrons in MoS_2 is sufficient to fill the valence band completely, rendering MoS_2 a semiconductor with an indirect band gap of 1.23 eV and a direct band gap at the gamma point of 1.92 eV. However, NbS_2 has one electron less per metal atom so that the top of its valence band is half filled with metallic behavior. Consequently, substituting molybdenum with niobium is expected to lead to p-type doping of the nano-

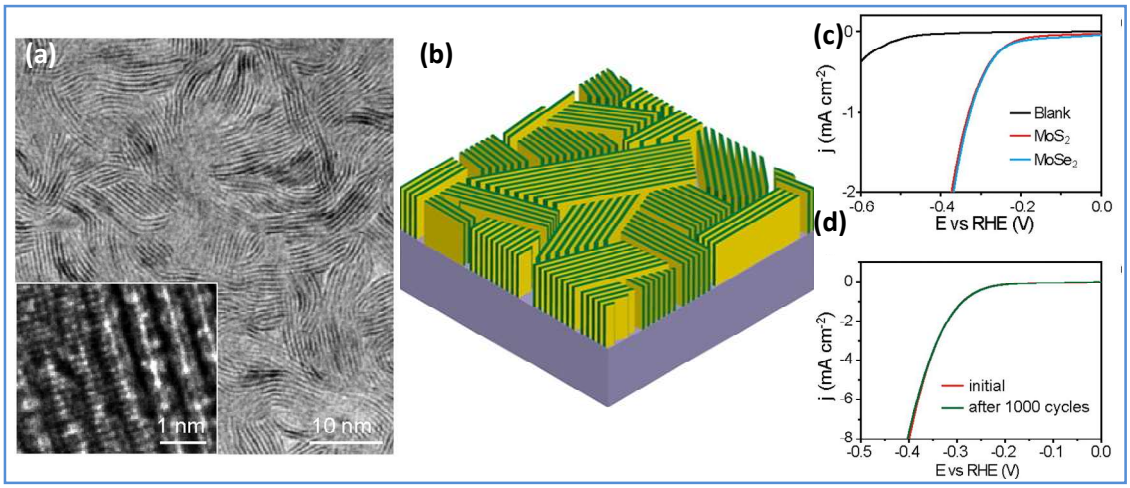

Figure 3.3: (a) TEM image of a MoS_2 film produced by rapid sulfurization showing exposed edges. High-resolution TEM image (inset) reveals individual layers consisting of three atomic planes in the sequence of S−Mo−S. (b) Idealized structure of edge-terminated MoS_2 films with the layers aligned perpendicular to the substrate, maximally exposing the edges of the layers. (c) LSV curves of edge-terminated MoS_2 and $MoSe_2$ films as well as a blank glassy carbon substrate for HER. (d) Stability tests for MoS_2 after 1000 cycles in the cathodic potentials windows. Reprinted with permission[15], Copyright 2013, American Chemical Society.

-particles[24-25], which would acquire positive charge on their surface. To control the position of the Fermi level, exquisite control of the doping level below 1000 ppm is necessary, which is not trivial. Unlike the case of rhenium-doping of IF-MoS_2, Nb_2O_5 is not volatile at the reactor temperatures of 800–900^{o}C needed to sulfidize the MoO_3 nanoparticles. Therefore, congruent evaporation of the minor phase (Nb_2O_5), like in the case of ReMo, is not possible[21-22]. A new strategy for the Nb-doping of IF-MoS_2 nanoparticles was therefore developed by Tenne and co workers[21] to ensure uniform doping density in the MoS_2 of nanoparticles through careful control of the reaction conditions. The Re- and Nb-doping level in the IF-MoS_2 nanoparticles was determined by using inductive coupled plasma mass spectrometry (ICP-MS) analysis. The detailed synthesis and morphology analysis has been done by Reshef Tenne's group[21-22, 27-29]. It is noteworthy to realize that there was no systematic study regarding designing the strategy to improve the HER activity in both acidic and basic medium based on the nature of dopants.

The effect of pH of electrolyte on HER can help in developing active, stable, and affordable HER catalysts for hydroxide exchange membrane fuel cells and electrolyzers. Over a broad pH range (0 to 13), the dependence of Hydrogen Binding Energy (HBE) and exchange

current density has already been studied for metals indicating the HBE is the dominant descriptor for HER activities[30].

2. Scope of the present Investigation

The present study shows how the electrochemical activity can be tuned at different pH by introducing p- and n-type dopants in IF-MoS_2. The p- and n- type dopants were induced on IF-MoS_2 by in situ doping of fullerene-like nanoparticles of MoS_2 with niobium and rhenium atoms, respectively. Owing to this difference in the dopant nature of Nb and Re, we observe different activities of the modified MoS_2. This study may provide an attempt to better designing strategies of electrocatalysts for various practical applications like PEM electrolyzers, PEMFC etc that can operate in wide range of pH values depending on the need of situation. Doping results in higher current density, lower onset potential and lower charge transfer resistance compared to few-layer MoS_2 and undoped IF-MoS_2.

3. Experimental Section:

3.1. Materials:

$(NH)_4Mo_7O_{24}{\cdot}4H_2O$ (99% pure) and thiourea (99%). 5 wt% Nafion solution (Sigma Aldrich). sulphuric acid (98% pure) and KOH (min. 85% assay) (S.D. Fine Chemicals, India), Molybdenum(VI) oxide, Niobium(V) Oxide and Rhenium(VI) oxide (Sigma-Aldrich).

3.2. Characterizations:

The synthesized IF-MoS_2 nanoparticles were characterized by transmission electron microscopy (TEM) and high-resolution transmission electron microscopy (HRTEM) images, obtained using an FEI-Tecnai microscope working at 200 keV and an FEI Tecnai F30-UT high-resolution transmission electron microscope (HRTEM) operating at 300 kV. Methods such as X-ray diffraction (XRD), energy-dispersive X-ray spectroscopy (EDS) within the TEM, X-ray photoelectron spectroscopy (XPS) and others were extensively used throughout this work. Nonetheless, these methods are unable to resolve and accurately determine the Re and Nb

content in the lattice below 0.1 at%. Therefore, extensive analysis of the samples by inductively coupled plasma mass spectrometry (ICP-MS) and X-ray fluorescence (XRF) has been carried out along with time-of-flight secondary ion mass spectrometry (ToF-SIMS).

3.3. Synthesis of IF-MoS_2:

A mixture of MoO_3 powder and Sulfur was prepared in different proportions and thoroughly grounded with mortar and pestle to obtain a uniform powder. The mixture was then put in ampoule inside glove box with solid hydrogen releasing agent ($LiAlH_4$ or $NaBH_4$). The ampoule was sealed in an argon atmosphere. The ampoule was then evacuated to 10^{-4} mbar. Sealed quartz ampoules 12 mm in diameter and 100 mm in length were positioned vertically in a furnace which had been preheated to the desired temperature. The temperatures varied between 600 and 900 °C. Reaction time was varied from 10 to 120 min, after which the ampoule was removed from the heated furnace and allowed to cool to room temperature.

The chemical reactions involved in synthesis:

The metal oxides react with H_2S and H_2

$$MoO_3 + 2H_2S + H_2 \rightarrow MoS_2 + 3H_2O$$

Sulfur volatilizes at ~400 °C and reacts with the hydrogen (generated from $LiAlH_4$) to form H_2S in-situ. Metal oxide particles which are already partially reduced by the hydrogen present in excess readily reacts with hydrogen sulfide.

$$2MoO_3 + 3NaBH_4 + 4S \rightarrow 2MoS_2 + 3NaBO_2 + 6H_2$$

3.4. Synthesis of doped IF-MoS_2:

The mixed oxides of Mo and Nb were prepared using high purity grade precursors from Aldrich. Thoroughly ground weighted and mixed powders of MoO_3 (99.5%) and Nb_2O_5 (99.9%) were heated in nitrogen flow in quartz crucibles, for 18 hours at a temperature of 973°C.The boat with crucibles was then moved out of the furnace and cooled naturally to room temperature in nitrogen flow. The subsequent conversion of the Nb-Mo oxide cake into the Nb doped IF-MoS_2 nanoparticles (Nb: IF-MoS_2) possesses some similarity to that of pure (undoped)

IF-MoS_2 NP or Re:IF-MoS_2. The synthesis may be separated into four consecutive steps: Evaporation of the Nb-Mo oxide cake at temperature about 810 °C, Partial reduction of the oxide vapor with consequent condensation into Nb-doped MoO_{3-y} nanoparticles, Fast sulfidization of the first few layers of the oxide nanoparticles in the volume of the reactor, Further sulfidization of the nanoparticles proceeding on the collecting quartz wool filter and subsequent annealing in the presence of H_2S /H_2 at 870-900 °C for 35-40 h. It should be noted that about 70% of the product is high quality IF nanoparticles, the rest being larger IF nanoparticles and platelets of MoS_2. The Re-doped IF-MoS_2 powder was prepared from a preprepared densified (Re-doped) oxide precursor, in an analogous procedure to that for the undoped IF-MoS_2. An auxiliary reactor was used to prepare the $Mo_xRe_{1-x}O_3$ powder that served as a precursor for the synthesis of the doped IF-MoS_2.

3.5. Synthesis of FL-MoS_2 (few-layer):

Few-layer MoS_2 was synthesized using $(NH)_4Mo_7O_{24}{\cdot}4H_2O$ and an excess of thiourea, in a molar ratio of 1 : 48, under a N_2 environment at 800°C.

3.5. Electrochemical HER performance analysis:

3.5.1 Turn over Frequency (TOF): TOF is a crucial parameter to test the efficiency of hydrogen evolution activity of a catalyst. It is the amount of hydrogen obtained per unit active site per unit time. As such, the calculation of number of active sites on the electrode surface is important. The calculation of number of active sites on the electrode is based on method described in details below. However the inferences from these calculations can only be considered as an estimate because of the assumptions made. We assumed dopant atoms (Re/Nb) to be the origin of active site. However, the origin of active site for HER is not unambiguously known. The theoretical calculations does not account for the loss in the surface area upon the attachment of the particles on the electrode and among themselves. Assuming 100 percent faradic efficiency the amount of hydrogen was calculated from the I-t curve by calculating the charge (in coulombs). From the morphology characterizations it can be assumed that IF-MoS_2 and doped IF-MoS_2 nanoparticles have an average radius of 70 nm with a

hollow core of 6 nm.

Surface area: $S = 4\pi r^2 = 6.16 \times 10^4\ nm^2 = 6.16 \times 10^{-10}\ cm^2$

And Volume: $V = \frac{4}{3}\pi\left(r_{sphere}^3 - r_{core}^3\right) = \frac{4}{3}(70^3 - 3^3) = 1.44 \times 10^6 nm^3 = 1.4 \times 10^{-15} cm^3$

The packing density of IF-MoS_2 is 75% as compared to bulk and the specific gravity of MoS_2 is 4.8 g/cm^3. Hence the weight of IF-MoS_2 is 5.2 x10^{-12} mg. ($M_{np} = \rho V$)

In our electrochemical studies we took 2 mg of the IF-MoS_2 and dispersed it in 200 µL solution. 5 µL of this was used in electrode preparation, i.e. 0.05 mg. Hence,

$$number\ of\ IF - MoS_2\ on\ electrode = \frac{0.05}{5.2 \times 10^{-1}} = 9.6 \times 10^9\ particles$$

Since the volume of the 2H-MoS_2 unit cell is 0.10699 nm^3, we get the number of the 2H cells is 1.3x10^7(derived by dividing the volume of the IF-MoS_2 by volume of the cell). So the number of atoms can be calculated (by multiplying the number of cells by 2 for Mo and 4 for S).

$$N_{cells} = \frac{V_{IF-MoS_2}}{V_{cell}} = 1.34 \times 10^7$$

$$N_{Mo-atoms\ in\ IF-MoS_2} = 1.34 \times 10^7 \times 2 = 2.68 \times 10^7$$

$$N_{S-atoms\ in\ IF-MoS_2} = 1.34 \times 10^7 \times 4 = 5.36 \times 10^7$$

Also, $molar\ volume\ (M_v) = \frac{44.46\ cm^3}{mol}$ and $molar\ mass\ (M_m) = 160.07 g/mol$

$$mass\ of\ catalyst\ deposited\ on\ electrode\ per\ cm^2 = 0.707\ g/cm^2$$

With the density (d) of bulk MoS_2 is 4.8 g/cm^3 (or 3.6g/cm^3 for IF-MoS_2) and the packing density as assumed earlier is 0.75 compared to bulk, we can calculate,

$$surface\ area\ per\ mg(S_A) = S_{IF-Mo_2} \times \frac{1}{V_{IF-MoS_2}} \times \frac{1}{d} = 119.7\ cm^2/mg$$

$$Average\ surface\ (A_s)\ atoms\ per\ cm^2 for\ 4H - MoS_2 = \left(n \times 6.02 \times 10^{23} \times \frac{1}{M_v}\right)^{\frac{2}{3}}$$

$$= 0.707 \times \left(6 \times 6.02 \times 10^{23} \times \frac{1}{44.46} cm^3\right)^{\frac{2}{3}} = 1.32 \times 10^{15} cm^{-2}$$

$$Surface\ atom\ per\ testing(S_t) = S_A \times A_S = 119.7 \times 1.32 \times 10^{15} = 1.58 \times 10^{17}$$

Hence, TOF can be calculated by the formula, $TOF(s^{-1}) per\ cm^2 = \frac{1}{2e^-} \times \frac{current\ density}{F \times 6.02 \times 10^{23} e^-} \times \frac{1}{S_t}$

where $F = 96500\ C$ (Faraday constant)

3.5.2 Electrochemical Studies: The electrochemical HER activity of the catalysts was tested by cyclic voltammetry (CV), linear sweep voltammetry (LSV) and electrochemical impedance spectroscopy (EIS) techniques. The measurements were performed on an electrochemical workstation (CHI760E and RRDE-3A) using a three-electrode system—a glassy carbon electrode (GCE) (3 mm in diameter) as substrate for the working electrode, Ag/AgCl (3 M NaCl) as the reference electrode and a platinum wire as the counter electrode. Prior to use, the GCE was mirror-polished by sequential use of 1 µ, 0.3 µ and 0.05 µ alumina powders and a nylon polishing pad. Catalyst ink for the working electrode was prepared by dispersing 2 mg of IF-MoS_2, Re-doped IF-MoS_2 and FL-MoS_2 (FL = few-layer) in 200 µL of Nafion solution (5 wt% Nafion : IPA : H_2O = 0.05 : 1 : 4 (v/v/v)). 5 µL of this ink was drop-casted on the polished GCE and was allowed to dry overnight under an ambient atmosphere. The electrolyte used for the the analysis was 0.5 M H_2SO_4, saturated with argon gas (purging for 20 min to remove all dissolved gases present). The catalyst surface was cleaned electrochemically by cyclic voltammetry in the potential range of 0.1 to 0.8 V for 20 cycles prior to measurements. The HER activity at different pH values (0.5 M H_2SO_4, 0.1 M KOH, pH = 9.2 and pH = 7.2 buffer solutions) was studied for the Re-doped sample.

4. Results and discussion:

We have systematically studied the effects of p- and n- type dopants in IF-MoS_2 on the electrochemical HER performance. In this pursuit we also compare the activity of FL-MoS_2 with IF-MoS_2 and bring out the advantages of inorganic fullerene morphology. The following section

discusses the rationale behind the successful p- and n- type doping in brief. The strategy to improve the HER activity at different pH of an electrolyte is elucidated. A comprehensive analysis of the HER activity enhancement at different pH with its mechanism as predicted by theoretical works is also included in contrast to our findings.

4.1. Structural and compositional studies of doped and undoped IF-MoS_2:

The morphologies of the few-layer-(FL-) MoS_2, Nb-doped and Re-doped IF-MoS_2 were revealed by TEM and are shown in **Figure 3.4**. TEM micrographs show that the inorganic fullerene form of MoS_2 has a higher density of ordered edge sites as compared to FL-MoS_2 (**Figure 3.4**). The inorganic fullerene structure of MoS_2 imparts it a higher density of active edge sites in comparison to few layer (FL) MoS_2[22] due to the onion like morphology. This in turn increases the active edge sites in the catalyst as the edge sites of MoS_2 is known to be HER active[9].

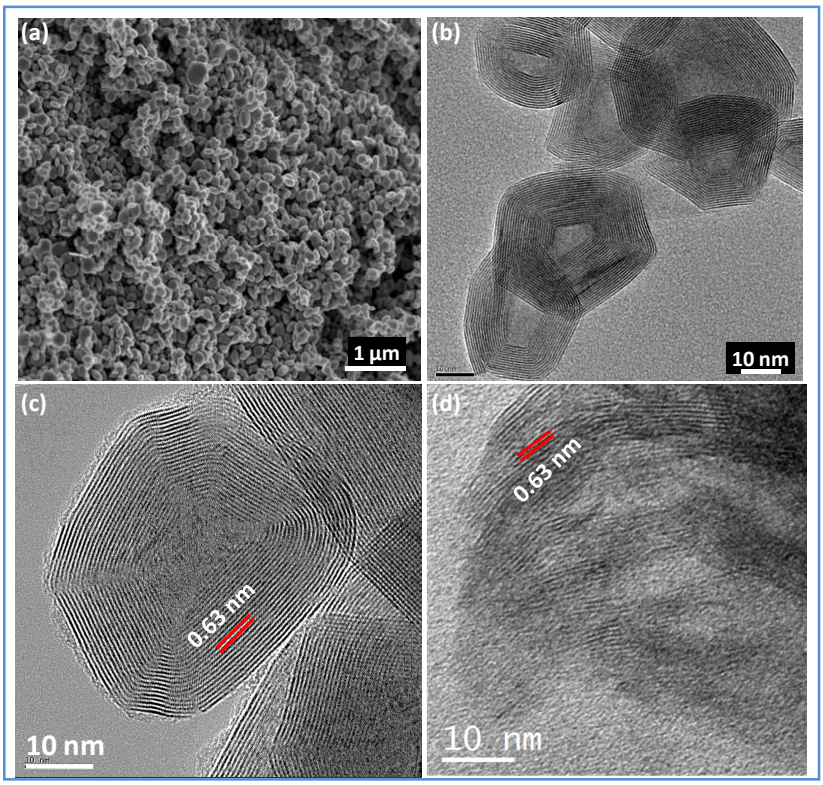

Figure 3.4: TEM image (a) and HRTEM images (b and c) of doped IF-MoS_2, (spacing between fringes is 0.63nm and FL-MoS_2 (d).

4.2. Generating p- and n-type dopant nature in IF-MoS_2:

Doping IF-MoS_2 with Re and Nb atoms can induce p- and n- type doping charecteristics respectively. Doping of MoS_2 with Re atoms at 10–100 ppm can increase the free charge carriers by 10^{16}–10^{17} cm^{-3} in the conduction band. These charge carriers lie on the surface of inorganic fullerenes (IF) or nanotubes of MoS_2 and increase the n-type character and conductivity of the pristine IF-MoS_2[21-22]. It should be emphasized that both experiments and theoretical calculations show that a Re doping level in excess of e.g. 500 ppm (0.005 at%) in IF-MoS2 nanoparticles leads to segregation of the rhenium atoms and changes their electronic structure. Therefore, much effort has been invested in controlling the Re level in the nanoparticles to below 200 ppm[21-22]. The Mo-substitutional site of the Re atoms in the lattice, i.e. ReMo, is essential for its electronic character as an electron donor. This was carefully confirmed through high-resolution (aberration-corrected) transmission electron microscopy (TEM), X-ray absorption fine structure (XAFS) and X-ray absorption near edge structure (XANES) analyses in previous reports[21-22]. Excess Re atoms in the 2H-MoS_2 lattice (trigonal biprismatic coordination) was shown to convert it into the 1T phase with octahedral coordination and metallic character[31-33]. On the other hand, Niobium is located to the left of molybdenum in the periodic table and would therefore induce p-type doping. In mixed $Mo_{1-x}Nb_xS_2$ (x< 1 wt%), the bottom of the valence band corresponds to 3p-S and 4d-Mo(Nb) hybrid states and the upper part of the $4d_z^2$ Mo (Nb) states[24-26]. The number of valence electrons in MoS_2 is sufficient to fill the valence band completely, rendering MoS_2 a semiconductor with an indirect bandgap of 1.23 eV and a direct bandgap at the Gamma point of 1.92 eV. However, NbS_2 has one electron less per metal atom so that the top of its valence band is half filled with metallic behavior. Consequently, substituting molybdenum by niobium is expected to lead to p-type doping of the nanoparticles[24-25], which would acquire positive charge on their surface. To control the position of the Fermi level, exquisite control of the doping level below 1000 ppm is necessary, which is not trivial. Unlike the case of rhenium doping of IF-MoS_2, Nb_2O_5 is not volatile at the reactor temperatures of 800-900°C needed to sulfidize the MoO_3 nanoparticles. Therefore, congruent evaporation of the minor phase (Nb_2O_5), like the case of ReMo is not possible[21-22].
A new strategy for the Nb doping of IF-MoS_2 nanoparticles was therefore developed by Tenne

and co workers[21-22, 34] to ensure uniform doping density in the MoS_2 of nanoparticles through careful control of the reaction conditions. The analysis of minute amounts of the dopant atoms (<500 pm) in the nanoparticles is a difficult task. The Re- and Nb- doping level in the IF-MoS_2 nanoparticles was determined using inductive coupled plasma mass spectrometry (ICP-MS) analysis[17, 35-36]. These charecterizations have been performed in earlier reports by Tenne's group[20-22, 26-29, 31, 34, 36]. Hence due to this difference in the dopant nature of Nb and Re, we observe different activities of modified MoS_2.

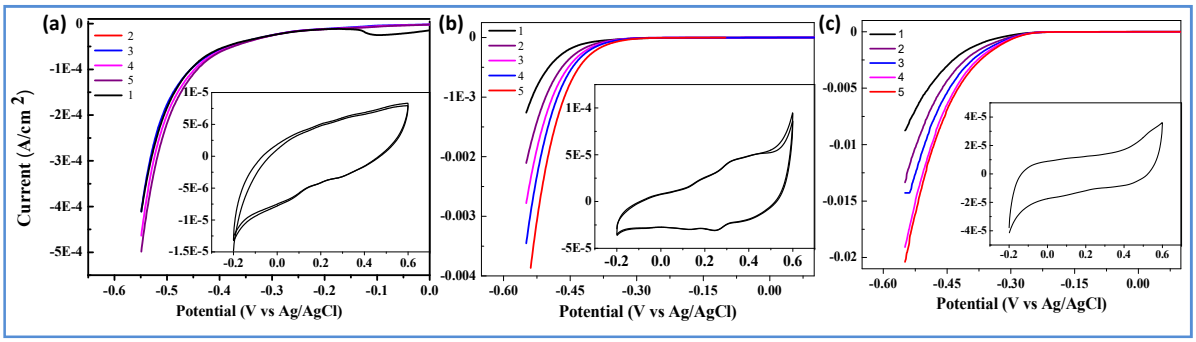

Figure 3.5: Linear sweep voltametry curve and cyclic voltametry (inset) of (a) FL-MoS_2 (b) IF-MoS_2 (c) Re-doped-IFMoS_2. The numbers correspond to the cathodic polarization cycle number.

4.3. Electrochemical study:

Inorganic fullerene morphology of MoS_2 activates it for electrochemical HER. The HER onset potential for FL-MoS_2 is −0.39 V (vs. Ag/AgCl) with a current density of 0.21 mA cm^{-2} at -0.5 V, vs Ag/AgCl whereas that for IF-MoS_2, it is −0.36 V, vs Ag/AgCl with a current density of 2.0 mA cm^{-2} at -0.5 V, vs Ag/AgCl (**Figure 3.5**) which is about 10 times higher than that of FL-MoS_2 due to its onion-like ring structure with maximal edge sites, and hence the total surface area exposure for a given mass of catalyst is greater. Hence, IF-MoS_2 increases the efficient charge flow from the electrode to the surface active sites of the IF nanoparticles. Similar results have previously been obtained for MoS_2 by improving the density of edge sites[11-12, 37].

Though IF-MoS_2 increases the current density, it is still low for practical applications. As discussed earlier, Re doping, at as low as a few 10 to 100 ppm, leads to an increase in the density of free carriers in the conduction band of MoS_2 at room temperature, which reside on the nanoparticles surface or close to it. This extra charge would be expected to lead to a further decrease in the charge transfer resistance, thereby reducing the overpotential for the

electrochemical HER. As a proof of concept, we have investigated the electrocatalytic HER activity of various catalysts under similar conditions as those for IF-MoS_2. As seen from **Figure 3.5** we observed a drastic reduction of the onset potential (−0.3 V, vs Ag/AgCl) for Re-doped MoS_2 by 60 and 80 mV with respect to both IF- and FL-MoS_2. The shift in the onset potential is indicative of reduced charge transfer resistance from the catalyst electrode to the solution, which thus facilitates HER, as seen from the Nyquist plot **(Figure 3.6c)**. The onset potential of Re-doped MoS_2 was comparable to that of 20 wt% Pt/C (-0.24 V, vs Ag/AgCl), the standard electrocatalyst for HER (**Figure 3.6**). In comparison to the FL- and IF-MoS_2, for the Re-doped IF-MoS_2, current density at overpotential of 0.5 V, vs Ag/AgCl was enhanced by 67 times and 6 times, respectively. The overpotentials to obtain current densities of 10 $mAcm^{-2}$ and 20 $mAcm^{-2}$ were found to be 0.48 V and 0.54 V, vs Ag/AgCl. The turnover frequency (TOF) of the Re-doped IF-MoS_2 was calculated to be 0.2 and 0.4 s^{-1} cm^{-2}, respectively.

Density functional theoretical (DFT) calculations indicate that upon doping (randomly) Re in MoS_2, a new impurity band appears at −0.2 eV below the conduction band of MoS_2; the new band is associated with the Re 5d orbital. As the dopant level increases, the new impurity band gets populated with a high density of n-type dopants. Re-doping of 10–100 ppm creates an n-type charge carrier density of 10^{16}–10^{17} cm^{-3} in the conduction band of the IF-MoS_2 at room temperature. The activation energy of the dopant atoms is as low as 0.1–0.2 eV, thereby decreasing the onset potential and increasing the current density[21-22].

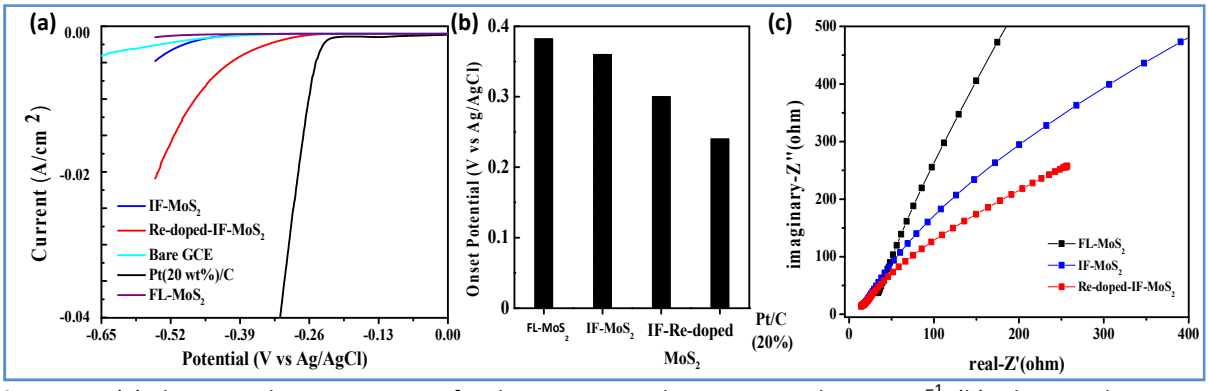

Figure 3.6: (a) The LSV polarization curves for the various catalysts measured at 5 mVs^{-1}. (b) A bar graph comparing the onset potential for HER activity of the catalysts. Comparison of charge transfer resistance of FL-MoS_2, IF-MoS_2 and Re-doped IF-MoS_2 in a Nyquist plot.

We realized that, there was no systematic study in designing the strategy to improve the HER activity in both acidic and basic medium based on the nature of dopants. Hence, we introduced Nb as dopant in IF-MoS_2 and compared its activity with Re doped IF-MoS_2 at different pH of an electrolyte in the light of understanding the underlying mechanism and develop an empirical strategy to improve HER activity at varied pH range.

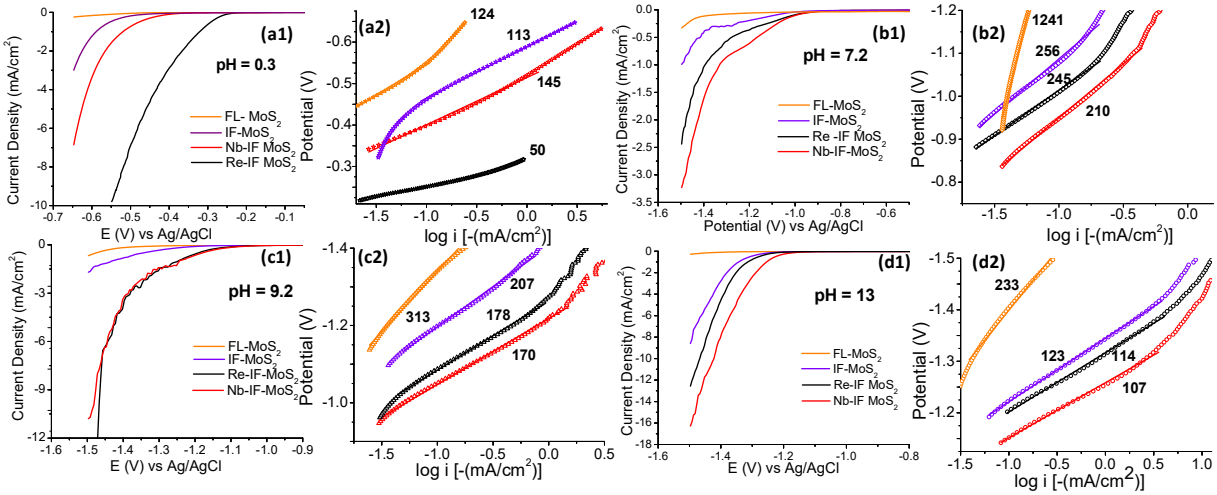

Figure 3.7: The LSV polarization curves and tafel slope analysis for the various catalysts (FL-, IF-, Re-doped and Nb-doped MoS2) measured at 5 mVs^{-1} at pH (a) 0.3, (b) 7.2 (c) 9.2, and(d) 13 of the electrolyte. (The potential here is w.r.t Ag/AgCl, 3 M NaCl and the unit of tafel slope is mV/dec).

We observed that the onset overpotentials (η) for Re and Nb-doped IF-MoS_2 differ at different pH of the electrolyte. All potentials reported hereon are with respect to RHE unless mentioned otherwise. While in lower pH, the η is less for Re-doped IF-MoS_2, Nb-doped counterpart showed lower η at higher pH. The onset potential difference (OPD) between Re- and Nb-doped IF-MoS_2 is ~170 mV at pH-0.3. As the pH of the electrolyte increases (7.2, 9.2 and 13), the overpotential for Nb-doped IF-MoS_2 becomes less than that of the Re-doped IF-MoS_2 (OPD of ~ 0- 70 mV) (**Figure 3.7**).

The features in the trend in activity suggests improvement in HER activity in both acidic and basic media by the modification in MoS_2 (FL to IF structure) and doping with Re and Nb atoms. Modification of the properties of MoS_2 by doping can lead to changes in the electronic structure which are necessary for HER[36]. Previous works by Trassatti[38] and Norskov[39] on the volcano plot for hydrogen evolution helps predicting the higher activity of Re in comparison to Nb in the acidic medium as observed in the present study. However the effect of nanoclusters

or low doping of metals on the substrate was not considered, and there would be additional effects caused by local strain[40] on the adsorption-desorption process in HER. The dopant sites

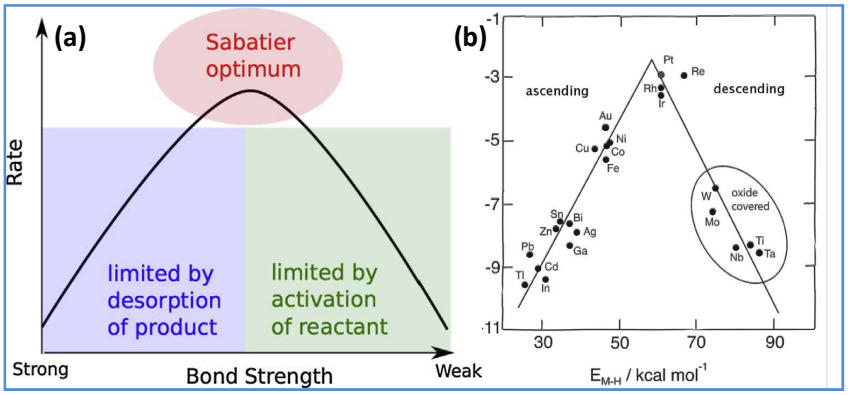

Figure 3.8: (a) Schematic representation of the qualitative Sabatier principle. Reprinted with permission[41], Copyright 2015, Elsevier. (b) Exchange current for HER vs intermediate metal-hydrogen bond formed during reaction. Reprinted with permission [38], Copyright 1972, Elsevier.

act as active sites for catalysis. Considering the volcano plot (Sabatier's principle), the activity of the metals, which lie in the ascending region is controlled by desorption of the product whereas those lying in the descending region is limited by the activation of the reactant[39] (**Figure 3.8**).

Thus the descending region of volcano plot is mainly occupied by metals which form oxide films during the evolution of hydrogen. This implies that by changing the experimental condition, the activity of Nb for HER can be enhanced and hence we propose that this is why the activity of Nb-doped IF-MoS_2 is higher than that of the Re-doped counterpart in the basic medium.

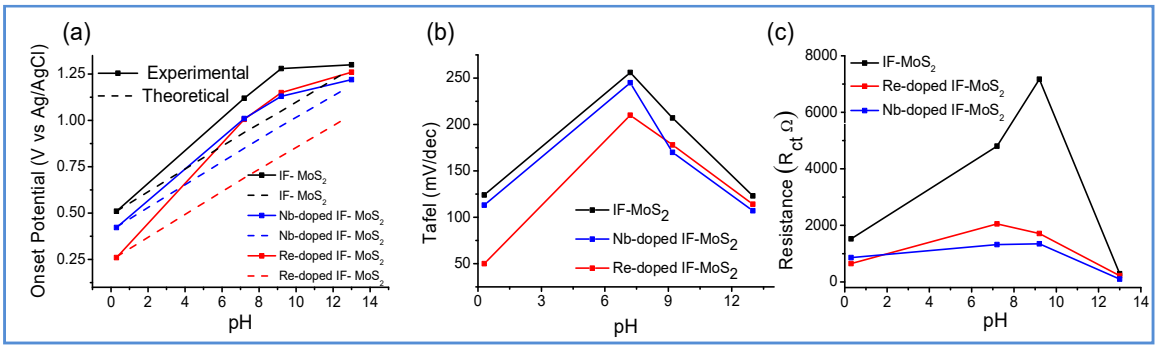

Figure 3.9: Comparative analysis of p- and n- type of dopant in IF-MoS_2 for HER as a function of pH of the electrolyte (a) onset overpotential (b) Tafel slope and (c) charge transfer resistance (R_{ct}).

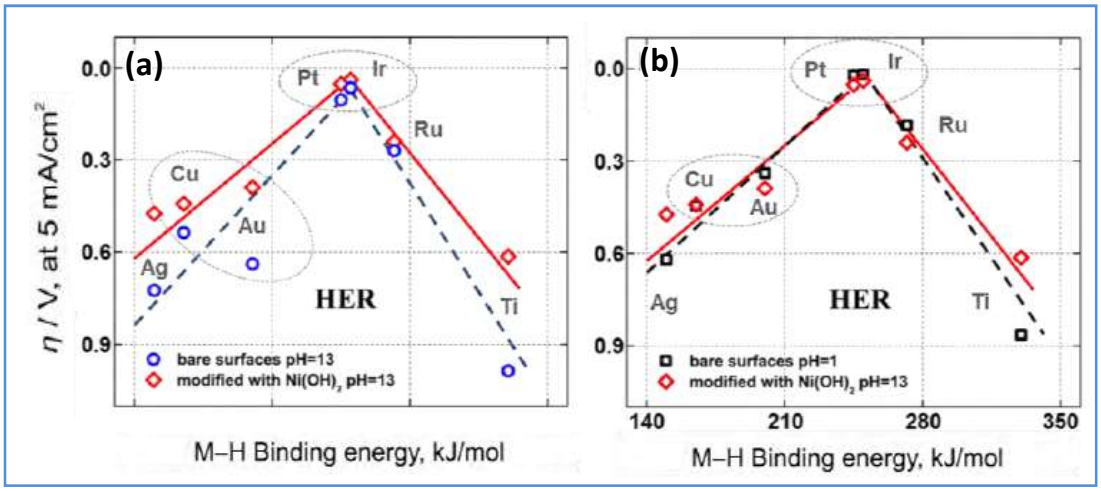

Figure 3.10: (a) Two volcano plots are overlaid, both measured in 0.1 M KOH (pH 13). One shows the HER activity of bare unmodified metals, while the second was measured on $Ni(OH)_2$ modified metal surfaces. Note that the HER is activated by the presence of $Ni(OH)_2$ on all of the bare metal surfaces. Furthermore, on the $Ni(OH)_2$-modified surfaces, the activities for Pt and Ir are nearly identical, and the trend of the coinage metals follows the trend in their M–H binding energies, Au > Cu > Ag. (b) Two volcano plots are overlaid, in one the HER was measured in 0.1 M $HClO_4$ (pH 1) on bare metal surfaces while the other is constructed from HER activities measured in 0.1 M KOH (pH 13) on $Ni(OH)_2$-modified metal surfaces. The activities and positions of the elements are nearly identical suggesting that the elimination of the role of the water dissociation step in alkaline HER is the only way to validate the use of M–H binding energies as alkaline HER catalyst descriptors. Reprinted with permission[42], Copyright 2013, Serbian Chemical Society.

At pH-7.2, the onset potential for Nb- and Re-doped samples is -0.36 V whereas that for the undoped sample it is -0.44 V suggesting an improvement in overpotential difference (OPD) by 80mV. The improvement in the onset overpotential difference with Nb-doped MoS_2 fullerene over Re-doped and undoped IF-MoS_2 samples is 10 mV and 130 mV at pH-9.2; 73 mV and 93 mV at pH-13 respectively (**Figure 3.9**). The question of the activity of Nb doped sample being better than that of Re doped counterpart in basic medium is worth investigating. The same observation of a difference in HER activity was noticed in previous studies by Nenad et al.[42]. However the investigation was based on transition metals with primary interest in the inter-relationship between the type of electrode and the HER activity at higher pH. HER activity at higher pH is dictated by the hydrogen binding energy (HBE) and also by its relation to the kinetic energy necessary for the dissociation of water (**Figure 3.10**)[42-43]. We also made a similar observation which gives insight about the relation between the type of electrode and the HER activity at different pH values. Therefore the mechanism of HER in both acidic and basic medium is expected to be different depending on the nature of the MoS_2 based catalyst. The trend in the values as a function of pH of the electrolyte was found to be the same as that of

the onset potentials. While the Nb-doped IF-MoS_2 shows improved performance in HER at higher pH values Re doped sample shows the opposite. The activity comparison is further manifested by Tafel slope analysis obtained from the LSV curves.

The results obtained (**Table 1**) clearly indicates that by Nb-doping we have further enhanced the HER activity in basic medium. The values of the Tafel slope are 107 mV/dec, 170 mV/dec and 245 mV/dec at pH 13, 9.2 and 7.2 respectively for Nb-doped IF-MoS_2 (**Figures 3.6 and Figure 3.9**). Except for pH-0.3 the values of tafel slope for Nb doped sample indicates its superior activity in comparison to Re doped sample in basic medium (**see table 1**). In the process of hydrogen evolution by cathodic reduction of H^+ ion the electrode encounters a significant charge transfer resistance (R_{ct}) at the electrode-electrolyte interface, which also depends on the electrolyte used. To incorporate this effect we have examined the R_{ct} by electrochemical impedance spectroscopy (EIS), and the results are listed in **table 1**. The lower R_{ct} values for Nb-doped IF-MoS_2 in comparison to the Re-doped counterpart at higher pH explain the better activity of Nb-doped sample (**Figure 3.11**).

Table 1: Comparison and summary of results between undoped, Re- and Nb- doped and IF-MoS_2.

Sample	pH	Onset (V) vs Ag/AgCl	Tafel (mV/dec)	R_{ct} (ohm)
Nb-IF	13	-1.21	107	100
	9.2	-1.13	170	1348
	7.2	-1.00	245	1320
	0.3	-0.42	113	860
Re-IF	13	-1.25	114	220
	9.2	-1.15	178	1712
	7.2	-1.00	210	2055
	0.3	-0.26	50	649
IF	13	-1.29	123	288
	9.2	-1.28	207	7172
	7.2	-1.11	256	4801
	0.3	-0.51	124	1525

The mechanism of hydrogen evolution in acidic and basic media are given as,

$$H^+ + e^- \rightarrow H_{ad}\ (acidic)$$
$$H_2O + e^- \rightarrow H_{ad} + OH^-\ \ (alkaline)$$

H_{ad} is the surface adsorbed hydrogen which leads to formation of H_2 in further steps (Tafel and Heyrovsky) depending upon the particular mechanism followed. Unlike the case of Re, the 4d orbitals in Nb are compact and hence interaction with H^+ ions falls off quickly with distance. The electron transfer rate at the electrode/electrolyte interface is therefore sluggish. In alkaline medium, on the other hand, H_2O interacts with the catalyst in the electrode/electrolyte interface; due to the p-type nature of the Nb, interaction with H_2O is expected to lead to enhanced charge transfer and activity in alkaline medium in comparison to Re-doped IF-MoS_2 (n-type dopant). Nb has more vacant d-orbitals compared to that of Re. Hence, the lower R_{ct} for Re-doped IF at pH=0.3 and opposite at higher pH. The trends in activity and the R_{ct} value therefore is expected to reverse as the pH increases. Another factor to note is the low concentration of dopant and its effect on the electronic properties and local strain at the dopant site of IF-MoS_2. The summary of the results obtained from the above study is given in **table 1.**

The Tafel slope and charge transfer resistance (R_{ct}) at varying pH values suggests that the Nb-doped fullerene is better than the Re-doped one at alkaline pH while the reverse holds at acidic pH (**Figures 3.6b and c**). With this strategy of doping it appears that one should be able to tune HER activity of MoS_2 fullerenes over a range of pH values.

5. Conclusions

We observed that doping MoS_2 based fullerene with minute concentrations of p- and n-type dopants (~500 ppm) gives rise to excellent electrochemical catalytic activity in HER. Our empirical findings suggests that Nb- and Re-doped IF-MoS_2 catalysts are active in both acidic and basic media, with Nb-doping being superior to Re-doping in alkaline media. Similar studies can be performed with IF sulfides of W, Ti, Ta etc. to understand their role in HER. We propose

this study may provide an attempt to better designing strategies of electrocatalysts for various

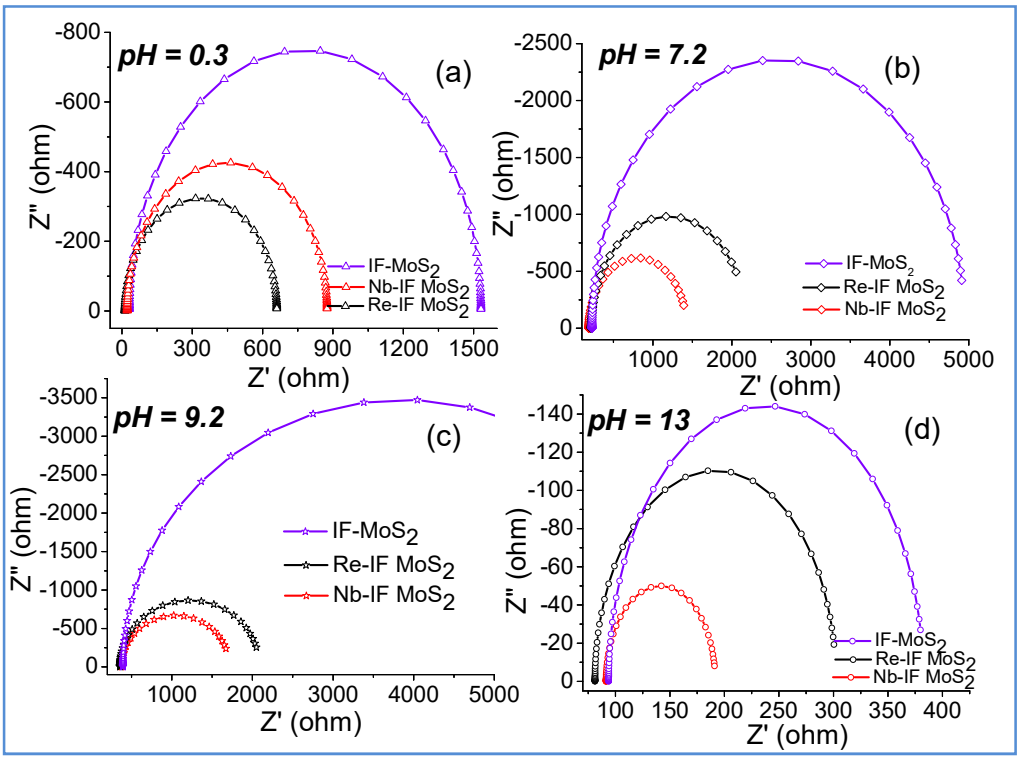

Figure 3.11: Electrochemical impedance spectroscopy (Nyquist plot) of various catalyst (FL-, IF-, Re-doped and Nb-doped MoS2) at onset potential at different pH (a) 0.3, (b) 7.2 (c) 9.2 and (d) 13

practical applications like PEM electrolyzers, PEMFC etc that can operate in wide range of pH values depending on the need of situation. Doping results in higher current density, lower onset potential and lower charge transfer resistance compared to few-layer MoS_2 and undoped IF-MoS_2. Our study at different pH values suggests the prospect of using dopants to tune the hydrogen binding energy.

6. References:

[1] J. Greeley, T. F. Jaramillo, J. Bonde, I. Chorkendorff, J. K. Nørskov, Nat. Mater. 2006, 5, 909.
[2] S. Cobo, J. Heidkamp, P.-A. Jacques, J. Fize, V. Fourmond, L. Guetaz, B. Jousselme, V. Ivanova, H. Dau, S. Palacin, M. Fontecave, V. Artero, Nat. Mater. 2012, 11, 802.
[3] D. Merki, X. Hu, Energy Environ. Sci. 2011, 4, 3878.
[4] W.-F. Chen, K. Sasaki, C. Ma, A. I. Frenkel, N. Marinkovic, J. T. Muckerman, Y. Zhu, R. R. Adzic, Angew. Chem. Int. Ed. 2012, 51, 6131.
[5] W. F. Chen, C. H. Wang, K. Sasaki, N. Marinkovic, W. Xu, J. T. Muckerman, Y. Zhu, R. R. Adzic, Energy Environ. Sci. 2013, 6, 943.

[6] E. J. Popczun, J. R. McKone, C. G. Read, A. J. Biacchi, A. M. Wiltrout, N. S. Lewis, R. E. Schaak, J. Am. Chem. Soc. 2013, 135, 9267.
[7] H. Vrubel, X. Hu, Angew. Chem. Int. Ed. 2012, 51, 12703.
[8] D. J. Evans, C. J. Pickett, Chem. Soc. Rev. 2003, 32, 268.
[9] H. I. Karunadasa, C. J. Chang, J. R. Long, Nature 2010, 464, 1329.
[10] H. Tributsch, J. C. Bennett, J. Electroanal. Chem. 1977, 81, 97.
[11] B. Hinnemann, P. G. Moses, J. Bonde, K. P. Jørgensen, J. H. Nielsen, S. Horch, I. Chorkendorff, J. K. Nørskov, J. Am. Chem. Soc. 2005, 127, 5308.
[12] T. F. Jaramillo, K. P. Jørgensen, J. Bonde, J. H. Nielsen, S. Horch, I. Chorkendorff, Science 2007, 317, 100.
[13] J. Bonde, P. G. Moses, T. F. Jaramillo, J. K. Nørskov, I. Chorkendorff, Faraday Discuss 2009, 140, 219.
[14] Z. Chen, D. Cummins, B. N. Reinecke, E. Clark, M. K. Sunkara, T. F. Jaramillo, Nano Lett. 2011, 11, 4168.
[15] D. Kong, H. Wang, J. J. Cha, M. Pasta, K. J. Koski, J. Yao, Y. Cui, Nano Lett. 2013, 13, 1341.
[16] J. Kibsgaard, Z. Chen, B. N. Reinecke, T. F. Jaramillo, Nat. Mater. 2012, 11, 963.
[17] D. Merki, S. Fierro, H. Vrubel, X. Hu, Chem. Sci. 2011, 2, 1262.
[18] M. Chhowalla, H. S. Shin, G. Eda, L.-J. Li, K. P. Loh, H. Zhang, Nat. Chem. 2013, 5, 263.
[19] M. A. Lukowski, A. S. Daniel, F. Meng, A. Forticaux, L. Li, S. Jin, J. Am. Chem. Soc. 2013, 135, 10274.
[20] R. Rosentsveig, A. Margolin, A. Gorodnev, R. Popovitz-Biro, Y. Feldman, L. Rapoport, Y. Novema, G. Naveh, R. Tenne, J. Mater. Chem. 2009, 19, 4368.
[21] L. Yadgarov, R. Rosentsveig, G. Leitus, A. Albu-Yaron, A. Moshkovich, V. Perfilyev, R. Vasic, A. I. Frenkel, A. N. Enyashin, G. Seifert, L. Rapoport, R. Tenne, Angew. Chem. Int. Ed. 2012, 51, 1148.
[22] L. Yadgarov, D. G. Stroppa, R. Rosentsveig, R. Ron, A. N. Enyashin, L. Houben, R. Tenne, Z. Anorg. Allg. Chem. 2012, 638, 2610.
[23] B. Seo, G. Y. Jung, Y. J. Sa, H. Y. Jeong, J. Y. Cheon, J. H. Lee, H. Y. Kim, J. C. Kim, H. S. Shin, S. K. Kwak, S. H. Joo, ACS Nano 2015, 9, 3728.
[24] V. V. Ivanovskaya, A. Zobelli, A. Gloter, N. Brun, V. Serin, C. Colliex, Phys. Rev. B 2008, 78, 134104.
[25] V. V. Ivanovskaya, G. Seifert, A. L. Ivanovskii, Russ. J. Inorg. Chem. 2006, 51, 320.
[26] F. L. Deepak, R. Popovitz-Biro, Y. Feldman, H. Cohen, A. Enyashin, G. Seifert, R. Tenne, Chem. Asian J. 2008, 3, 1568.
[27] R. Tenne, M. Redlich, Chem. Soc. Rev. 2010, 39, 1423.
[28] L. Rapoport, A. Moshkovich, V. Perfilyev, A. Laikhtman, I. Lapsker, L. Yadgarov, R. Rosentsveig, R. Tenne, Tribol. Lett. 2012, 45, 257.
[29] I. Wiesel, R. Popovitz-Biro, R. Tenne, Nanoscale 2013, 5, 1499.
[30] J. Zheng, W. Sheng, Z. Zhuang, B. Xu, Y. Yan, Science Adv. 2016, 2.
[31] A. N. Enyashin, L. Yadgarov, L. Houben, I. Popov, M. Weidenbach, R. Tenne, M. Bar-Sadan, G. Seifert, J. Phys. Chem. C 2011, 115, 24586.
[32] Y.-C. Lin, D. O. Dumcenco, Y.-S. Huang, K. Suenaga, Nat. Nanotechnol. 2014, 9, 391.
[33] C. G. Morales-Guio, L.-A. Stern, X. Hu, Chem. Soc. Rev. 2014, 43, 6555.
[34] R. Rosentsveig, L. Yadgarov, Y. Feldman, S. Shilstein, R. Popovitz-Biro, B. Visic, A. Sedova, S. R. Cohen, Y. Li, A. I. Frenkel, R. Tenne, Part. Part. Syst. Charact. 2017, 35, 1700165.
[35] J. D. Benck, Z. Chen, L. Y. Kuritzky, A. J. Forman, T. F. Jaramillo, ACS Catal. 2012, 2, 1916.
[36] M. Chhetri, U. Gupta, L. Yadgarov, R. Rosentsveig, R. Tenne, C. N. R. Rao, Dalton Trans. 2015, 44, 16399.
[37] H. Vrubel, D. Merki, X. Hu, Energy Environ. Sci. 2012, 5, 6136.

[38] S. Trasatti, J. Electroanal. Chem. 1972, 39, 163.
[39] J. K. Nørskov, T. Bligaard, J. Rossmeisl, C. H. Christensen, Nat. Chem. 2009, 1, 37.
[40] J. K. Nørskov, T. Bligaard, A. Logadottir, J. R. Kitchin, J. G. Chen, S. Pandelov, U. Stimming, J. Electrochem. Soc. 2005, 152, J23.
[41] A. J. Medford, A. Vojvodic, J. S. Hummelshøj, J. Voss, F. Abild-Pedersen, F. Studt, T. Bligaard, A. Nilsson, J. K. Nørskov, J. Catal. 2015, 328, 36.
[42] N. Danilovic, R. Subbaraman, D. Strmcnik, R. Stamenkovic Vojislav, M. Markovic Nenad, J. Serb. Chem. Soc. 2013, 78, 2007.
[43] W. Sheng, M. Myint, J. G. Chen, Y. Yan, Energy Environ. Sci. 2013, 6, 1509.

Chapter-4

Electrochemical Hydrogen Evolution Reaction by Metal-free Borocarbonitrides and Related Materials

Electrochemical Hydrogen Evolution Reaction by Metal-free Borocarbonitrides and Related Materials

Summary*

Hydrogen utilization as a clean and efficient fuel can potentially replace scarce carbon based fuels and produce only water as the product thus making it environmentally benign. One of the ways to generate hydrogen is by the electrolysis of water by cathodically reducing hydrogen ions. However, hydrogen ion reduction is accompanied by a substantial overpotential unless an effective catalyst is used to reduce the gap between standard reduction potential of hydrogen ions and the overpotential. Pt or Pt group metals (PGMs) have been extensively used for the hydrogen evolution reaction (HER) owing to their low overpotential and larger current density. However they suffer activity loss by poisons (like CO) in the fuel cell electrochemical environment. Their high cost and limited availability are also drawbacks. Clearly there is a need to replace Pt or PGM catalysts by less costly and easily synthesizable catalysts. In this context, non-precious metal catalysts especially carbon based materials have been under the limelight of research. We have found for the first time borocarbonitrides (BCNs) to be efficient HER electrocatalysts, with a carbon-rich sample exhibiting an onset potential of -56 mV (vs. RHE) and a current density of 10 $mAcm^{-2}$ at an overpotential of 70 mV (vs. RHE). BCNs are low cost materials and have the potential to replace Pt based electrocatalysts.

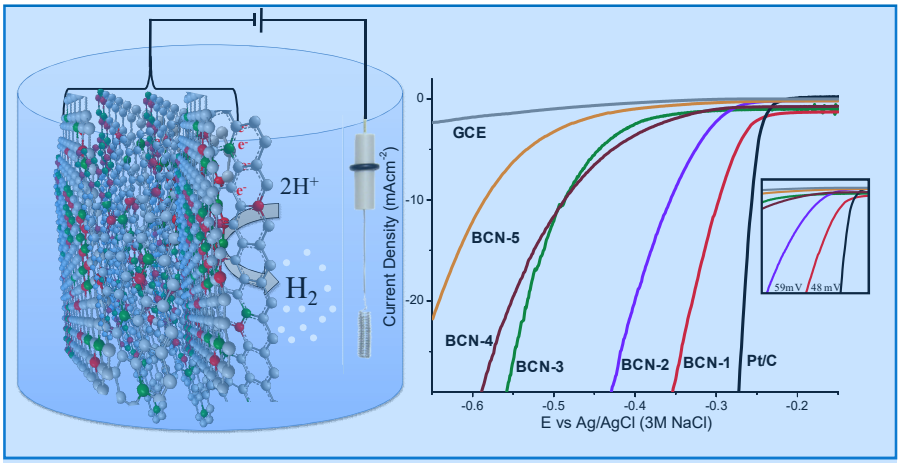

** Paper based on this chapter has appeared in **Energy Environ. Sci. (2015), Adv. Mater. (2018). J. Phys. Chem. C (2017), ACS Appl. Mater. Interfaces (2017).***

1. Introduction:

Producing green fuel by generating hydrogen from water is potentially an important means of using solar energy for the benefit of mankind. The hydrogen evolution reaction (HER) is not only a vital part of electrochemical water splitting but also provides a way to understand the underlying mechanism of electron transfer processes in electrocatalysis. It is well known that platinum supported on carbon exhibits very good electrocatalytic HER activity[1]. Other transition metal catalysts have also been tried for HER[2-4], but it would be ideal to have a metal-free catalyst for the purpose, partly because of the scarcity and high cost of Pt. While noble metal based catalysts like Pt are ideal for HER, alloyed materials[5-6] have been used to attain improved activity. In most of the metal based catalysts such as the HER catalysts, carbon is used as the catalyst support because of its good conductivity and to avoid agglomeration of the active catalysts over time due to Ostwald's ripening. Efforts have also been made to use nonmetal catalysts, especially carbon related materials such as graphene[7], doped graphenes[8-9] and graphitic carbon nitide (g-C_3N_4)[10-11]. However, the H-adsorption energy on graphene is more positive (~0.8 eV) and that on g-C_3N_4 is more negative (-0.5 eV), implying the difficulty in adsorption/desorption processes and hence poor HER activity. g-C_3N_4@graphene[11] and g-C_3N_4@nitrogenated graphene[10], on the other hand exhibits HER activity comparable to many active metal based electrocatalysts. Compositionally warped graphene based matrix with improved electronic structures can act as good electrocatalysts. The delocalized π-electrons, active sites provided by heteroatom doping can modulate the H adsorption/desorption energies close to zero in favor of HER. Apart from this an appropriate composite of carbon materials have been used as an electrocatalysts. For instance a composite of carbon nitride (C_3N_4) and nitrogen-doped graphene (NG) has recently been reported to possess unique properties for successful electrocatalytic H_2 production[10] **(Figure 4.1).** Films of porous C_3N_4 layers with NG have also been shown to display excellent electrochemical HER performance with a highly positive onset potential[12] and high exchange current density and stability comparable to platinum. The use of bimetallic core–shell electrocatalysts with carbonitrides for fuel cell applications has also been reported. In fact, some of the 2D nanomaterials exhibit high catalytic performance for the HER by water splitting to produce H_2.

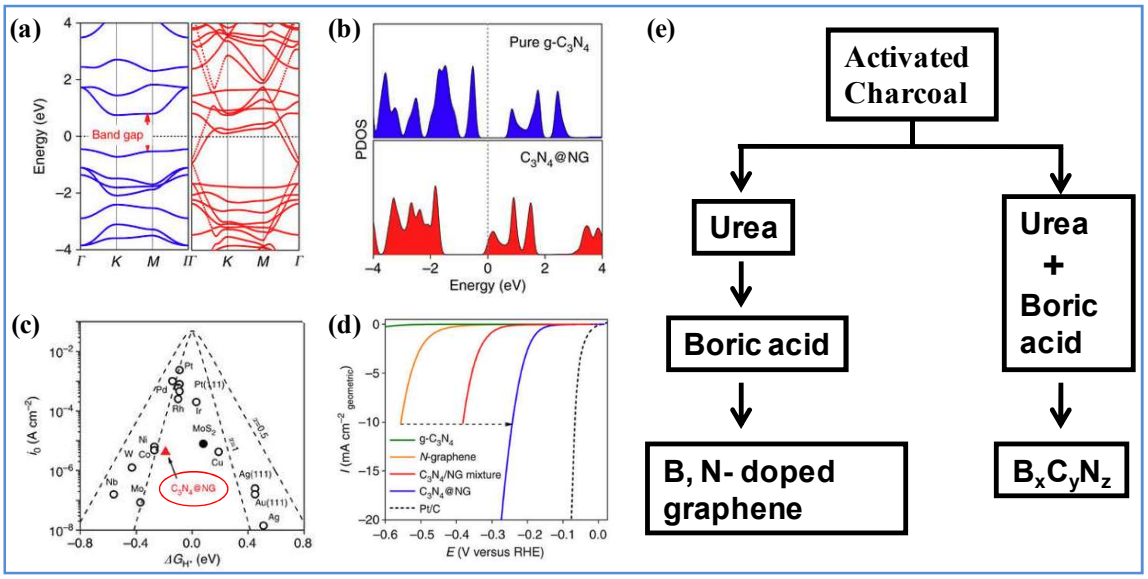

Figure 4.1: (a) Band structure and (b) The projected density of states of g-C_3N_4 (blue) and C_3N_4@NG hybrid (red). (c) Fitting of C_3N_4@NG into the Volcano plot (red triangle) for comparison with other catalysts. (d) The comparative linear sweep voltametry curves for four metal-free electrocatalysts in comparison to 20% Pt/C. Reprinted with permission[10], Copyright 2014, Nature Publishing Group. (e) Difference in synthetic processes for $B_xN_yC_z$ and B, N-doped graphene.

Transition metal oxides[13-14], disulphides[15-16], nitrides [17], carbides[20], selenides[21], and phosphides[22] have also been investigated and there has been efforts to increase the active sites for accelerated charge transfer kinetics induced by appropriate doping with heteroatoms[2-24] or strain introduction in the basal plane of the 2D material. [25-26] Non-metals (N, B, S, P) doping of graphene[27] is one approach in this direction. With all the efforts platinum has remained unrivalled for electrochemical HER and much interest has been given recently in metal (Pt) free catalysts. Other materials which have shown promising electrocatalytic HER activity are MoS_2 nanoparticles grown on graphene[28] and Mo_2C-carbon nanocomposites[29] (**Figure 4.2**). A comparative activity analysis of all the recent state-of-art 2D material electrocatalysts are listed in **Table 1**. These mainly include graphene and graphene oxide based catalysts loaded onto various HER co-catalysts. They may also be some carbides, phophides and sulfides of low cost metals. The heteroatom doped carbon matrix with various morphologies including nanosheets, nanowires, quantum dots etc.

Table 1: Comparison of various doped and undoped 2D materials for electrocatalytic HER.

Catalyst	η	η@10mA/cm^2	Tafel Slope	Reference
MoS_2 NS@CC	50	78	53	[30]
MoS_2 defect- & S- rich NS	100	135	48	[31]
1T@2H MoS_2/C NS	64	75	49	[32]
O-doped MoS_2 NS	120	150	51	[33]
Se-doped MoS_2 NS	140	230	55	[34]
Co-doped MoS_2 NS	44	111	57	[35]
Co-doped edge rich MoS_2	90	190	59	[36]
MoS_2/rGO	100	150	41	[37]
WO_2/mp-C NW	35	58	46	[38]
MoO_2P_x/Mo	80	135	62	[3]
G-C_3N_4@N,P doped G	76	114	90	[8]
N,S doped Carbon	12	100	57	[40]
Carbon nanosheets	63	137	132	[41]
Co@NC/Ti mesh	56	106	78	[42]
PCN@graphene	8	80	49	[12]
N-doped hexagonal Carbon	65	180	56	[43]
N, P-doped Carbon	76	204	58	[44]
porous g-C_3N_4 NR@N-graphene	80	257	54	[45]
N,P doped graphene	280	420	145	[46]
g-C_3N_4@S-Se-pGr	92	290	86	[47]
C_3N_4@N-doped graphene	140	240	51	[10]
Co@N-doped graphene	30	147	82	[48]
N,P codoped Carbon	60	140	89	[49]

*NS=nanosheets; CC=carbon cloth; NW=nanowire; NR= nanoribbon; mp=mesoporous, η= overpotential. Potentials are reported with respect to RHE; Unit of tafel slope is mV/dec

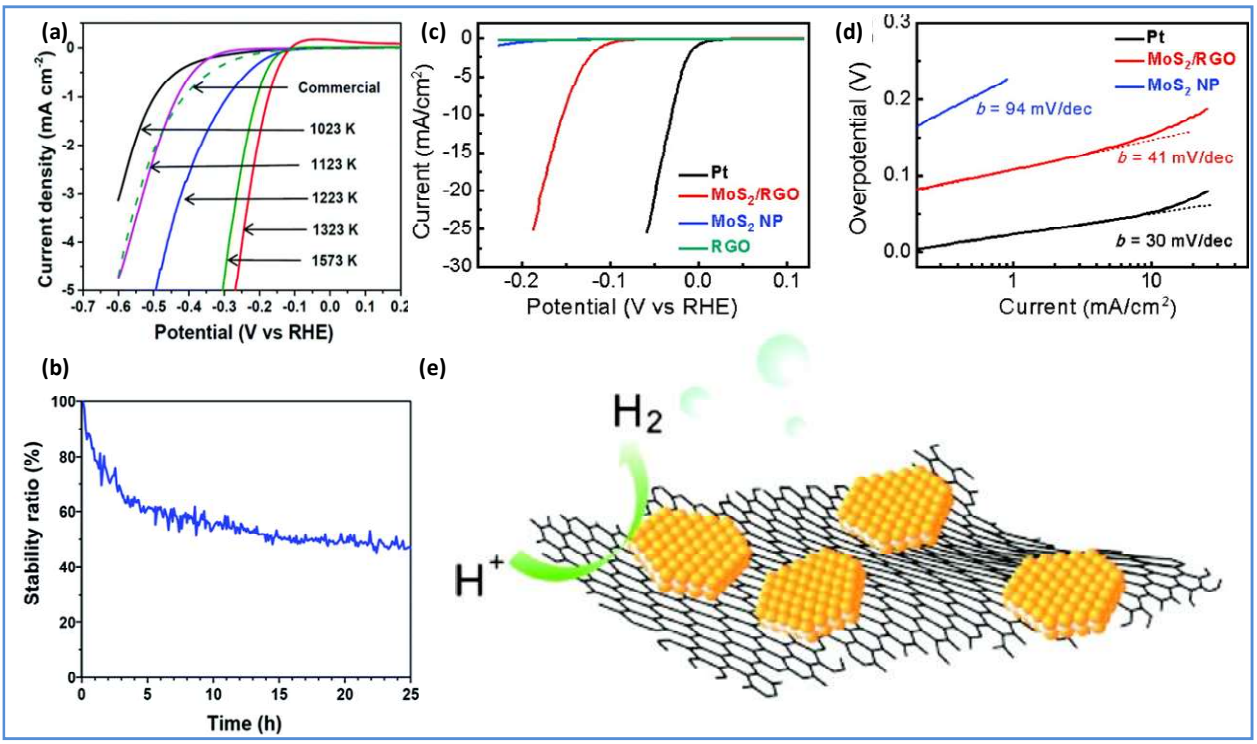

Figure 4.2: (a) Linear Sweep Voltamogram (LSV) of Mo_2C/C nanocomposites in comparison to commercial Mo_2C. All the samples represented in graph are synthesized at different temperatures under N_2 flow. (b) The Stability test of Mo_2C at −0.18 V *vs.* RHE. Reprinted with permission[29], Copyright 2014, Royal Society of Chemistry**.** (c) LSV of MoS_2/RGO in comparison to Pt and other catalysts and (d) tafel slope corresponding to the HER activity. (e) Schematic representation of MoS_2 nanoparticles on reduced graphene oxide sheets. Reprinted with permission[28], Copyright 2011, Americal Chemical Society.

With the knowledge of all these materials in literature for electrochemical activity, we considered it most appropriate to investigate the electrochemical HER activity of borocarbonitrides, $B_xC_yN_z$, which have been shown to have impressive surface and catalytic properties[50-51] and are also low cost materials. These materials are nanoplatelets containing graphene and BN domains, possibly along with BCN rings [52]. They contain B–C, B–N, C–N, C–C bonds but no B–B and N–N bonds. They would have defect sites (e.g. sp^3–C, Stone–Wales defects) in the carbon network which can act as active sites (as nucleophiles for H^+ ions) for electron transfer reactions. $B_xC_yN_z$ is different from B, N-codoped graphene in some ways such as thermal stability and the presence of covalent BN domains in the carbon matrix. Although excess of BN domains impedes the electrochemical activity, their presence in trace amounts gives rise to the $(BN)_x/C_y$ interface which is shown to have interesting adsorption properties. To the best of our knowledge, there has been no report in the literature on the use of BCNs as

electrocatalysts for hydrogen production although they have been used for the oxygen reduction reaction (ORR).

2. Scope of the Investigations

This chapter demonstrates that the carbon-rich BCN (BC_7N_2) exhibits outstanding electrocatalytic activity for HER. The experimental results and theoretical understandings complement each other. We have carried out first-principles calculations which reveal the unique features of the highly active carbon-rich BCN. This chapter comprehensively describes various important features of BCN materials and show how they posses excellent and comparable electrochemical HER activity to that of Pt. Furthermore, discussions pertaining to the BCNs covalently cross linked to other 2D materials such as MoS_2 exhibiting outstanding electrochemical as well as photochemical HER activity is also included.

3. Experimental Section

3.1. Materials:

Urea, Boric acid and Activated charcoal were purchased from SD Fine Chemicals, India. Nafion (perfluorosulfonic acid cation exchange polymer; 5 wt% in aliphatic alcohols) solution was a bought from Sigma Aldrich. 40% commercial Pt/C catalyst was purchased from Sigma Aldrich and used for comparison purpose. Absolute ethanol (HPLC grade) and Sulphuric acid (H_2SO_4, analytical grade) were obtained from SD Fine Chemicals, India. All the chemicals were used as it is without further purification.

3.2. Characterizations:

The morphology of the obtained BCN nanosheets were studied by Transmission electron microscopy (TEM, Technai F30 UHR, 200 kV) . The atomic ratio of the elements and the corresponding elemental composition of the samples were studied by XPS measurements, carried out with an Omicron spectrometer using Al Kα as the X-ray source (1486.6 eV), Perkin–Elmer 2400 CHN analyzer and FEI Quanta FESEM equipped with energy dispersive X-ray spectroscopy (EDX), under 10 kV accelerating voltage and 10 microsecond accumulation time.

Surface area measurements were carried out with a Quanta Chrome Autosorb- 1 instrument. Powder X-ray diffraction (XRD) patterns of the reaction products were recorded using a Bruker Diffractometer with Cu Kα radiation (D8 Advance X-ray diffractometer, Cu Kα, λ = 1.5406 Å, 40 kV, and 30 mA). Raman spectra were recorded at different locations of the sample using a Jobin Yvon LabRam HR spectrometer with 632 nm Ar laser.

3.3. Synthesis of $B_xC_yN_z$:

Required amounts of boric acid, urea and activated charcoal were mixed step by step ensuring full solubility of boric acid and urea in 20 mL DI water. Then the proportionate mixture was ultrasonicated (Elmasonic P30H model, 37 kHz, 100% power) for 20 minutes to obtain a homogeneous dispersion which was heated at 80°C. When a slurry was obtained as a result of evaporation of the solvent, it was transferred into a quartz boat and heated in a tubular furnace at 900°C for 10 h under N_2 atmosphere (heating rate=4°C/min). Then subsequently the obtained black sample was treated with NH_3 at 900°C for 4 h (heating rate=4°C/min). 5 different compositions of BCN nanosheets were obtained by varying the initial amount of B, N and C precursor viz. boric acid, urea, activated charcoal respectively (**Table 1 in results and discussion section**).

3.4. Synthesis of nanocomposites of $B_xC_yN_z$ with other 2D materials:

1T-MoS_2: Exfoliated phase of MoS_2 was obtained by the Li-intercalation of bulk MoS_2 which gives Li_xMoS_2 with n-butyl lithium as the reagent and its subsequent exfoliation using deionized water. Briefly, bulk MoS_2 (300 mg) powder was stirred in a solution of n-butyl lithium (n-BuLi, 3 mL, 1.6 M hexane) and refluxed at 70°C under nitrogen atmosphere over a period of 48 hours. The black Li-intercalated (Li_xMoS_2) sample was collected by filtration under nitrogen, and washed extensively with hexane (3 × 100 mL). The obtained Li_xMoS_2 sample was ultrasonicated in water (1 mg/mL) for 1 h and the resultant solution centrifuged at high speed (8000 rpm) to remove LiOH and any non exfoliated materials. From ICP analysis the final concentration of exfoliated MoS_2 in water was found to be 0.7 mg/mL.

3.5. Surface Functionalization: Carboxylate-1T-MoS_2 (MoS_2-CH_2COOH): 10-fold excess of 2-bromoacetic acid was added to the exfoliated 1T-MoS_2 (1 mg/mL) solution and allowed to stir for 5 days at room temperature. The precipitated product was filtered and washed with 2-propanol, water, and ethanol and dried at 60 °C under vacuum. Amine functionalized 1T-MoS_2 (MoS_2–$C_6H_4NH_2$): It was obtained by reacting 1T-MoS_2 with a solution of the iodobenzene reagent (12 fold excess) dissolved in DMF (60 mL) and the resulting mixture was allowed to stir at room temperature for 72 h. The black precipitate obtained was separated by centrifugation and then washed with DMF and ethanol to remove unreacted reagents, organic byproducts.

3.6. BCN–MoS_2 composites: These were prepared by mixing BC_7N (50 mg) and MoS_2–CH_2COOH (50 mg) samples in dry DMF (5 mL) in a Schlenck flask through bath sonication. To the resultant dispersion, coupling reagents N-(3-(dimethylamino)propyl) N'-ethylcarbodiimidehydrochloride (EDC·HCl, 20 mg) and 1-hydroxybenzotriazole (HOBt, 20mg) were added under a N_2 atmosphere and allowed to stir for 48 h. The obtained product was collected by vacuum filtration and washed several times with copious amounts of DMF and water to remove by products. When BC_7N (50 mg) and MoS_2–$C_6H_4NH_2$ (50 mg) samples were taken, G/BCN– MoS_2 nanocomposites were formed.

3.7. Detection of surface functional groups:

To know the efficient formation of nanocomposites the surface concentrations of functional groups in MoS_2 were determined by chemical tagging and photoluminescence spectroscopy before and after the reaction. The technique used is Fluorescence labeling of Surface Species (FLOSS)[53]. Tagging of amine groups using NHS-Cy5 was carried out as follows. To a 2 mg sample under study, 10 µL of 1.42 mM of NHS-Cy5 dye solution, 100 µL of triethylamine (TEA), and 6 mL of DMSO were added, and the resulting solution was stirred in the dark at room temperature for 12 h[54]. After the reaction, the obtained solutions were centrifuged and supernatant was transferred to a flask. Fluorescence tagging of the carboxyl group using 1-bromoacetyl pyrene was carried out as follows. To a 2 mg sample, 2 mL of 1.7

mM solution of 1-(bromoacetyl) pyrene in DMF, 1.0 mg of K_2CO_3 and 1.0 mg of KI were added. The resulting solution was stirred in dark at 50 °C for 12 h and the aforementioned procedure was repeated.

3.8. Electrochemical HER performance analysis:

All the electrochemical analysis was performed using an electrochemical workstation (CHI760E and RRDE-3A, CH Instrument, USA) with a typical three electrode system. Platinum coil was used as the counter electrode, Ag/AgCl (3M NaCl) as the reference electrode and Glassy carbon electrode (GCE, 3 mm diameter) was used as the working electrode. Prior to measurements, GCE was thoroughly polished with 1µ, 0.3µ and 0.05µ alumina powder (CH Instruments Inc.) and subjected to N_2 flow for 30 minutes. For the preparation of working electrode 2 mg of the catalyst was ultrasonically dispersed in 300 µL Nafion solution (Millipore water: Isopropanol: 5wt% nafion = 4 mL: 1 mL: 60 µL) until homogenous dispersion was obtained. 10 µL of this dispersion was carefully drop casted on the GCE and allowed to dry overnight under ambient atmosphere. Internal and solution (iRs) drop within the cell was compensated for all the cathodically polarized curves. The electrolyte used was 0.5 M H_2SO_4 saturated with Ar gas flow for 30 minutes to remove the dissolved oxygen. During the measurement, flow of Ar was maintained on the headspace of electrolyte to minimize the disturbance due to gas purging. The working electrode was rotated at 1600 r.p.m throughout the measurement to remove hydrogen gas bubbles formed at the catalyst surface. The catalyst was electrochemically washed between the potential ranges of 0.2-0.9 V before the measurement. Linear Sweep Voltametry (LSV) was performed at 1600 rpm and scan rate of 5 mV/s. Electrochemical Impedance Spectroscopy (EIS) was done at the voltage corresponding to the onset potential of Hydrogen Evolution Reaction (HER). For testing the stability of the catalyst Chronopotentiometry (CP) and Chronoamperometry (CA) was performed at current density of 20 mA/cm^2 and overpotentail (η) of -0.32 V respectively. All the measurements were done at room temperature.

Electrochemical Impedance Spectroscopy (EIS) was done at the voltage corresponding to the onset potential of HER. The potential reported in this study is with respect to reversible

hydrogen electrode (RHE).

For this the potential with respect to Ag/AgCl was converted to RHE based on following equation,

$$E(RHE) = E^0(Ag/AgCl, sat.KCl) + E_{expt.}(Ag/AgCl) + (0.059 \times pH)$$

where E^o is the standard reduction potential of Ag/AgCl.

3.9. Calculation of double layer capacitance (C_{dl}):

Since most of the electrochemical activities of the catalysts reported in literature for HER are either mass normalized or electrochemically active surface area normalized, we calculated the C_{dl} using a simple CV method. And the value of C_{dl} is linearly proportional to the electrochemically active surface area of the electrode. A potential range of 0.2-0.4 V was selected for the capacitance measurements because in this potential window no faradaic process corresponding to HER occurs and the electrode can be expected to behave as an ideally polarizable electrode (IPE). The variation of current of such an electrode as a function of time when the measurement is done at a certain voltage ramp say v V/s is given by[55],

$$i = vC_{dl}\left[1 - exp\left(\frac{t}{R_s C_{dl}}\right)\right]$$

Where, R_s is the solution resistance. vC_{dl} is the saturation current at large time. Thus plot of ΔI i.e $|i_a - i_c|$ at 0.25 V against scan rate v gives a straight line with slope twice the value of C_{dl}.

3.10. Note on Tafel slope:

Water splitting through HER occurs via electrochemical reduction of H^+ ions or H_2O (equations below) depending on the medium used.

$$2H^+(aq) + 2e^- \rightarrow H_2(gas)\ (acidic)$$
$$2H_2O + 2e^- \rightarrow 2OH^-(aq) + H_2(gas)\ \ (basic)$$

Here, the proton source is the hydronium cation (H_3O^+) in the acidic electrolyte and the water molecule in alkaline solutions. It is a multistep reaction: first discharge or adsorption of H^+ (H_{ad})

(common step) ion on catalyst surface followed by proceeding via two pathways to produce H_2. H_{ad} either recombines with another H_{ad} to give H_2 or forms H_2 by reacting with another H^+ on the surface of catalyst[56](**Figure 4.3**).

$$(1)\ Volmer\ \ step: H^+ + M^+ + e^- \leftrightarrow M - H^*$$

$$(2)\ Heyrovsky\ step: M - H^* + H^* + e^- \leftrightarrow M + H_2$$

$$(3)\ Tafel\ step: 2[M - H^*] \leftrightarrow 2M + H_2$$

where *H** is the chemically adsorbed hydrogen atom on the active site of catalyst (*M*). To find the probable pathway of H_2 generation, tafel slope is generally employed. From the Butler Volmer equation, theoretically calculated tafel slope for Pt as a model catalyst should be 29 mV/dec assuming that the tafel step as the rate determining step (rds). If Heyrovsky step is the rds then tafel slope should be 38 mV/dec. However if the first step, discharge or the volmer step is slowest then irrespective of whether H_2 evolution takes place by later two steps, the tafel slope should be 116mV/dec[56] . It should be noted that lower the value of tafel slope better is the catalyst for HER. In addition to this exchange current density (i_0) is the vital depicter of catalysts' inherent activity. It is defined as the current density in one direction (cathodic or anodic) at an equilibrium potential of a reaction. It correlates the rate of electron transfer under reversible conditions with the overpotential. The tafel equation can be used to calculate the value of i_0 and charge transfer coefficient (α). From the reduced Butler-Volmer equation we have,

$$\eta = a + b\ log\left(\frac{i}{i_0}\right)$$

Where $b = -\frac{2.303RT}{\alpha F}$ is the tafel slope and $a = -\frac{2.303RT}{\alpha F}\ \log(i_0)$

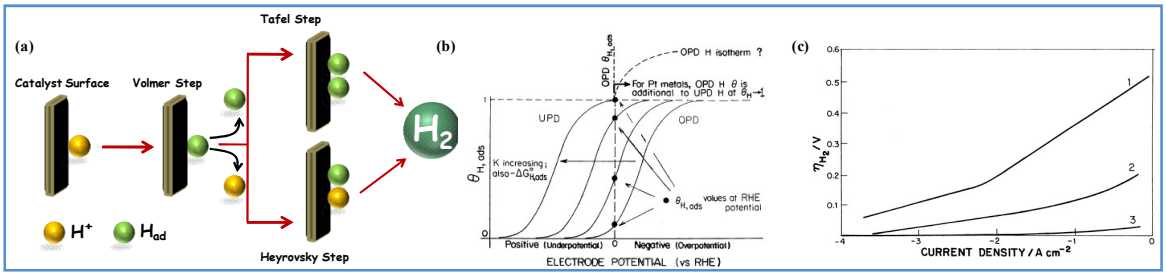

Figure 4.3: (a) Schematic representation of the mechanism of electrochemical hydrogen evolution reaction, (b) Illustraion of the relation between Langmuir isotherm functions for underpotential deposition of H and the various values of ln K or $\Delta G^0_{H,UPD}$, with respect to RHE. (c) The relationship between tafel slope and the HER on (1) smooth Pt; (2) high-area Pt formed thermally; and (3) Teflon-bonded Pt on Pt screen. Reprinted with permission[57], Copyright 2002, Elsevier.

As the HER process includes adsorption and desorption processes, an ideal catalyst is expected to have optimum Gibbs free energy change for these processes close to zero (ΔG~0). For a deeper understanding of mechanism, Conway et al. [57] examined the underpotential deposition (UPD) **(Figure 4.3)** of hydrogen. It was concluded that depending on the nature of electrocatalysts, results from tafel slope analysis for predicting mechanism can vary.[58] So a mechanistic understanding of carbon based electrocatalysts would be different from that of metal based ones. With extensively unexplored actives sites on catalysts surface a further understanding is needed to decipher the HER mechanism and the calculation of other important parameters like turnover frequency (TOF) and exchange current density (i_0).

3.11. Methods of first principles calculations:

Our calculations are based on first-principles density functional theory (DFT) as implemented in the Quantum ESPRESSO code[59]. We use a generalized gradient approximation (GGA) with Perdew-Burke-Ernzerhof (PBE)[60] parameterization of exchange correlation energy functional with ultrasoft pseudopotentials[61]. An energy cut off of 30 Ry was used for truncating the plane wave basis set to represent wave functions, and 240 Ry for the density. We use periodic boundary conditions with a supercell that keeps vacuum in the separation between periodic images of width 8 Å. The structures were relaxed till the magnitude of Hellman-Feynman force on each ion becomes smaller than 0.03 eV $Å^{-1}$. Brillouin zone integrations were carried out with a uniform 12 X 10 X 1 mesh of *k*-points. We use first-principles density functional theoretical calculations to determine electronic structure and energetics of various compositions of carbon rich $B_xC_{1-x-y}N_y$ with a goal to understand their electrocatalytic activity in HER observed here. We focus on three compositions: BC_7N_2 (I), $B_2C_2N_2$ (II) and BC_8N (III) which show great contrast in their electrocatalytic activity. For the schematic representation see next sections. We consider four symmetry inequivalent configurations of (I) obtained by replacing a carbon atom in the 10-atoms supercell of graphene with boron, and substituting two N atoms at different pairs of carbon sites. Both N atoms are bonded to B atom in configurations (Ia), while only one of them is bonded to B in the other two

configurations (Ib and Ic) and none of them in Id (**Section 3.6.3**). Consistent with earlier works[52], the configurations, Ia has the lowest energy, followed by Ic, Ib and Id (Table 7 later section). Similarly, we considered one configuration of composition (II) and two configurations of composition (III).

4. Important features of $B_xC_yN_z$ for use as an electrocatalyst:

From the previous works in our lab and the competing parallel research works on dual doped carbon materials and borocarbonitrides, it has been convincingly shown that BCNs exhibits some of the unique features that can be utilized for various energy applications including electrocatalysis. The following discussions will summarize these properties in light of its use as an electrocatalysts as studied by us and various other groups.

4.1. Surface area:

Surface area is a crucial property for an electrocatalyst. As opposed to other carbon source preparation methods, BCN prepared from activated charcoal (BC_2N, BC_5N etc.) exhibits surface areas as high as 1900 m^2/g with type IV adsorption behavior with mesoporous features[50-51,62]. BCNs synthesized using exfoliated graphene (EG) and consisting of BN domains also exhibit excellent gas adsorption properties (type II and IV)[63-64]. Further improvement in surface area and creation of more accessible sites (for electyrolyte in electrocatalysis or gases in gas adsorption study) is achieved by covalent cross linking of layers of BCNs among themselves and with other 2D materials which will be discussed in the later sections. From the XPS, electron energy loss spectroscopy (EELS), EDAX and CHNS elemental analysis the composition and chemical nature of BCN are examined. Core level spectra of the elements suggest the presence of B–C and B–N bonds for boron, C–B and C–N bonds for carbon and pyrollic and pyridinic N–C bonds for nitrogen in BCN**.** One finds the C-O bond if GO is the carbon source.

4.2. Electrochemical properties:

The BET surface area or the apparent surface area approximated from the FESEM and TEM images are different from the actual electrochemically usable surface areas forming the

electrode/electrolyte interface. One of the ways to approximate this electrochemically active surface area (ECSA) is by cyclic voltametry (CV) in the non-faradic potential region[55]. Various compositional ratios of BCNs have been compared using this method and was found that the higher carbon content results in higher ECSA (**Figure 4.4**). Due to the available surface area it can be used for energy storage applications. Bhat et al.[65] reported the electrochemical Li storage of carbon rich BCNs. The higher B and N content, the more coulombic efficiency. Different compositions of BCN were found to give different discharge capacities depending on the ECSA and carbon content[50]. With high ECSA, carbon rich BCN have been investigated for selective electrochemical sensing[66] as well as supercapacitor[67-68] applications.

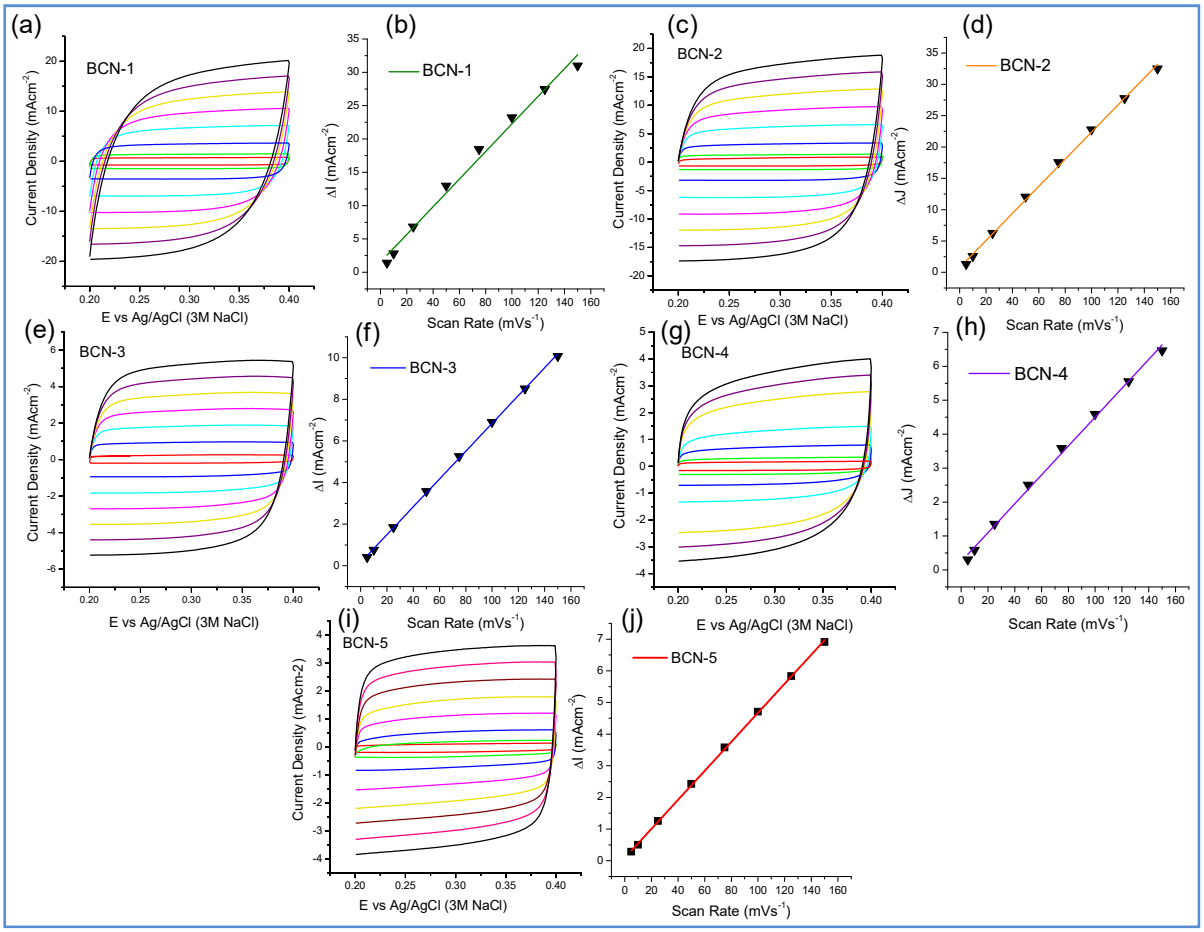

Figure 4.4: (a, c, e, g, i) are the CV curves and (b, d, f, h, j) are the corresponding difference in the current density at 0.25 V plotted against scan rate to calculate the Cdl value form the slope after the linear fit.

4.3. Electronic properties:

Electronic properties of BCN can be tuned by varying the B:C:N ratio or by configurational changes in the structure of BCN which is a composite of BN and graphene domains, B- and N- co-doped graphene sheets, hexagonal BCN rings. In between graphene (gapless) and BN (insulator, bandgap ~6eV), the electronic properties like resistivity[62], carrier concentration[69], mobility[70-71] and band gap[72-73] can be modulated by varying the composition. It is found that 33% - 50% substitution of B and N in carbon matrix in BCN (BC_3N, BC_2N) leads to about 1.5–2% graphene lattice expansion. This in turn provides a clue that composition plays a crucial role in modulating the electronic properties of BCN materials. Slightly larger carbon content results in the lower electronic resistance (as in BC_5N) useful for electrochemical applications. Thus, BC_5N shows lower resistance than BCN due to rich carbon content. DFT and Monte Carlo simulations have been employed in this work and previous works to understand the effect of B- and N- doping, their relative ratio and the arrangements[52] to give rise to specific electronic properties for electrocatalysis. There are two views related to the active sites. While some reports suggest that the heteroatom acts as the active site on the catalysts surface[23-24,8], there are reports suggesting that the dopant atoms near carbon atoms activates its electron and hence the carbon behaves as the active sites[9]. From electronic structure considerations, the B, N- doped graphene and BCNs are coherent in active site generation. However, BCNs has to some extent added advantage in terms of its composition (heterocomposites consisting of nanodomains of BN and BCN rings) which improves the properties like adsorption of ions (H^+ and OH^-) due to the presence of $(BN)_x/C_y$ and $(BCN)_x/C_y$ interfaces which are absent in B, N- co-doped graphene. In addition to this, the relative configuration of B and N atoms in carbon matrix for different compositions of $B_xC_yN_z$ for the efficiency in HER process has also been investigated inferring the carbon atom close to N and B being most active site due to increased charge population and density. The variation in the composition of BN and CN domains within the graphene matrix has also been studied[66]. Thus relative proportion of pyrollic and pyridinic nitrogens play a role in catalytic and other properties. The conduction band states of BC_7N_2 have a major contribution from p-orbitals of N and C atoms. Additionally different chemical characteristics have been found for the two

substituted N atoms (amongst various configurations of same BC_7N_2 composition). Thus slightly higher nitrogen content may be advantageous in HER. (Details in Section 6.3)

4.4. Surface functional groups and their quantitative determination:

Electrochemical properties study involves electrode/electrolyte interface. This interface is made up of the electrocatalyst surface and hence decoding the exact nature of surface is crucial to understand the activity. The electronic properties of graphene based 2D materials are dictated by the dopants and the oxygen functional groups present on the surface. The oxygen functional groups (C=O, COOH, -O- and oxygen attached to the graphitic carbon with nitrogen in it) has a negative effect in the conductivity of the electrocatalyst. Though oxygen is more electronegative than N and C, it is still not electroactive for HER in the form of the surface functional groups mentioned above. Unlike B and N it is not the part of sp^2 carbon rings and hence cannot contribute to the electron delocalization and faster electron transfer reactions. It is desirable to have a minimum of oxygen functional groups as possible. The surface characterization is generally based on XPS study and BET surface area calculations. O-1s can be decomposed into three peaks corresponding to 530.2 eV, 532 eV, 533.6 eV which are respectively due to the presence of C=O, COOH and oxygen attached to the graphitic carbon with nitrogen in it. These functional groups help in effective doping of N and B by acting as a reactive site during the reaction. The presence of both oxygen and nitrogen where oxygen is bonded to nitrogen in the carbon ring has been shown to be electroactiveactive than the oxygen devoid of nitrogen attachment in case of ORR[74] but its activity is negligible in comparison to N. However the aim is to reduce these oxygen functionalities from the carbon (tried by treatment with ammonia vapor in our case) moiety due to its negative effect in the conductivity of the electrocatalyst. The XPS analysis concretely does not quantify the relative ratios of different oxygen functionalities on the surface of catalyst. In this regards, fluorescence labeling of surface species (FLOSS), which is chemical labeling of catalysts surface using fluorescent probes helps to exactly detect as well as quantify surface functionalities in carbon based catalysts like nanotubes, nanofibers. An empirical relationship has been drawn between surface functionalities and electrochemical properties like supercapacitor, oxygen reduction

reaction activity of BCNs of different compositions by our group[75].

5. $B_xC_yN_z$ as a HER catalyst:

Doping graphene etc. by heteroatoms, B, S, P and N is an established technique to modulate the electronic properties[76-77]. When doped with elements (with higher and lower electronegativity than carbon) it can theoretically create an advantageous electronic structure and catalytically active sites. For example, opening the band gap of graphene around its Dirac point has been achieved by B and N codoping with the gap below/above the Fermi level[72] and hence modulation of its electronic properties[77]. Since B-N bond is simillar to C-C bond length, codoping does not necessarily cause alterations of 2D lattice and disturb the conjugation. Dai and coworkers[78] found that the carbon π electrons can be activated by lone-pair electrons from doped N atoms, which can be used in reduction reactions[79], the effect being more profound in dual doped carbon matrix[80-81]. Charge delocalization of carbon atom in carbon based catalyst induced by B and N codoping was found to be vital for ORR[82], while the dopant sites acts as electrochemically active site for ion adsorption[83]. The insulating effect of BN domains for the electrochemical activity can be reduced by meticulous selection of initial precursors composition ratio, however $(BN)_x/C_y$ interface generated by trace amounts of BN domains have been shown to have unique adsorption properties[52]. The main advantage of BCNs prepared by the solid state route is that we can vary the electronic properties as well as other properties by varying the composition.

6. Results and Discussion:

In this section the detailed morphology and compositional analysis of BCN is discussed. The Electrochemical activity investigations and the corresponding theoretical study to understand the activity of BCN has been deduced. The nanocomposites of BCN with MoS_2 for further improvement in activity and the comparison of its activity with many state-of-art catalysts are tabulated.

We prepared five compositions (BCN-1 to BCN-5) of borocarbonitrides, $B_xC_yN_z$, by the reaction of boric acid, urea and activated charcoal (**see table 1**). Of these, BCN-1 is the most carbon rich sample with the composition of BC_7N_2 and BCN-5 has the least carbon content with the composition of $BC_{1.1}N$ (**see Table 1**). The morphology analysis reveals the nanosheets of BCNs as shown in **Figure 4.5**.

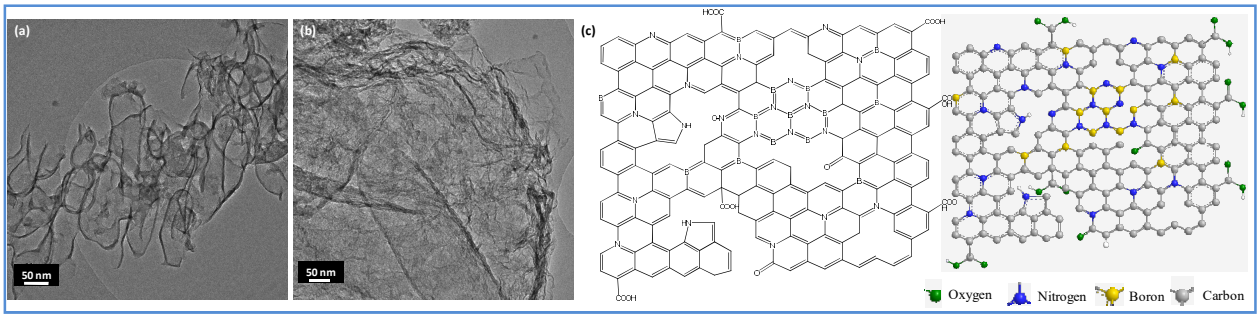

Figure 4.5: (a) and (b) TEM images of BCN-1 showing the sheet morphology. (c) Schematic of carbon rich BxCyNz sheets depicting the incorporation of B and N into the carbon network.

The surface areas were obtained from N_2 adsorption isotherms and BCN-1 was shown to have the highest surface area (1950 m^2g^{-1}) (**Figure 4.6**) and BCN-4 the lowest surface area of 1241 m^2g^{-1}. The presence of mesopores and micropores is indicated by the isotherms and pore size distribution (**inset of Figure 4.6**). The pore diameter calculated by the DFT method is in the range of 3–19 nm and the pore volume in the range of 0.7–1.1 cm^3g^{-1} for all the samples.

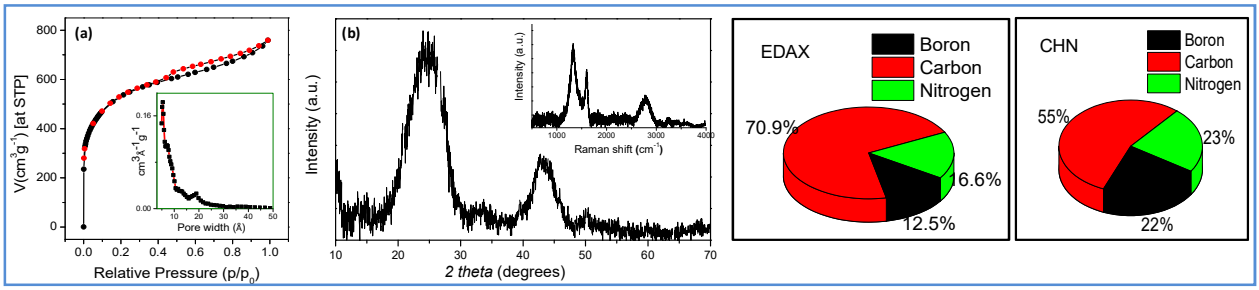

Figure 4.6: (a) BET adsorption isotherm of BCN-1 showing typical type-IV behavior consisting of mesopores. Inset shows the pore size distribution in BCN-1. (b) PXRD patern of BCN-1. Inset shows the Raman spectra.

The powder X-ray diffraction pattern of BCN-1 shows broad peaks centered at 24.91 and 43.21 (2θ with FWHM values of 6.8 and 3.5 respectively) (**Figure 4.6**), due to the (002) and (100) reflections, the broadening of peaks arising from the nanosized domains. Raman spectra show a prominent D-band (1335 cm^{-1}) due to defects along with the G-band (1590 cm^{-1}) and a weak 2D-band (2775 cm^{-1}) (see inset of **Figure 4.6**). X-ray photoelectron spectroscopy (XPS) was

employed to establish the nature of the chemical species in the BCN samples (**see Figure 4.7** for the spectra of BCN-1). **Table 1** gives a summary of the compositions of the BCN samples. The core level spectra of the individual elements were deconvulated to obtain a detailed understanding of the bonding characteristics (**see Figure 4.7**). The B 1s signal consists of two peaks centered at 190.8 eV and 192.3 eV, which corresponds to the presence of B–C and B–N bonds respectively. The C-1s peak can be deconvoluted to four peaks at 284.4, 285.1, 285.9, and 298.8 eV attributed to sp^2 carbon, C–B, C–N and C–O respectively. The deconvolution of the N-1s peak suggests the presence of different kinds of N–C bonds in BCN-1 (mainly pyridinic and pyrollic) as shown in **Table 2**. Thus the XPS analysis revealed the presence of B–C, B–N, C–N, and C–C bonds in BCN samples suggesting the presence of graphene and BN (as depicted in **schematic Figure 4.8)**. **Table 3** gives the percentages of B–C and B–N bonds on the surface of the BCN samples. We have also analyzed the O-1s signal. EDAX and CHN elemental analysis gave results which corresponded well with the compositions obtained from XPS.

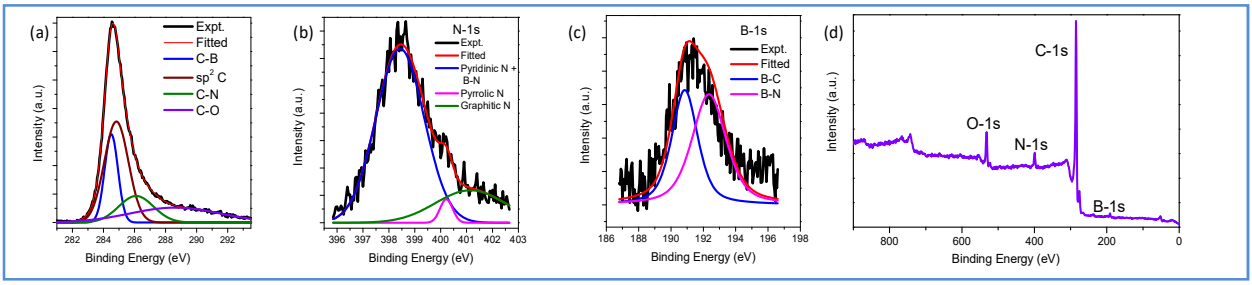

Figure 4.7: (a) to (c) X-ray photoelectron spectrum of BCN-1 showing the core level spectrum of C, N and B respectively and (d) XPS Survey scan for the elements in BCN-1.

6.1. Metal-free electrocatalyst for hydrogen evolution reaction:

The presence of trace metal impurities will lead to abrupt change in the electrochemistry of the parent material. Recent studies have extensively revealed this fact that for carbon based "metal-free" electrocatalysts, if these trace amounts of metals (Fe, Ni, Co, Mn, Cr etc) are present in the sp^2 carbon nanomaterials, it leads to dramatic influence in the electrocatalytic activity especially in ORR. Hence it has become imperative to check its presence in "metal-free" catalysts as has been argued by many researchers[84-85]. We selected 7 probable

electrochemically active metal impurities (Pt, Fe, Mn, Co, Cr, Ni and Cu). We confirm the absence of these metal impurities [except Fe, 1.5 wt% (30.1 µg) in the catalyst ink] in our catalyst by ICP-OES. We tested BCN-1 and also the initial precursors-Boric acid, Urea and activated charcoal. The findings are detailed in **table 4**.

Table 1: Composition and the sample names used in our experiment

Sample	Composition*	Boric acid (mg)	Activated Charcoal (mg)	Urea (g)
BCN-1	BC_7N_2	60	500	2.4
BCN-2	$BC_4N_{1.2}$	60	250	2.4
BCN-3	$BC_{1.7}N_{0.7}$	60	150	2.4
BCN-4	$BC_{1.7}N_{0.8}$	30	250	2.4
BCN-5	$BC_{1.1}N$	30	150	2.4

*From XPS, EDAX, ICP-OES and CHN elemental analysis.

Table 2: Relative percentage of different kinds of nitrogen on the surface of the BCN samples

Sample	Type of Nitrogen and its percentage (%)			
	Pyridinic-N	Pyrrolic	C-N-B	Pyridinic-N oxide
BCN-1	37	34	29	--
BCN-2	74.5	25.5	--	--
BCN-3	54.5	45.5	--	--
BCN-4	52.8	35.2	--	12
BCN-5	56.6	--	--	43.4

Table 3: Relative percentage of B-C and B-N on the surface of the BCN samples

Sample	B-C (%)	B-N (%)
BCN-1	86.9	13.1
BCN-2	59.8	40.2
BCN-3	37.5	62.5
BCN-4	100	--
BCN-5	17.4	82.6

The effect of the presence of Fe on HER activity has been studied by introducing Fe into the BCN sample (3%, 6% and 9%). BCN was ultrasonicated in $FeCl_3$ solution and was reduced by $NaBH_4$ to introduce Fe in the BCN. There was no appreciable linear change in the onset potential seen due to presence of Fe. Hence we conclusively propose that the electrocatalytic HER activity of BCN is not due to the probable presence of trace metal impurities.

Table 4: Study of the presence of trace metal impurities in the catalyst ink and the initial precursors.

Sample	Pt (µg)	Fe(µg)	Mn(µg)	Cu(µg)	Ni(µg)	Co(µg)	Cr(µg)
H_3BO_3 (in 60 mg)	8.6	12.2	13.6	13.3	13.3	8.6	24.7
Urea (in 2.4 g)	230	468	538	509.5	583.6	353	492
Act. Charcoal (in 500 mg)	5.6	81.8	14.0	3.9	14.4	8.5	24.1
BCN-1 (in 0.05 mg)	2.1 ng	30.1	5.7 ng	5.1 ng	0.9	3.4 ng	19.1ng

ng= nanograms Mass of sample deposited on GCE is 0.05 mg.

6.2. Electrochemical HER analysis:

Electrochemical performance of the BCN samples for HER was investigated by Linear Sweep Voltammetry (LSV) at 1600 rpm and 5 mVs^{-1} scan rate with deaerated 0.5 M H_2SO_4 as the electrolyte. The cathodic polarization curves of all the samples are shown in **Figure 4.8**. For the purpose of comparison, data for commercial 40% Pt/C and the bare GCE are also included. The GCE exhibits almost null activity in comparison with BCN and Pt/C polarization curves. The onset potential for HER was found to be -0.28 V whereas that for Pt/C was -0.23 V (Ag/AgCl). The value of the overpotential (η) gives an idea of the extent of polarization upon passage of faradaic current (in this case due to H_2 evolution), a lower η signifying better catalytic activity generating more H_2 upon application of smaller cathodic potential. The values of η at 10 and 20 $mAcm^{-2}$ are -298 mV and -330 mV signifying the rapid rate of electron transfer on BCN-1 (**see Table 5**). The inset in **Figure 4.8a** shows the difference in the overpotential required to produce a current density of 10 $mAcm^{-2}$ for the BCN samples and the Pt/C. In comparison with the recently reported non-precious metal catalysts, BCN-1 shows markedly better performance for

HER (**Table 6**). For the ease of comparison, the potentials reported in **Table 5** are against the reversible Hydrogen Electrode (RHE) obtained through RHE calibration using the equation[86] discussed earlier.

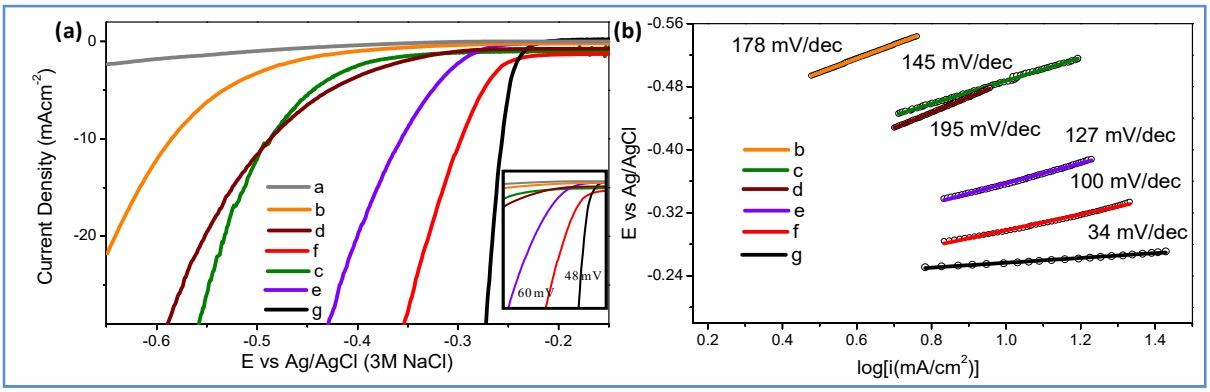

Figure 4.8: HER electrocatalytic performance comparison. (a) Linear Sweep Voltammetry curve of all the $B_xC_yN_z$ samples including Pt/C and the bare GCE. The inset compares the overpotential required to produce a current density of 10 $mAcm^{-2}$. (b) Tafel plots as deduced from the polarization curves in (a). The letters within brackets in the figure respectively represent the following: (a) bare GCE, (b) BCN-5, (c) BCN-4, (d) BCN-3, (e) BCN-2, (f) BCN-1, and (g) commercial 40% Pt/C.

The high HER activity of BCN nanosheets is further manifested by the Tafel plots (**Figure 6b**) and the corresponding mechanism for H_2 generation. We found that the hydrogen evolution by BCN samples follows the Volmer mechanism[56] giving a Tafel slope of 100 $mVdec^{-1}$. In order to probe the interfacial properties of the BCN samples and ease the electrical exchange between the solution and the electrode, electrochemical impedance spectroscopy was performed at the onset potential of the sample from 10^5 to 1 Hz with an AC voltage of 5 mV. **Figure 4.9a and b** show the Nyquist plots for the samples. BCN-1 shows a minimum charge transfer resistance (R_{ct}) of 13.6 ohm. Lower R_{ct} reveals that faster electron transfer rate between BCNs and the GCE and the electrolyte results in acceleration of HER kinetics. This is also corroborated from the polarization curves and the Tafel slope values.

Table 5: Comparison Table for BCN samples and Pt/C.

Sample	BET (m^2/g)	Onset (a)	η@10 mA/cm^2*	η@20 mA/cm^2 [(a)]	Tafel Slope	I_o (A/cm^2)	R_{ct} (Ω)	C_{dl} (mF/cm^2)
BCN-1	1950	-284 V	-298 mV	-330 mV	100	5.1×10^{-5}	13.6	0.108
BCN-2	1635	-314 V	-357 mV	-401 mV	127	3.2×10^{-5}	60.1	0.103
BCN-3	1470	-451 V	-487 mV	-642 mV	195	1.0×10^{-5}	64.3	0.033
BCN-4	1241	-444 V	-487 mV	-533 mV	145	9.1×10^{-6}	268.9	0.022
BCN-5	1580	-428 V	-586 mV	-542 mV	178	4.4×10^{-6}	384.6	0.020
Pt/C	--	-230 V	-250 mV	-266 mV	34	--	--	--

[(a)]Against RHE the values can be converted by adding 227.7 mV, following the equation for calibration against.

Table 6: Electrocatalytic HER performance comparion of BCN-1 with recently reported non precious metal catalysts in literature.

Catalyst	Onset (mV)	η@10mA/cm^2 vs RHE	Tafel slope (mV/dec)	Ref.
3D-MoS_2/N-GAs	-236	-261	230	[93]
N-MPG	-220	-239	109	[94]
C_3N_4@NG	-180	-240	51	[95]
g-C_3N_4 NRs	-80	-200	54	[45]
MoS_2/RGO	-100	-150	41	[28]
Mo_2C/C NC	-100	-270@5mA/cm^2	110	[29]
BC_7N_2	-56	-70	100	This work

For the determination of the Faradaic efficiency (FE) of HER catalysed by BC_7N_2, we measured the amount of H_2 produced by electrolysis for 2 hours. The measured value matches well with the calculated value (assuming 100% efficiency). To confirm the high activity and lower charge transfer resistance we have compared the electrochemical active surface areas of the samples by calculating the double layer capacitance (discussed earlier **Figure 4.4**). The value of C_{dl} is 0.108 mF cm^{-2} for BCN-1, which is the highest value amongst all the BCN samples (**Table 5**). Since double layer capacitance is directly proportional to the electrochemical active surface area for carbon based materials, the values obtained for BCN-1 correspond to an enhancement factor of one order of magnitude relative to the other samples.

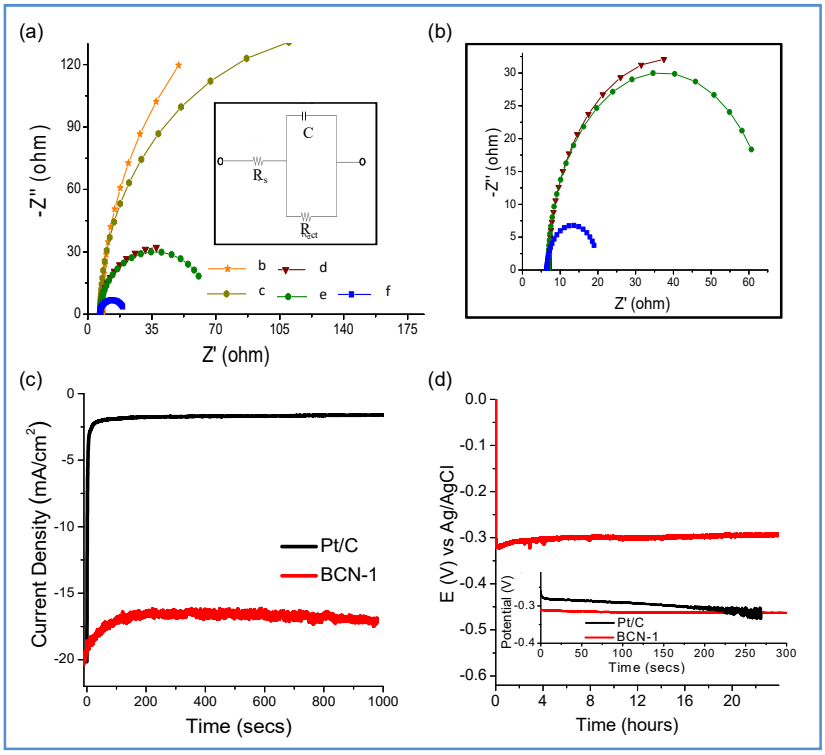

Figure 4.9: Electrocatalytic performance testing of BxCyNz. (a) Nyquist plot of $B_xC_yN_z$ at the onset potential. (b) Magnified image of (a) to show the same plot for low R_{ct} value. (c) Activity retention test by amperometric i–t plot taken at -0.32 V for BCN-1 in comparison to Pt/C. (d) Chronopotentiometry plot to produce a current density of 20 $mAcm^{-2}$. The inset shows the comparative plot for BCN-1 and Pt/C. The letters in (a) represent the same as in **Figure 4.6**.

The higher activity with lower R_{ct} for BCN-1 is due to the high electrical conductivity owing to the higher proportion of carbon in the network[62] and the larger active surface area. It is noteworthy that the electronic structure and properties which enhance electron transfer reactions are related to the composition and the relative ordering of graphene and BN domains. Furthermore graphitic N–C interaction would favor defect sites which play a key role in electron transfer reactions. The samples obtained from the controlled experiments without urea and boric acid respectively show that singly doped carbon (with N and B) does not show enhanced HER activity.

Stability is an important parameter of catalyst activity. We have employed chronoamperometry (CA), chronopotentiometry (CP) (Fig. 4c and d) and cyclic voltammetry (CV) to test the % retention of the electrochemical activity as a function of time or cycle. CA was performed at -0.32 V (Ag/AgCl, 3 M NaCl) and CP was done at a current density of 20 $mAcm^{-2}$.

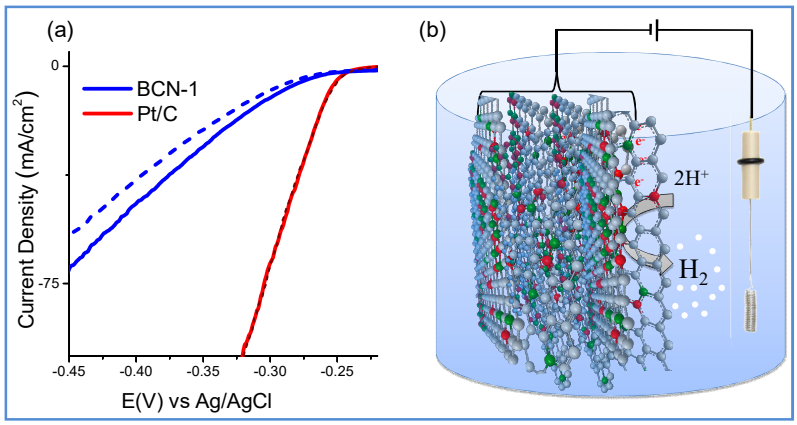

Figure 4.10: (a) Electrocatalytic HER activity retention comparison of BCN-1 with Pt/C. Data was collected from the chronoamperometric i-t curve performed at -0.32 V for 1000 seconds. (b) Quantity of H_2 gas evolved as a function of time for BCN-1.

Samples were also potentially swiped between 0.1 V and -0.35 V and after the cycling then LSV was again taken for comparison. BCN-1 shows exceptional stability in comparison to the Pt/C catalyst where ca. 80% of the activity is retained in comparison to Pt/C (only ~10% activity retention) in 1000 seconds (**Figure 4.9c and d; Figure 4.10a**) to obtain current at -0.32 V. From the CP study, (see the inset of **Figure 4.9d**), BCN-1 shows activity at par with Pt/C to produce a current density of 20 mAcm^{-2}. We performed CP for 24 hours (**Figure 4.9d**) and found BCN-1 to be a highly stable catalyst for HER. To reinforce these conclusions, we have performed CV in the potential window of -0.35 V to 0.1 V for 1000 cycles, recording the polarization curves before and after the cycling (**Figure 4.11a**). We observe ~83% retention in activity as also seen from the chronoamperometric i–t test. The degradation of graphitic carbon in acidic medium is

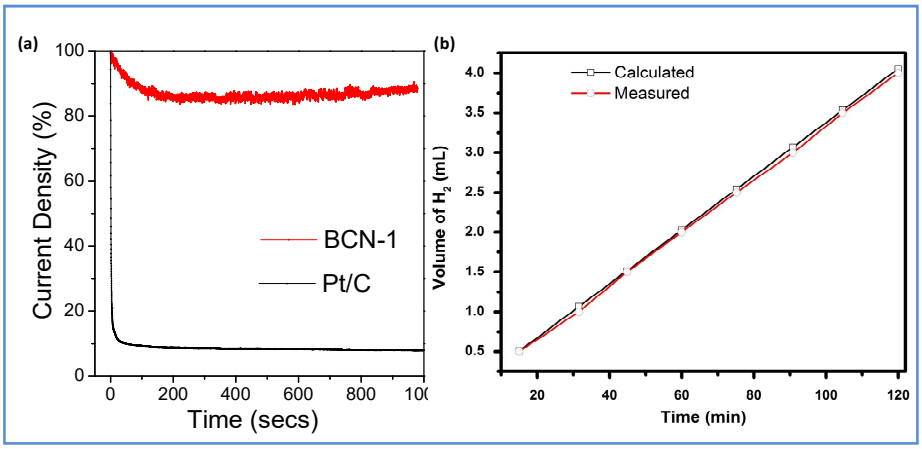

Figure 4.11: (a) LSV plot before and after 1000 cycles (between -0.35 V and 0.1 V) for both BCN-1 and Pt/C. (b) Schematic showing the HER activity of $B_xC_yN_z$ sheets.

negligible and the possible loss of active surface area is less than that for Pt/C (catalyst detachment, agglomeration, carbon corrosion, etc.).

6.3. First-principles calculations: (in collaboration with Prof. Waghmare, JNCASR**)**

We used first-principles density functional theoretical calculations* to determine electronic structure and energetics of various compositions of carbon rich $B_xC_{1-x-y}N_y$ with a goal to understand their electrocatalytic activity in HER observed here. We focus on three compositions: BC_7N_2 (I), $B_2C_2N_2$ (II) and BC_8N (III) **(Figure 4.12**), which show great contrast in their electrocatalytic activity. We consider four symmetry inequivalent configurations of (I) obtained by replacing a carbon atom in the 10-atoms supercell of graphene (**Figure 4.12**) with boron, and substituting two N atoms at different pairs of carbon sites. Both N atoms are bonded to B atom in configurations (Ia), while only one of them is bonded to B in the other three configurations (Ib, Ic and Id) consistent with earlier work[52]. The configuration Ia has the lowest energy, followed by Ic, Ib and Id (**Table 7**). Similarly, we considered one configuration of composition (II) and two configurations of composition (III).

The electronic density of states (DOS) and the partial density of states (PDOS) of these configurations were studied by first principles calculations. We have examined them by shifting the energy suitably to have a vacuum level at 0 eV. For all the configurations of BC_7N_2, Fermi energy (E_F) is around -3.2 eV, which gives an overpotential of about 1.2 eV relative to the redox potential of HER. Secondly, it is in a conduction band separated by a gap of about 0.5 eV from the valence band giving n-type carriers at relatively high density, highest for the configuration Ia (**Figure 4.13**). The bottom of the conduction band is just above the HER potential. From the PDOS, it is clear that these states are contributed largely by p orbitals of C and N atoms, and reflect that the two substituted N atoms have different chemical characters. Visualization of the frontier occupied state of the lowest energy configurations reveals that C–C and C–N bonds are relevant to the electrocatalytic activity. The electronic structures of both BC_8N and $B_2C_2N_2$ (**Figure 4.13c and d**) exhibit a gap of about 0.5 eV, and the top of the valence band (with fairly low density of states) is just above or barely touches the redox potential of the HER,

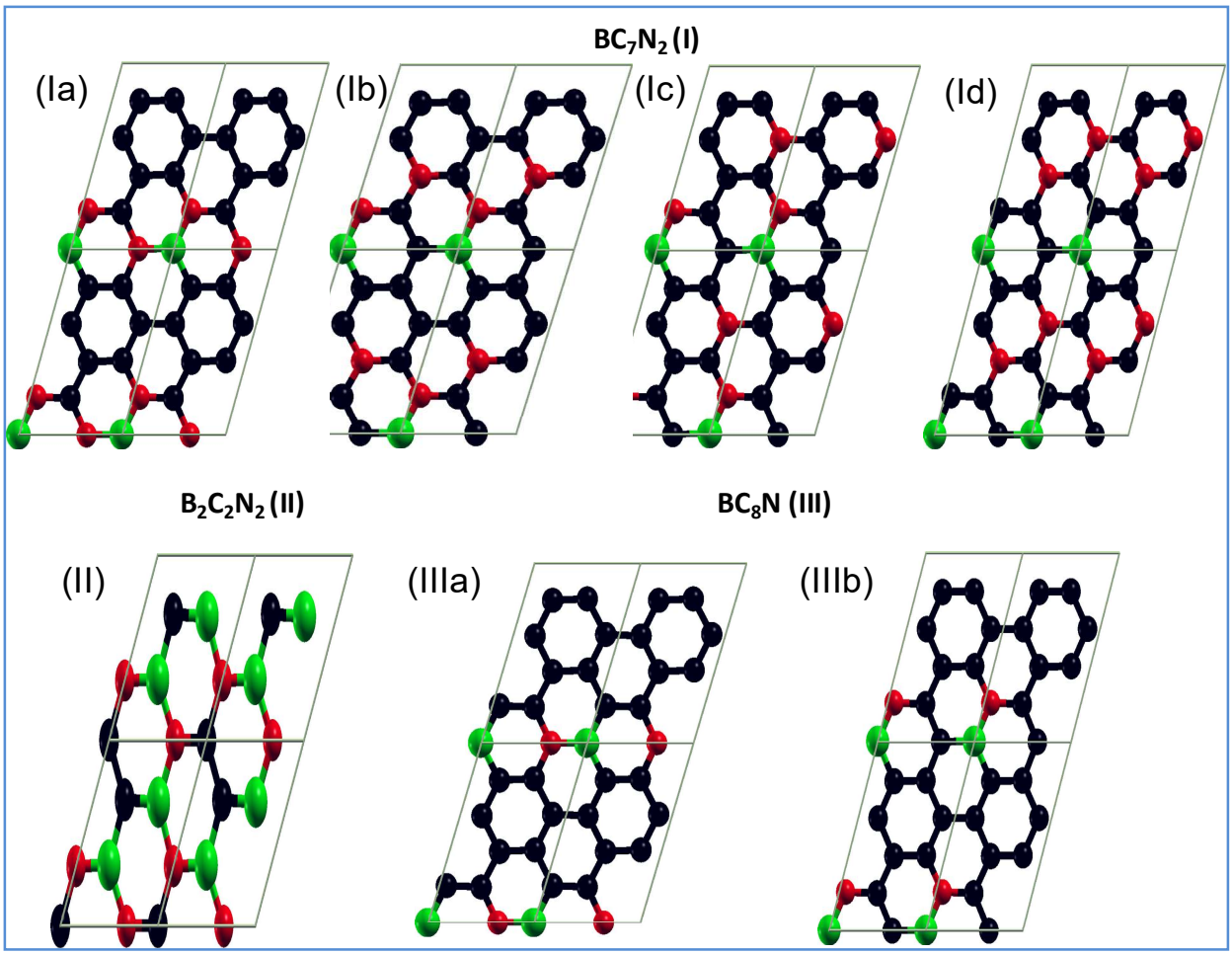

Figure 4.12: Schematics of three compositions (I, II and III), along with their symmetrically inequivalent configurations. C atoms are denoted by black, B by green and N by red.

Table 7: Comparison of valence band maxima, conduction band minima (VBM and CBM), EF and DOS (EF) of different configurations studied. For each composition (I, II and III), the relative energies of their configurations are mentioned with respect to the lowest energy configuration.

Configuration	Relative Energy E(config)-E(lowest) (eV/supercell)	VBM (eV)	CBM (eV)	E_F (eV)	DoS(E_F) (arb. units)
Ia	0	-4.888	-4.094	-2.934	1.747
Ib	1.076	-4.738	-4.341	-3.127	1.312
Ic	0.819	-4.976	-4.377	-3.086	1.143
Id	2.078	-4.830	-4.558	-3.171	1.193
II	-	-4.112	-3.595	-3.833	0
IIIa	0	-4.335	-3.832	-4.078	0
IIIb	0.132	-4.252	-3.966	-4.109	0

Their frontier occupied states involve mainly C–C bonds. While the valence and conduction band edges of the configurations of BC_7N_2 (Ia, Ib and Ic) straddle the HER redox potential (-4.44 eV), those of BC_8N and $B_2C_2N_2$ do not (**Figure 4.14 and Table 7**). A comparative study of the electronic structures of C_8N_2 and BC_7N_2 reveals that the electrostatic balance provided by the B atom is essential to get stability and optimal alignment of the electronic structure with respect to the HER potential (**see Figure 4.15**). We have also examined around 60 configurations for the interaction between H_2O and BC_7N_2 (including van der Waals interactions, **Figure 4.15a** on 1a, 1b, 1c and 1d chemically ordered states of BC_7N_2 (**Figure 4.15**). These configurations are obtained by considering different sites of adsorption of H_2O (above the atoms (B, C and N), and above the centre of hexagonal rings), with the water molecule oriented parallel to the BC_7N_2 plane, at a distance of 1.4 Å. We find that their adsorption energies lie in the range of 11-28 kJ mol^{-1} (**Figure 4.15c)**. The weakest adsorption occurs when H_2O interacts with N site of 1a state, and it is the strongest at the centre of hexagonal rings for 1a and 1b states. Moreover, the electric dipoles of H_2O and the N–B–N structural motifs of 1a configuration couple with each other and with the external electric field, an aspect of relevance to the electrocatalytic properties. While all the four chemically ordered states of BC_7N_2 are comparable in their electronic properties, our results indicate that 1a may be more optimal for electrocatalysis in HER. Thus, of the four configurations, Ia, where both N atoms are bonded to B atoms, is the best candidate as an electrocatalyst for hydrogen generation. We also include a comparative analysis of the electronic structure of $B_2C_5N_3$ containing carbon nitride rings, and BC_7N_2 with assessment of their activity towards HER (**Figure 4.16**). Electronic DOS of $B_2C_5N_3$ and BC_7N_2 are qualitatively similar, but with a lower overpotential of the former for HER, with the conduction band edge above the HER by ~0.25 eV. $B_2C_5N_3$ with CN-rings is indeed suitable for the catalysis of HER and water splitting (**Figure 4.16 bottom**), However, a comparison of the energies of $B_2C_5N_3$, $B_2C_6N_2$ and BC_6N_2 relative to graphene, boronitride and BC_7N_2 shows that the two structures are energetically not favorable, with $B_2C_5N_3$ less stable than $B_2C_6N_2$. The BCN containing carbon-nitride rings is energetically less favorable than BC_7N_2. The BCN containing carbon-nitride rings is energetically less favorable than BC_7N_2.

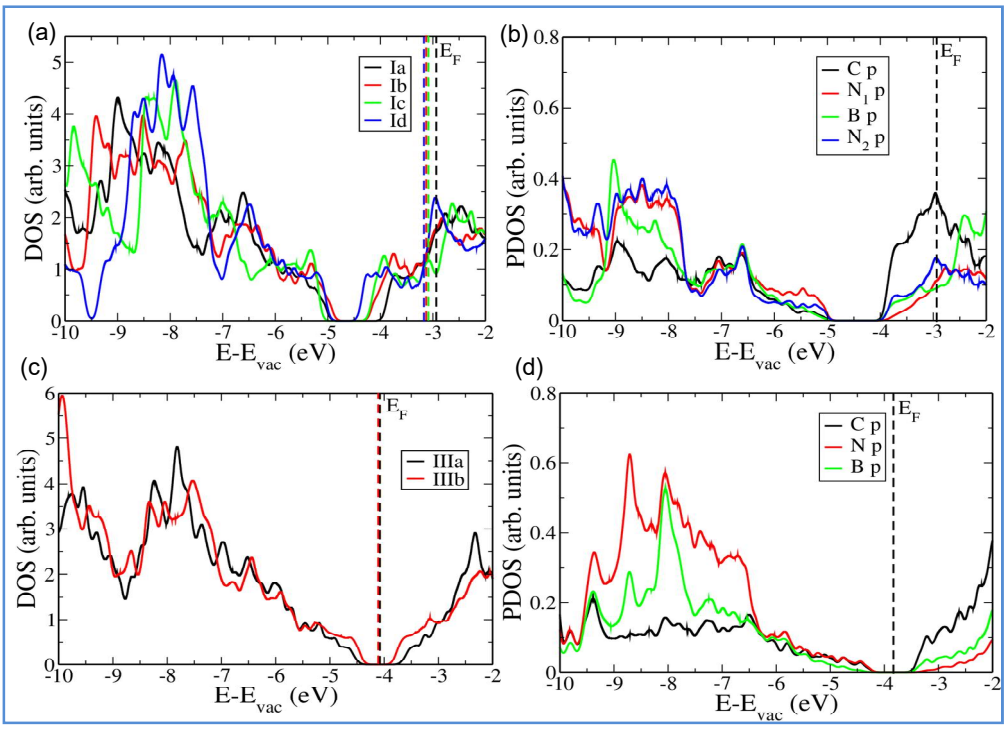

Figure 4.13: (a) DOS for four configurations of BC_7N_2 (I), (b) PDOS of its first configuration (Ia), (c) DOS for two configurations of BC_8N (III) and (d) PDOS of $B_2C_2N_2$ (II). See Figure 12 for different configurations.

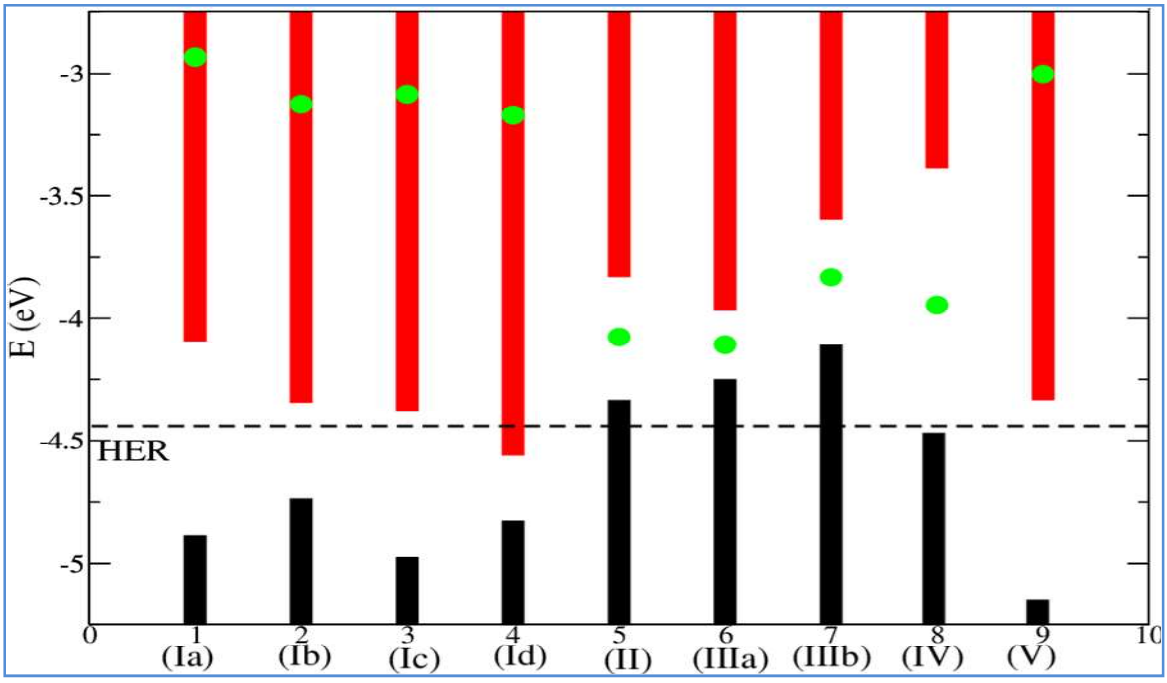

Figure 4.14: Bandgaps and valence (black) and conduction (red) band edge positions of the different configurations. The energy level for hydrogen evolution reaction (HER) is denoted by a dotted line and their Fermi energies by green circles. Here, IV and V refer to $B_2C_6N_2$ and $B_2C_5N_3$ (see Figure 12 for configurations).

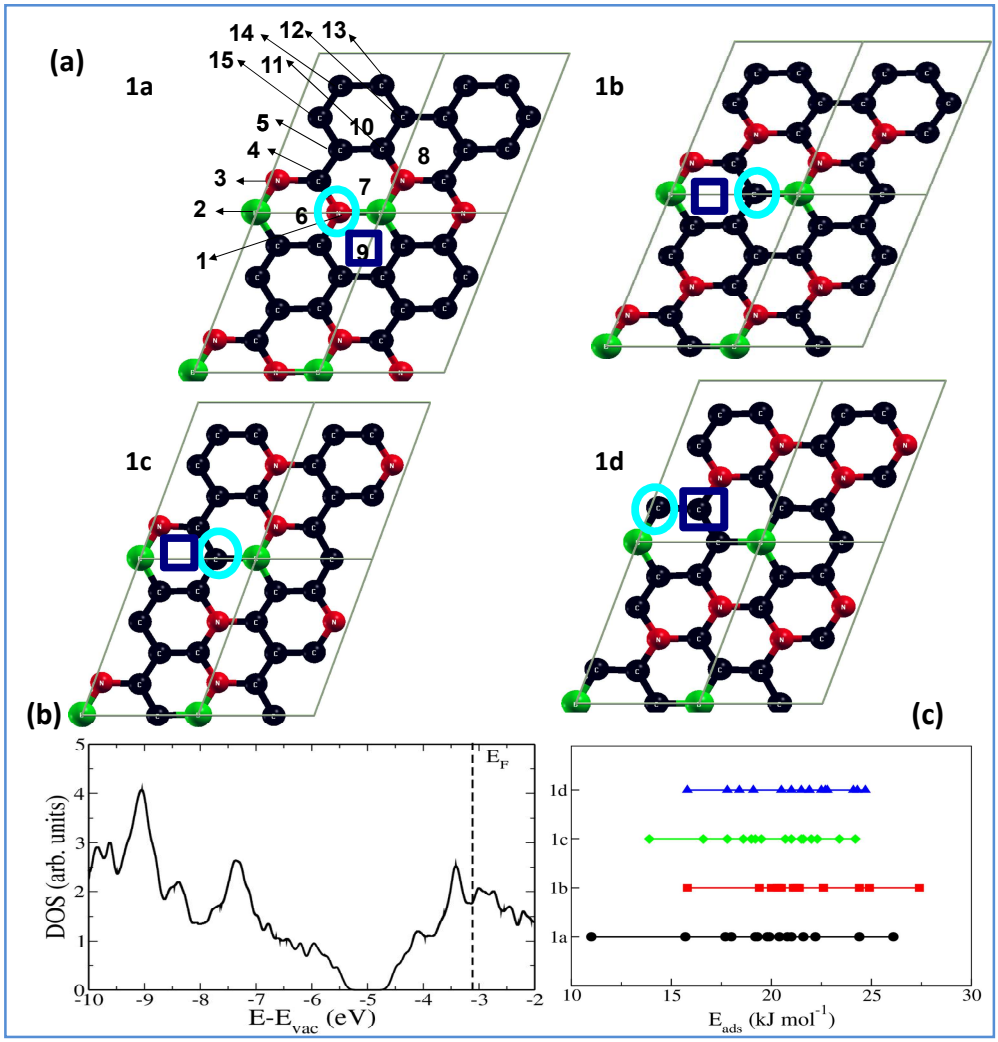

Figure 4.15: (a) Different absorption sites of H_2O molecule in 1a (same for 1b, 1c and 1d configurations). The weakest and strongest absorption sites are marked by circles and squares respectively. (b) DOS of C_8N_2. (c) Comparison of the absorption energies at different adsorption sites for 1a—1d configurations of BC_7N_2.

From the theoretical analysis we find that the substitution of B and N at equal concentration opens up a gap with valence band unfavorably located (above) relative to the HER potential. Substitution of excess N results in the population of the conduction bands with electrons shifts the valence and conduction bands to lower energy, and hence favour the alignment of bands to facilitate electrocatalysis for HER. Therefore, out of the four configurations, Ia is the best candidate as an electrocatalyst for hydrogen generation.

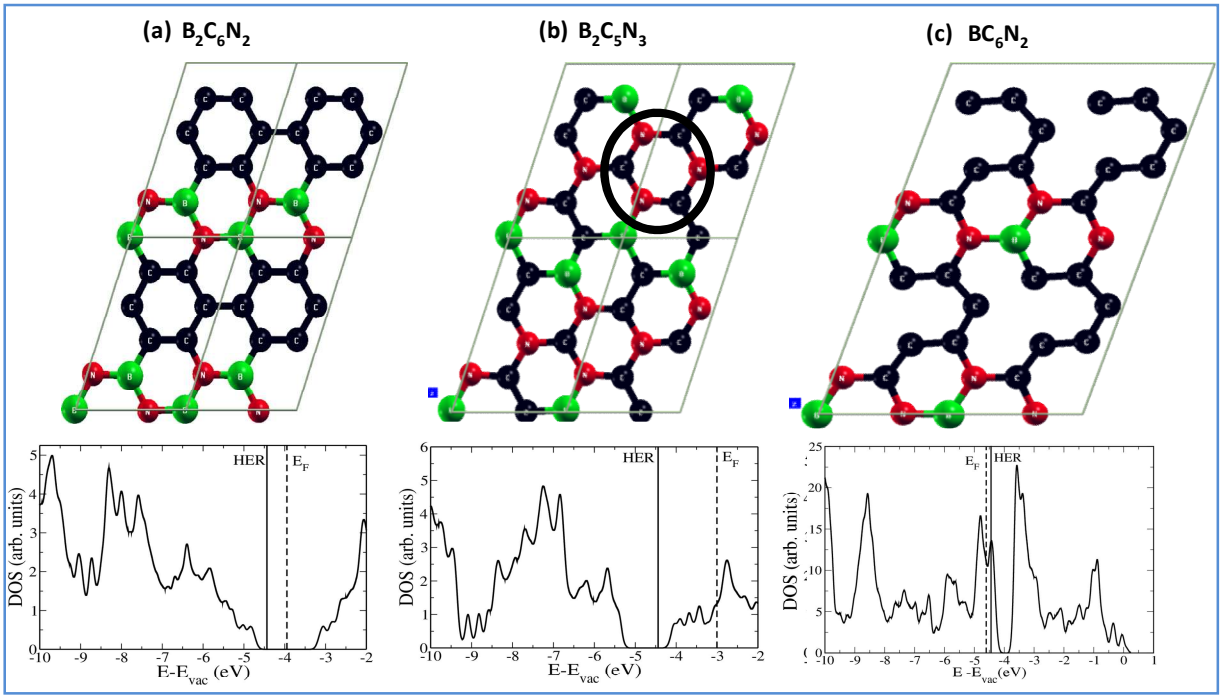

Figure 4.16: Schematic of (a) $B_2C_6N_2$, (b) $B_2C_5N_3$ (C-N ring is marked by black circle) and (c) BC_6N_2 and their corresponding DOS.

In summary we have reported for the first time the efficacy of BCNs as electrochemical HER catalysts. It is noteworthy that the carbon rich BCN shows enhanced HER activity in comparison to other compositions. The lower onset potential, higher current density and the stability makes BC_7N_2 as a competitive catalysts comparable to many state of art metal based catalysts and better than metal-free electrocatalysts. The best performing composition of BCN consist of a larger proportion of pyridinic than pyrollic nitrogens and a high percentage of B–C bonds, the low proportion of BN bonds also contributing to higher conductivity. The theoretical studies shows that excess N results in the population of the conduction bands with electrons and thus shifts the valence and conduction bands to lower energy favouring electrocatalysis.

Part B:

Nanocomposites of $B_xC_yN_z$ with other 2D materials for improved Hydrogen evolution activity

Nanocomposites of $B_xC_yN_z$ with other 2D materials for enhanced HER activity (in collaboration with Dr. Pramoda and Dr. Uttam, JNCASR)

For practical applications, high current density at minimum over overpotential is a crucial factor to judge an electrocatalyst. Therefore, tafel slopes and η@10mA/cm^2 or η@20mA/cm^2 are very important parameters. Even though the doped carbon based catalysts have shown onset overpotential very close to that of state-of-art catalysts, including Pt/C, their higher tafel slopes impede their practical applicability. Various strategies have been employed to overcome this by combining two active catalysts in the form of composites.[10]

An appropriate combination of active 2D electrocatalysts can enhance the HER activity by synergistic effects[87-88], but a mere composite mixture would not be fruitful. A meticulous effort has to be put in order to reinforce a good connectivity for efficient charge transfer between them[89-90]. Such composites can be prepared by hydrothermal or solid state routes showing enhanced activity. For example, Zheng at al.[10] reported metal-free C_3N_4@NG hybrid form robust highly efficient metal-free electrocatalyst for HER which is also shown by DFT calculations. Hou et al.[87] found that g-C_3N_4 and MoS_2 form interfacial nanojunctions with improved charge separations and activity in hydrogen generation. In order to bring an appreciable improvement in catalytic activity based on more than one 2D structures, covalently cross-linked hetero layers of 2D materials have been employed by us. This not only improves the chemical connectivity and interaction between the heterolayers, but also increases the porosity and surface area to give rise to better HER activity. EDC coupling reaction has been used to achieve such heterostructures after appropriately functionalizing the individual layers (MoS_2, C_3N_4 and BC_7N) with relevant groups (amine and carboxylic groups) to facilitate the reaction (**Figure 4.17**). The surface concentrations of the –NH_2 and -COOH groups were calculated by FLOSS technique as mentioned in earlier experimental section. The BC_7N with the amino (1.7×10^{19} groups/g) and carboxylic groups (8×10^{20} groups/g) and MoS_2 with carboxylic group (1.34×10^{18} groups/g) could be transformed to MoS_2-BC_7N composites leading to onset overpotential as low as 30 mV (**Figure 4.17b1**). Theoretical studies show that increased planarity, enhanced charge transfer (through space as well as bonds) and higher surface area gives rise to higher activity.

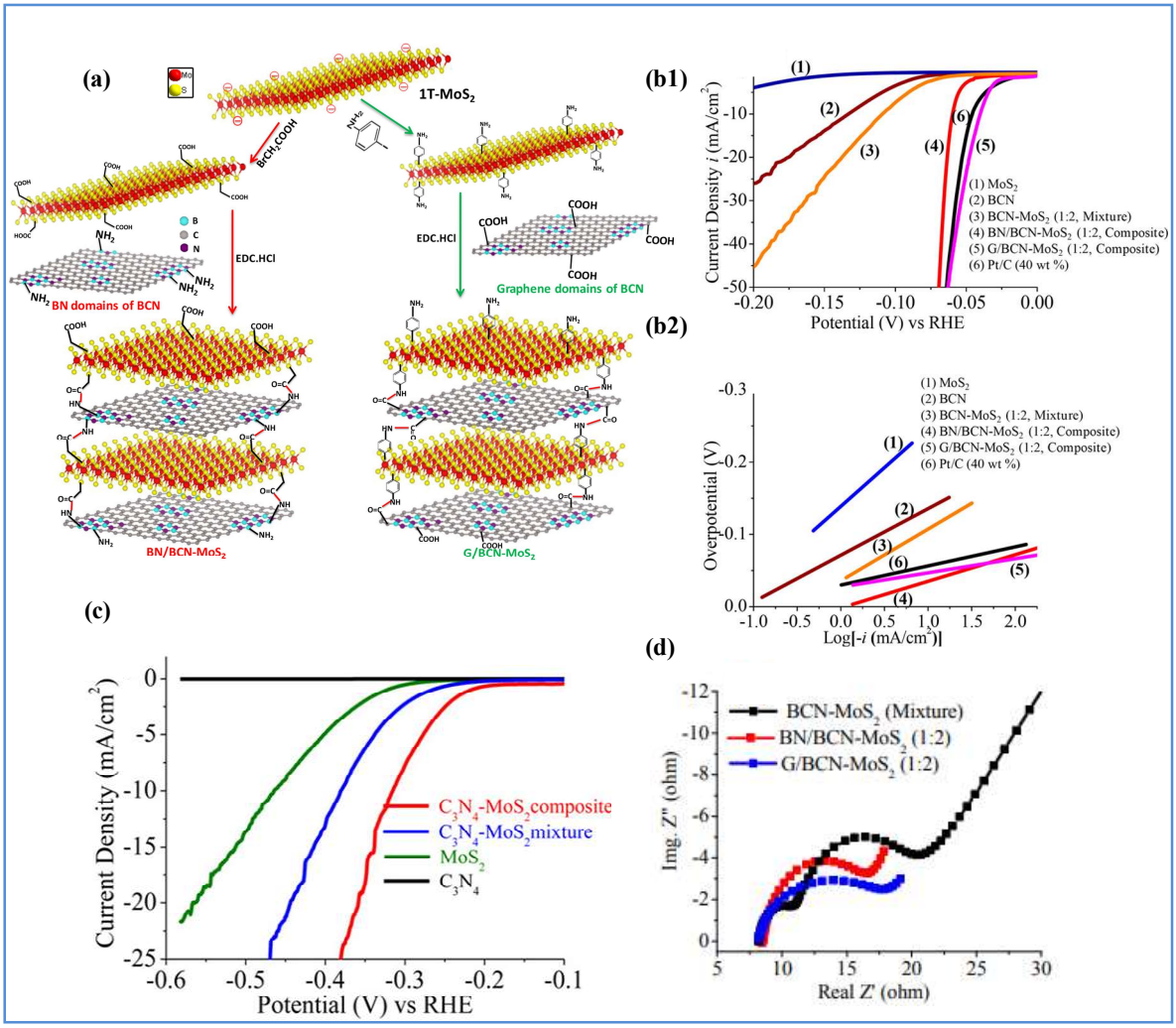

Figure 4.17: (a) Illustration of covalently cross-linking between two different 2D materials BN/BCN–MoS_2 and G/BCN–MoS_2 (by EDC coupling). (b) Electrocatalytic Hydrogen evolution activity comparison: (b1) LSV curves and (b2) tafel plots of various nanocomposites made by this strategyin comparison with Pt/C (40 wt%). (c) LSV polarization curves to test the eletrocatalytic HER activity of C_3N_4, MoS_2, physical mixture of C_3N_4 and NRGO, and covalently cross linked C_3N_4–MoS_2 nanocomposites. (d) Nyquist plot at the onset potential for the comparison of charge transfer resistance in various ratios of BCN-MoS_2 nanocomposites.

BCNs are versatile materials with its potential and demonstrated uses in various applications like supercapacitors, Sensors and other electrocatalytical processes like ORR and HER as discussed in earlier sections. Due to the feasible tunability of bandgap of BCN, they can have potential applications in photocatalytic applications. For example, BCNs also exhibits good H_2 generation photocatalytically from water and sacrificial agent mixtures without any metal co-catalyst in the presence of visible light and UV illumination. Liu et al.[91] showed different activities of $B_{4.3}C$ and $B_{13}C_2$ for H_2 production. Under visible light, the H_2 production of $B_{4.3}C$ showed 3 times increment than that for $B_{13}C_2$ (study done without co-catalysts in water–

methanol solution). Also, Huang et al.[92] found that the ternary alloys of B–C–N are active photocatalysts under visible light for H_2 generation. It is noteworthy that apart from composition control, introduction of porous nanostructures on heteroatom doped carbon materials can also enhance HER activity. It results into more exposed active sites and better permeability and mass diffusion of electrolytes and the evolved bubbles. These porous architectures have been obtained by cross linking two similar or different 2D materials. For instance, covalent cross linking of BCN, MoS_2 and C_3N_4 have been obtained by us by appropriate coupling reactions after functionalizing their surfaces with suitable groups (see experimental section). Covalently cross linked C_3N_4 and MoS_2 gives excellent photochemical hydrogen generation activity (12778 $\mu molh^{-1}g^{-1}$ and a TOF of 2.35 h^{-1}) with an onset overpotential of 230 mV. The strategy of employing heterostructures yields 246 times increased photochemical H_2 evolution activity compared to individual layers and 11 to 68 times higher activity than composites made by hydrothermal and physically mixing. C_3N_4 has a band gap of ca.2.7 eV with the electron conductivity less than MoS_2 and BCN. While appropriate band alignment renders BCN and MoS_2 as electrochemical HER catalysts, C_3N_4 exhibits poor HER activity. Hence covalently cross-linked heterstructures of BCN-MoS_2 show better HER performance than C_3N_4-MoS_2. The photoexcited e^- transfer at 440 nm between the cross-linked layers of C_3N_4 is considerably quenched due to charge transfer (CT) as evident from Photoluminescence (PL) studies and DFT calculations where the CT occurs via space and bonds in cross-linked composites implying the importance of covalent cross linking. On the other hand, extending the cross linking concept to two HER active 2D materials would further enhance the photochemical as well as electrochemical activity. As a proof of concept, BCN-MoS_2 cross linked nanocomposites have been studied. For instance, a relatively lower active 2H phase of MoS_2, can be made highly active upon cross-linking with BCN. BCN exhibits fairly good activity of 136 $\mu molh^{-1}g^{-1}$. Simple mixture of BCN and MoS_2 improves the photochemical HER activity by 2 times, while the cross-linked composites [BN/BCN−MoS_2 (1:2) and G/BCN−MoS_2 (1:2)] shows 5 times increment with respect to MoS_2 (**Figure 4.18**). The catalytic activity of the MoS_2 is enhanced by cross linking it to carbon rich BCN acting as electron transfer channels to active sites in the network. The detailed study of electrochemical HER activity of these composites is

listed in **Table 8** along with the comparative study with other heterostructures in **Table 9**. This has been confirmed by the photochemical results obtained on BN–MoS_2 nanocomposites (absence of carbon rich channel), which show negligible activity (**Figure 4.16**).

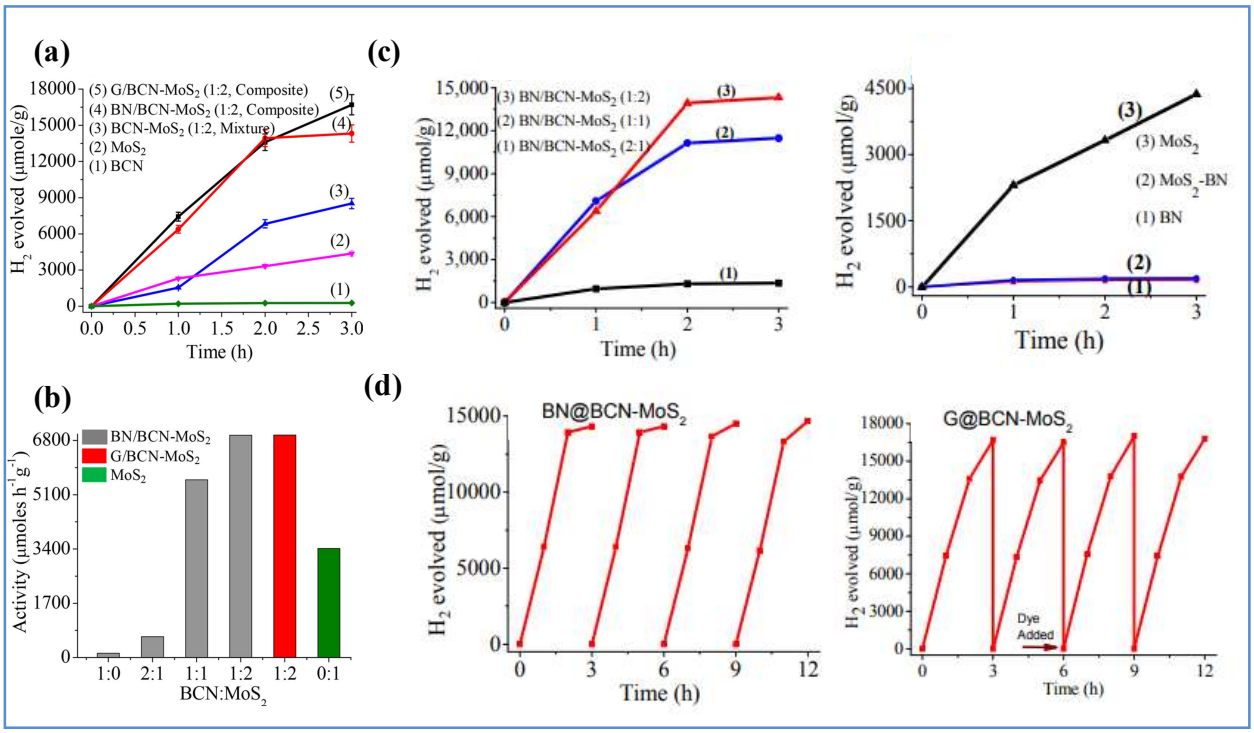

Figure 4.16: Photochemical hydrogen generation activity comparison of (a) various ratios of BCN–MoS_2 and the corresponding bar diagram showing the increase in HER activity with the increase in MoS_2 content (b). (c) Comparison of the photochemical HER activity and (d) Cycling studies of various BCN-MoS_2 assemblies of different ratios.

Table 8: Electrochemical performance comparison of BN@BCN-MoS_2, G@BCN-MoS_2 nanocomposites and Pt/C.

Sample	Onset (mV) vs. RHE	η@10 $mAcm^{-2}$ (mV) vs. RHE	Tafel slope (mV/dec)
MoS_2	-180	-260	106
BCN	-80	-130	62
1:2 mixture[a]	-60	-110	71
2:1 Composite[b]	-60	-90	58
1:1 Composite[b]	-50	-60	46
1:2 Composite[b]	-50	-60	36
1:2 Composite[c]	-30	-35	33
Pt/C (40 wt%)	-20	-40	29

a= physical mixture; b= covalently cross linked composite of BN@BCN-MoS_2; c= covalently cross linked composite of G@BCN-MoS_2

Table 9: Comparison of electrochemical HER performance of cross-linked BN@BCN-MoS_2 and G@BCN-MoS_2 with the MoS_2-carbon based nanocomposites

Catalyst	Onset[a]	η@10 $mAcm^{-2}$ [a]	Tafel slope[b]
G@BCN-MoS_2 (1:2)	-30	-35	33
BN@BCN-MoS_2(1:2)	-50	-60	36
RGO supported MoS_2[96]	-105	-150	41
MoS_2-RGO[97]	-75	-104	63
MoS_2 QDs-RGO[98]	-100	-150	101
MoS_2 -Carbon[99]	-80	-85	40
MoS_2-Carbon cloth[100]	-100	-165	50
MoS_2-N doped GAs[101]	-236	-261[(b)]	230
MoS_2-Carbon[102]	-140	-190	59
MoS_2-C_3N_4[28]	-236	-320	95

a= in mV vs RHE; b= mV/dec; QDs= quantum dots; Gas=graphen aerogels;

7. Conclusions and Outlook:

In this work we have successfully demonstrated the efficacy of borocarbonitride sheets as excellent low-cost, metal-free catalysts for hydrogen generation. This is the first report on the use of BCNs as HER catalysts. Amongst all the BCN samples, carbon-rich BCN-1 shows the best activity with a performance superior to that of other non-precious metal electrocatalysts. The onset potential of-0.28 V (vs. Ag/AgCl) is close to that of Pt (-0.23 V). BCN-1 also exhibits stability up to 24 hours requiring an overpotential of -0.32 V (vs. Ag/AgCl) to produce a current density of 20 $mAcm^{-2}$. It is noteworthy that BCN-1 contains a larger proportion of pyridinic than pyrollic nitrogens and a high percentage of B–C bonds, the low proportion of BN bonds also contributing to higher conductivity. Our theoretical studies show that substitution of B and N at equal concentrations opens up a gap, with the valence band unfavourably located relative to the HER potential. Substitution of excess N results in the population of the conduction bands with electrons shifts the valence and conduction bands to lower energy and favors the alignment of bands to facilitate electrocatalysis. We believe that with compositional and morphological modifications, the electrochemical activity of BCNs can be further improved.

Furthermore, Borocarbonitrides have emerged to be useful materials in energy related applications. They have already been used in supercapacitors and ORR in fuel cells. To our knowledge no other non-metallic material has shown electrochemical characteristics related to HER close to Pt as the BCNs. There is much to be done yet to effect the practical applications. Furthermore the exact nature of the borocarbonitrides materials throughout the substance (in terms of of BN, CN, BCN domains and the presence of defects) is yet to be unravalled. BCNs with high charge carrier mobility which could promote efficient light harvesting. High electrical conductivity as well as high can indeed favor BCNs as photoelectrode. However the limitation posed by photoelectrode fabrication may restrict their use. A reliable method to fabricate a firmly adhered catalyst on the substrate which can retain its activity over large number of cycles in electrolyzers is thus, an absolute requirement. Since BCN has a tunable band gap, coupling electrochemical and photochemical activity might reduce the input energy for hydrogen production thus making the process economical. It may be fruitful to examine the van der Waals heterostructures formed by BCN layers with other 2D materials. The success achieved with covalently linked heterostructures is noteworthy in this regard. The ease with which the compositions of BCN can be varied to cause changes in various properties is indeed noteworthy. A novel strategy would be to prepare heterostructures by employing supramolecular means of linking layers.

8. References:

[1] J. K. Nørskov, T. Bligaard, J. Rossmeisl, C. H. Christensen, Nat. Chem. 2009, 1, 37.
[2] E. J. Popczun, J. R. McKone, C. G. Read, A. J. Biacchi, A. M. Wiltrout, N. S. Lewis, R. E. Schaak, J. Am. Chem. Soc. 2013, 135, 9267.
[3] M. Wang, L. Chen, L. Sun, Ener. Environ. Sci. 2012, 5, 6763.
[4] C. Fan, D. L. Piron, A. Sleb, P. Paradis, J. Electrochem. Soc. 1994, 141, 382.
[5] Q. Lu, G. S. Hutchings, W. Yu, Y. Zhou, R. V. Forest, R. Tao, J. Rosen, B. T. Yonemoto, Z. Cao, H. Zheng, J. Q. Xiao, F. Jiao, J. G. Chen, Nat. Commun. 2015, 6, 6567.
[6] Y. Jia, Y. Jiang, J. Zhang, L. Zhang, Q. Chen, Z. Xie, L. Zheng, J. Am. Chem. Soc. 2014, 136, 3748.
[7] B. Konkena, J. Masa, W. Xia, M. Muhler, W. Schuhmann, Nano Energy 2016, 29, 46.
[8] S. S. Shinde, A. Sami, J.-H. Lee, ChemCatChem 2015, 7, 3873.
[9] Y. Ito, W. Cong, T. Fujita, Z. Tang, M. Chen, Angew. Chem. Int. Ed. 2015, 54, 2131.
[10] Y. Zheng, Y. Jiao, Y. Zhu, L. H. Li, Y. Han, Y. Chen, A. Du, M. Jaroniec, S. Z. Qiao, Nat. Commun. 2014, 5, 3783.
[11] Q. Han, Z. Cheng, J. Gao, Y. Zhao, Z. Zhang, L. Dai, L. Qu, Adv. Funct. Mater. 2017, 27, 1606352.

[12] J. Duan, S. Chen, M. Jaroniec, S. Z. Qiao, ACS Nano 2015, 9, 931.
[13] V. Di Noto, E. Negro, S. Polizzi, K. Vezzù, L. Toniolo, G. Cavinato, Int. J. Hydrog. Energy 2014, 39, 2812.
[14] V. Di Noto, E. Negro, S. Polizzi, F. Agresti, G. A. Giffin, ChemSusChem 2012, 5, 2451.
[15] Y.-J. Tang, M.-R. Gao, C.-H. Liu, S.-L. Li, H.-L. Jiang, Y.-Q. Lan, M. Han, S.-H. Yu, Angew. Chem. Int. Ed. 2015, 54, 12928.
[16] X. Liu, W. Liu, M. Ko, M. Park, M. G. Kim, P. Oh, S. Chae, S. Park, A. Casimir, G. Wu, J. Cho, Adv. Funct. Mater. 2015, 25, 5799.
[17] D. Voiry, H. Yamaguchi, J. Li, R. Silva, D. C. B. Alves, T. Fujita, M. Chen, T. Asefa, V. B. Shenoy, G. Eda, M. Chhowalla, Nat. Mater. 2013, 12, 850.
[18] D. Voiry, A. Mohite, M. Chhowalla, Chem. Soc. Rev. 2015, 44, 2702.
[19] W.-F. Chen, S. Iyer, S. Iyer, K. Sasaki, C.-H. Wang, Y. Zhu, J. T. Muckerman, E. Fujita, Ener. Environ. Sci. 2013, 6, 1818.
[20] J.-S. Li, Y. Wang, C.-H. Liu, S.-L. Li, Y.-G. Wang, L.-Z. Dong, Z.-H. Dai, Y.-F. Li, Y.-Q. Lan, Nat. Commun. 2016, 7, 11204.
[21] X. Chen, G. Liu, W. Zheng, W. Feng, W. Cao, W. Hu, P. Hu, Adv. Funct. Mater. 2016, 26, 8537.
[22] E. J. Popczun, C. G. Read, C. W. Roske, N. S. Lewis, R. E. Schaak, Angew. Chem. Int. Ed. 2014, 53, 5427.
[23] Q. Fu, L. Yang, W. Wang, A. Han, J. Huang, P. Du, Z. Fan, J. Zhang, B. Xiang, Adv. Mater. 2015, 27, 4732.
[24] C. L. Hedegaard, E. C. Collin, C. Redondo-Gómez, L. T. H. Nguyen, K. W. Ng, A. A. Castrejón-Pita, J. R. Castrejón-Pita, A. Mata, Adv. Funct. Mater. 2018, 28, 1703716.
[25] H. Li, C. Tsai, A. L. Koh, L. Cai, A. W. Contryman, A. H. Fragapane, J. Zhao, H. S. Han, H. C. Manoharan, F. Abild-Pedersen, J. K. Nørskov, X. Zheng, Nat. Mater. 2015, 15, 48.
[26] H. Li, M. Du, M. J. Mleczko, A. L. Koh, Y. Nishi, E. Pop, A. J. Bard, X. Zheng, J. Am. Chem. Soc. 2016, 138, 5123.
[27] W. Zhou, J. Jia, J. Lu, L. Yang, D. Hou, G. Li, S. Chen, Nano Energy 2016, 28, 29.
[28] Y. Li, H. Wang, L. Xie, Y. Liang, G. Hong, H. Dai, J. Am. Chem. Soc. 2011, 133, 7296.
[29] N. S. Alhajri, D. H. Anjum, K. Takanabe, J. Mater. Chem. A 2014, 2, 10548.
[30] Z. Zhang, W. Li, M. F. Yuen, T.-W. Ng, Y. Tang, C.-S. Lee, X. Chen, W. Zhang, Nano Energy 2015, 18, 196.
[31] Y. Guo, X. Zhang, X. Zhang, T. You, J. Mater. Chem. A 2015, 3, 15927.
[32] S. Shi, D. Gao, B. Xia, P. Liu, D. Xue, J. Mater. Chem. A 2015, 3, 24414.
[33] J. Guo, F. Li, Y. Sun, X. Zhang, L. Tang, J. Power Sources 2015, 291, 195.
[34] X. Ren, Q. Ma, H. Fan, L. Pang, Y. Zhang, Y. Yao, X. Ren, S. Liu, Chem. Comm. 2015, 51, 15997.
[35] H. Zhang, Y. Li, T. Xu, J. Wang, Z. Huo, P. Wan, X. Sun, J. Mater. Chem. A 2015, 3, 15020.
[36] L. Ma, L. Xu, X. Xu, X. Zhou, J. Luo, L. Zhang, Mater. Sci. Eng. B 2016, 212, 30.
[37] Y. Li, H. Wang, L. Xie, Y. Liang, G. Hong, H. Dai, J. Am. Chem. Soc. 2011, 133, 7296.
[38] R. Wu, J. Zhang, Y. Shi, D. Liu, B. Zhang, J. Am. Chem. Soc. 2015, 137, 6983.
[39] X. Xie, R. Yu, N. Xue, A. B. Yousaf, H. Du, K. Liang, N. Jiang, A.-W. Xu, J. Mater. Chem. A 2016, 4, 1647.
[40] X. Liu, W. Zhou, L. Yang, L. Li, Z. Zhang, Y. Ke, S. Chen, J. Mater. Chem. A 2015, 3, 8840.
[41] X. Liu, M. Zhang, D. Yu, T. Li, M. Wan, H. Zhu, M. Du, J. Yao, Electrochim. Acta 2016, 215, 223.
[42] W. Zhou, Y. Zhou, L. Yang, J. Huang, Y. Ke, K. Zhou, L. Li, S. Chen, J. Mater. Chem. A 2015, 3, 1915.
[43] Y. Liu, H. Yu, X. Quan, S. Chen, H. Zhao, Y. Zhang, Sci. Rep. 2014, 4, 6843.
[44] L. Wei, H. E. Karahan, K. Goh, W. Jiang, D. Yu, Ö. Birer, R. Jiang, Y. Chen, J. Mater. Chem. A 2015, 3, 7210.

[45] Y. Zhao, F. Zhao, X. Wang, C. Xu, Z. Zhang, G. Shi, L. Qu, Angew. Chem. Int. Ed. 2014, 53, 13934.
[46] Y. Zheng, Y. Jiao, L. H. Li, T. Xing, Y. Chen, M. Jaroniec, S. Z. Qiao, ACS Nano 2014, 8, 5290.
[47] S. S. Shinde, A. Sami, J.-H. Lee, J. Mater. Chem. A 2015, 3, 12810.
[48] H. Fei, J. Dong, M. J. Arellano-Jiménez, G. Ye, N. Dong Kim, E. L. G. Samuel, Z. Peng, Z. Zhu, F. Qin, J. Bao, M. J. Yacaman, P. M. Ajayan, D. Chen, J. M. Tour, Nat. Commun. 2015, 6, 8668.
[49] K. Gong, F. Du, Z. Xia, M. Durstock, L. Dai, Science 2009, 323, 760.
[50] S. Sen, K. Moses, A. J. Bhattacharyya, C. N. R. Rao, Chem – Asian J. 2014, 9, 100.
[51] K. Raidongia, A. Nag, K. P. S. S. Hembram, U. V. Waghmare, R. Datta, C. N. R. Rao, Chem. – Eur. J. 2010, 16, 149.
[52] N. Kumar, K. Moses, K. Pramoda, S. N. Shirodkar, A. K. Mishra, U. V. Waghmare, A. Sundaresan, C. N. R. Rao, J. Mater. Chem. A 2013, 1, 5806.
[53] Y. Xing, E. Borguet, Langmuir 2007, 23, 684.
[54] B. Gong, B.-K. Choi, J.-Y. Kim, D. Shetty, Y. H. Ko, N. Selvapalam, N. K. Lee, K. Kim, J. Am. Chem. Soc. 2015, 137, 8908.
[55] Allen J bard, Larry Faulkner, Fundamentals of Electrochemistry- Methods and Applications. 2nd edition, Wiley, 2000.
[56] C. G. Morales-Guio, L.-A. Stern, X. Hu, Chem. Soc. Rev. 2014, 43, 6555.
[57] B. E. Conway, B. V. Tilak, Electrochim. Acta 2002, 47, 3571.
[58] Q. Li, Z. Xing, A. M. Asiri, P. Jiang, X. Sun, Int. J. Hydrog. Energy 2014, 39, 16806.
[59] G. Paolo, B. Stefano, B. Nicola, C. Matteo, C. Roberto, C. a. c. Carlo, M. W. Renata, J. Phys: Condens Matter 2009, 21, 395502.
[60] J. P. Perdew, K. Burke, M. Ernzerhof, Phys. Rev. Lett. 1996, 77, 3865.
[61] D. Vanderbilt, Phys. Rev. B 1990, 41, 7892.
[62] M. Kota, N. S. Sharmila, U. V. Waghmare, C. N. R. Rao, Mater. Res. Express 2014, 1, 025603.
[63] C. N. R. Rao, K. Gopalakrishnan, ACS Appl. Mater. Interfaces 2017, 9, 19478.
[64] N. Kumar, K. S. Subrahmanyam, P. Chaturbedy, K. Raidongia, A. Govindaraj, K. P. S. S. Hembram, A. K. Mishra, U. V. Waghmare, C. N. R. Rao, ChemSusChem 2011, 4, 1662.
[65] S. Bhat, P. Sasikumar, L. Molina-Luna, M. Graczyk-Zajac, H.-J. Kleebe, R. Riedel, C 2016, 2, 9.
[66] K. Pramoda, K. Moses, U. Maitra, C. N. R. Rao, Electroanalysis 2015, 27, 1892.
[67] R. Kumar, K. Gopalakrishnan, I. Ahmad, C. N. R. Rao, Adv. Funct. Mater. 2015, 25, 5910.
[68] M. B. Sreedhara, K. Gopalakrishnan, B. Bharath, R. Kumar, G. U. Kulkarni, C. N. R. Rao, Chem. Phys. Lett. 2016, 657, 124.
[69] R. Nascimento, J. d. R. Martins, R. J. C. Batista, H. Chacham, J. Phys. Chem. C 2015, 119, 5055.
[70] S. Banerjee, S. K. Pati, Nanoscale 2014, 6, 13430.
[71] R. P. J. T. P. Kaloni, N. P. Adhikari, and U. Schwingenschlögl, Appl. Phys. Lett. 2014, 104, 073116.
[72] P. Rani, V. K. Jindal, Appl. Nanosci. 2014, 4, 989.
[73] X. Fan, Z. Shen, A. Q. Liu, J.-L. Kuo, Nanoscale 2012, 4, 2157.
[74] R.-S. Zhong, Y.-H. Qin, D.-F. Niu, J.-W. Tian, X.-S. Zhang, X.-G. Zhou, S.-G. Sun, W.-K. Yuan, J. Power Sources 2013, 225, 192.
[75] M. Barua, M. B. Sreedhara, K. Pramoda, C. N. R. Rao, Chem. Phys. Lett. 2017, 683, 459.
[76] J. Zhang, L. Dai, Angew. Chem. Int. Ed. 2016, 55, 13296.
[77] P. Rani, V. K. Jindal, RSC Adv. 2013, 3, 802.
[78] S. Wang, L. Zhang, Z. Xia, A. Roy, D. W. Chang, J.-B. Baek, L. Dai, Angew. Chem. Int. Ed. 2012, 51, 4209.
[79] S. Hou, X. Cai, H. Wu, X. Yu, M. Peng, K. Yan, D. Zou, Ener. Environ. Sci. 2013, 6, 3356.
[80] Y. Xue, J. Liu, H. Chen, R. Wang, D. Li, J. Qu, L. Dai, Angew. Chem. Int. Ed. 2012, 51, 12124.
[81] C. Yu, H. Fang, Z. Liu, H. Hu, X. Meng, J. Qiu, Nano Energy 2016, 25, 184.
[82] C. H. Choi, S. H. Park, S. I. Woo, ACS Nano 2012, 6, 7084

[83] K. Gong, F. Du, Z. Xia, M. Durstock, L. Dai, Science 2009, 323, 760.
[84] L. Wang, A. Ambrosi, M. Pumera, Angew. Chem. Int. Ed. 2013, 52, 13818.
[85] L. Wang, M. Pumera, Chem. Comm. 2014, 50, 12662.
[86] C. E. Banks, A. Crossley, C. Salter, S. J. Wilkins, R. G. Compton, Angew. Chem. Int. Ed. 2006, 45, 2533.
[87] Y. Hou, A. B. Laursen, J. Zhang, G. Zhang, Y. Zhu, X. Wang, S. Dahl, I. Chorkendorff, Angew. Chem. Int. Ed. 2013, 52, 3621.
[88] Y. Hou, Z. Wen, S. Cui, X. Guo, J. Chen, Adv. Mater. 2013, 25, 6291.
[89] U. Maitra, U. Gupta, M. De, R. Datta, A. Govindaraj, C. N. R. Rao, Angew. Chem. Int. Ed. 2013, 52, 13057.
[90] D. Chen, W. Chen, L. Ma, G. Ji, K. Chang, J. Y. Lee, Mater. Today 2014, 17, 184.
[91] J. Liu, S. Wen, Y. Hou, F. Zuo, G. J. O. Beran, P. Feng, Angew. Chem. Int. Ed. 2013, 52, 3241.
[92] C. Huang, C. Chen, M. Zhang, L. Lin, X. Ye, S. Lin, M. Antonietti, X. Wang, Nat. Commun. 2015, 6, 7698.
[93] Y. Hou, B. Zhang, Z. Wen, S. Cui, X. Guo, Z. He, J. Chen, J. Mater. Chem. A 2014, 2, 13795.
[94] X. Huang, Y. Zhao, Z. Ao, G. Wang, Sci. Rep. 2014, 4, 7557.
[95] U. Sim, T.-Y. Yang, J. Moon, J. An, J. Hwang, J.-H. Seo, J. Lee, K. Y. Kim, J. Lee, S. Han, B. H. Hong, K. T. Nam, Energy Environ. Sci. 2013, 6, 3658.
[96] Y. Zhao, L. Kuai, Y. Liu, P. Wang, H. Arandiyan, S. Cao, J. Zhang, F. Li, Q. Wang, B. Geng, H. Sun, Sci. Rep. 2015, 5, 8722.
[97] A. A. Jeffrey, S. R. Rao, M. Rajamathi, Carbon 2017, 112, 8.
[98] K. Yuan, Y. Xu, J. Uihlein, G. Brunklaus, L. Shi, R. Heiderhoff, M. Que, M. Forster, T. Chassé, T. Pichler, T. Riedl, Y. Chen, U. Scherf, Adv. Mater. 2015, 27, 6714.
[99] C. N. R. Rao, K. Pramoda, R. Kumar, Chem. Commun. 2017, 53, 10093.
[100] K. Pramoda, U. Gupta, I. Ahmad, R. Kumar, C. N. R. Rao, J. Mater. Chem. A 2016, 4, 8989.
[101] M. Chatti, T. Gengenbach, R. King, L. Spiccia, A. Simonov, Chem. Mater. 2017, 29, 3092.
[102] T. P. Nguyen, S. Choi, J. M. Jeon, K. C. Kwon, H. W. Jang, S. Y. Kim, J. Phys. Chem. C 2016, 120, 3929.

Chapter-5

Remarkable Electrocatalytic HER Activity exhibited by the Ni/Ni(OH)$_2$/graphite Electrode

Remarkable Electrocatalytic HER Activity exhibited by the $Ni/Ni(OH)_2$/graphite Electrode

Summary*

The successful utilization of solar energy to economically produce green fuel should involve facile and inexpensive means for electrolysis of water. To do so, it is necessary to replace the platinum catalyst with an in situ electrode fabrication process involving active catalyst with readily available materials. Electrochemical dual-pulse plating with sequential galvanostatic and potentiostatic pulses has been used to fabricate an electrocatalytically active $Ni/Ni(OH)_2$/graphite electrode. This inexpensive $Ni/Ni(OH)_2$/graphite electrode exhibits very high activity towards hydrogen evolution. By a suitable choice of the relative proportion of Ni and $Ni(OH)_2$, we obtain high current density at low overpotentials. The sequential galvanostatic and potentiostatic pulses used for the electrodeposition of Ni on the graphite rod provide control over the morphology and composition and the improved electrochemical performance. This electrode design strategy to generate the $Ni/Ni(OH)_2$ interface on graphite from Ni deposits is promising for electrochemical applications and has been used by us for hydrogen generation. The synergetic effect of nickel, colloidal nickel hydroxide islands, and the enhanced surface area of the graphite substrate facilitating HO–H cleavage followed by adsorped-H (H_{ad}) recombination, results in the high current density [200 mA/cm^2 at an overpotential of 0.3 V]. While Ni itself is not active for HER under these conditions, its heterojunction with $Ni(OH)_2$ in graphite substrate makes it highly active. The main bottleneck at present with the electrode is its stability in acidic media and less activity in higher pH or basic media which needs to be improved by further engineering of catalyst design. The easy method of fabrication of the electrode, which is also inexpensive, can prompt to explore its use in fabrication of solar-driven electrolysis (PV-Electrolyzers).

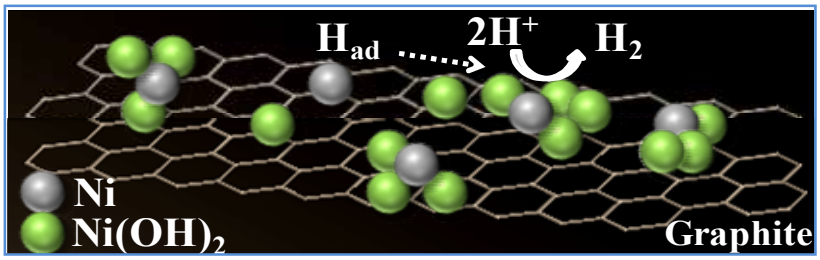

* Paper based on this chapter has appeared in ***Proc. Natl. Acad. Sci. U.S.A. (2017)***

1. Introduction:

Solar energy can be utilized in photo-splitting of water to store hydrogen gas as an eco-friendly fuel. Coupling photovoltaic devices to acid/alkaline electrolyzers could be one of the approaches for solar-driven hydrogen generation (**Figure 5.1**). Since the source of input energy for this type of hydrogen generation is sunlight (and therefore, incumbent efficiency of solar cells) high activity and long term stability is required for the catalysts needed for hydrogen and oxygen generation.

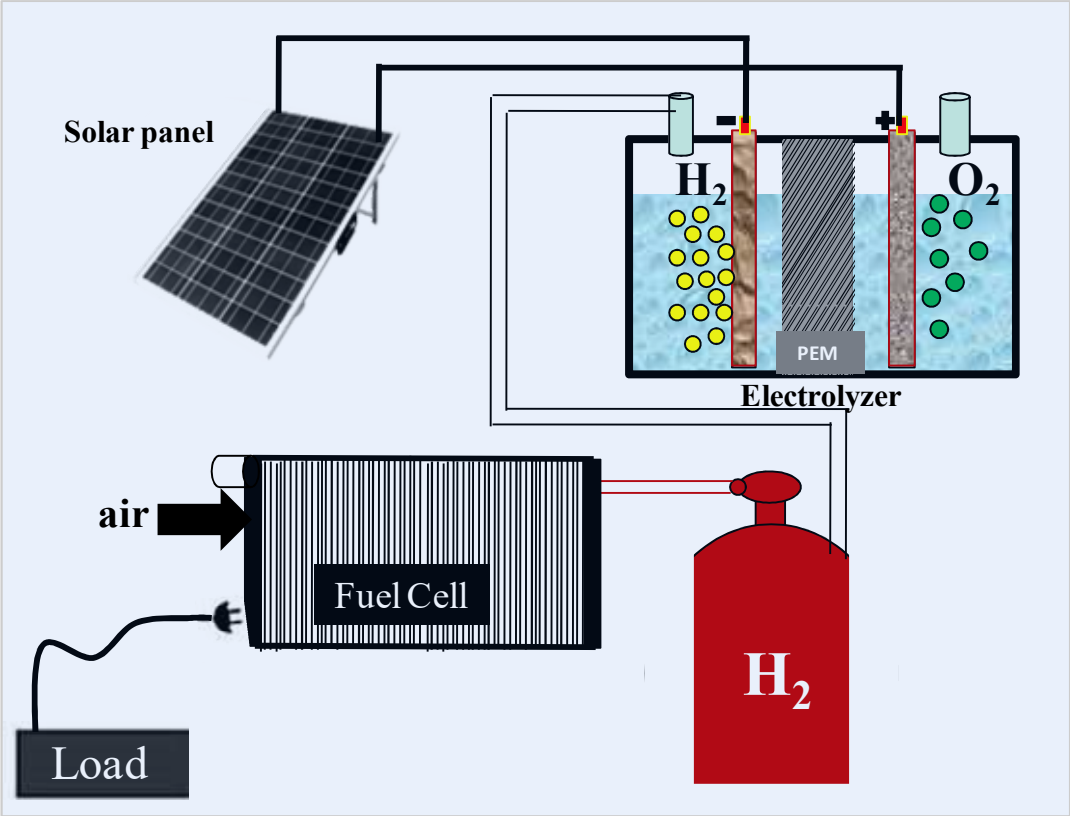

Figure 5.1: Solar driven energy production via hydrogen generation through electrolyzer.

Limited availability and cost factor of noble metals has resulted in a huge surge for identifying highly active catalyst as a replacement. Both transition metal based heterostructures[1-6] and metal-free based catalysts[7-11] have been reported. Particularly, Ni based catalysts like Ni_2P[12-13] , NiFeP[14], $Ni(OH)_2$[15-16] etc. for water splitting have received much attention owing to higher activity of Ni(111) facet as has been observed in our study in this chapter.

In spite of tremendous progress in electrochemical hydrogen evolution catalysts, there has been only handful of catalysts suitable for commercial electrolyzer plants. Today there are catalysts whose HER activity is even better or almost similar to that of standard Pt catalyst. **Table 1** shows the recently reported (till 2017) state-of-art catalysts (precious metal-free) with its activity in comparison to the activity of commercial Platinum catalyst.

Table 1: Recently reported (till 2017) state-of-art catalysts with its activity.

Catalyst	Onset potential (mV) vs RHE	η@10mA/cm^2 (mV) vs RHE	Reference
MoS_2 QDots/RGO	8	64	[17]
MoS_2/ NRGO	5	56	[18]
MoS_x/CNT Hybrid	75	110	[19]
MoS_2/RGO	75	104	[20]
MoS_2/ Carbon	80	85	[21]
MoS_2/Carbon Cloth	100	145	[22]
RGO / MoS_2	105	150	[23]
MoS_2-BCN	50	60	[24]
BC_7N_2	56	70	[25]
Ni_2P/Ni	80	100	[13]
Ni_2P	90	105	[5]
Ni/NiO/CNT	10	85	[26]
Pt/C	3	23	[25]

In most cases HER activity has been tested in 3 electrode systems, where catalyst film formed on glassy carbon electrode (GCE) or Ni foam has been used as the working electrode. Though highly active catalysts are reported, but commercial exploitation necessitates easy reproducible fabrication technique avoiding extra steps required for electrode fabrication from powdered sample. Some of the impeding reasons may include many crucial factors (considering conventional drop cast-drying of catalyst ink on GCE method) like drying time, ink homogeneity, film thickness and stability (adherence) of film on GCE surface (**Figure 5.2**). Hence reproducibility and scaling up of Lab research is hindered. It is, therefore, necessary to identify a reusable cheap, durable, mesoporous conducting electrode as substrate for the growth of an active catalyst for electrochemical applications. Commonly used substrates are Ni foam[13-14],

GCE[27-28], carbon cloth[21-23] etc. In addition to this, carbon based catalyst supports are used to reduce catalyst agglomeration, increase stability, provide electron conducting channel, avoid mass usage of active catalyst, thus reducing the cost. However, firm adherence with the substrate electrode material for long term applications is not provided by available methods, mainly involving drop-drying. Hence a suitable in-situ electrode fabrication process in order to obtain good film of catalyst on a substrate, for later use as working electrode is essential to be realized. After a series of literature search and control experiments done on metal strips,

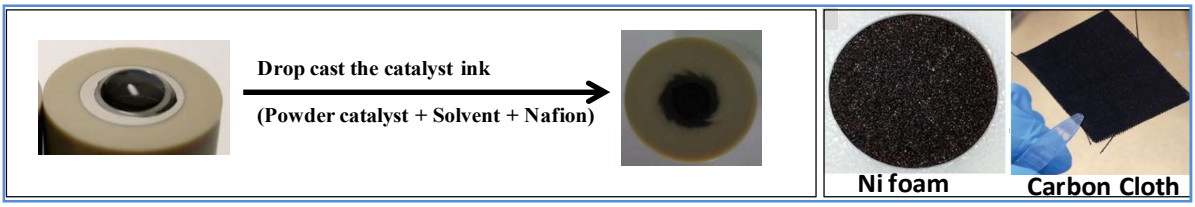

Figure 5.2: Pitfalls of drop drying and other substrates for electrochemical HER activity tests.

Carbon fiber and Graphite and due realization of the ease of electrode processing (washing, polishing to obtain smooth surface, free of impurity), we chose graphite rod as the electrode substrate. Graphite rod is advantageous in the sense that multiple uses are possible by simple re-polishing. It is a sturdy, self supporting, carbon based cheap electrode. As a suitable replacement of Pt for HER catalyst, the importance of optimum ratio of metal/oxide or hydroxide interface has been highlighted [16, 30-34]. Eight fold enhancement in activity HER could be achieved through bi-functional metal/metal hydroxide clusters. While Pt and Pt-group metals are good as adsorption and recombination sites for Hydrogen, these are not effective in cleaving efficiently HO-H bond as is the case with metal oxides or sulfides.

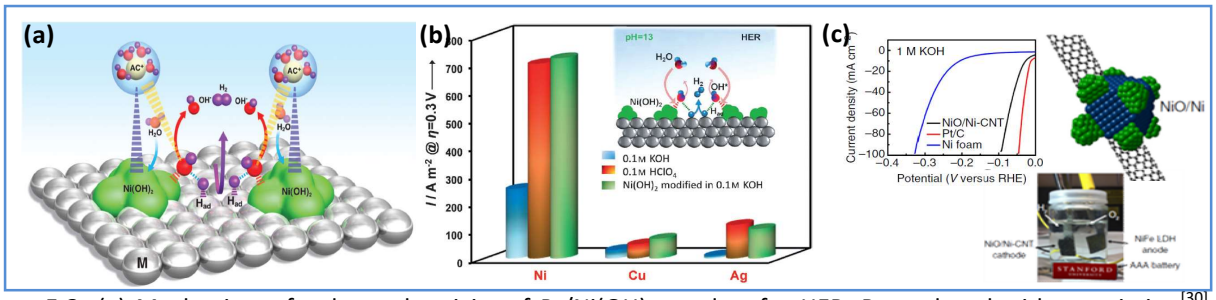

Figure 5.3: (a) Mechanism of enhanced activity of Pt/Ni(OH)$_2$ catalyst for HER. Reproduced with permission[30], copyright 2013 American Association for the Advancement of Science. (b) Comparative study of Metal/Metal hydroxide for HER activity tests for different metals. Reproduced with permission[34], copyright 2012 WILEY-VCH Verlag GmbH & Co. KGaA, Weinheim. (c) Electrocatalytic activity of Ni/NiO towards hydrogen evolution. Reproduced with permission[26], copyright 2014 Springer Nature Ltd.

Conducting ultra thin Ni(OH)$_2$ clusters with Pt single crystals or Pt ad-islands were observed to catalyze hydrogen evolution reaction through effective water dissociation on colloidal Ni(OH)$_2$ cluster sites leading to hydrogen intermediates (H_{ad}) and its recombination on Pt[30]. Ni(OH)$_2$ addition to other metals like Ni, Ag and Cu was also tested for bi-functionality and its role for HER. Interestingly, Ni was found to be the most active[34] (**Figure 5.3**). The major hurdle is to realize such electrochemically active metal/metal hydroxide interfaces with an efficient electrode fabrication technique. In the context of such electrode synthesis, electrodeposition has been widely used to obtain a metal/hydroxide interface[35-37]. Electroplating (instead of electroless deposition involving complicated pretreatment of graphite powder) of nickel on graphite powder, to have a composite material possessing properties of both graphite powders (excellent electrical conductivity) and metal (thermal conductivity), has been studied in order to improve cathode current efficiency[38]. Electrodeposited Ni(OH)$_2$ nanoflowers, for supercapacitor applications, has also been obtained on porous HOPG substrate when 0.1 M Ni-Ac was used as electrolyte[39]. Potential sweep electrodeposition (linear and cyclic) has been used to obtain porous $Co_{1-x}Ni_x(OH)_2$ films[40], Ni/Ni(OH)$_2$ catalyst[35,37]. It is interesting to note that during electrodeposition, metal deposition quenches due to formation of blocking layer of hydroxide which could be lifted by adjusting the potential to values congruent with conventional metal deposition[41] (**Figure 5.4**). Hence we thought of incorporating dual pulse plating electrodeposition into our fabrication strategy to obtain Ni/Ni(OH)$_2$ which could provide a better way of creating such hetero-interfaces of metal/metal hydroxide. The effect of two or three pulse plating has been studied for layered deposition of different materials. For example giant magnetoresistance multilayers of Co and Copper has been obtained through G/P i.e. Galvanostatic followed by Potentiostatic pulse-plating. In galvanostatic mode a Cobalt rich Copper deposit is obtained which is then followed by depositing a layer of pure Copper in potentiostatic mode[42].

In our effort to fabricate Ni/Ni(OH)$_2$ interface, we observed that galvanostatic pulses shift cathodic potential in the negative direction to such an extent that ensuing water splitting give rise to hydrogen evolution followed by simultaneous incorporation of colloidal nickel hydroxides in deposits. This cycling of potentiostatic and galvanostatic pulses change the

morphology of nickel deposits from pure nickel to layered nickel/colloidal nickel hydroxide deposits as evidenced by various analyses of samples of silvery nickel electrodeposited on Graphite, discussed in detail in earlier literature[35,43]. Thus we could obtain Ni/Ni(OH)$_2$ interface.

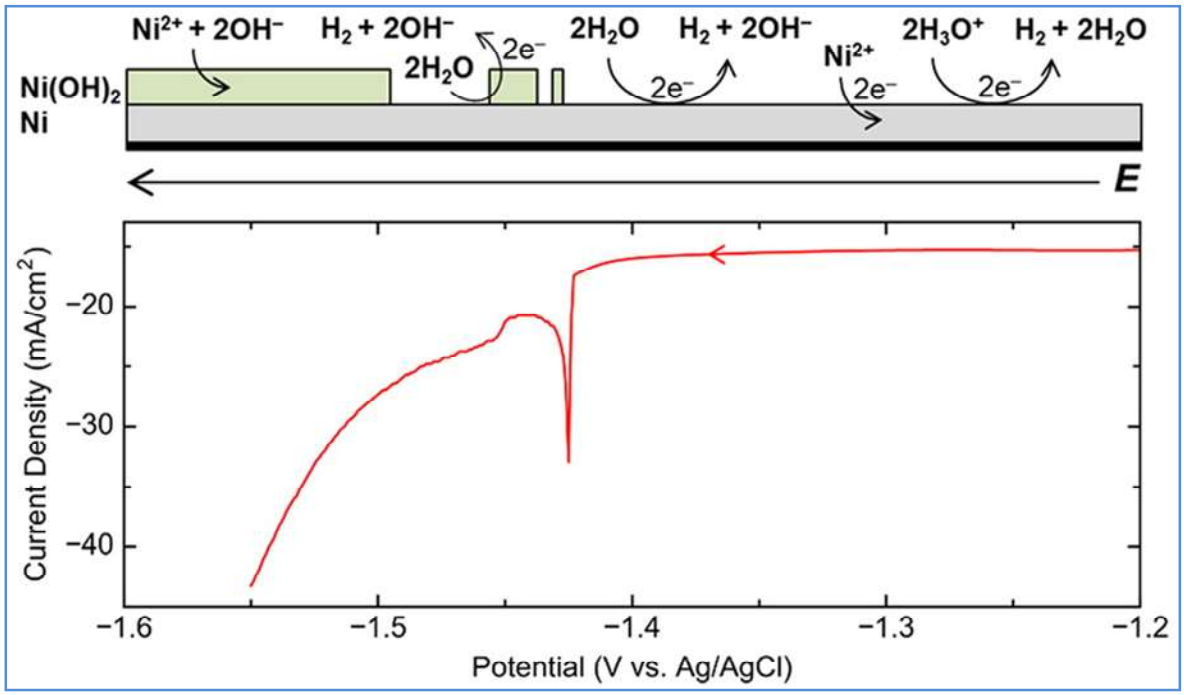

Figure 5.4: Simultaneous deposition of Ni and Ni(OH)$_2$ on the electrode surface by manipulating the potential. Reproduced with permission[41], copyright 2016 American Chemical Society.

2. Scope of the Investigations

In this chapter, we discuss in detail the importance of Ni/Ni(OH)$_2$ interface embedded in graphene sheets on graphite rod substrate along with its fabrication technique. To the best of our knowledge the use of dual pulse plating synthesis strategy has been hitherto not reported for improving the HER activity on graphite rod. The current density of ca. 200 mA/cm^2 (at -0.31 V vs RHE) and a retention of activity (overpotential of ~190 mV required to sustain a current density of 20 mA/cm^2) for long term (24 hours) as observed in our study is noteworthy. The catalyst can be reused until the graphite surface is available for deposition. This study introduces a concept of fabricating ready to use electrode for electrolyzers, thus avoiding the pitfalls of powder catalysts being used as electrode materials. Of course, the stability of

catalyst is an issue in acidic media and further necessary steps must be introduced to circumvent this bottleneck.

Graphite rod as the electrode substrate material

At present, one uses substrates like Ni foam, GCE, carbon cloth, etc. However, firm adherence with the substrate electrode material for long-term applications is not provided by available methods, mainly involving drop-drying. It is, therefore, important to explore a suitable in situ electrode fabrication process to obtain good films of the catalyst on a substrate, for use as a working electrode. Electrodeposition would be an obvious choice. After a detailed examination of the literature and control experiments on metal strips and carbon fiber, we have chosen graphite rod as the electrode substrate. Graphite rod is advantageous in the sense that multiple uses are possible by simple re-polishing. It is a sturdy, self-supporting, and inexpensive electrode. We have electrodeposited nickel on the clean graphite substrate.

3.2. Experimental section:

3.2.1. Materials:

Graphite rod, Silicon Carbide paper, Teflon tape, Insulating double sided tape, Nickel foil, N-methylformamide (NMF) (SD Fine Chem.).

3.2.2. Characterization:

Transmission electron microscopy (TEM, Technai F30 UHR, 200 kV) was used to study the morphology and Field emission scanning electron microscopy (FESEM, FEI Quanta operated at 15 kV, equipped with EDAX) was used to investigate the composition, morphology and thickness of electrodes. The elemental ratios of the as prepared electrodes were confirmed by optical emission spectrometry-inductively coupled plasma spectrometry (OES−ICP) (Perkin Elmer Optima 7000 DV). X-ray photoelectron spectroscopy (XPS, Mg–Kα X ray source, 1253.6 eV) was recorded to analyze the composition of samples. Atomic Force Microscopy (AFM) was carried out on scanning probe microscope in tapping mode in air under ambient conditions using silicon cantilevers (Bruker Innova). Typical image sizes are 20x20 μm^2 at a scan rate 40

µm/s with 256 lines per image. Electrochemical synthesis was performed by CHI760E electrochemical workstation (CH Instruments Inc.).

3.2.3. Fabrication of electrodes:

3.2.3a. Polishing electrode: 5 cm graphite rod was taken with the ends cut into square shapes. One side was polished rigorously with different quality Silicon Carbide paper sequentially followed by sonicating in acetone to degrease. Leaving an area of 0.6 cm^2, the rest part was electrically insulated by double sided insulating tape followed by covering with Teflon tape. Mechanically polished copper strips were treated for few seconds in dil HNO_3 (1:3), rinsed with water, degreased with acetone and prior to putting in the plating cell (having Nickel foil as anode) were activated for few seconds in dil HCl (1:3) and washed with DI water. Graphite substrates were prepared in the following way: polished on 2000 CRR, sonicated in DI water (10 min), wiped on polishing cloth, sonicated in DI water (10 min), polished on diamond paper, sonicated in DI water (10 min) and acetone (2 min), dried under vacuum at 50^0C. The smooth and clean polished graphite surface was used to deposit Ni. For initial investigation purpose Cu strips and carbon fiber with same surface area were also used as electrode.

3.2.3b. Electrodeposition of Ni: 0.3 M Nickel Acetate – tetra hydrate (SD Fine Chem) solution in 5 mol% N-methylformamide (NMF)-water mixture was prepared for electrodeposition of Nickel on different substrates like Copper strip, carbon fiber and Graphite. pH of freshly prepared nickel plating solution was 6.7 and the pH was observed to go down slightly with successive electrodeposition runs. Nickel was deposited on Copper strips as well as on Graphite rod. Ni strip was used a counter electrode, Ag/AgCl as the reference electrode and the polished graphite as the working electrode. Nickel electrodeposition was done through successive potentiostatic/ galvanostatic pulses (P/G pulse-plating with CHI760E). For potentiostatic pulse, voltage ranged between -0.9 to-1.2 V with respective hold times as 10 and 100 seconds while in the galvanostatic pulse current densities were fixed at 34 and 8.4mA/cm^2. Five segments consisting of P-G-P-G-P were employed during electrodeposition (**Figure 5.5**). The activation of Ni-Gr electrode was observed in successive LSV cycles during hydrogen

evolution activity test in 0.5 M HCl with appearance of fresh Ni-Gr turning black as discussed below.

3.2.3c. Obtaining active electrode: The activation of Ni-Gr electrode was observed in successive LSV cycles during hydrogen evolution activity test. In presence of 0.5 M HCl and increasing cathodic potential, the fresh Ni deposits etches out successively leaving behind Ni/Ni(OH)$_2$ interface and the nascent graphite surface with corrugated nanospikes. This gives a burst of H_2 evolution as evident from the figures discussed later. The active electrode is black in appearance and the presence of Ni^{2+} was proved initially by DMG test. A cotton pad dipped in DMG solution (0.5 M in ammonia and ethanol) and rubbed on the surface of active Ni-Gr. Pink coloration was observed.

4. Results and discussion:

The dual pulse plating (PP) method adopted by us gives rise to colloidal hydroxide inclusions in the electrodeposits [Ni/Ni(OH)$_2$/graphite electrode]. This particular observation was also encountered by other researchers [37]. The experimental procedure suggests that while fabricating the Ni/Ni(OH)$_2$ interface, the galvanostatic pulses shift the cathodic potential in the negative direction to such an extent that the ensuing water splitting yielding hydrogen is followed by the simultaneous incorporation of colloidal nickel hydroxide **(Figures 5.1 and 5.2)**.

Thus, the use of dual PP affords in obtaining Ni and Ni(OH)$_2$ from the sequential galvanostatic and potentiostatic conditions. While only Ni deposition is expected in the potentiostatic pulse, both Ni and Ni(OH)$_2$ get deposited in the galvanostatic pulse due to variable potentials. The reduction of hydronium ions at the catholyte leads to the codeposition of Ni(OH)$_2$ along with Ni. The origin of Ni(OH)$_2$ generation has been explained earlier[35-38,43].

Compared with direct current deposition (DP), cycling potentiostatic and galvanostatic pulses in PP changes the morphology of nickel deposits from pure nickel to layered Ni/colloidal Ni(OH)$_2$ deposits on the graphite substrate to a greater extent (**Figures 5.5a and b, 5.6a**). The fresh deposits of Ni on graphite referred to as “fresh Ni-Gr” get converted into “active Ni-Gr” during electrochemical HER in linear sweep voltammetry (LSV).

Fresh Ni-Gr consists of walnut shaped particles distributed throughout the electrode surface as observed in field emission scanning electron microscopy (FESEM) image (**Figure 5.6a**), and this morphology is lost after activation of the electrode at HER-4. The active Ni-Gr electrode surface consists of Ni/Ni(OH)$_2$ embedded in a sea of graphite sheets (**Figure 5.6b and Figure 5.5c**) as confirmed by energy dispersive X-ray analysis (EDAX) (**Inset of Figure 5.6a and b**), high-resolution TEM (HRTEM) images, inductively coupled plasma spectrometry–optical emission spectrometry (ICP-OES) analysis and the dimethylglyoxime (DMG) test. HRTEM images (**Figure 5.6c and d**) of fresh and active electrodes reveal the presence of Ni/Ni(OH)$_2$ interfaces throughout the catalyst. An analysis of the composition and morphology is provided in the **Figures 5.7-5.9**.

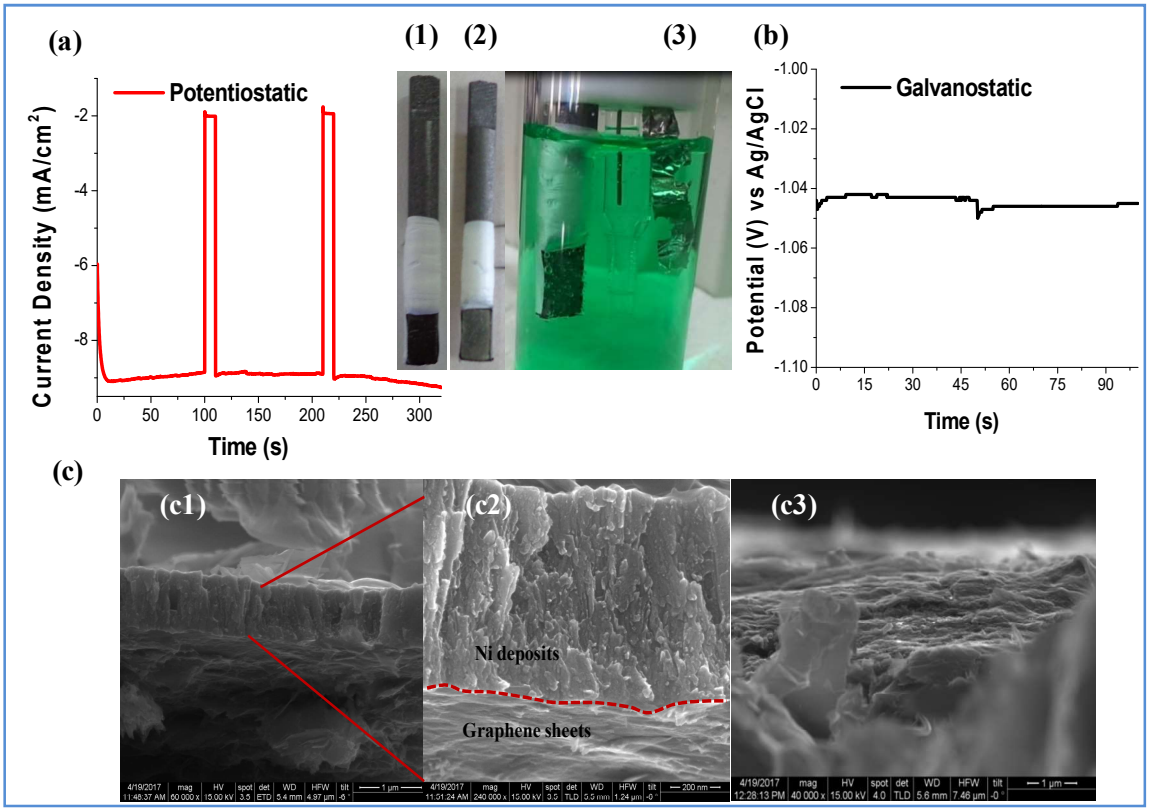

Figure 5.5: Fabrication of electrode: (a and b) are the potentiostatic (P) and galvanostatic (G) graphs during the electrochemical fabrication of electrode. The five sequential steps involve P-G-P-G-P. (1) and (2) are the photographs of the polished graphite electrode before and after Ni pulse-plated electrodeposition, respectively. (3) Autocatalytic generation of fine H_2 bubbles during Ni electrodeposition. (c) Cross-sectional FESEM images of electrodes: (c1 and c2) are low and high magnified images of "fresh Ni-Gr." The interface of Ni deposits and graphene sheets is marked by red dots. (c3) Magnified image of "active Ni-Gr" showing Ni/Ni(OH)$_2$ embedded within the graphene sheets.

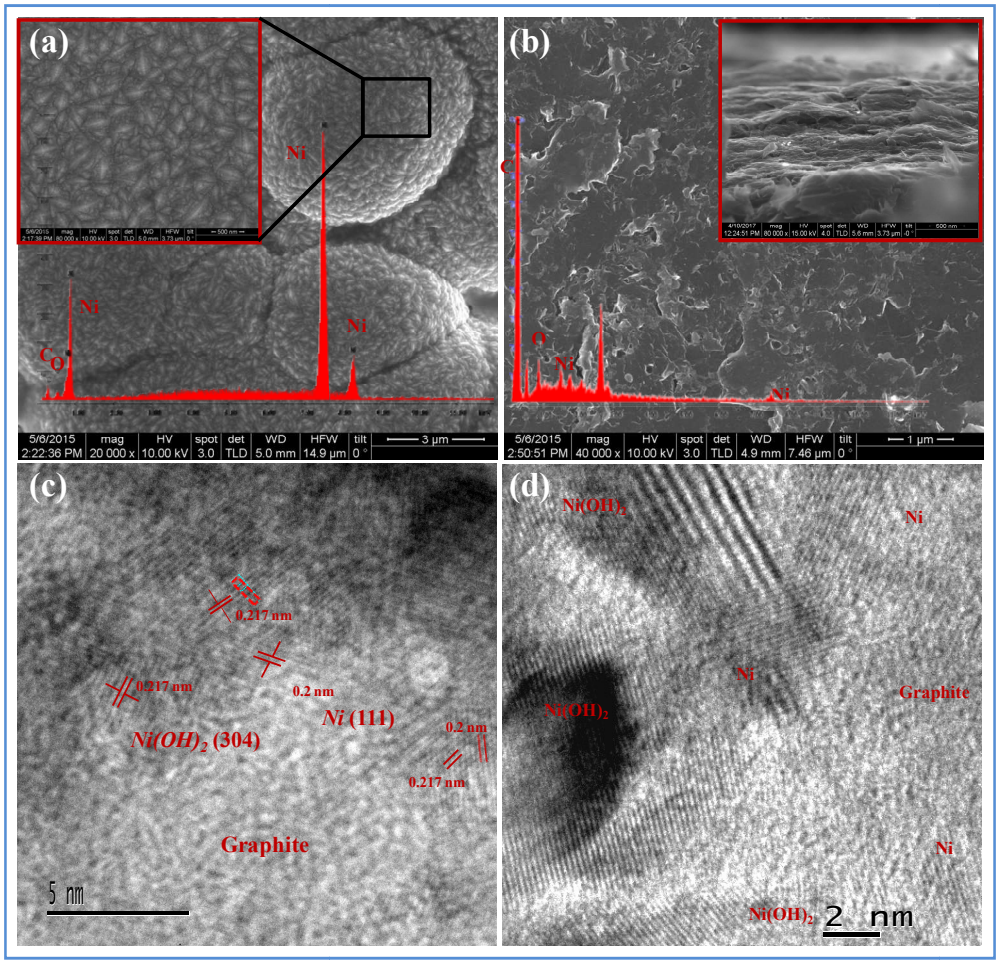

Figure 5.6: Morphology study of the electrode. (a) FESEM image of Ni-deposited graphite electrodes. Inset shows the magnified image and EDAX data for the deposit. (b) The FESEM images of active Ni-Gr electrode. The Inset shows cross-sectional view of the electrode surface. The elemental composition is also depicted. The active electrode consists of Ni/Ni(OH)$_2$ embedded in the graphite sheets. (c and d) are HRTEM images of active Ni-Gr electrode illustrating Ni, Ni(OH)$_2$, and graphite interfaces.

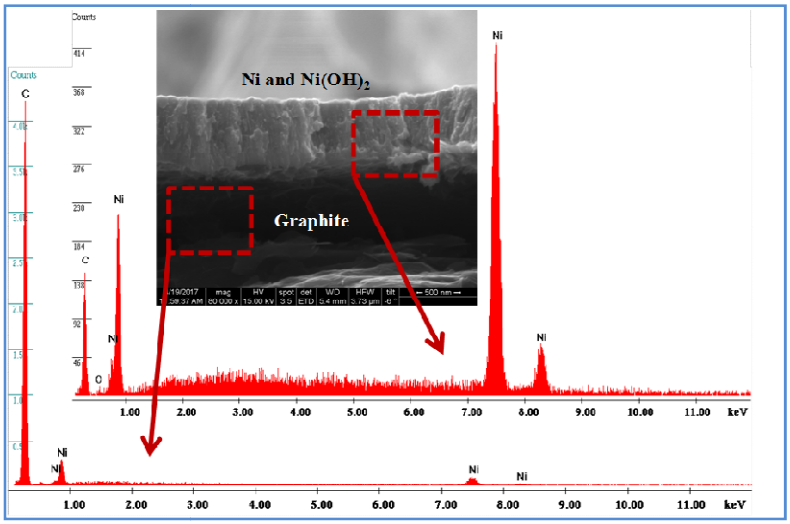

Figure 5.7: The compositional analysis of fresh Ni-Gr at different places on electrode surface. The places are marked by arrows, and the corresponding EDAX elemental mapping plot is given accordingly.

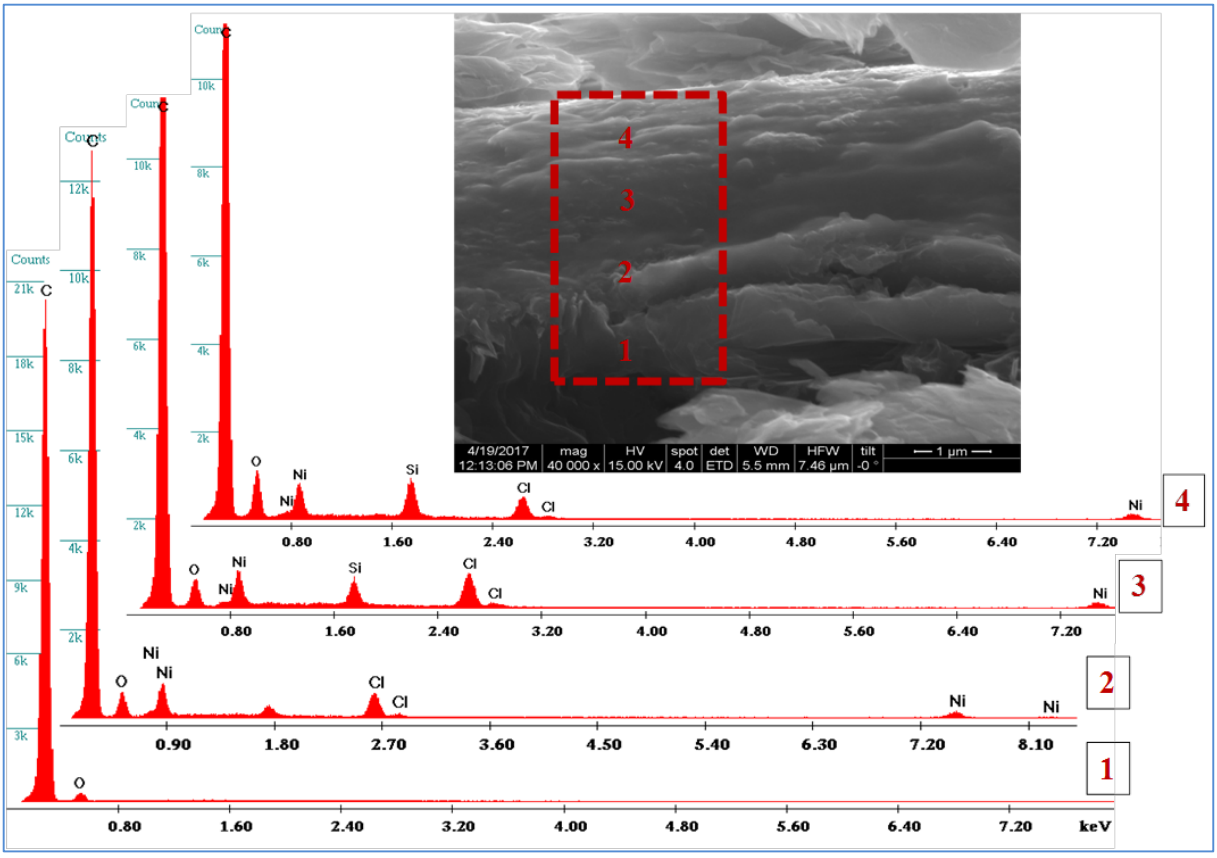

Figure 5.8: The compositional analysis of cross-section of active Ni-Gr at different depths. The places are marked as numbers, and the corresponding EDAX elemental mapping plot is given accordingly. The variation of Ni and O percentage from substrate surface to electrode surface indicates the presence of $Ni(OH)_2$ along with Ni.

X-ray photoelectron spectroscopy (XPS) substantiates the generation of colloidal $Ni(OH)_2$ embedded within the fresh Ni deposit and graphene sheets. We have studied the catalytic activity of the $Ni/Ni(OH)_2$/ graphite electrode by means of LSV plots (**Figure 5.10a**) in comparison with a Pt wire. The overpotentials required for obtaining current densities of 100 and 200 mA/cm^2 are 270 and 299 mV for active Ni-Gr, while for Pt it was 243 and 442 mV, respectively (**Figure 5.10**), making active Ni-Gr a competitive, ready-to-use electrode in commercial electrolyzers. The tafel slopes are close to 116 mV/dec (**Figure 5.11a**) suggesting adsorption of hydronium ions to be the rate-determining step. Butler-Volmer equation predicts an asymptotic linear dependence for large overpotentials, where the slope is related to the transfer coefficient and the y-intercept gives the exchange current in tafel plot. The Tafel plot of log(current) versus overpotential for the same is represented in **Figure 5.11.** Due to the small tafel slope of Pt catalyst, the curve looks linear (**Figure 10b inset**). This is consistent with various

other reports in literature. To check the efficacy of our method of electrode fabrication, a comparative study of the HER activity was carried out with an electrode fabricated through conventional DP of Ni. The results showed much higher current density (12 times increment at 300 mV) with the electrode prepared by the PP method (**Figure 5.11b**).

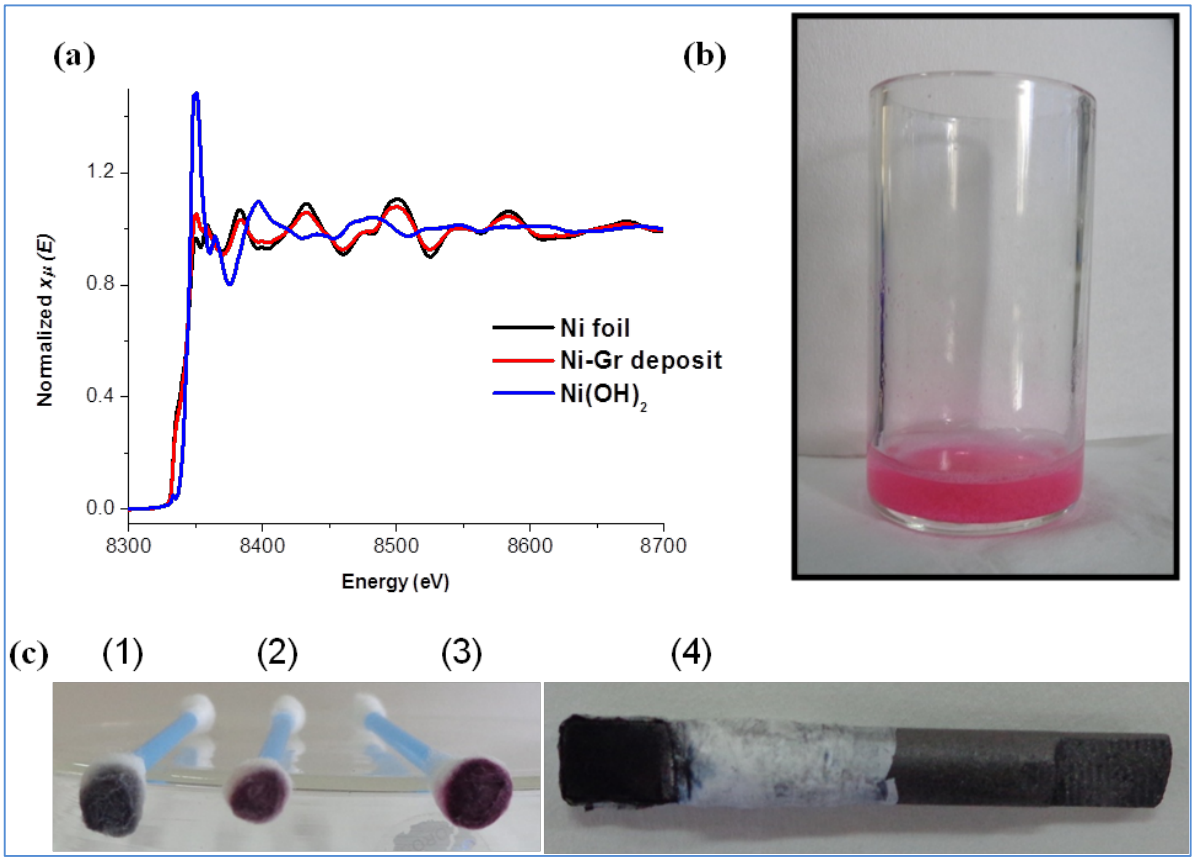

Figure 5.9: (a) The normalized XAFS spectra of Ni-K edge of the fresh Ni-Gr electrode, Ni foil, and Ni(OH)$_2$ as reference samples, showing the presence of Ni(OH)$_2$/ Ni interface on the fresh Ni-Gr electrode. (b) The DMG test of electrolyte after the HER-4 shows the presence of etched Ni. (c) The DMG test done with cotton plugs, dipped in DMG solution rubbed on the surface of (1) polished graphite electrode, (2) active Ni-Gr, and (3) fresh Ni-Gr. (4) shows the photograph of active Ni-Gr electrode.

This significant difference is ascribed to the absence of the active Ni/Ni(OH)$_2$ interface embedded within the graphene sheets in DP-fabricated Ni-Gr. Presence of the polished graphite electrode is crucial for the successful fabrication of active Ni- Gr electrode as confirmed by controlled experiments using a conducting carbon fiber (**Figure 5.12**). We propose that, during HER in acidic medium, dissolution of the nickel deposit gives rise to or expose Ni/Ni(OH)$_2$ interfaces, which then catalyze hydrogen evolution at this interface. Formation of

Ni(OH)$_2$ gets enhanced with successive HER tests due to electrogeneration of the base in the catholyte by the reduction of hydrogen ions. We have examined the stability of active Ni-Gr by cyclic voltammetry (**Figure 5.10d**), as well as chronopotentiometric (**Figure 5.13a**) and chronoamperometric studies (**Figure 5.11c**). An activity retention of ~96% was observed up to 200 cyclic voltammetry (CV) cycles between −0.18 and −0.28 V at a scan rate of 5 mV/s (Fig. 2D). Active Ni-Gr can sustain a current density of 20mA/cm^2 for 24 h requiring overpotential of only 190 mV (**Figure 5.13a).** While Ni itself is not active for HER under these conditions, its heterojunction with Ni(OH)$_2$ in graphite substrate makes it highly active.

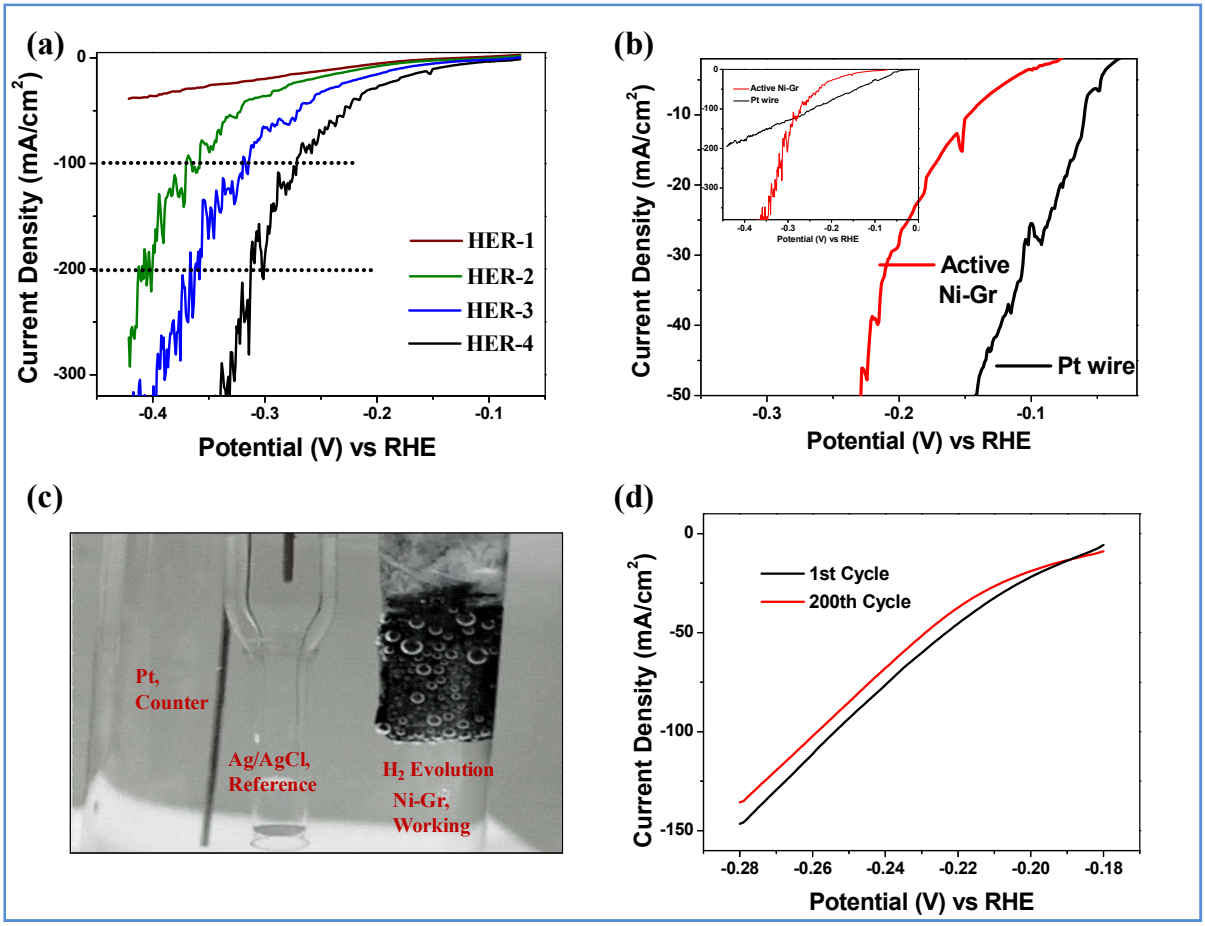

Figure 5.10: Electrochemical hydrogen evolution activity test. (a) Hydrogen evolution activity (HER) tests of the electrode by linear sweep voltammetry (LSV). HER-1 to HER-4 represents successive LSV runs. (b) The comparison of HER activity of Pt wire (0.5-mm diameter × 30.25-mm length; CH Instruments, Pt counter electrode CHI 115) and active Ni-Gr. The inset shows the catalyst comparison in wide potential window to highlight the comparable activity with respect to Pt. (c) Photograph of hydrogen evolution (bubbles) during the HER tests through LSV. (d) Stability test of "active Ni-Gr electrode" before and after 200 CV cycles between −0.18 and −0.28 V vs. RHE at a scan rate of 5 mV/s. For HER testing, 0.5 M HCl was the electrolyte, and LSV was run at a scan rate of 5 mV/s. Pt wire and Ag/AgCl were used as counter and reference electrodes, respectively. The potentials were reported with respect to RHE according to following equation: $E_{RHE} = E_{(vs.\ Ag/AgCl)} + E^{\circ}_{(Ag/AgCl)} + 0.059pH$.

Since the adsorption of hydronium ions is the rate determining step, we performed electrochemical impedance spectroscopic studies at onset potential to estimate the resistance involved in charge transfer (R_{ct}) between the electrode and the electrolyte. **Figure 5.13b** shows the Nyquist plot for the Ni-Gr and the equivalent circuit used to fit the data in the Inset, giving the value of R_{ct} as 58 Ω.

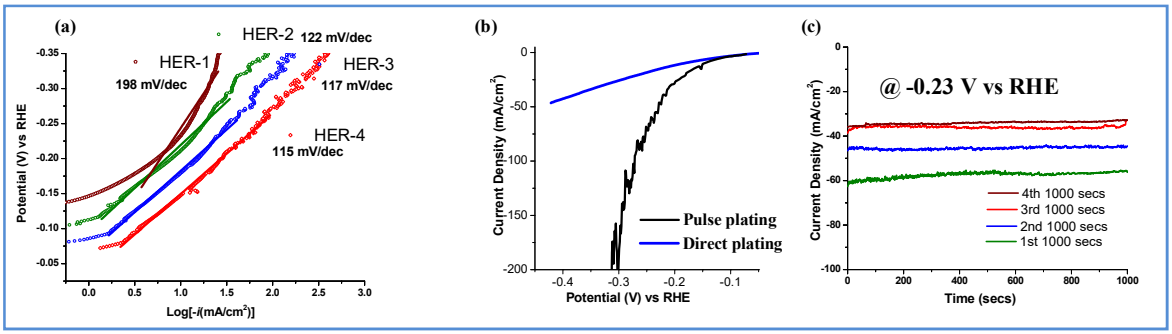

Figure 5.11: (a) Comparison of tafel slope of electrode obtained from successive LSV runs. (b) Comparison of HER activity of electrode fabricated by DP and PP methods. (c) The amperometric I–t stability curve for active Ni-Gr showing current density vs. time at −0.23 V for different time intervals.

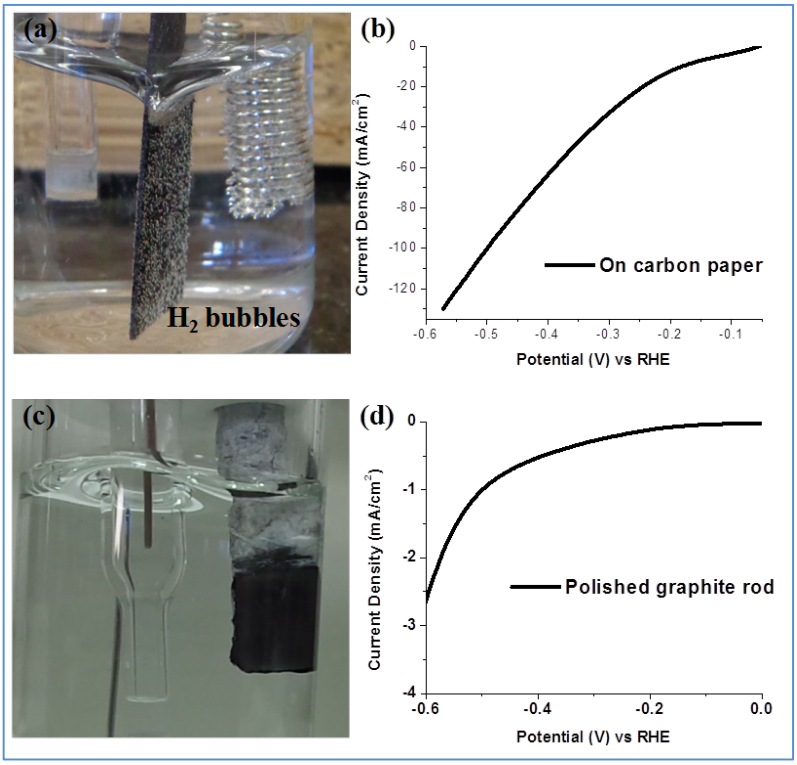

Figure 5.12: (a and b) are the photograph of HER activity test and LSV graph of Ni deposited on carbon fiber, respectively. (c and d) are the photographs of HER test of polished graphite rod and its corresponding LSV graph.

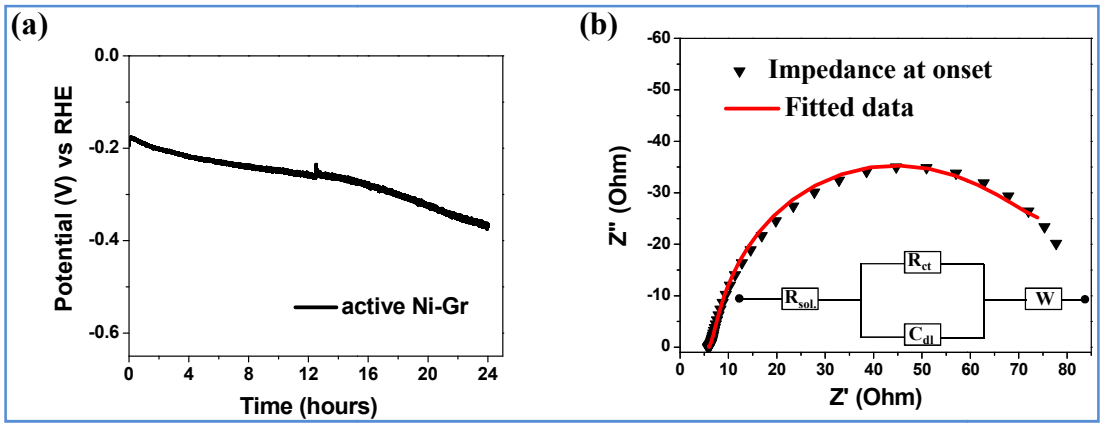

Figure 5.13: Electrochemical properties: (a) Chronopotentiometric V-t graph showing the overpotential required to sustain a current density of 20 mA/cm^2 over long time. (b) Nyquist plot of active Ni-Gr at onset potential and the equivalent circuit.

4.1. XPS Analysis

XPS studies show a drastic change occurs in relative proportion of Ni and Ni(OH)$_2$ on the active Ni-Gr electrode surface during successive LSV runs in HER tests. We see a greater fraction of Ni(OH)$_2$ on the surface of active Ni-Gr electrode (**Figure 5.14**) as corroborated by EDAX analysis (**Inset of Figure 5.6**).

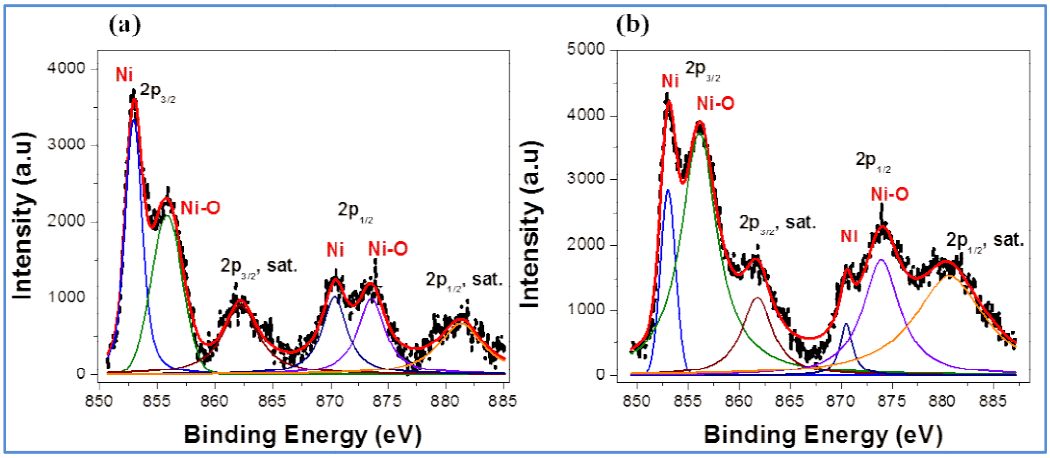

Figure 5.14: Analysis of oxidation state by XPS. (a and b) are the Ni-2p core level XPS plots for fresh Ni-Gr and the active Ni-Gr electrodes, respectively. The peaks at 853.01, 855.77, and 862.07 eV can be assigned to 3p3/2 and peaks at 870.47, 873.61, and 881.23 eV to 3p1/2 for Ni, Ni(OH)$_2$, and Ni(OH)$_2$ satellite peaks, respectively. The XPS analysis hints to two inferences: First, generation of colloidal Ni(OH)$_2$ embedded within the fresh Ni deposit and graphene sheets during the synthesis, and second, drastic change in relative proportion of Ni and Ni(OH)$_2$ on the active electrode surface during HER tests. We see greater fraction of Ni(OH)$_2$ on the surface of active Ni-Gr electrode, also corroborated by EDAX analysis (Inset of Figure 5.2a and b) and XANES analysis.

We observed the characteristic multiplet splitting and satellite peaks at higher binding energies (BEs) with broad maxima for Ni-3p in both samples. The peaks at 853.01, 855.77, and 862.07 eV can be assigned to 3p3/2 and peaks at 870.47, 873.61, and 881.23 eV to 3p1/2 for Ni, $Ni(OH)_2$, and $Ni(OH)_2$ satellite peaks, respectively. The assigned peaks are in accordance with previously reported results. The XPS analysis prompted us toward two inferences: First, as stated earlier, generation of colloidal $Ni(OH)_2$ embedded within the fresh Ni deposit and graphene sheets during the synthesis, and second, drastic change in relative proportion of Ni and $Ni(OH)_2$ on the active electrode surface during HER tests. As discussed earlier, these heterointerfaces are crucial for electrochemical applications, and therefore, it was important to find the exact ratio of these two species on the catalyst surface as a function of successive HER cycles (see electrochemical HER discussion). To confirm this, we carried out XANES studies.

4.2. XANES Analysis: LCF Method

All probable Ni species viz. Ni foil, NiO, $Ni(OH)_2$, and Ni^{2+} surrounded by water molecules were taken as reference material for fitting purpose. The collected data at Ni-K edge for all of these samples along with the electrodes were then analyzed by Linear Combination Fit (LCF) method. Best fit was selected in terms of the values of R factor, $\chi 2$ and reduced $\chi 2$, and visual observation of the fit between the graphs (**Figure 5.15d and Figure 5.9a**). The fitting range was selected up to maximum limit possible, that is, from −20 to 200 eV. In all cases, it was observed that the principal contributions are from Ni foil and $Ni(OH)_2$ species, and hence NiO and "Ni^{2+} in water" data were not included. XANES spectra at the Ni-K edge shows a gradual evolution of $Ni(OH)_2$ with increasing HER cycles (**Figure 5.15a**). The coordination environment of Ni changes as evident from the intensity of the white line. The relative composition of Ni and $Ni(OH)_2$ on the electrodes estimated by a linear combination fit (LCF) method (**Figure 5.15 b-d**) gives the optimum ratio to be 14.3:64.3 at the Ni/$Ni(OH)_2$ interface responsible for the burst of hydrogen evolution activity observed in our experiment (**Table 2**).

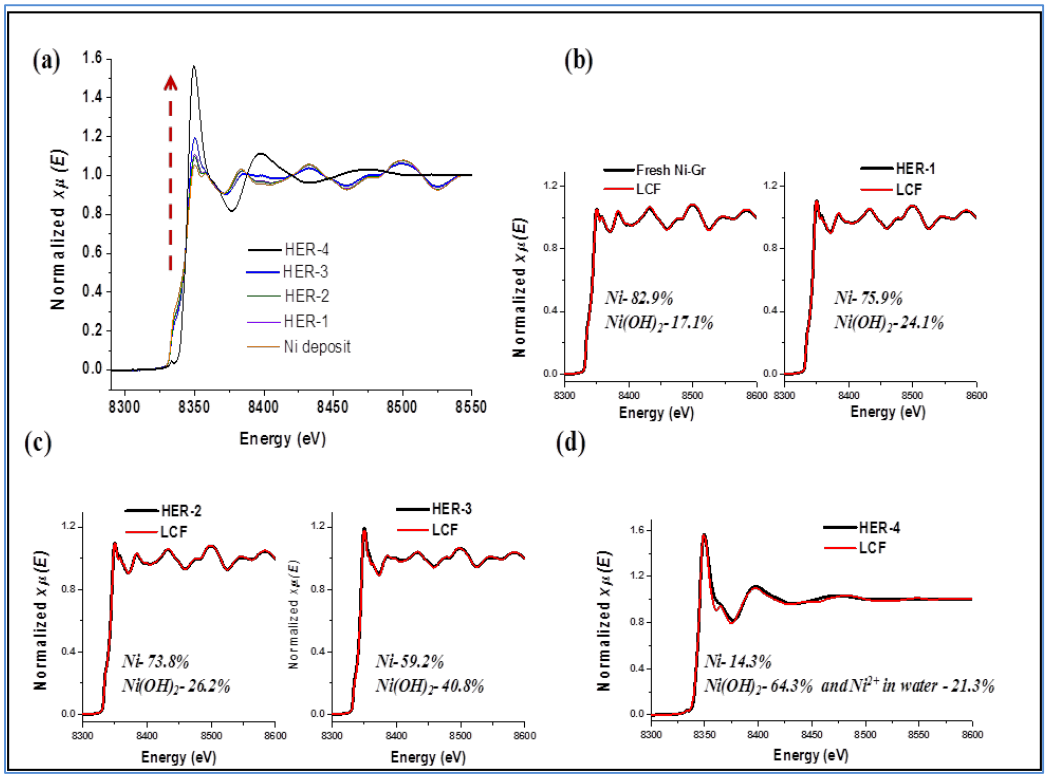

Figure 5.15: Analysis of oxidation state and relative proportion of Ni and Ni(OH)$_2$. (a) Normalized XAFS spectra of Ni-K edge of the electrodes as a function of successive LSV runs depicted as HER numbers showing the evolution of Ni(OH)$_2$/Ni interface. (b–d) The linear combination fitted normalized XAFS analysis of the electrodes to determine the percentage of Ni metal and Ni(OH)$_2$ with increasing HER numbers. All probable Ni species viz. Ni foil, NiO, Ni(OH)$_2$, and Ni^{2+} surrounded by water molecules were taken as reference material for fitting purpose. The collected data at Ni-K edge for all these samples along with the electrodes were then analyzed by LCF method. Fitting was done in Athena software. The fitting range was selected up to maximum limit possible, that is, from −20 to 200 eV. In all cases, it was observed that the principal contributions are from Ni foil and Ni(OH)$_2$ species, and hence NiO and "Ni^{2+} in water" data were not included.

Table 2: LCF data parameters of 'fresh and active Ni-Gr'

Sample	Ni metal (%)	Ni(OH)$_2$ (%)	R-factor	χ^2	Reduced χ^2
Fresh Ni-Gr	82.9	17.1	0.0011842	0.0324	0.000040
HER-1	75.5	24.5	0.0006258	0.0170	0.000022
HER-2	73.1	26.9	0.0006483	0.0185	0.000023
HER-3	59.2	40.8	0.0022793	0.0615	0.000083
HER-4*	14.3	64.3	0.007684	0.3161	0.000398

*the percentage sum is not equal to 100 since 21.3 % is contributed by Ni^{2+} in aqueous solution. This is similar to Ni(OH)$_2$ environment with one hydrogen less. Hence the presence of Ni^{2+} surrounded by OH^- ion is inferred. The exact coordination number and nature of coordination shell is beyond the scope of discussion for this study.

4.3. AFM topography analysis:

Atomic force microscopy (AFM)-assisted topographic analysis of active Ni-Gr and fresh Ni-Gr electrodes provide insight to HER activity (**Figure 5.16**). The 3D topography of these electrodes is contrastingly different in terms of surface roughness (**Figure 5.16 c and d, and Figures 5.17 and 5.18**). There are frequent spikes and sharp corrugation seen on active Ni-Gr electrode surface which gives rise to two important aspects in HER activity analysis- the availability of excess surface area and the nascent graphite electrode surface with narrow edges that can concentrate the electronic charge density provided by polarizing the electrode in cathodic potential during linear sweep voltametry (LSV). These sharp edges favor the increased electronic charge density during LSV, thus, aiding the high activity.

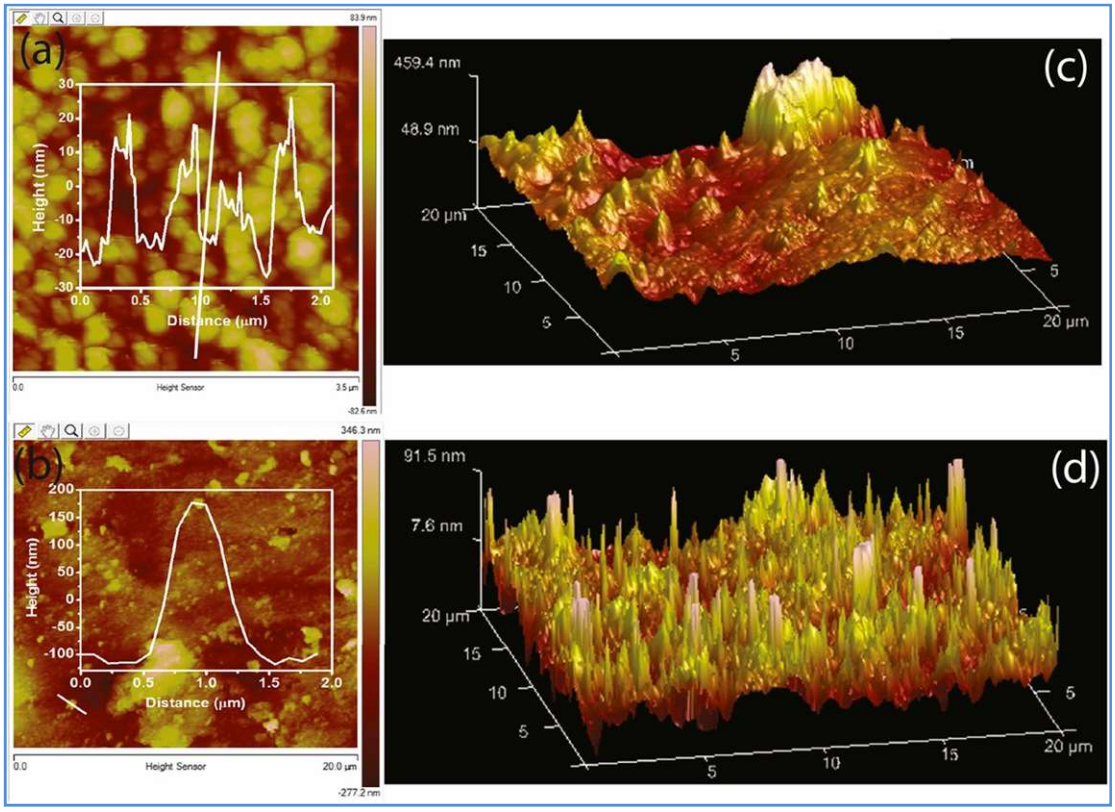

Figure 5.16: Surface roughness and topographic analysis: atomic force microscopy (AFM) image of (a) fresh Ni-Gr surface, (b) active Ni-Gr electrode surface. The Inset shows the height profile of the electrode surface along white line in the AFM image. Three-dimensional topographic AFM images (20 × 20 μm^2 in size) of fresh Ni-Gr and active Ni-Gr electrodes are given in (c and d). The increased surface area and the induced surface mesoporosity (by H_2 evolution as a function of HER numbers) along with difference in the population of catalytically active interface are evident from the 3D images.

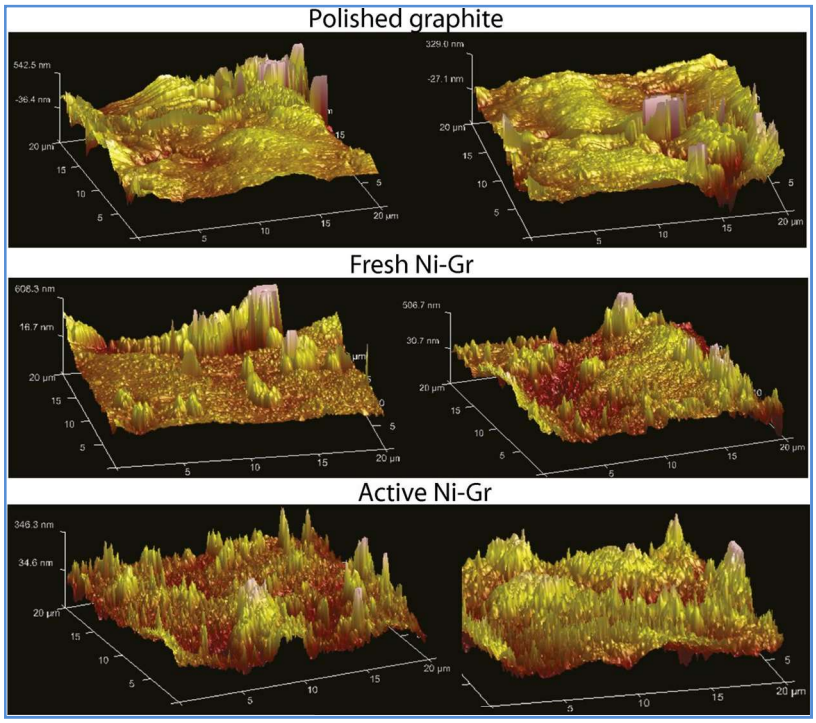

Figure 5.17: Comparison of the 3D AFM images of electrodes highlighting the difference in their surface morphology. Enhanced population of nanospikes with resultant increase in surface area is noticeable for active Ni-Gr in comparison with other two electrode surfaces.

4.4. Mechanistic understanding:

During the electrode fabrication, dual pulse electrolysis in the form of potentiostatic wave form followed by galvanostatic was used to deposit Nickel on Polished/cleaned Graphite from 0.3M Ni-acetate-5 mol% NMF-water bath. Evolution of stream of fine bubbles at the cathode was observed during electrodeposition. This high pH electrolyte solution is conducive to generation of colloidal nickel hydroxide and its inclusion in nickel electrodeposits during the course of nickel plating on graphite. Initial Nickel nucleation on Graphite surface, thus dynamically modified in the form of Ni/Ni(OH)$_2$ interfaces, catalyzes hydrogen evolution reaction. As was reported earlier, autocatalytic generation of hydrogen was observed during direct current as well as pulse plated electrodeposition studies of Nickel. The presence of Ni(OH)$_2$ and Ni is confirmed from various spectroscopic analysis as discussed earlier. Hence we obtain Ni(OH)$_2$ embedded within graphite and Ni deposits during synthesis.

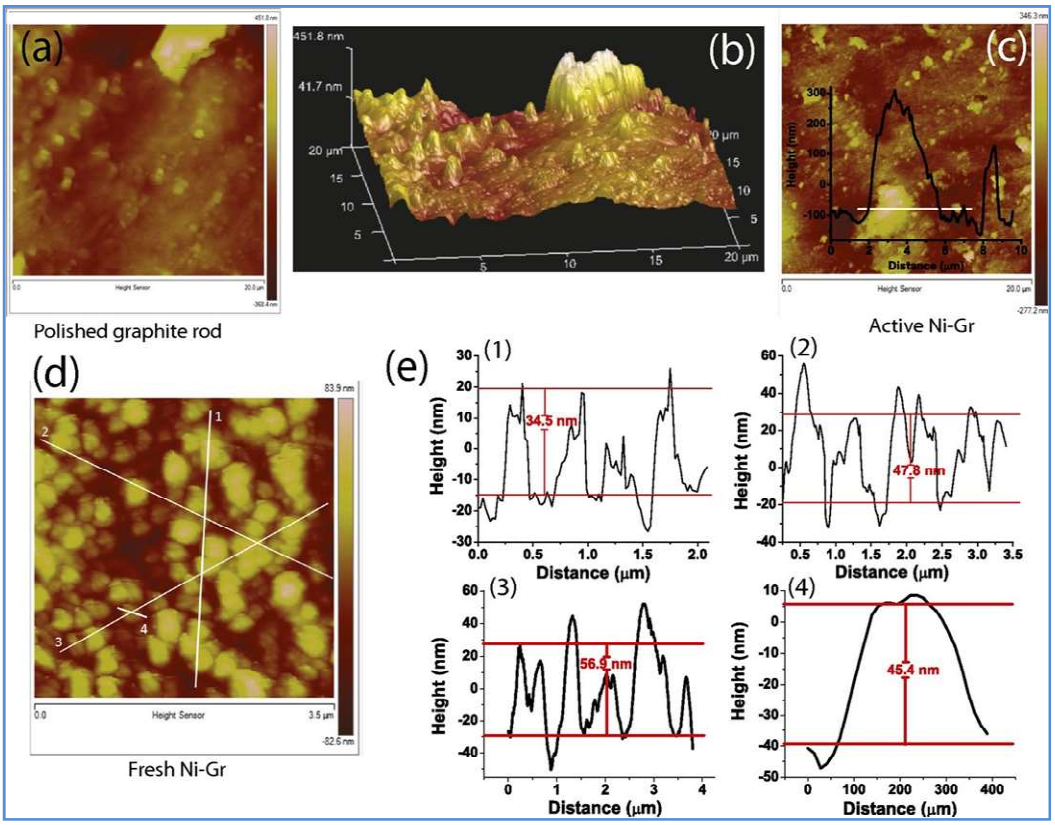

Figure 5.18: Comparison of the height profiles of electrodes highlighting the difference of their surface morphology. (a and b) Polished graphite electrode. (c) Active Ni-Gr. (d and e) Fresh Ni-Gr electrode. The height profiles are given in (e) along with the representative line numbers to represent the area in (d) taken for height profiling. Since the graphite base is not well defined due to continuous deposition of Ni on graphite, the height may not truly represent the actual thickness of deposits. However, a clear picture is given by cross-sectional FESEM in Figure 2.

Based on these rationale and the observations in present case, we propose that PP favor embedding of colloidal nickel hydroxides during nucleation of nickel, thus giving rise to layered deposits consisting of nickel as well as colloidal nickel hydroxides. While testing these nickel plated graphites for HER in 0.5M HCl, dissolution (etching) of superficial nickel deposit may give rise to Ni/Ni(OH)$_2$ interfaces which then catalyzes hydrogen evolution reaction to such an extent that a burst of activity related to bubble formation and evolution is observed during 3rd or 4th HER tests, successive LSV. In our study it is highly plausible that with successive HER tests due to electrogeneration of base in the catholyte by $2H^+$ to H_2 reduction process, Ni(OH)$_2$ is the dominant species, as supported by performed characterizations. The acidic environment itself etches out exposed Ni deposits [when freshly deposited Ni on graphite was immersed in electrolyte overnight, black active Ni-Gr consisting of Ni/Ni(OH)$_2$ was still observed (ICP-OES and

DMG test). However the HER activity was not similar to the ones obtained in this study, the reason for which is presently unexplored and needs further understanding], thus creating an optimum ratio for Nickel and colloidal nickel hydroxide (ICP-OES of 0.5M HCl solution after HER runs showed substantial nickel concentration 569 ppm in 16 ml). It also exposes, at places, fresh surface of nascent graphite substrate along with mesoporosity due to tremendous evolution of hydrogen gas bubbles. This combination of Ni/colloidal Ni(OH)$_2$ interfaces (**Figure 5.19**), mesoporous graphite and enhanced surface area with nanospikes plays synergetic role to transform nickel deposited Graphite into remarkably active catalyst. Based on the results of the present study, it would be desirable to examine the fabrication of acid/alkaline prototype electrolyzers operating at a low voltage and combining them with solar driven electrolyzers. It must be noted that PP is not only a reproducible, inexpensive, and easy method, but it also avoids the pitfalls of the drop-casting method of electrode fabrication technique.

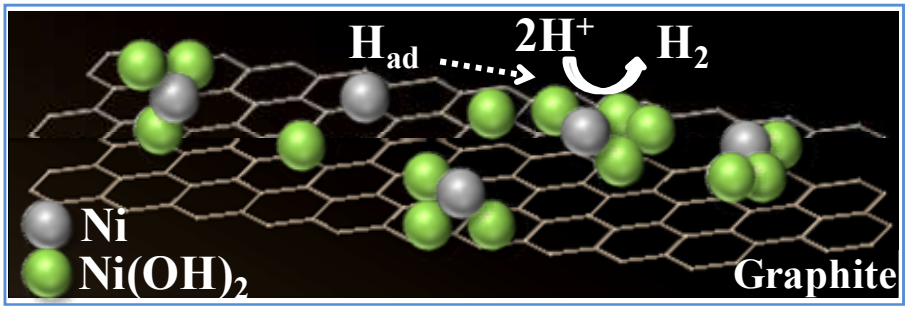

Figure 5.19: The mechanistic understanding of HER. Ni acts as Had sites and Ni/Ni(OH)$_2$ interface facilitates in splitting of water. The combination of Ni/colloidal Ni(OH)$_2$ interfaces, mesoporous graphite, and enhanced surface area with nanospikes plays a synergetic role to transform nickel-deposited graphite into a remarkably active catalyst.

However an important aspect of the catalyst stability in acidic medium should be considered here. While the practically important long term stability cannot be rendered for this catalysts electrode, this study provides an important method to generate electrochemically active Ni/Ni(OH)$_2$ interface which was not obtained previously on conducting graphite rod to the best of our knowledge. In light with the recent report by Chen et al. [53], when Pt is used as the counter electrode, both chemical and electrochemical dissolution of Pt into the electrolyte and its re-deposition onto the working electrode may affect the performance of working electrode. So it is necessary to confirm that Pt dissolution has negligible effect on HER

performance. Since our study is limited to very narrow negative potential regime (350 mV vs RHE) the probability of Pt re-deposition on working electrode surface is less. Also the physical characterizations like EDAX, ICP-OES, PXRD etc does not indicate any signature of Pt on the surface of electrode. An additional experiment including graphite rod as the counter electrode is needed to be performed to unambiguously confirm that the above effect does not affect the activity of $Ni/Ni(OH)_2$/graphite electrode.

5. Conclusions:

In summary, we have found that nanoscale $Ni/Ni(OH)_2$/ graphite is an outstanding catalyst with high HER activity exhibiting high current density over a range of overpotentials. The design and electrode fabrication strategy to generate the highly catalytic $Ni/Ni(OH)_2$ interface on graphite from Ni deposits (the coaction effect of nickel, colloidal nickel hydroxide islands, and the enhanced surface area of the graphite substrate facilitating HO–H cleavage followed by H(ad) recombination, results in the high current density) used by us are unique and unprecedented. To the best of our knowledge, dual-PP synthesis has not been studied for improving the HER activity on graphite. There is a need for an optimum ratio between Ni and $Ni(OH)_2$ for high activity. In situ growth of the catalyst on the graphite surface eliminates cumbersome electrode fabrication procedures. The current density of ~200 mA/cm^2 (at −0.3 V vs. RHE) and a retention of activity (overpotential of ~190 mV required to sustain a current density of 20 mA/cm^2) for long term (24 h) is noteworthy. While Ni itself is not active for HER under these conditions, its heterojunction with $Ni(OH)_2$ in graphite substrate makes it highly active. Having said that, the main bottleneck at present with the electrode is its stability in acidic media and less activity in higher pH or basic media. If we can circumvent this problem by any synthetic design which exposes the $Ni/Ni(OH)_2$ interface and maintaining the stability or enhance the activity in neutral pH values, the electrode can be successfully be used in scale-up electrolyzers. The catalyst can advantageously be reused, thus making the process economical.

6. References:

[1] J. Zhang, T. Wang, D. Pohl, B. Rellinghaus, R. Dong, S. Liu, X. Zhuang, X. Feng, Angew. Chem. Int. Ed. 2016, 55, 6702.
[2] Z. Yin, C. Zhu, C. Li, S. Zhang, X. Zhang, Y. Chen, Nanoscale 2016, 8, 19129.
[3] J. M. McEnaney, J. Chance Crompton, J. F. Callejas, E. J. Popczun, C. G. Read, N. S. Lewis, R. E. Schaak, Chem. Commun. 2014, 50, 11026.
[4] E. J. Popczun, C. G. Read, C. W. Roske, N. S. Lewis, R. E. Schaak, Angew. Chem. Int. Ed. 2014, 53, 5427.
[5] E. J. Popczun, J. R. McKone, C. G. Read, A. J. Biacchi, A. M. Wiltrout, N. S. Lewis, R. E. Schaak, J. Am. Chem. Soc. 2013, 135, 9267.
[6] J. Deng, P. Ren, D. Deng, X. Bao, Angew. Chem. Int. Ed. 2015, 54, 2100.
[7] Y. Zheng, Y. Jiao, Y. Zhu, L. H. Li, Y. Han, Y. Chen, A. Du, M. Jaroniec, S. Z. Qiao, Nat. Commun. 2014, 5, 3783.
[8] Y. Zheng, Y. Jiao, L. H. Li, T. Xing, Y. Chen, M. Jaroniec, S. Z. Qiao, ACS Nano 2014, 8, 5290.
[9] W. Cui, Q. Liu, N. Cheng, A. M. Asiri, X. Sun, Chem. Commun. 2014, 50, 9340.
[10] Y. Ito, W. Cong, T. Fujita, Z. Tang, M. Chen, Angew. Chem. Int. Ed. 2015, 54, 2131.
[11] Y. Zhao, F. Zhao, X. Wang, C. Xu, Z. Zhang, G. Shi, L. Qu, Angew. Chem. Int. Ed. 2014, 53, 13934.
[12] L. Feng, H. Vrubel, M. Bensimon, X. Hu, Phys. Chem. Chem. Phys. 2014, 16, 5917.
[13] Y. Shi, Y. Xu, S. Zhuo, J. Zhang, B. Zhang, ACS Appl. Mater. Interfaces 2015, 7, 2376.
[14] H. Liang, A. N. Gandi, C. Xia, M. N. Hedhili, D. H. Anjum, U. Schwingenschlögl, H. N. Alshareef, ACS Energy Lett. 2017, 2, 1035.
[15] Y. Rao, Y. Wang, H. Ning, P. Li, M. Wu, ACS Appl. Mater. Interfaces 2016, 8, 33601.
[16] N. Danilovic, R. Subbaraman, D. Strmcnik, K.-C. Chang, A. P. Paulikas, V. R. Stamenkovic, N. M. Markovic, Angew. Chem. Int. Ed. 2012, 124, 12663.
[17] F. Li, J. Li, Z. Cao, X. Lin, X. Li, Y. Fang, X. An, Y. Fu, J. Jin, R. Li, J. Mater. Chem. A 2015, 3, 21772.
[18] Y.-J. Tang, Y. Wang, X.-L. Wang, S.-L. Li, W. Huang, L.-Z. Dong, C.-H. Liu, Y.-F. Li, Y.-Q. Lan, Adv. Energy Mater. 2016, 6, 1600116.
[19] D. J. Li, U. N. Maiti, J. Lim, D. S. Choi, W. J. Lee, Y. Oh, G. Y. Lee, S. O. Kim, Nano Lett. 2014, 14, 1228.
[20] M. Chatti, T. Gengenbach, R. King, L. Spiccia, A. N. Simonov, Chem. Mater. 2017, 29, 3092.
[21] X. Zhao, H. Zhu, X. Yang, Nanoscale 2014, 6, 10680.
[22] N. Zhang, S. Gan, T. Wu, W. Ma, D. Han, L. Niu, ACS Appl. Mater. Interfaces 2015, 7, 12193.
[23] Y. Li, H. Wang, L. Xie, Y. Liang, G. Hong, H. Dai, J. Am. Chem. Soc. 2011, 133, 7296.
[24] K. Pramoda, M. M. Ayyub, N. K. Singh, M. Chhetri, U. Gupta, A. Soni, C. N. R. Rao, J. Phys. Chem. C 2018, 122, 13376.
[25] M. Chhetri, S. Maitra, H. Chakraborty, U. V. Waghmare, C. N. R. Rao, Energy Environ. Sci. 2016, 9, 95.
[26] M. Gong, W. Zhou, M.-C. Tsai, J. Zhou, M. Guan, M.-C. Lin, B. Zhang, Y. Hu, D.-Y. Wang, J. Yang, S. J. Pennycook, B.-J. Hwang, H. Dai, Nat. Commun. 2014, 5, 4695.
[27] W.-F. Cai, D.-L. Geng, Y.-H. Wang, RSC Adv. 2016, 6, 31732.
[28] Q. Li, Z. Xing, D. Wang, X. Sun, X. Yang, ACS Catal. 2016, 6, 2797.
[29] Z. Pu, Y. Xue, W. Li, I. S. Amiinu, S. Mu, New J. Chem. 2017, 41, 2154.
[30] R. Subbaraman, D. Tripkovic, D. Strmcnik, K.-C. Chang, M. Uchimura, A. P. Paulikas, V. Stamenkovic, N. M. Markovic, Science 2011, 334, 1256.
[31] R. Subbaraman, D. Tripkovic, K.-C. Chang, D. Strmcnik, A. P. Paulikas, P. Hirunsit, M. Chan, J. Greeley, V. Stamenkovic, N. M. Markovic, Nat. Mater. 2012, 11, 550.
[32] H. Yin, S. Zhao, K. Zhao, A. Muqsit, H. Tang, L. Chang, H. Zhao, Y. Gao, Z. Tang, Nat. Commun. 2015, 6, 6430.

[33] L. Wang, Y. Zhu, Z. Zeng, C. Lin, M. Giroux, L. Jiang, Y. Han, J. Greeley, C. Wang, J. Jin, Nano Energy 2017, 31, 456.
[34] N. Danilovic, R. Subbaraman, D. Strmcnik, K.-C. Chang, A. P. Paulikas, V. R. Stamenkovic, N. M. Markovic, Angew. Chem. Int. Ed. 2012, 51, 12495.
[35] N. L. Ritzert, T. P. Moffat, J. Phys. Chem. C 2016, 120, 27478.
[36] T. Nguyen, M. Boudard, M. J. Carmezim, M. F. Montemor, Sci. Rep. 2017, 7, 39980.
[37] H. Yuan, R. R. Lunt, J. I. Thompson, R. Y. Ofoli, ChemElectroChem 2017, 4, 241.
[38] Q. Dong, T. Ma, G. Yu, B. Hu, C. Guo, X. Zhang, Russ. J. Electrochem. 2015, 51, 236.
[39] S. Shahrokhian, R. Mohammadi, M. K. Amini, Electrochim. Acta 2016, 206, 317.
[40] S. B. Kulkarni, A. D. Jagadale, V. S. Kumbhar, R. N. Bulakhe, S. S. Joshi, C. D. Lokhande, Int. J. Hydrog. Energy 2013, 38, 4046.
[41] R. Wang, U. Bertocci, H. Tan, L. A. Bendersky, T. P. Moffat, J. Phys. Chem. C 2016, 120, 16228.
[42] N. Rajasekaran, L. Pogány, Á. Révész, B. G. Tóth, S. Mohan, L. Péter, I. Bakonyi, J. Electrochem. Soc. 2014, 161, D339.
[43] J. B. O'Sullivan, Trans. Farad. Soc. 1930, 26, 540. ; S. Sultan, Mater. Sci. Res. India 2006, 3(1a), 47.
[44] Y. Yu, S.-Y. Huang, Y. Li, S. N. Steinmann, W. Yang, L. Cao, Nano Lett. 2014, 14, 553.
[45] D. Kong, J. J. Cha, H. Wang, H. R. Lee, Y. Cui, Ener. Environ. Sci. 2013, 6, 3553.
[46] J. F. Callejas, J. M. McEnaney, C. G. Read, J. C. Crompton, A. J. Biacchi, E. J. Popczun, T. R. Gordon, N. S. Lewis, R. E. Schaak, ACS Nano 2014, 8, 11101.
[47] S. Sultan, P. K. Tikoo, Surf. Technol. 1984, 22, 241.
[48] T. Shinagawa, A. T. Garcia-Esparza, K. Takanabe, Sci. Rep. 2015, 5, 13801.
[49] L. Salvati, L. E. Makovsky, J. M. Stencel, F. R. Brown, D. M. Hercules, J. Phys. Chem. 1981, 85, 3700.
[50] A. N. Mansour, Surf. Sci. Spectra 1994, 3, 239.
[51] A. M. Venezia, R. Bertoncello, G. Deganello, Surf. Interface Anal. 1995, 23, 239.
[52] K. K. Lian, D. W. Kirk, S. J. Thorpe, J. Electrochem. Soc. 1995, 142, 3704.
[53] R. Chen, C. Yang, W. Cai, H. Wang, J. Miao, L. Zhang, S. Chen, B. Liu, ACS Energy Lett., 2017, 2, 1070.

Chapter-6

Photo-Electrochemical Water Splitting to Produce Hydrogen.

Photo-Electrochemical Water Splitting to Produce Hydrogen

Summary*

Strategically introducing band edge energetics concept in semiconducting films and integrating semiconductor films with an efficient water oxidation/water reduction catalyst to reduce charge recombination and photocorrosion can bring improvements in the photocurrent density which has been the strategies in PEC water splitting technology. Photodegradation limitations of Cu_2O can be overcome by introducing CuO and Ni_xP_y into Cu_2O films to form Cu_2O–CuO–NixPy photocathode. The individual effects of CuO and Ni_xP_y have been investigated and it is found that the activity enhancement stems mainly from the contribution of Ni_xP_y, whereas CuO helps with the unidirectional flow of photogenerated charges to prevent the photocorrosion of Cu_2O. On the other hand, amorphous catalysts, especially the mixed metal oxides/hydroxides, show better stability and activity in water oxidation because of their unique morphology. Facile, reproducible synthesis of these catalysts by a simple method has been problematic. We show for the first time the application of pulse plating to synthesize amorphous Co−La mixed double hydroxide (MDH) on $BiVO_4$/FTO (FTO, flourine-doped tin oxide). The method provides better adhesion and uniform deposits with controlled composition and grain size and facilitates fast charge transport, while lowering the charge recombination at the interface of the electrolyte and the semiconductor. It would be purposeful if the two electrode configuration for the complete water splitting is performed using sea water as the H_2 source with minimum bias. These photoelectrodes successfully split sea water in comparison to the phosphate buffer but photocathode tends to be less stable than the photoanode.

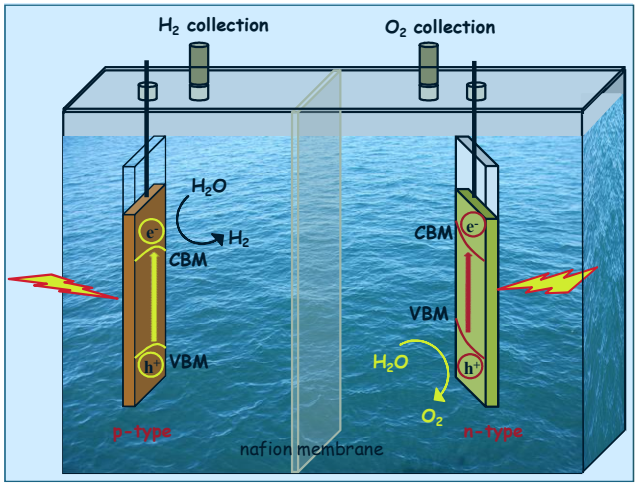

* Papers based on this chapter have appeared in ***ACS Energy Lett. (2017)***. ***Phys. Chem. Chem. Phys. (2018)*** and ***Chem. Eur. J (2018)***

1. Introduction:

In the earlier chapters we have investigated the possibility of various precious metal-free electrocatalysts especially doped carbon based materials for hydrogen generation by splitting water through electrochemical techniques. Among the various ways to produce hydrogen from water as discussed in **chapter 1,** most economical would be the use of decentralized energy source, the Sun. So photochemical water splitting does not require any additional energy input apart from a highly active catalyst. However, due to the limitations imposed by the inherent nature of the semiconductor materials used as catalysts like rapid charge recombination, lower solar-to-hydrogen (STH) yield, the need for use of sacrificial agents, this method has serious drawbacks before being applied in large scale hydrogen production. On the other hand, purely electrochemical technique for water electrolysis to produce oxygen and hydrogen has an advantage in the fact that large scale production can be attainable. The bottleneck here is the constraint imposed by the thermodynamic redox potential of water (H_2O/O_2 = 1.23 V and H^+/H_2 = 0 V, vs RHE). Hence the involved input energy in the form of electrical energy (voltage or current) is too much to compensate for the low cost energy production methods. In fact, for practical applications, steam reforming of various non renewable sources of energy is more efficient method to produce H_2 than electrolysis taking into account all the cost factors in the production involved. [For the commercial production of hydrogen, there are four major sources: natural gas (48%), oil (30%), coal (18%), and electrolysis (4%) with the percentages representing world's hydrogen production by those means. That is why steam reforming accounts for ~96% of hydrogen production where as electrolysis only accounts for 4% in industry scale hydrogen generation][1]. One of the ways to reduce the cost of hydrogen production is to couple electrochemical and photochemical techniques in water splitting-what is called as photoelectrochemical (PEC) water splitting. This would a long-term technology goal for energy related issues, with the prospects of zero emission of greenhouse gases.

Coupling solar energy with minimal electrical energy[2] to amplify the production of H_2 without compromising the cost is presently being attempted. This can be achieved by PEC water splitting devices (**Figure 6.1**). In PEC device hydrogen is produced from water using

sunlight and appropriate semiconductors used as calatysts referred as PEC materials. PEC material uses light energy to split water molecules into its constituent gases- hydrogen and oxygen. While the practical implacability may be complex, this is a long-term technology pathway, with the potential for low or no greenhouse gas emissions.

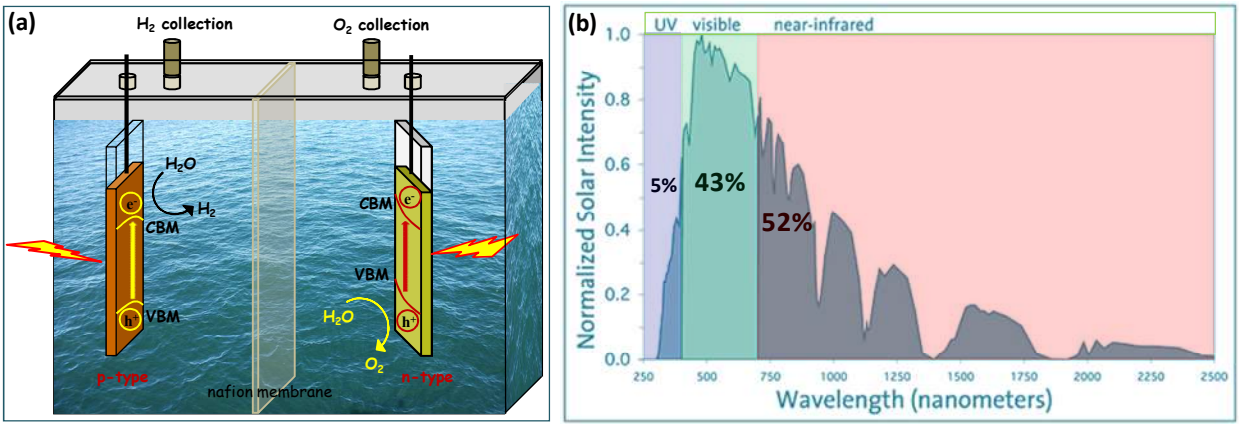

Figure 6.1: (a) Representation of Photoelectrochemical device in parallel configuration of photoanode and photocathode. (b) Solar radiation spectrum .

For a PEC material to be active in PEC water splitting technology, two basic requirements can be thought of as a photoelectrode - *Optical function* and *Catalytic function*. From the solar spectra depicted in **Figure 6.1b**, it is evident that maximum fraction of solar radiation spectrum falls within the wavelength range of 400-1000 nm corresponding to 1.2–3 eV range. This implies that materials within this band gap range would be ideal for PEC applications. Moreover harvesting solar energy by PEC water splitting to generate hydrogen is accomplished by two steps: separating the photogenerated charge carriers and carrying out the redox reaction at the electrode/electrolyte interface. The limiting efficiency of the photoelectrode is mainly due to the photocorrosive nature of the semiconductor, the recombination of charge carriers within the semiconductor or at the interface and the slow rate of the redox reaction (water splitting). Engineering the interfacial band edge energetics as well as the generation of excess usable charge carriers provides a means to improve the efficiency of PEC water splitting. For Photo anodes, semiconductors such as Fe_2O_3[3] and WO_3[4] serve the purpose for water splitting, while n-type $BiVO_4$ with its direct bandgap of ~2.4 eV, wherein the valence band maximum (VBM) is sufficiently positive relative to the water oxidation potential,

is effective for PEC water splitting. It also has its conduction band minimum (CBM) close to the H^+/H_2 redox potential, which helps in attaining low onset overpotential for the water-splitting process. Out of the scarcely reported oxide based p-type semiconductor photocathodes[5] compared to the extensively reported n-type semiconductor photoanodes[6], Cu_2O with a band gap of ~2 eV has been considered the only candidate that meets all the requirements[7] pertaining to both economical and practical factors like earth abundance, non toxicity, scalable low-cost fabrication processes and remarkable PEC activity. With a theoretical STH of 18%, Cu_2O could be considered to be a major competitor for PEC water splitting devices[8].

We selected $BiVO_4$ and Cu_2O as the parent semiconductor materials for the purpose overall PEC water splitting. We have addressed few limitations (mentioned below) in the activity enhancement by modifications in synthetic procedures and adopting new methods. $BiVO_4$ gives a low water oxidation photocurrent because of the small photogenerated carrier separation efficiency and meager light-harvesting ability as well as surface carrier transport efficiency.[9] These limitations can be minimized by the use of a suitable cocatalyst for water oxidation and introduction of heterojunctions[10] in the photoanodes or by impurity doping.[11] A strategic combination of an oxygen evolution catalyst (OEC) with $BiVO_4$ effectively increases the charge carrier concentration and reduces the recombination of photogenerated electrons and holes.[2] Most of the active OECs with high activity that have been reported are amorphous.[12-14] The short-range order in amorphous OECs creates abundant active sites, and their structural flexibility leads to long-term photoelectrochemical stability and efficient shuttling of charges in the redox process during water oxidation.[15] Amorphous monometallic oxide/hydroxide compositions, however, exhibit slow water oxidation kinetics due to higher Tafel slopes and a significant overpotential.[16]

It has been shown that a rational combination of heterogeneous 3d transition metals outperforms the activity shown by monometallic compositions.[17-18] In this regard, the use of mixed metal amorphous hydroxides and oxides seems to be beneficial because they favor charge transfer and structural modifications while retaining the stability.[19-20] Only a handful of amorphous mixed metal hydroxides/oxides have been exploited for photoelectrochemical (PEC)

purposes on $BiVO_4$ films, possibly because of the difficulties in fabrication techniques. In particular, the application is mostly limited to Co-, Ni-, Fe-, and Mn-based amorphous OECs with

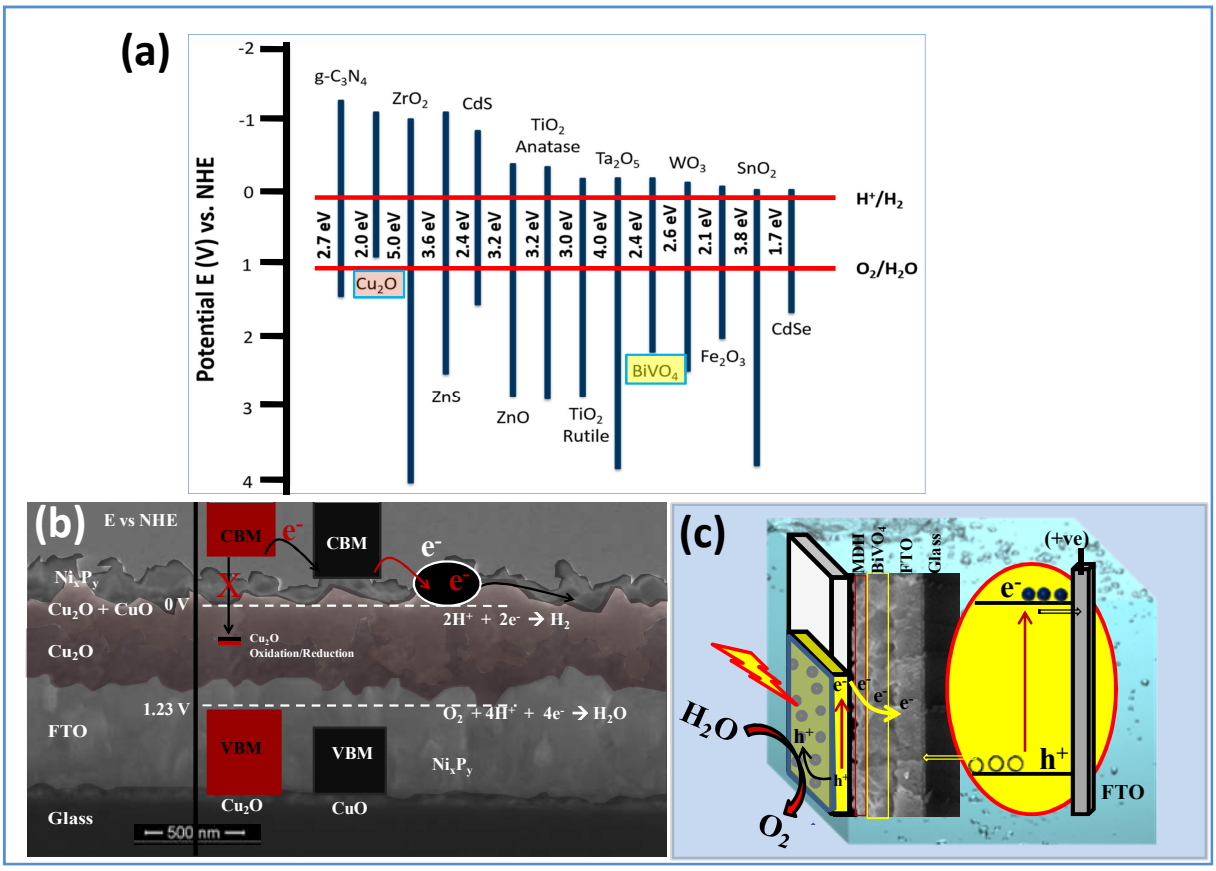

Figure 6.2: (a) Selection of appropriate semiconductor material for PEC water splitting based on the relative band position alignments with respect to water redox potential. Plot shows the position of the conduction and valence band in comparison to water redox potential vs potential (NHE). Reproduced with permission[54], Copyright 2016, MDPI AG, Basel, Switzerland. (b) and (c) are respectively the schematic representation of PEC water splitting activity in Cu_2O and $BiVO_4$ based systems with appropriate modifications.

comparable ionic sizes. Incorporation of rare earth cations[21-22] in transition-metal-based mixed oxides/LDHs is shown to enhance the catalytic efficiency, but these materials have not been explored adequately for PEC water oxidation. The transition metal here acts as the redox active center, while the rare earth ion induces the changes in crystallinity.[23] Although synthesis of some amorphous metal oxides and hydroxides has been achieved using photochemical metal–organic deposition (PMOD),[3] electrodeposition,[24] and photoelectrodeposition (PED),[25] it remains a challenge to use these methods for every metal combination. These approaches are excellent for synthesizing metal oxide OECs, but a proper control on the

thickness and the amount of OECs on the semiconductor film remains the limiting aspect due to factors like voltage protocols and synthesis conditions; hence, they are not agreeably expandable to the mixed metal hydroxides for an array of metal combinations.

Hence in this chapter we demonstrate the use of the pulse plating method to generate amorphous mixed metal hydroxides on a $BiVO_4$ photoanode, which showed higher activity and stability. Also to address the issue of fast charge recombination by applying appropriate band edge energetic concept, we have made Cu_2O–CuO–Ni_xP_y as the electrode with modified interfacial band edges to promote hydrogen generation. Both the schematics are represented in **Figure 6.2**. The redox potentials of Cu_2O are positioned in between the water splitting redox potentials, rendering the photogenerated charge carriers to be thermodynamically more liable to photocorrode Cu_2O upon light illumination.[26] This can be blocked by the appropriate thickness of successive protective layers[7,27] in the heterojunction configuration wherein the band edge positions are such that the photogenerated minority carriers (electrons) are unidirectionally utilized for water reduction while the majority carriers (holes) move towards the bulk Cu_2O.

In order to obtain a high current density, an optimum thickness of the layers of protective materials and of the hydrogen evolution reaction (HER) catalyst is essential. This is dependent on the minority carrier diffusion length and the space charge region at the electrode/electrolyte interface. Furthermore, the interfacial electron transfer kinetics has to be fast enough to promote water reduction. With this objective, we have fabricated the Cu_2O–CuO–Ni_xP_y photocathode with an optimized thickness of successive layers by electrodeposition combined with pulse plating, affording a uniform thickness and morphology of the layers. Nickel phosphide has been shown to be an excellent electrocatlytic HER catalyst with an activity close to Pt.[28-29] To the best of our knowledge, the use of Ni_xP_y on Cu_2O–CuO to obtain a high current density has not been reported for water splitting.

2. Scope of the present investigations

In this chapter, we demonstrate a convenient method to synthesize amorphous mixed metal hydroxides (MDH) of La and Co on $BiVO_4$/FTO as a photoanode and investigate the PEC

water-splitting activity. The same strategy has been applied to fabricate photocathode Cu_2O–CuO–Ni_xP_y which has modified interfacial band edges to promote hydrogen generation. In the La-Co based photoanode, Co acts as an electron-transfer agent while La causes an increase in the amorphous nature of the catalyst, leading to its stability. The study shows pulse plating for the electrochemical deposition of MDH or Ni_xP_y to be an apt strategy to deposit on respective photoelectrodes: $BiVO_4$/FTO and Cu_2O-CuO. This method is reproducible and can be extended to other combinations of metals. The use of $BiVO_4$/Co−La$(OH)_x$ MDH for PEC water splitting has not been extensively explored until now. Interestingly, this system exhibits excellent early photocurrent in comparison to the state-of-art photoanodes. The detailed discussion related to enhanced activity and surface charge-transfer efficiency (η_{trans}) of ~75% and lower charge-transfer resistance (R_{ct}) in OER kinetics is included. Considering the abundance of sea water and limited availability of fresh water, overall sea water splitting would be advantageous. Hence the efficacy of these photoelectrodes towards sea water splitting has also been studied.

3. Experimental section:

3.1. Materials:

Bismuth Nitrate [Sigma Aldrich, $Bi(NO_3)_3.5H_2O$], Potassium Iodide [Merck Ltd. KI], p-Benzoquinone [Sigma Aldrich, $C_6H_4(=O)_2$], Lanthanum Nitrate [Alfa Aesar, $La(NO_3)_3.\ xH_2O$], Cobalt Nitrate [Sigma Aldrich, $Co(NO_3)_3$, Vanadyl acetylacetonate [Sigma Aldrich, $VO(acac)_2$], Copper sulfate pentahydrate [Sigma Aldrich, $CuSO_4.5H_2O$], Lactic acid [SD Fine Chem. India], Sodium Hydroxide [Sigma Aldrich, NaOH], Nickel Acetate [Sigma Aldrich, $Ni(OAc)_2$], Phosphoric acid [H_3PO_4 SD Fine Chem. India], Phosphorous acid [H_3PO_3, SD Fine Chem. India], N-methylformamide (NMF) [SD Fine Chem. India], FTO slide [Sigma Aldrich, surface resistivity ~7 ohm/cm^2], Cu wires, Enamel remover, Ag paste.

3.2 Fabrication of electrodes:

3.2.1. Photoanode:

3.2.1.a. FTO/$BiVO_4$: $BiVO_4$ film on FTO was obtained by electrochemical deposition in three electrode setup. FTO was used as the working electrode, Ag/AgCl as the reference and Pt coil as

the counter electrode. Prior to all electrochemical deposition process, surface of FTO was cleaned by soap solution followed by ultra-sonicating in ethanol-acetone (1:1) mixture for 30 minutes. First, BiOI was deposited cathodically on FTO substrate at -0.2 V (vs Ag/AgCl) for 6 minutes by passing an equivalent charge of ~350 mC/cm^2. 100 mL of 0.2 M VO(acac)$_2$ dissolved in DMSO was then dropcasted on the freshly prepared FTO/BiOI film and annealed at 500^{o}C for 2 hours at a heating rate of 2^{o}C/min. Finally the excess V_2O_5 produced due to annealing was removed from the $BiVO_4$ electrode by soaking it in 1 M NaOH solution for 20 minutes.

3.2.1.b. FTO/$BiVO_4$/CoLa MDH: For the deposition of Co and La MDH on the $BiVO_4$ film, pulse plating technique was employed. Chronopotentiometry (CP) method was used for the co-deposition of Co and La MDH. We selected two extremes of potential -0.9 V and -1.2 V vs Ag/AgCl (anodic and cathodic potential limits respectively) and fix the current values of -0.005 A (anodic) and 0.01 A (cathodic). We used 4 segments in steps between these two current values with a hold time of 2.5 seconds at each value. The deposition was carried out for different number of cycles to vary the amount and thickness of the deposited Co-La MDH film on $BiVO_4$ (**Figure 3**). These parameters were optimized after series of control experiments on bare FTO and on $BiVO_4$ and recording the absorbance and analyzing FESEM images to control the amount and thickness of MDH on $BiVO_4$. In addition to this, to test the effect of single hydroxides, and the effect of $BiVO_4$/hydroxide and electrode/electrolyte interface, only Co and La hydroxides and layer-by -layer deposition were carried out on $BiVO_4$ keeping the parameters unaltered as that for CoLa MDH.

Optimized CP Parameters:

High E Limit (V) = -1.1	Cathodic current: 0.01 A
High E Hold Time (s) = 1	Anodic current: -0.005A
Low E Limit (V) = -1.2	Low E Hold Time (s) = 1
Cathodic Time (s) = 2.5	Anodic Time (s) = 2.5
Segments = 4	

3.2.2. Photocathode:

For photoanode deposition, FTO as the working electrode, Hg/Hg_2Cl_2 as the reference and a Pt coil as the counter electrode.

3.2.2.a. FTO–Cu_2O: Cu_2O was electrodeposited as follows. The first electrolyte was prepared by dissolving 15 g $CuSO_4$ in 90% lactic acid (25 mL) in a RB flask with continuous stirring. 75 mL of 5 M NaOH was then slowly added with stirring and the obtained dark blue solution was stirred for 8 hours. The pH of the electrolyte was maintained at 12 by adding 5 M NaOH.

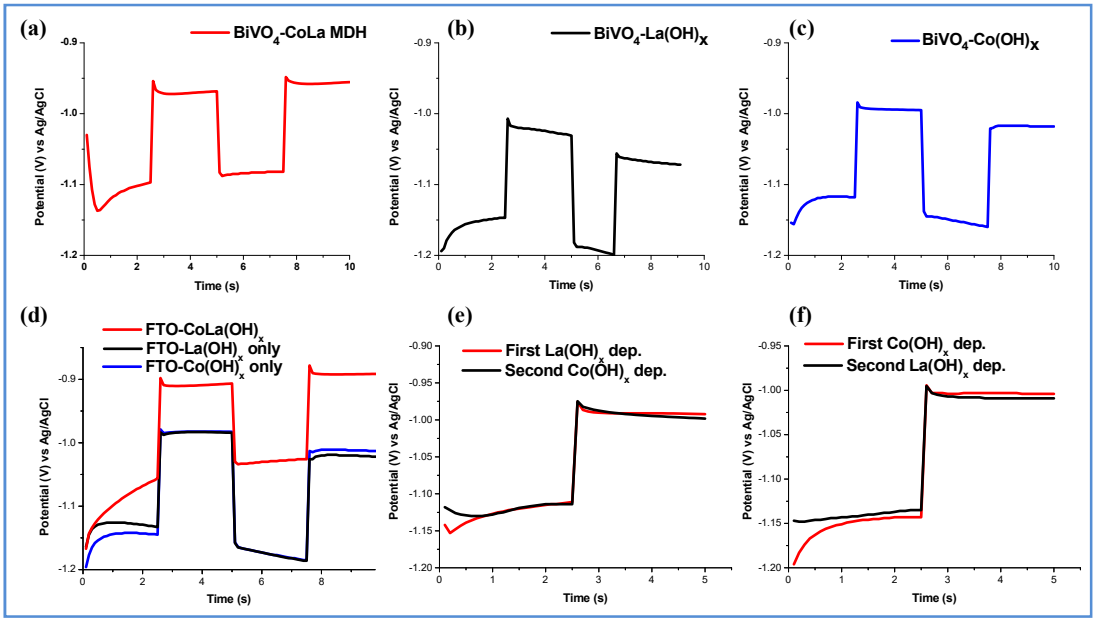

Figure 6.3: Chronopotentiometry plot of pulse plating cycles adopted during potential sweep for various of hydroxides of La and Co on $BiVO_4$ and FTO.(a) to (c) on $BiVO_4$; (d) on FTO ; (e) and (f) layer by layer deposition of monometallic hydroxides on $BiVO_4$.

Potentiostatic (at -0.45 V) and potentiostatic/galvanostatic pulse plating deposition were carried out for 30 minutes with an approximate charge deposition of ca. 500 mC.

3.2.2.b. FTO–Cu_2O–CuO: The Cu_2O–CuO interface was created by controlled thermal annealing of Cu_2O film at 350°C in air for 20 minutes. The oxidation of Cu_2O to CuO can be tuned by controlling the duration and temperature of the process.[27,30] After a series of control experiments, we could get an optimum composition of the Cu_2O + CuO layer.

3.2.2.c. FTO–Cu_2O–CuO–Ni_xP_y: On FTO–Cu_2O–CuO film, controlled pulse plating electrodeposition of amorphous Ni–P was carried out from a mixture of 50 mL of 0.5 M nickel acetate in 5 wt% NMF, 1.1 mL H_3PO_4 and 1.25 g H_3PO_3. Dual pulse plating as demonstrated in our earlier studies was used to deposit a controlled thickness of amorphous Ni–P layer which upon annealing at 550°C for 30 minutes resulted in the formation of the FTO–Cu_2O–CuO–Ni_xP_y photocathode. 8 cycles of sequential potentiostatic and galvanostatic cycles with cathodic and

anodic hold times of 4 and 1 seconds, respectively, and cathodic and anodic currents of 3 mA and 3.6 mA within the limits of -1 V and 0.3 V were applied.

3.3. Characterizations:

Powder X-ray diffraction (PXRD) of photoelectrodes were recorded using a Bruker AXS D8 Discover diffractometer attached with Cu Kα radiation. UV–Vis absorption spectra were examined using a UV-Perkin Elmer UV/Vis spectrometer. Transmission electron microscopy (TEM, Technai F30 UHR, 200 kV) was used to study the crystal morphology and Field emission scanning electron microscopy (FESEM, FEI Quanta operated at 15 kV, equipped with EDAX) was used to investigate the composition, morphology and thickness of various layers in electrodes. The elemental ratios of the as prepared electrodes were confirmed by optical emission spectrometry-inductively coupled plasma spectrometry (OES−ICP) (Perkin Elmer Optima 7000 DV). X-ray photoelectron spectroscopy (XPS, Mg–Kα X ray source, 1253.6 eV) was recorded to analyze the composition of samples. Raman spectra were recorded on LABRAMHR-800 using green laser (514 nm) at ca. 10 locations on the electrode film. FT-IR study was carried out on a Bruker IFS 66v/S instrument.

3.4. Electrochemical Impedance Spectroscopy analysis:

The data points were fitted by CHI760E inbuilt software (Model 700E Series Electrochemical Analyzer/Workstation, CHI Inc., with simulations and fitting commands) by proposing an equivalent modified Randles' circuit model described. An impedance simulator is integrated into the program. The fitting error is ~0.01 and elapsed time ~450 seconds. The symbols represent the experimental data and the lines represents fitting results utilizing the equivalent circuit.1

Circuit Element Properties: R=Resistor; C=Capacitor; Q= Constant phase element; j=current density; ω= frequency. Y=Conductance.

Element	Impedance	Conductance	Phase
R (resistor)	$Z_R = R$	$Y_R = 1/R$	$\Phi = 0$
C (capacitor)	$Z_C = -j/C$	$Y_C = j\omega C$	$\Phi = \pi/2$
Q (phase)	$Z_Q = (j\omega)^{-n}/Y_o$	$Y_Q = (j\omega)^n Y_o$	$\Phi = n\pi/2,\ 0 < n < 1$

From CHI Instruments Manual; J. R. Macdonald, Ann. Biomed. Eng., 20, 289-305 (1992) or "Impedance Spectroscopy", E. Barsoukov and J. R. Macdonald, Wiley, Hoboken, 1987 (1st ed), 2005 (2nd ed).

3.5. X-Ray Photoelectron Spectroscopy analysis:

XPS analysis was done using XPSPEAK4.1 software. Background subtraction was performed using Shirley functions with the optimizations to bring the Shirley background data points which are higher than the signal intensities at some points. The optimization helps in increasing the slope value until the Shirley background is below the signal intensities. To add peaks for the deconvulation of XPS core level peak, Gaussian-Lorentzian sum function was used with adjustable parameters like peak position, peak area, FWHM and % Gaussian-Lorentzian functions. Depending on the number of anticipated peaks, the peak were deconvulated by adjusting the parameters until the final combined peak from various added peaks matched with the actual data obtained from XPS measurement (raw data).

3.5. PEC water splitting study:

The photoelectrochemical (PEC) measurements were performed in a three-electrode open cell with vertical illumination of the light on the photoelectrode surface. The electrode connections with Cu wire were provided by Ag-paste (in amyl acetate solvent) covered by epoxy resin (araldite) as an insulating cover. Solar simulator (Newport, model: 91160-1000, 300W Xe lamp) equipped with AM1.5G filter with the simulated light intensity adjusted to 100 $mWcm^{-2}$ on the FTO surface (calibrated using thermopile detector and reference solar cell certified by NREL) was used as a light source for photocurrent measurements. The illuminated area was 1 cm^2. For the photocurrent measurements, LSV was taken at a scan rate of 5 mV/s. (CHI760E workstation) and Potassium phosphate, 0.5 M (K-Pi, pH-7) and 0.5 M Na_2SO_4 was used as electrolyte. Na_2SO_3 (0.5M) was used as a hole scavenger for few specific experiments. The electrolyte was thoroughly purged with N_2 prior to measurements.

The potentials referenced to the Ag/AgCl and Hg/Hg_2Cl_2 reference electrode were converted to potentials referenced to the reversible hydrogen electrode (RHE) using the Nernst equation.

$$E_{RHE} = E^0 + (0.059 \times pH) + E_{expt.}$$

where E^0 is the standard reduction potential of Ag/AgCl or Hg/Hg_2Cl_2.

3.6. Mott-Schottky (MS) Analysis:

Mott-Schottky plots for the electrodes were obtained using a CHI760E electrochemical workstation. An amplitude modulation of 5 mV at frequencies of 1 kHz was applied. The three-electrode setup was used with a 0.5 M phosphate buffer (pH 7) or 0.5 M Na_2SO_4 solution.

3.7. Detection and quantification of H_2 and O_2 gases

For the collection of gases, custom made PEC cell with two separate compartments divided by nafion membrane was used. O_2 measurements were carried out using an Ocean Optics fluorescence-based oxygen sensor (FOSPOR-R 1/16”). The measurement was done in mole% for both- the headspace and the dissolved oxygen. O_2 measurements were recorded at 1.23 V (vs RHE) and compared with the expected O_2 evolution based on the charge flowing in the process of amperometric i-t study (Faradaic efficiency). For Hydrogen detection, 3 mL of headspace evolved gas was manually collected from the cell and analyzed in PerkinElmer Clarus ARNEL 580 gas chromatograph.

4. Results and discussion:

The two photoelectrodes fabricated by us have been individually studied for Photoelectrochemical application towards water splitting to produce hydrogen and oxygen. These form components of a full water splitting cell separated by gas separating membrane (as discussed in introduction). The discussion comprise of three parts: part-A: Photoanode, part-B: Photocathode and part-C: overall water splitting using sea water. In part C the two electrode configuration for the complete water splitting has been studied with minimum bias in phosphate buffer as well as sea water splitting. The rationale of synthetic protocol, PEC activity and conclusion from the study is discussed as follows:

Part A: Photoanode

Photoelectrochemical Oxygen Evolution Reaction Activity of Amorphous Co–La Double Hydroxide-$BiVO_4$ Fabricated by Pulse Plating Electrodeposition

The parameters for pulse plating deposition of MDH on $BiVO_4$ were optimized after a series of control experiments on bare FTO and on $BiVO_4$, with post analysis of absorbance and FESEM images, to control the amount and thickness of MDH on $BiVO_4$. Control synthesis of only $La(OH)_x$ and $Co(OH)_x$ on $BiVO_4$ was also carried out to discern the origin and mechanism of catalytic activity. For the control experiments, three catalysts [Co–La MDH, $Co(OH)_x$, and $La(OH)_x$] were also deposited directly on the FTO substrate without $BiVO_4$. The X-ray diffraction patterns of $BiVO_4$-MDH on FTO (**Figure 6.4**) showed reflection due to monoclinic scheelite structure of $BiVO_4$ besides those of SnO_2 (ICSD-33242; space group, I112/b).

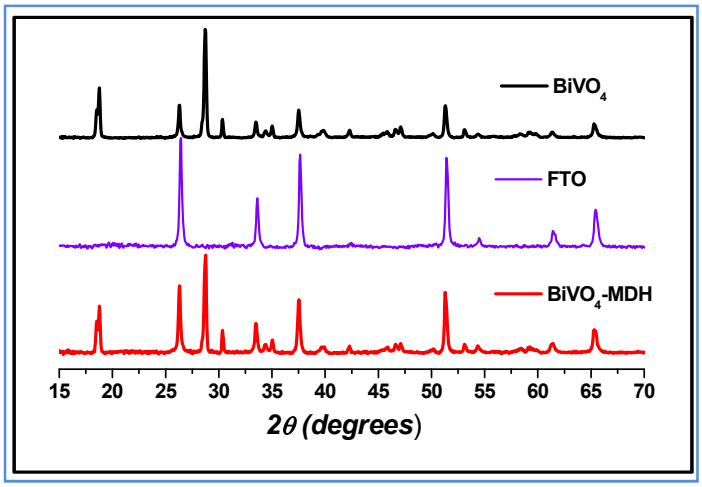

Figure 6.4: X-Ray diffraction patterns of $BiVO_4$ (black), FTO (purple) and $BiVO_4$-MDH (red). Space group = I112/b was obtained for both based on ICSD-33242. No visible changes could be found by comparing these patterns because of the amorphous nature of the deposited MDH. The amorphous nature of MDH was discerned from the controlled experiment whereby only La and Co hydroxides were deposited on FTO without $BiVO_4$.

The reflection corresponding to the hydroxides of La or Co was not found because of its amorphous nature. The layered deposition of nanoporous $BiVO_4$ and MDH on FTO is revealed by the cross-sectional scanning electron microscopy (FESEM) image (**inset of Figure 6.5a**). In the high magnification FESEM images, there were appearances of rough patches distributed uniformly over the $BiVO_4$ after the MDH deposition (**Figure 6.5b–e**) which depict the deposition of MDH. The micro- and nanostructural difference between the two is revealed by TEM analysis. **Figure 6.6a,b** confirms the crystalline nature of the as-deposited $BiVO_4$ on FTO (**SAED pattern in insets 6.6c1 and d1**). The HRTEM image and SAED pattern of $BiVO_4$-MDH (**Figure 6.6e and the insets e1 and e2**) confirm the deposition of amorphous MDH on $BiVO_4$ crystallites.

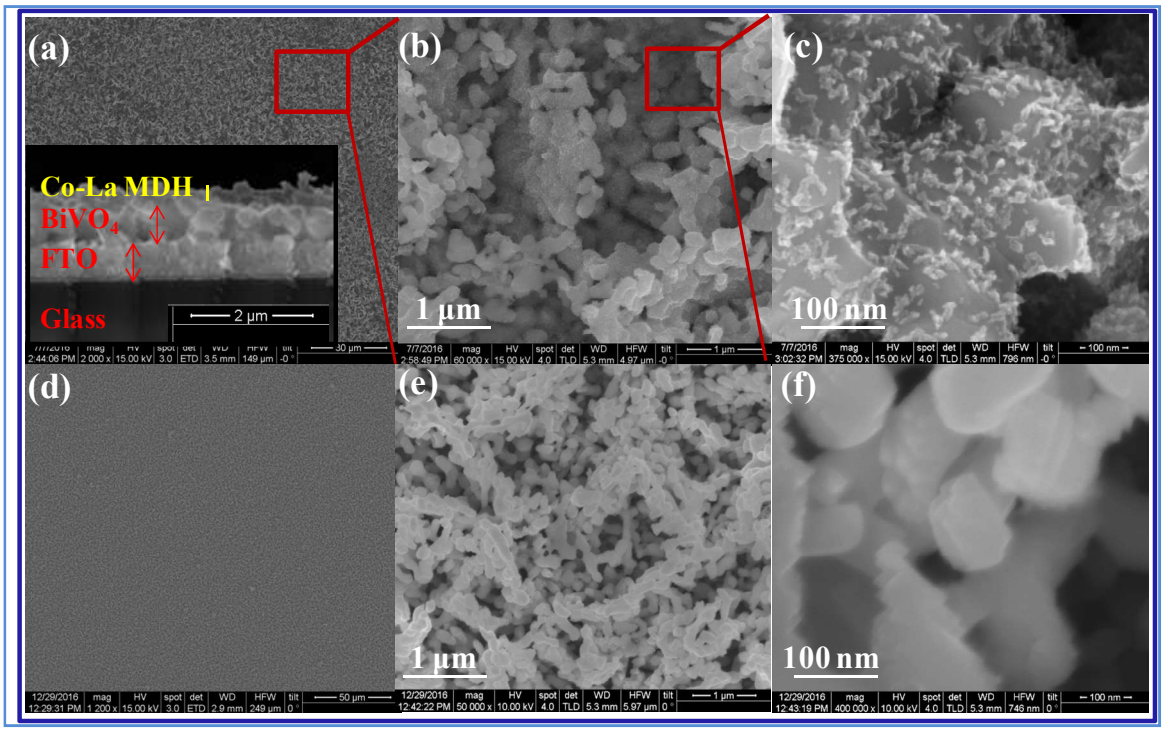

Figure 6.5: Morphology study of the electrodes. (a) FESEM image (top view) of the $BiVO_4$-MDH showing the porosity in the electrode. The inset shows the cross-sectional view of the electrode. FESEM images of (b) $BiVO_4$-MDH and (d, e) pristine $BiVO_4$. High-magnification SEM images show the presence of additional patches of cocatalyst on (c) $BiVO_4$-MDH in contrast with (f) $BiVO_4$.

The well-interconnected amorphous MDH particles and crystalline $BiVO_4$ (**Figure 6.6f and inset f1**) over a wide area in the deposited film provides proof of the remarkable advantage of the pulse plating technique we employed. The SAED pattern shows the presence of crystalline $BiVO_4$ (dots) and amorphous MDH (rings) (**Figure 6.6, insets e1, f1, and f2**). LaCo MDH/$BiVO_4$ was investigated by various other spectroscopic techniques. The survey scan of the X-ray photoelectron spectroscopy (XPS) spectrum shows the presence of La and Co on the surface of $BiVO_4$ (**Figure 6.6a**). The La 3d signal corresponds to $La(OH)_3$,[31] and the Co 2p signal along with satellite peaks (**Figure 6.6b,c**) shows the coexistence of Co^{2+} and Co^{3+} species (relative ratio of 1.90).[32-33] The La−Co ratio is close to 1.1 for the deposition of four cycles of MDH on $BiVO_4$ (ICP-OES and XPS). The X-ray absorption near-edge structure (XANES) region of the XAS spectra of $BiVO_4$-MDH was collected at Co K-edge and compared with that of the reference material Co_3O_4 (**Figure 6.7**). We emphasize mainly the main edge region of XANES spectra here for the confirmation of oxidation states of Co.

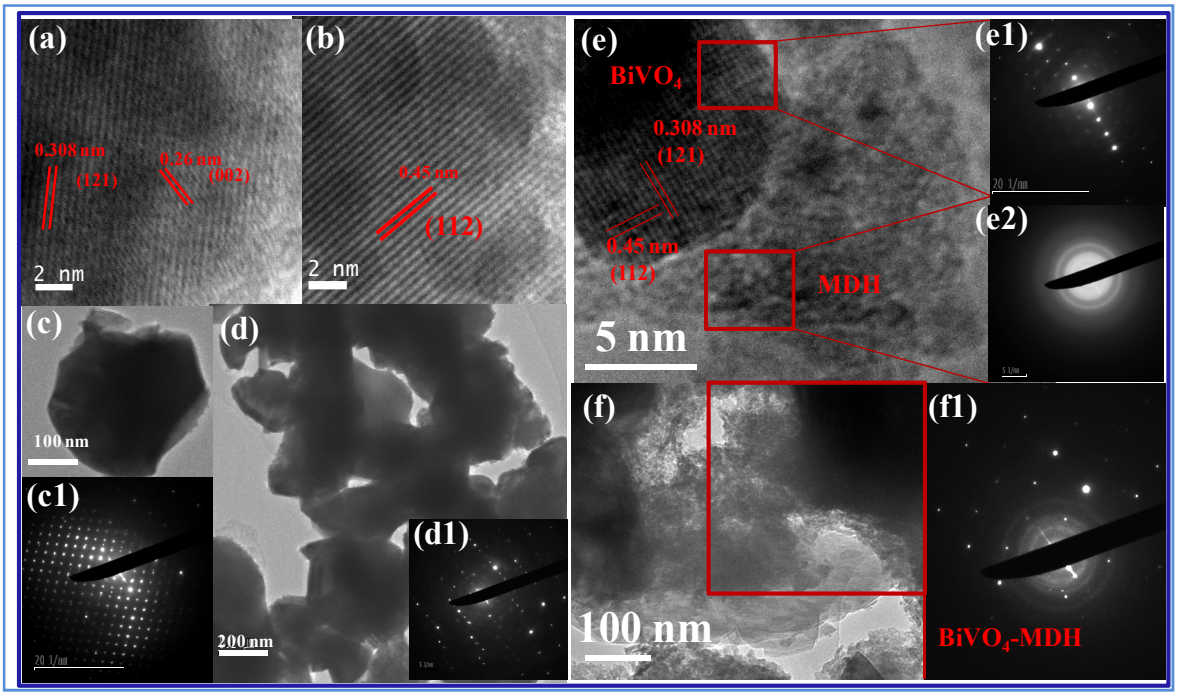

Figure 6.6: (a, b) HRTEM images of monoclinic scheelite phase of $BiVO_4$. Panels (c) and (d) show the crystalline $BiVO_4$ particles interconnected with each other in the film. The insets (c1 and (d1) are the SAED patterns highlighting the crystalline nature. Panels (e and f) show the presence of both $BiVO_4$ and amorphous MDH in the $BiVO_4$-MDH catalyst. The layer of LaCo MDH is homogeneously distributed over $BiVO_4$. SAED as shown by the diffraction patterns shows the presence of both crystalline and amorphous $BiVO_4$ and MDH, respectively (see insets e1, e2, and f1).

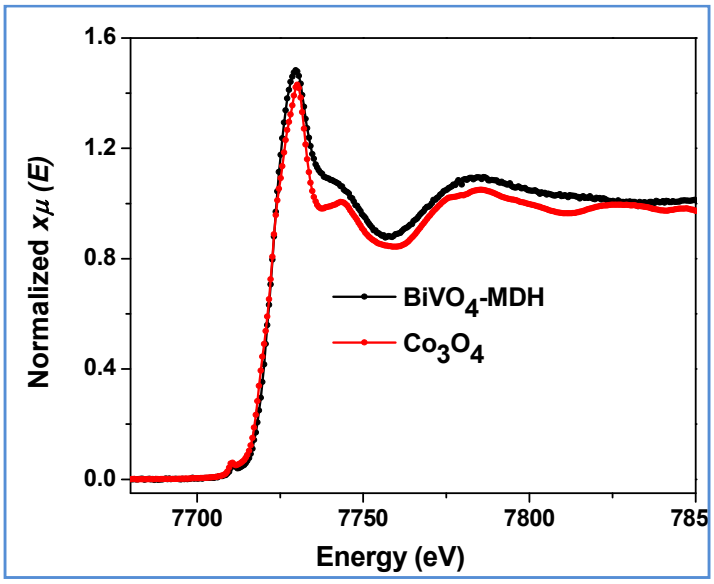

Figure 6.7: Normalized XANES spectra of Co-K edge, of the $BiVO_4$-MDH catalyst showing the presence of both 2+ and 3+ oxidation states of Co on $BiVO_4$-MDH

The normalized spectra at the main edge region for $BiVO_4$-MDH matches exactly with that of the Co_3O_4 confirming the presence of the 2+ and 3+ states of Co in the film. The appearance of three extra bands at 476 cm^{-1}, 519 and 680 cm^{-1} in the Raman spectra due to the MDH deposition on $BiVO_4$ is prominent from **Figure 6.8d**.

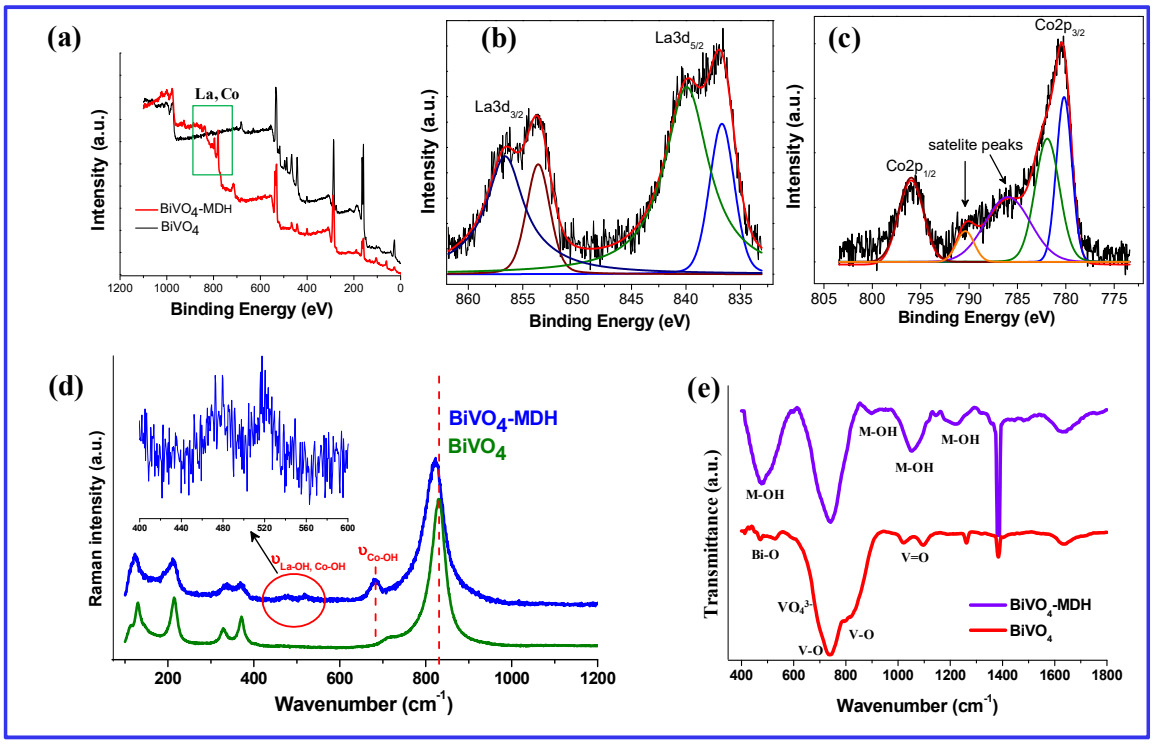

Figure 6.8: XPS spectra of pristine $BiVO_4$ and MDH deposited on $BiVO_4$. (a) Survey scan of the two catalysts showing the presence of La and Co on the surface of $BiVO_4$. Core-level spectra of (b) La 3d and (c) Co 2p on the surface of $BiVO_4$-MDH catalyst. (d) Raman spectra of $BiVO_4$ and $BiVO_4$-MDH showing significant broadening and shifting of various stretching and deformation modes of $BiVO_4$. Inset shows the presence of La and Co hydroxides bond in magnified view in 400–600 nm regions. (e) FTIR spectrum of the two catalysts showing the difference and the presence of M–O and M–OH bonds in addition to the bands due to $BiVO_4$.

The first two bands can be attributed to O-M-O (M = La,Co) bending modes while the last is due to the Co–OH stretching vibration. Notably, these bands are also observed for MDH directly deposited on FTO without $BiVO_4$ (**Figure 6.9**). The characteristic intense band at 830 cm^{-1} due to the symmetric stretching of the VO_4^{3-} tetrahedron becomes broad and appears at 826 cm^{-1} on MDH deposition. This could be caused by the elongation in V–O bond length as reported previously[34-36] (**Figure 6.8d**). The external modes (translational and rotational) of VO_4^{3-} at 128 and 214 cm^{-1} get shifted and become broad and weak upon MDH deposition,

implying that the metal hydroxide deposit is intimately bonded to the local structure of $BiVO_4$.[32-33]

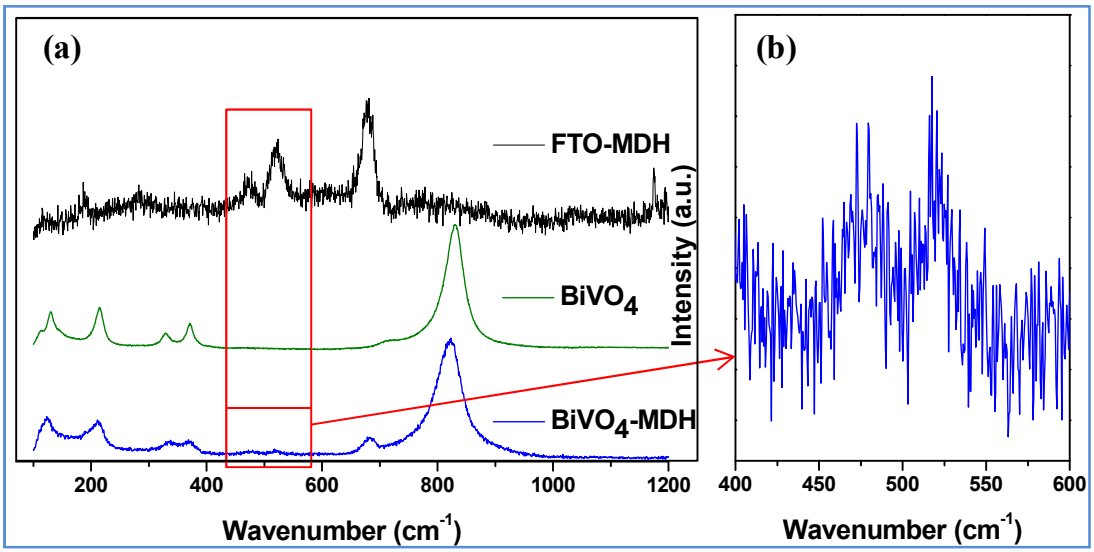

Figure 6.9: (a) Raman spectra of MDH and $BiVO_4$-MDH highlighting the presence of M-OH bonds from the $LaCo(OH)_x$ MDH. (b) The magnified image of the Raman spectra of $BiVO_4$-MDH.

A pair of bands which appears at 324 cm^{-1} and 366 cm^{-1} due to asymmetric and symmetric deformations of VO_4^{3-} tetrahedra respectively, becomes broad and weak in intensity on MDH deposition. The external modes (translational and rotational) of VO_4^{3-} are slightly red shifted and broadened due to the presence of metal hydroxide moiety and its interaction with the VO_4^{3-} tetrahedron. Since the translational mode is more sensitive to the mass change than the rotational band, the shift and the broadening (asymmetry of peak) is more prominent for this band. The asymmetry, the broadening of the peaks and shifting of the characteristic peaks of pristine $BiVO_4$ (129, 214 324, 366, 710 and 830 cm^{-1}) not only confirms the presence of MDH in the substrate matrix but also specify the metal hydroxide deposition on local structure of $BiVO_4$.

Additionally, the Fourier transform infrared (FTIR) spectrum of $BiVO_4$ differs strikingly after MDH deposition (**Figure 6.8e**). The IR bands at 477 and 530 cm^{-1} due to La−O and Co−OH, respectively, corroborate the conclusions from the Raman spectra. ICP-OES analysis revealed ca. 2−3 wt% of MDH on $BiVO_4$ (by Bi:Co or La ratio). The light absorption of various nanoporous electrodes was between 450 and 475 nm in accordance with its band gap of ~2.53 to 2.57 eV as

given by the tauc plot (**Figure 6.10**). It must be noted here that the pulse plating technique is the key for the excellent morphology in contrast to conventional direct cathodic or anodic deposition.

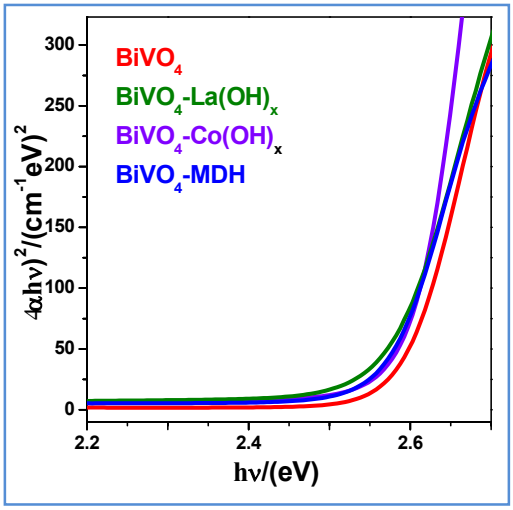

Figure 6.10: Tauc plot corresponding of UV-Vis absorption spectrum of $BiVO_4$ and various catalysts.

The photoelectrochemical water splitting activity of $BiVO_4$-MDH was measured under AM1.5G (100 mW cm^{-2}) illumination in 0.5 M potassium phosphate (K-Pi) buffer (pH 7). The photocurrent density–potential (*J*–*V*) curves of the electrodes are shown in **Figure 6.11**. $BiVO_4$ alone has an onset potential of ~0.72 V, while with MDH deposited on it, the onset potential shifts to a much more negative value, 0.19 V (**Table 1**).

The photocurrent density for $BiVO_4$-MDH is significantly higher than that for bare $BiVO_4$ and for monohydroxide. The early onset potential and high photocurrent at a lower potential (<0.6 V) make $BiVO_4$-MDH a promising electrode for water splitting cells or as a photoelectrochemical diode. It is understandable that $BiVO_4$–$Co(OH)_x$ shows improved photocurrent density as $Co(OH)_x$ is a good OER catalysts. While $La(OH)_x$ is not a good water oxidation catalyst (in the dark), the improved photocurrent of co-deposited La–$Co(OH)_x$ is due to either the synergistic effect and/or the improved interface of $BiVO_4$–MDH catalyst that brings efficient charge separation and transport.

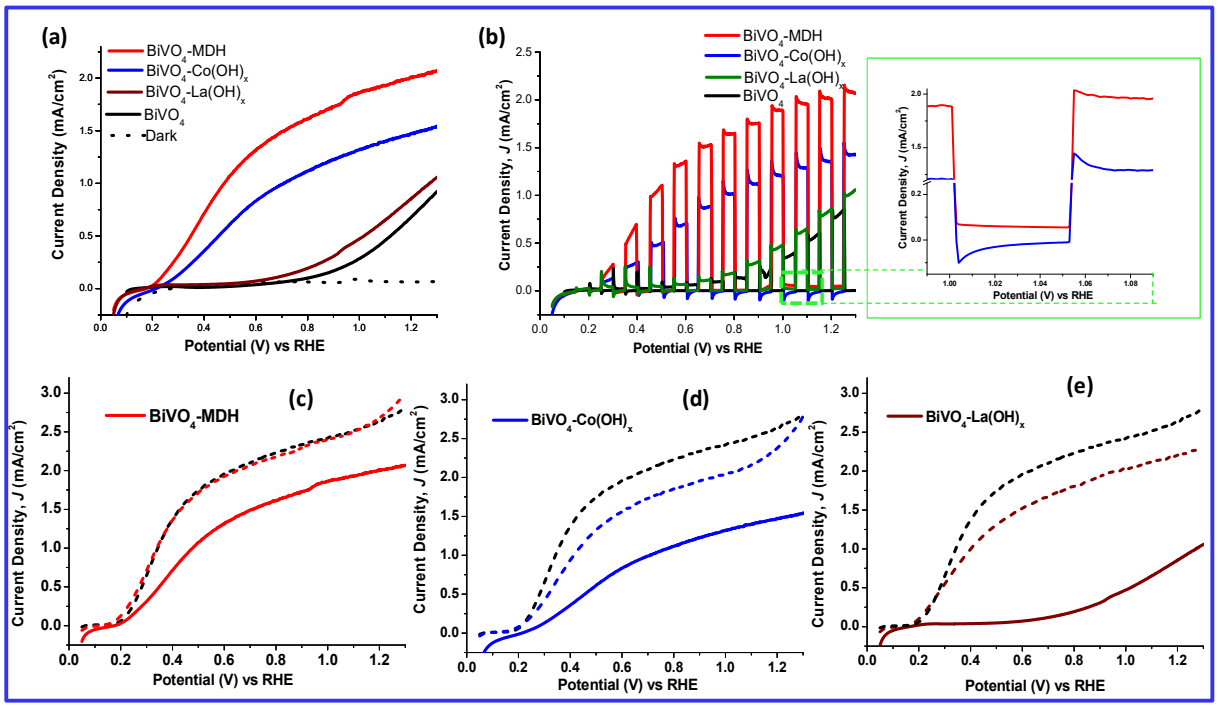

Figure 6.11: (a) *J*–*V* curves of $BiVO_4$ and different deposited OECs in a 0.5 M phosphate buffer (pH 7) under AM1.5G illumination. The dark current is shown as a dashed line. (b) *J*–*V* curves under chopped light illumination. Right Inset highlights expanded view of the photocurrent transients measured for a 30s pulse irradiation for $BiVO_4$–$Co(OH)_x$ and $BiVO_4$-MDH. Comparison of photocurrent for sulfite oxidation (dashed) and water oxidation (solid) for $BiVO_4$ (black dashed) and (c) MDH, (d) $Co(OH)_x$ only, and (e) $La(OH)_x$ only, with and without the presence of hole scavenger 1.0 M Na_2SO_3.

Table 1: Summary of PEC activity of the photoanodes.

Sample	KPi Buffer pH-7		KPi Buffer + Na_2SO_3	
	Onset (V)	*J* @ 0.6 V (mA/cm^2)	Onset (V)	*J* @ 0.6 V (mA/cm^2)
$BiVO_4$/MDH-4 cycles*	0.192	1.323	0.174	1.933
$BiVO_4$/MDH-2 cycles	0.209	0.502	0.172	0.852
$BiVO_4$/MDH-8 cycles	0.23	0.124	0.17	0.349
$BiVO_4$/$Co(OH)_x$	0.22	0.844	0.177	1.576
$BiVO_4$/$La(OH)_x$	0.57	0.07	0.175	1.52

*Cycles represents the number of pulse plating cycles employed in electrode fabrication.

To discern these two effects, we measured photocurrent in the presence of 1.0 M Na_2SO_3. Because the sulfite oxidation on the catalyst surface is fast in comparison to the kinetically and thermodynamically more difficult H_2O oxidation, it enables us to study the photocurrent and photoelectrochemical properties independently without the effects of slow kinetics of water oxidation at the electrode–electrolyte interface. It is noteworthy that, with only $BiVO_4$, *J* for water oxidation is significantly lower than that for sulfite oxidation (**Figure 6.11**).

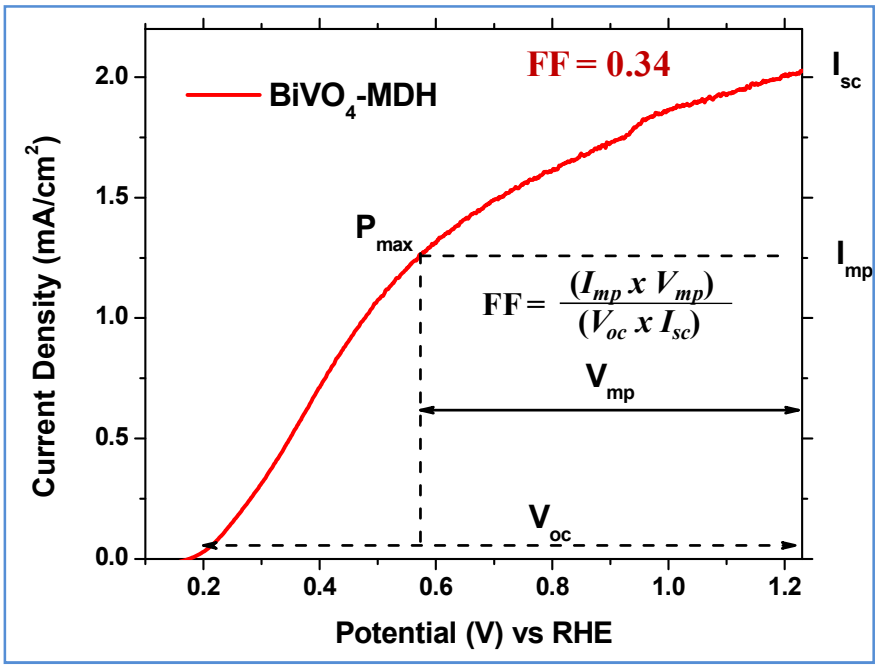

Figure 6.12: I_{mp} and V_{mp} are the current and voltage at maximum power point, P_{max}, respectively. I_{sc} and V_{oc} are short-circuit current and open-circuit voltage in a *J-V* curve obtained using a three electrode system for a solar water oxidation half reaction. FF is the fill factor.

The weak catalytic activity of $BiVO_4$ is because of the rapid e^-/h^+ recombination. However, for additional thin layer of amorphous metal hydroxide, the difference in photocurrents obtained for both water and sulfite oxidation decreases in the order LaCo MDH > $Co(OH)_x$ > $La(OH)_x$ (**Figure 11c–e**). Thus, Co–La MDH utilizes, if not completely, the maximum fraction of the surface-reaching holes in the water oxidation. This difference in photocurrent between water and sulfite oxidation can also be due to the e^-/h^+ recombination at the $BiVO_4$/OEC interface, which can be verified by comparing the *J–V* curves for sulfite oxidation of $BiVO_4$ with and without deposition of amorphous metal hydroxide layers (**Figure 6.11c–e**). As shown in **Figure 6.11c**, the *J–V* curves including the onset potential of $BiVO_4$–MDH is equal with

$BiVO_4$, whereas the values obtained for $BiVO_4$–$Co(OH)_x$ and $BiVO_4$–$La(OH)_x$ are considerably lower. It is surmised that the presence of amorphous MDH ceases the $BiVO_4$/OEC interfacial recombination completely, which has not been achieved with the use of single hydroxides as cocatalysts. $BiVO_4$/MDH shows a rapid increase in *J* in the lower potential region (<0.6 V vs RHE), thereby giving a decent fill factor of 0.34 for water oxidation half reaction (**Figure 6.12)**.

The LSV under chopped light irradiation shows transient photocurrent stability, which reflects that in comparison to the single hydroxides; MDH reduces surface recombination substantially (**inset of Figure 6.11b**). We have attempted to gain insight into the improvement of PEC activity in $BiVO_4$-MDH and the improved $BiVO_4$/Co–La MDH interface by electrochemical impedance spectroscopy (EIS) and transport efficiency (η_{trans}) measurements. To probe the exact electrochemical processes occurring during the water oxidation process directly to the EIS data, all the conditions were kept the same as that in case of LSV plots described earlier. The nyquist plots obtained at 0.7 V (vs Ag/AgCl) for $BiVO_4$, $BiVO_4$-MDH, La- and Co-$(OH)_x$, are presented in **Figure 6.13a** which can be understood in terms of the equivalent circuit given in **Figure 6.13b**. The proposed modified Randles' circuit fits well (fitting error ~0.01) with the experimental data points and helps in estimating the charge-transfer resistance (R_{ct}) and the resistance for the transport of charge within the catalyst (R_{cat}). The values of R_{ct} are 2×10^8, 9×10^9, 1537, and 187.4 Ω for bare $BiVO_4$, $BiVO_4$–$La(OH)_x$, $BiVO_4$–$Co(OH)_x$, and $BiVO_4$-MDH electrodes, respectively. The value of R_{cat} also decreases considerably in the case of $BiVO_4$-MDH compared to that of $BiVO_4$. The details are listed in **Table 1**. Charge transfer at the OEC/electrolyte and OEC/$BiVO_4$ interface is more facile for $BiVO_4$-MDH, inducing fast transport of charge carrier throughout the film. The kinetics of charge separation and transport in the OEC/electrolyte interface was studied by measuring η_{trans}. The η_{trans} was determined by comparing the photocurrents for water and sulfite oxidation according to the following formula:

$$\eta_{trans} = \frac{J_{H_2O}}{J_{Na_2SO_3}} \ (equation - 1)$$

According to equation-1, η_{trans} is plotted in **Figure 6.13c**. We obtained ~75% charge-transfer efficiency for $BiVO_4$-MDH, which could be due to the improved interface between $BiVO_4$ and MDH, signifying the importance of pulse plating.

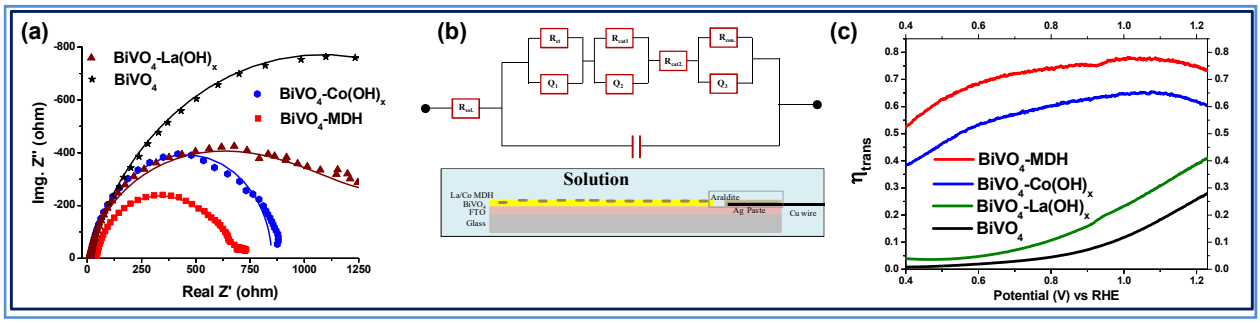

Figure 6.13: (a) Comparison of Nyquist plots of $BiVO_4$ and deposited MDH on $BiVO_4$ catalysts. (b) Equivalent circuit used to fit the EIS data obtained in panel a. Cat1 and Cat2 are the representatives for MDH layers and $BiVO_4$ respectively. The EIS was measured at 0.7 V (vs Ag/ AgCl) in 0.5 M phosphate buffer (pH 7) under AM1.5G simulated solar illumination. (c) Comparison of surface charge-transfer efficiency of the BiVO4 with modified catalysts.

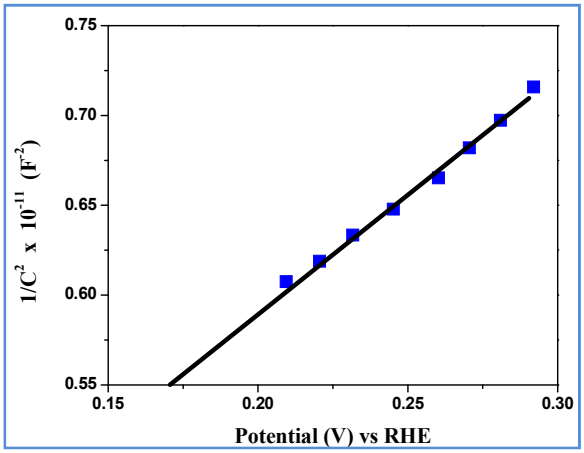

Figure 6.14: Mott-Schottky plots of $BiVO_4$-MDH, 4 cycles.

The onset potential for sulfite oxidation for $BiVO_4$ (0.16 V ± 0.02) is close to the flat band potential (E_{fb}). Similar E_{fb}, ca. 0.17 V, for $BiVO_4$-MDH was estimated from Mott−Schottky (MS) plots (**Figure 14**). Therefore, the improved PEC performance of amorphous Co−La MDH is mainly due to its $BiVO_4$/OEC interface engineering in order to reduce photogenerated surface charge recombination. The *J*−*V* plots obtained with annealed (500 °C, 0.5 h) $BiVO_4$-MDH electrodes showed (>2) times decrease in photocurrent (**Figure 16**), indicating that a more adaptive interface provided by the amorphousness of the structure plays a major role in photoelectrolysis.[37-38]

We also carried out additional experiments by depositing layer-by-layer $La(OH)_x$ and $Co(OH)_x$ on $BiVO_4$ in order to manipulate the $BiVO_4$/OER and OER/electrolyte interface, to study their effects in PEC water splitting, and to complement the data obtained from EIS and

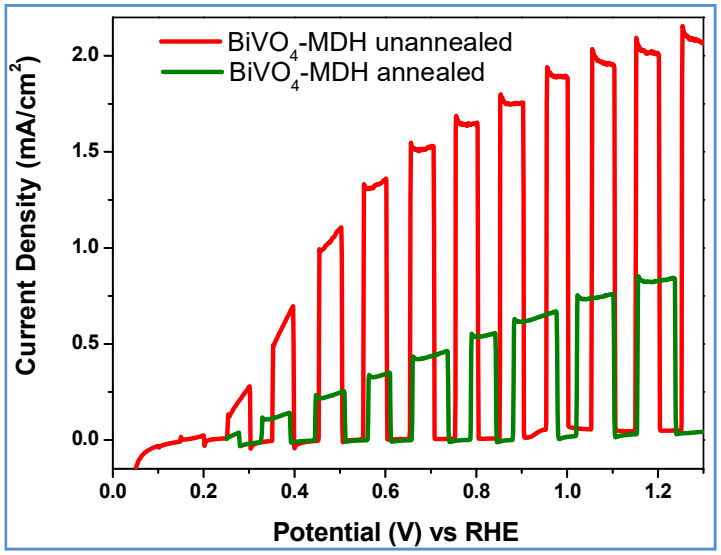

Figure 6.15: Comparison of PEC water splitting activity of annealed and unannealed MDH on $BiVO_4$.

Figure 6.11c–e. Synthesis related to this is given in **Figure 6.3e,f**. The higher transient photostability of the photoanode when $Co(OH)_x$ forms an interface with the electrolyte in comparison to that for $La(OH)_x$ is evident from **Figure 6.17**.

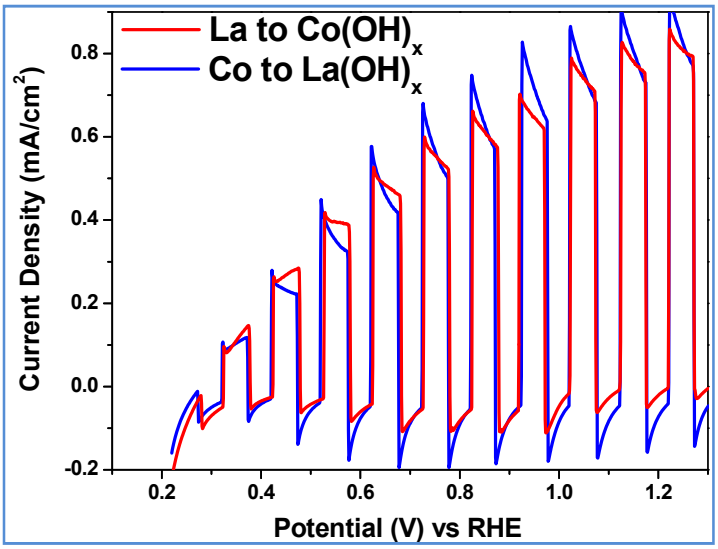

Figure 6.16: Comparison of layer-by-layer deposition of $Co(OH)_x$ and $La(OH)_x$ on $BiVO_4$ for the PEC water splitting activity.

There are two interesting differences: the difference of ca. 0.8 mA/cm^2 in the photocurrent and the transient photostability between the codeposited MDH and layer-by-layer deposition samples. We therefore propose that it is indeed the improved modified

$BiVO_4$/MDH interface obtained from the pulse plating technique that is the key factor for the higher PEC activity. We have compared the activity of the present catalyst with the performance of mono- and bi-metallic oxides and hydroxides integrated with $BiVO_4$ (**Table 2**). The onset potential of water oxidation, increment factor with respect to bare $BiVO_4$, and the photocurrent obtained at lower potential (0.5 V) for $BiVO_4$-MDH are comparable with those of the reported catalysts[39-45] (**Table 2**). The activity of four cycles deposited MDH was found to be superior to other cycles (two and eight cycles, **Figure 6.17**); hence, this was considered the optimized sample. The applied bias photon-to-current efficiency (ABPE), calculated from the *J*–*V* curve considering 100% faradic efficiency, is given in **Figure 6.18**. The increase in ABPE of ca. 5 times with simultaneous decrease in applied potential from 1.04 to 0.61 V for $BiVO_4$-MDH in comparison to bare $BiVO_4$ is noteworthy and makes it a potential system for PEC cells for solar-driven water splitting.

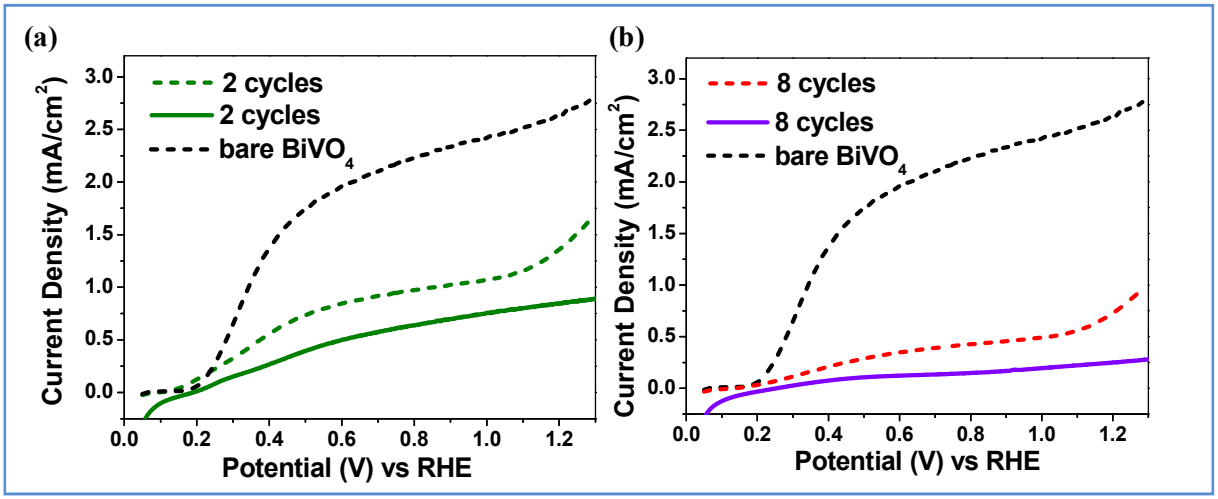

Figure 6.17: Comparison of photocurrent for sulfite oxidation (dashed) and water oxidation (solid) for $BiVO_4$ and (a) 2 cycles-MDH (b) 8 cycles-MDH.

The photostability of $BiVO_4$-MDH and bare $BiVO_4$ was examined from the J–t curve. A photocurrent density of 2.09 mA/cm^2, obtained by applying 0.8 V between the working and counter electrodes for 4000 s (**Figure 6.18b**) remained almost constant (93% retention), while in contrast, $BiVO_4$ loses 24% of its activity within 30 s of irradiation. These characteristics make $BiVO_4$/MDH a good photoanode for the construction of a PEC cell. The Faradaic efficiency calculated at 0.6 V was found to be greater than 80%. The amount of O_2 evolved with the

$BiVO_4$-MDH catalyst estimated using an O_2 sensor (Ocean Optics) is presented alongside the amounts calculated from chronoamperometric measurements (**Figure 6.18c**).

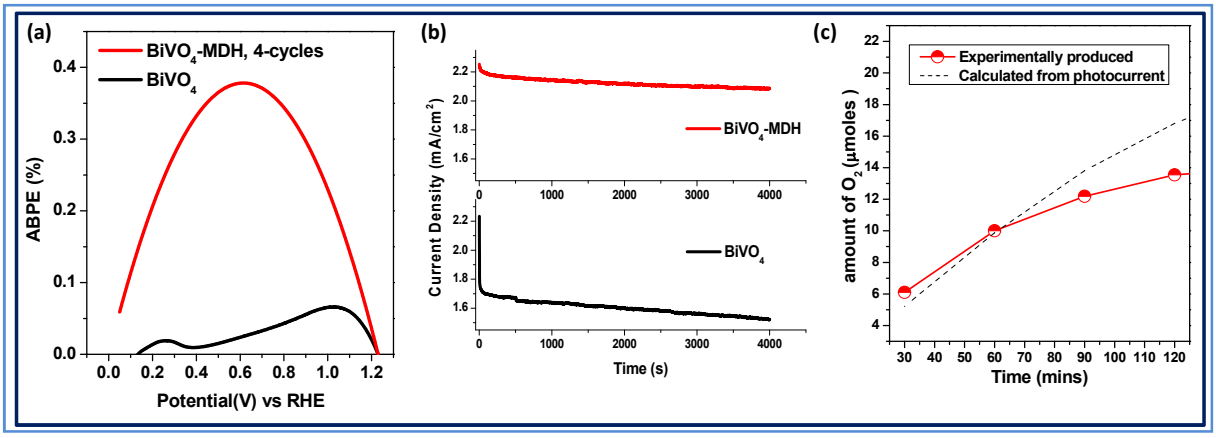

Figure 6.18: (a) ABPE obtained in three-electrode system. (b) J–t curve obtained under AM1.5G illumination comparing the stability of modified $BiVO_4$ catalyst by MDH deposition. (c) Comparison of produced O_2 with calculated value for $BiVO_4$-MDH catalysts.

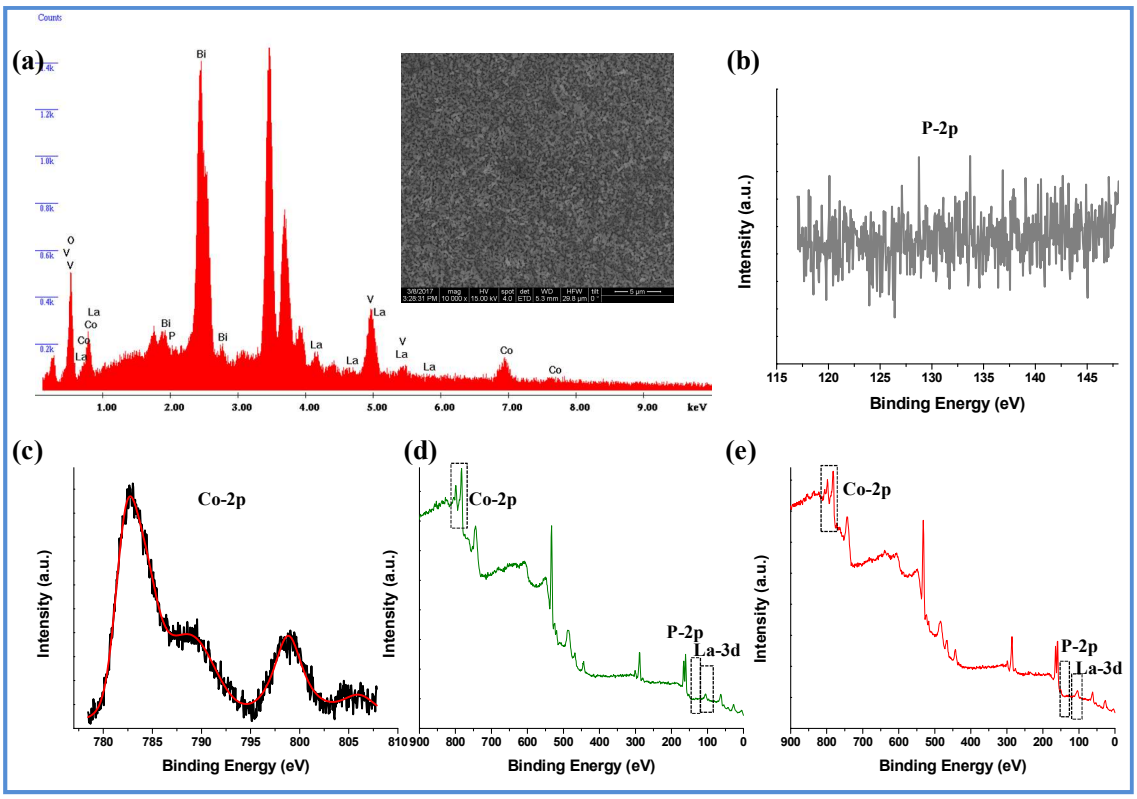

Figure 6.19: (a) EDAX spectra of $BiVO_4$/MDH after PEC studies. Inset shows the FESEM image of the photoanode after PEC studies. (b) and (c) are the core level XPS spectra of P 2p and Co 2p in $BiVO_4$/MDH photoanode after the PEC studies. (d) and (e) are the XPS elemental survey scan for $BiVO_4$/MDH and $BiVO_4/Co(OH)_x$ after PEC studies in K-Pi electrolyte (pH-7).

During the synthesis, pH 3.4 was optimized to avoid precipitation of hydroxides of La and Co at higher pH and to prevent dissolution of the deposit at lower pH. PEC studies were carried out at pH 7; therefore, it may be possible that active component Co−pi may form during the linear sweep voltametry study.[15,22] The presence of Co−pi and the relative composition of Co and La before and after the PEC study has been investigated with additional characterization techniques. We did not find the presence of any phosphorus or any appreciable change in the composition of Co and La obtained from the electrodes after the PEC study in ICP, EDAX, and XPS analyses (**Figure 6.19**). We can, therefore, exclude the possibility of Co−pi formation as well as the dynamic "chemically changing" nature of electrode during PEC study here. Also, if that indeed were the case, then we should have obtained similar PEC activity for Co−La MDH and monometallic $Co(OH)_x$ hydroxides. This clearly is not the case.

In a nutshell, we employed pulse plating for electrodepositing amorphous Co−$La(OH)_x$ mixed double hydroxide over nanoporous $BiVO_4$ with controlled layer thickness and improved adhesion. This approach helps in attaining an advantageous $BiVO_4$/MDH interface to reduce photogenerated charge recombination and enhance their transport by controlling the grain size. PEC water oxidation reveals reduction in the onset potential by 0.53 V besides 33.4 times increment in *J* at a lower potential (0.6 V) achieved by $BiVO_4$/MDH. The increased amorphous nature of the MDH and modified interface of $BiVO_4$/OEC obtained by the present method helps in gaining better transient photostability and PEC activity. The charge-transfer resistance of $BiVO_4$ decreases by a few orders of magnitude with MDH deposition. Deposition of Co−$La(OH)_x$-based MDH not only enhances the ABPE of $BiVO_4$ significantly even at a lower potential but also provides a remarkable resistance against photocorrosion, establishing it as a promising candidate for photoelectrochemical water splitting. The synthetic method we employed can be extended to other metal hydroxide/oxide combinations.

Table 2: PEC activity comparison of mono and bimetallic OECs on $BiVO_4$

Materials	Onset potential (V) vs RHE (shift w.r.t. unmodified $BiVO_4$) [a]	I @ 0.6 V mA/cm^2 (increment w.r.t. unmodified $BiVO_4$) [a]	I @ 1.23 V mA/cm^2 (increment w.r.t. unmodified $BiVO_4$) [a]	Reference no.	Synthesis conditions [b, c], pH, light source [d]
$BiVO_4/Co_3O_4$	0.5	~0.5(~2)	2.27 (~5)	[40]	Hydrothermal method+ dropcast+annealing, pH 7
$BiVO_4$/FeOOH	0.275	1.07	1.9	[45]	PD, pH 7
$BiVO_4/CoO_x$/NiO	0.35(-0.15)	2.5	3.5(~2.8)	[41]	Impregnation+ particle transfer+ALD, pH 7
$BiVO_4$/FeOOH/NiOOH	0.23(-0.2)	2.8 (7)	4.2(~2.3)	[2]	PD, pH 7
$BiVO_4/ZnFe_2O_4$	0.55 (-0.275)	0.3	2.5 (~2.3)	[9]	PD+annealing, pH 13
W:$BiVO_4$/Co-Pi	0.27 (-0.38)	0.52	1.4(1.75)	[25]	PED, pH 8
$BiVO_4/CoO_x$				[42]	Impregnation, 300W Xe lamp (λ>420 nm)
$BiVO_4$/Co-Pi	~0.25	~0.5	~1.7(2.3)	[43]	ED, pH 5.6
$BiVO_4$/LDH/CdTe Quantam dots	0.32 (-0.055)	0.7 (2.8)	2.16 (3.0)	[44]	Hydrothermal growth+ solution phase deposition, pH 7
$BiVO_4$/Co-Al Layer double hydroxide	0.36 (-0.54)	~0.15	~0.9 (2.25)	[46]	Hydrothermal method, pH 7
$BiVO_4/Fe_{0.5}Ce_{0.5}O_x$	0.5	0.1	~0.8	[21]	PED, pH 13
$BiVO_4/Fe_{0.5}Ce_{0.5}O_x$	0.4(-0.1)	0.2	~0.8		IJP, pH 13
$BiVO_4/Co(OH)_x$	**0.25 (-0.45)**	**0.83**	**1.49(~2)**	**This work**	**Pulse plating, pH 7**
$BiVO_4/LaCo(OH)_x$	**0.19(-0.51)**	**1.31**	**2.02(~2.7)**		

a The parenthesis are empty as either the values of BiVO4 are undefined or negligible; **b** The synthesis condition of co catalyst; **c** PD: photo deposition, ED: electro deposition, ALD: Atomic layer deposition, IJP: Inkjet printing, PED: photo electro deposition; **d** AM 1.5G 1sun illumination except where specified.

Part B: Photocathode

Photoelectrochemical hydrogen generation employing a Cu_2O-based photocathode with improved stability and activity by using Ni_xP_y as the cocatalyst

X-ray diffraction patterns of the Cu_2O electrodes with the photocorrosion protective layer of CuO and Ni_xP_y thin films are given in **Figure 6.20a.** Bare Cu_2O on a flourine doped SnO_2 (FTO) electrode shows the characteristic (110), (111), (200) reflections at 2θ of 30.41, 36.91, 42.51, respectively, indicating the formation of Cu_2O (ICSD-26963) on the substrate.

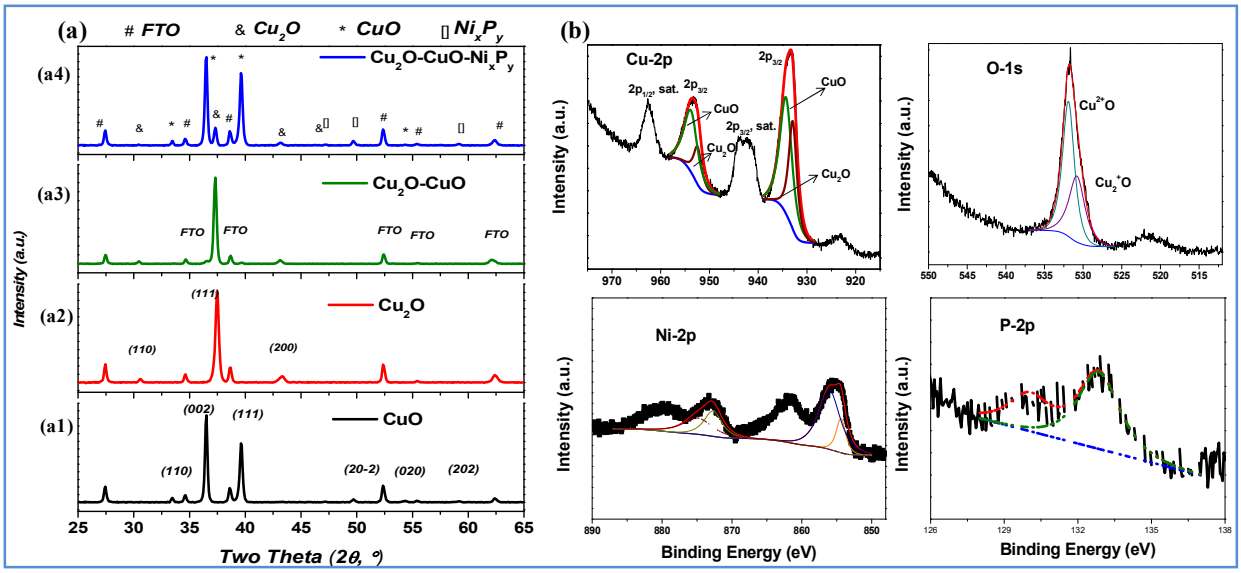

Figure 6.20: (a) X-ray diffraction patterns of the (a1) CuO, (a2) Cu_2O, (a3) Cu_2O– CuO and (a4) Cu_2O–CuO–Ni_xP_y electrodes. For a better signal, the XRD patterns were obtained from more deposited sample than contained by the actual electrode. (b) Core level X-ray photoelectron spectra (XPS) for Cu, O, Ni and P on the surface of the Cu_2O–CuO–Ni_xP_y electrode.

XRD patterns of the Cu_2O covered with thin layers of CuO and Ni_xP_y show the presence of CuO (ICSD-291387) and Ni_xP_y [$Ni_{12}P_5$ (ICSD-27158) and Ni_5P_4 (ICSD-43239)] on the electrode surface. Core-level XPS spectra of the photocathode thin films (**Figure 6.20b**) exhibit Cu $2p_{1/2}$ and $2p_{3/2}$ signals along with satellite peaks. The Cu 2p (1/2 and 3/2) signals at 952.7 and 933 eV could be deconvulated into contributions from Cu_2O and CuO.[46-48] The thin layer of Ni_xP_y was found to mostly consist of $Ni_{12}P_5$ and some Ni_5P_4 with the $2p_{3/2}$ signals at 856.0 and 854.4 eV due to $Ni_{12}P_5$ and Ni_5P_4.[49-50] **Figure 6.21** shows the optical absorption spectra of Cu_2O and the heterojunctions of Cu_2O–CuO and Cu_2O–CuO/ Ni_xP_y exhibiting a band gap of ca. 2.1 eV. Surface and cross sectional morphologies of the thin photocathode film (**Figures 6.22, 6.23**) reveal the small grain size and crack-free film obtained by electrodeposition. We obtained a porous film constituting particles of larger crystallite size upon thermal annealing.

From **Figure 6.22b and Figure 6.23** it can be seen that the working photocathode consists of sequential layers of smooth crack-free Cu_2O, a porous layer of Cu_2O–CuO obtained

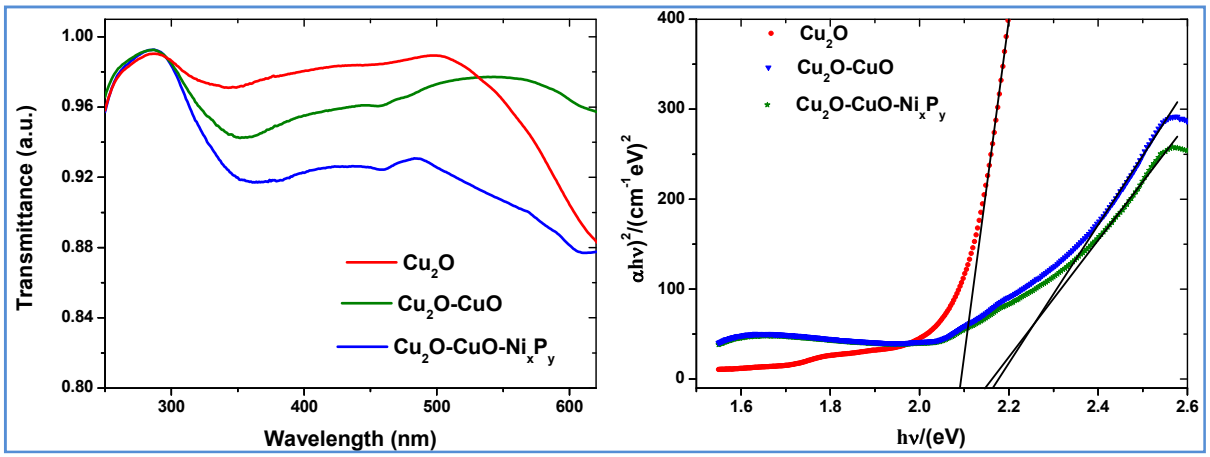

Figure 6.21: (a) Optical absorption (UV-NIR) spectra spectrum of the bare Cu_2O (red) and he Heterostructures of Cu_2O-CuO (green) and Cu_2O-CuO-Ni_xP_y (blue) thin films deposited on FTO. (b) The Tauc plot and band gap determination of the thin film electrodes. Colors have their defined representations.

by controlled annealing of the Cu_2O film and finally a very thin film of Ni_xP_y. The overall film thickness of ca. 500 nm was obtained by averaging the cross-sectional FESEM images of 5 electrodes. The exact thickness of the Ni_xP_y layer could not be assigned as we did not obtain any signals for Ni and P in EDAX due to their scarce presence. The photocathodes showed heterogeneous grain growth as evident from the TEM images (**Figure 6.22c and d**). HRTEM images confirm the presence of Cu_2O, CuO and the two different phases of Ni_xP_y, namely $Ni_{12}P_5$ and Ni_5P_4, complementing the PXRD data. The formation of the porous layer after annealing of the Cu_2O film and the deposition of amorphous Ni–P by pulse plating provides an increased electrochemical surface area, which is a critical requirement for the PEC activity. The relative thickness and compositional ratio of Cu^{1+} and Cu^{2+} are important for obtaining optimized light absorbance and the successful utilization of photogenerated electrons for H_2 generation via their transfer from the HER-active Ni_xP_y layer. Since the Cu^{+}:Cu^{2+} ratio could not be determined by XPS characterization, we report an estimated ratio of Cu_2O and CuO based on Auger and satellite peak analysis which was found to be 1 : 1.5.

The surface morphology of Cu_2O and its heterostructured electrodes was studied using AFM topographic images (**Figure 6.24**). The average height of the deposited Cu_2O film on FTO was found to be 450 nm with a root mean square (RMS) roughness (R_{rms}) of ca. 28 nm measured for a surface of 20x20 mm^2. Grain size analysis from AFM images gives a contrasting difference of the surface topography (**Figure 6.25**) whereby we see smaller grains in the case of

heterostructured Cu_2O films modified by CuO and Ni_xP_y layers.

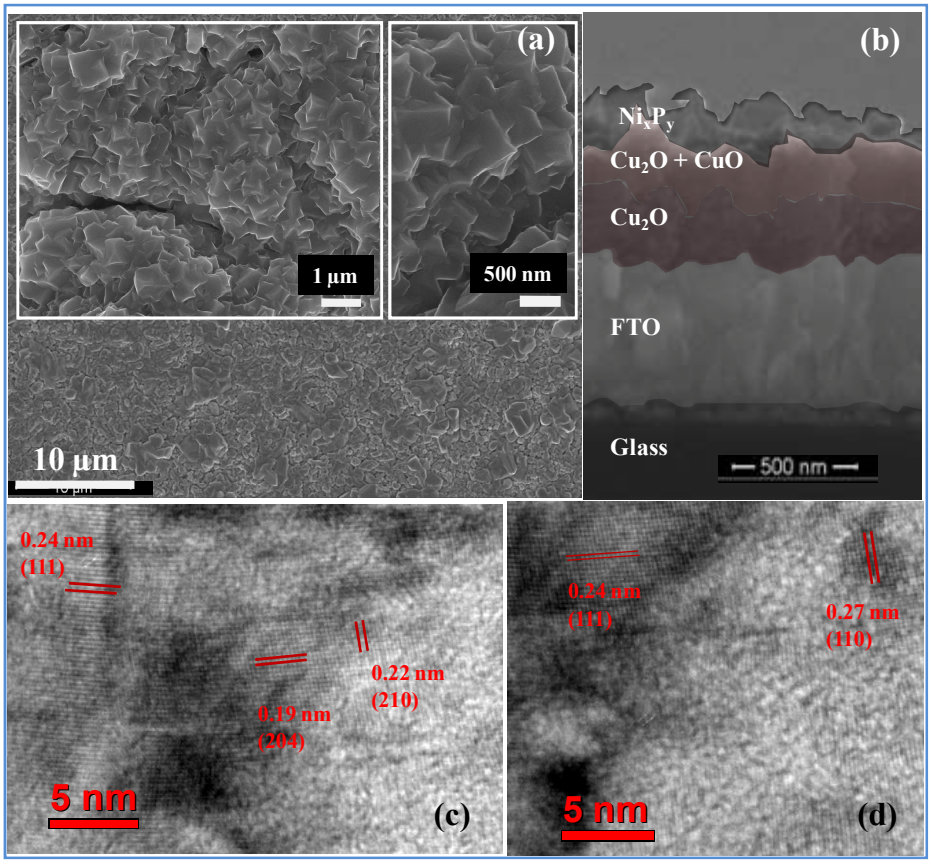

Figure 6.22: Morphology of the photocathode: (a) FESEM images of the Cu_2O–CuO–Ni_xP_y photocathode (insets show the higher magnification images). (b) Cross sectional FESEM image with representative film layers (schematic approximation of the thickness). Note that the cross sectional image is tilted by 2^o. (c) and (d) are HRTEM images of the photocathode showing the presence of Cu_2O, CuO and $Ni_{12}P_5$.

Although the R_{rms} values of all the three electrodes are close to each other (20 nm to 28 nm), the image surface area is maximum (3D topograph) for Cu_2O–CuO– Ni_xP_y suggesting a greater fraction of electrolyte interaction of the photocathode.

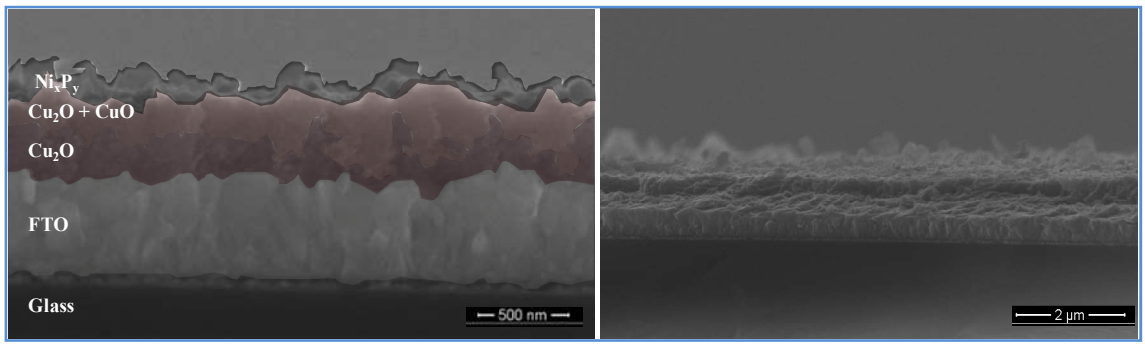

Figure 6.23: Cross Sectional FESEM images of Cu_2O-CuO-Ni_xP_y showing the representative gradual layers of hetero-interfaces (approximation in the thickness of different layers).

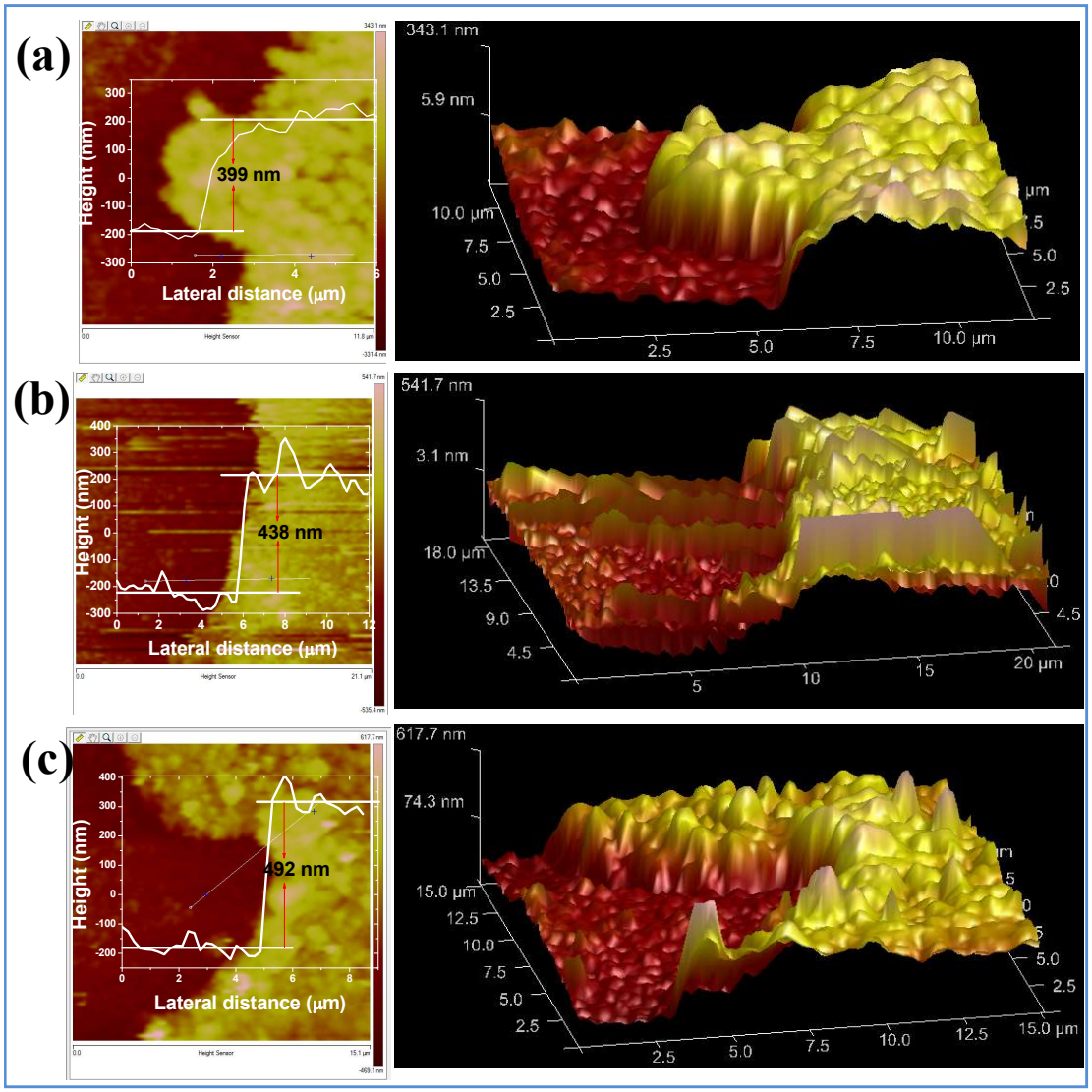

Figure 6.24: Tapping mode atomic force microscope (AFM) 2D (left) and 3D (right) images of the (a) Cu_2O, (b) Cu_2O–CuO and (c) Cu_2O–CuO–Ni_xP_y electrodes (20x20 mm^2) and the corresponding deposition thickness marked by the height profile drawn in the inset.

The increased surface area could arise from the nanoparticulates of electroactive Ni_xP_y forming a thin layer on Cu_2O–CuO as evident from the FESEM and TEM images. The layer of Ni_xP_y is not continuous as seen from the AFM images and FESEM studies conducted for various sets of samples. Although during the deposition, a uniform layer of amorphous Ni–P is formed, during the annealing process there may be aggregation of nanoparticles to form discontinuous films of Ni_xP_y on the Cu_2O–CuO film. This in turn is considered to be advantageous for PEC H_2 generation with increased electrode–electrolyte interacting surface area.

In order to examine whether the photocathode with protective heterolayers is efficient in improving activity and stability we carried out the PEC hydrogen activity test. The PEC

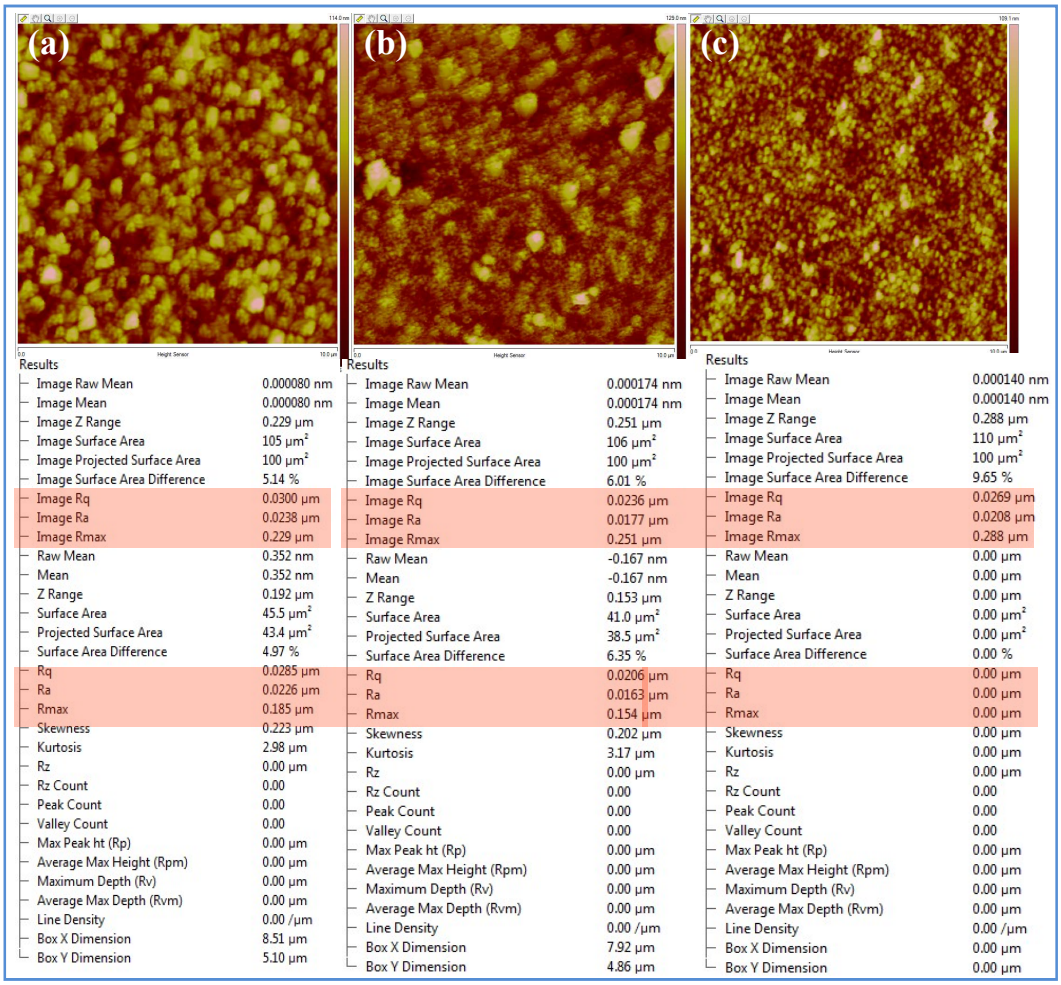

Figure 6.25: Detailed AFM topographic analysis of the electrode surfaces for estimation of roughness factor and grain size study (a) Cu_2O (b) Cu_2O-CuO and (c) Cu_2O-CuO-Ni_xP_y.

performance of the optimized electrodes in terms of composition and thickness along with CuO and Ni_xP_y modifications is shown in **Figure 6.26**. For the purpose of brevity and also to understand the contributions of bare CuO, we have also given the PEC results of the CuO electrode. As a proof of concept, the currents obtained under dark and light illumination conditions of the electrodes show that the photocurrent density of the modified Cu_2O by introduction of CuO and Ni_xP_y is remarkably increased relative to that of the bare Cu_2O and CuO photoelectrodes. At 0 V, the initial photocurrent density of Cu_2O–CuO– Ni_xP_y and Cu_2O–CuO is -3.19 mA cm^{-2} and -1.62 mA cm^{-2} respectively, which is 4.3 and 2.2 times greater than that of the bare Cu_2O (-0.72 mA cm^{-2}) and 2.7 and 1.3 times greater than that of the bare CuO (1.17 mA

cm^{-2}), respectively. To probe the contribution of CuO and Ni_xP_y to the photocurrent improvement, we have measured *J–V* curves for pure CuO and CuO– Ni_xP_y (**Figure 6.27**). It can be concluded that the photocurrent improvement stems mainly from the introduction of the

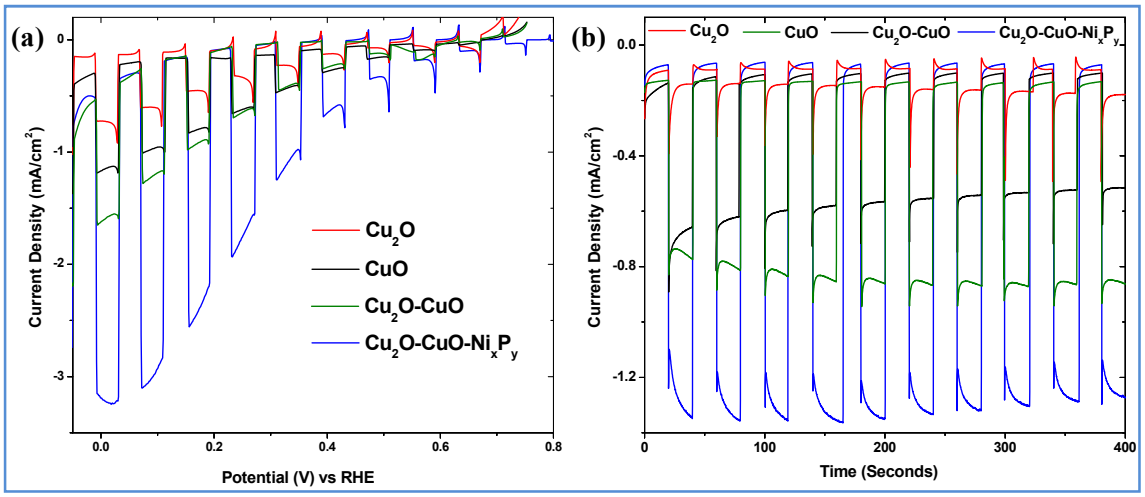

Figure 6.26: Current–voltage (I–V) characteristics of a photocathode: (a) PEC hydrogen evolution activity comparison between the photocathodes. (b) Transient photocurrent stability study using chronoamperometric stability measurements biased at 0.05 V (vs. RHE). All the measurements were carried out in pH 7, 0.5 M Na_2SO_4 electrolyte under chopped light irradiation

Ni_xP_y layer rather than the CuO layer alone. The introduction of the CuO layer builds a unidirectional flow of photogenerated electrons towards the electrode/electrolyte,[51-52] interface for H_2 generation, acting as an electronic ratchet (schematic band diagram). Amperometric I–t features examining the transient photostability of bare Cu_2O, CuO, Cu_2O–CuO and Cu_2O–CuO– Ni_xP_y under chopped light irradiation at 0.05 V are shown in **Figure 6.26b**. From the comparative photoelectrocatalytic stability of the four photocathodes, we find that the bare Cu_2O photocathode provides a maximum photocurrent density of -0.24 mA cm^{-2} for 20 seconds, after which the current decreases to -0.09 mA cm^{-2}.

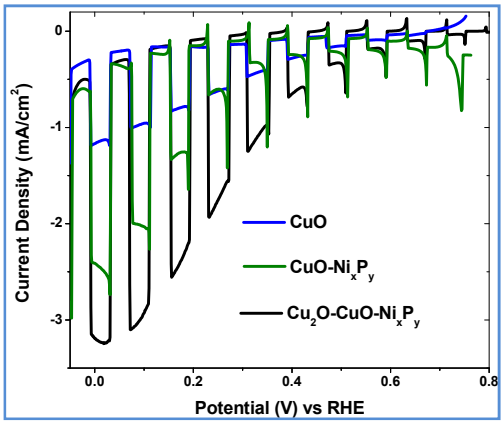

Figure 6.27: Current–Voltage (I-V) characteristics of a photocathodes: PEC hydrogen evolution activity comparison with and without the Cu_2O-CuO interface to understand the efficiency of photocathode and the role of CuO. All measurements were carried out in pH-7, 0.5 M Na_2SO_4 electrolyte under chopped light irradiation.

However, modification of the Cu_2O electrode with the introduction of CuO and Ni_xP_y results in a remarkable increase in the photocurrent density as well as in the photostability. There is no apparent decrease in the photocurrent for the electrode modified with Ni_xP_y, whereas the photocurrent quickly decreases in the case of the other electrodes. In terms of changes in the electrode as a result of the PEC test, we studied its morphology, phase and valence states after 1 hour of the PEC study (*J*–*t* at 0.05 V) of the electrode (**Figure 6.28–6.30**).

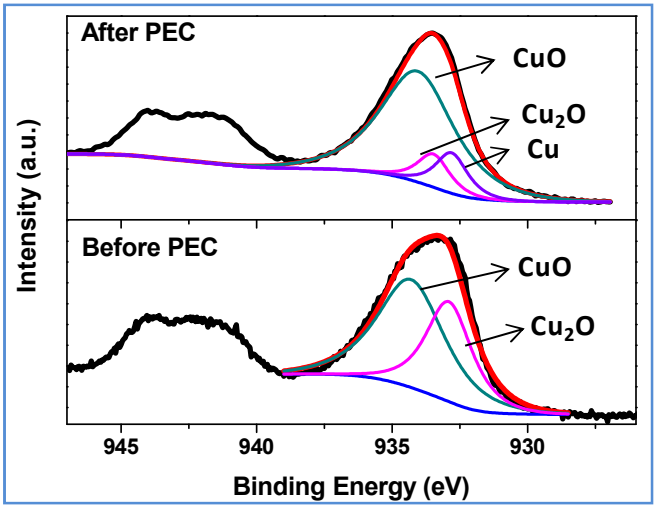

Figure 6.28: Core level X-ray photoelectron spectra for Cu-2p3/2 on the surface of the Cu_2O-CuO-Ni_xP_y electrode before and after PEC stability test. The shaded potion represents the shake of satellite peaks which is more prominent in after PEC sample suggesting greater fraction of CuO on the electrode surface resulting from the photocorrosion.

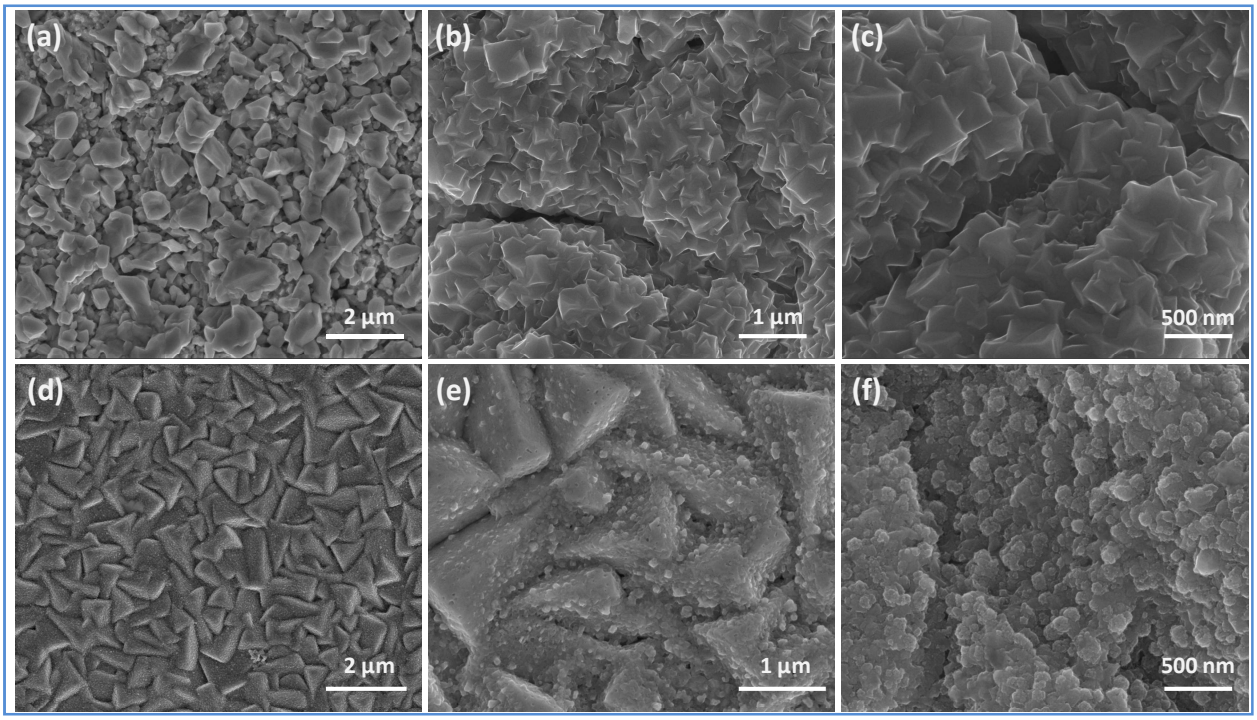

Figure 6.29: Morphology study of electrode: FESEM images of the electrode (a-c) before PEC study and (d-f) after PEC study.

We observe changes in the morphology and phase (FESEM and XRD), but these does not lead towards a drastic decrease in photocurrent as evident from the *J–t* study. The XPS study after the PEC study (**Figure 6.28**) shows larger proportion of CuO and traces of Cu due to the photoredox processes involved. According to the thermodynamic redox potential vs. relative alignment of the conduction and valence band edges with respect to water redox potentials, metal cations in metal oxides with oxidation state not highest or lowest are liable to be involved in the redox process and are likely to be unstable.[26] However the photocurrent does not decrease as much as the magnitude of the change in morphology and phases. This photostability improvement can be attributed to the combined effect of interfacial band edge energetic modification on introducing the CuO and Ni_xP_y layers as well as the efficient electrocatlytic activity of the Ni_xP_y layer towards HER.[28-29]

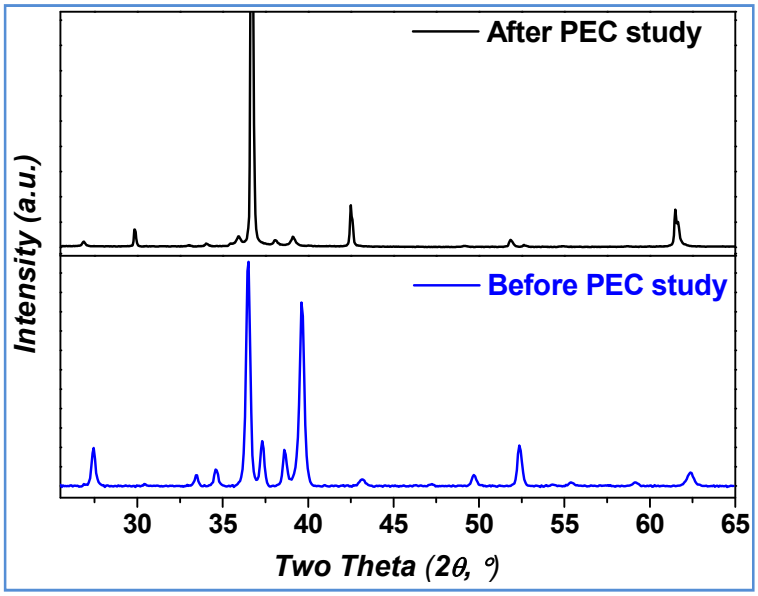

Figure 6.30: X-ray diffraction patterns of Cu_2O-CuO-Ni_xP_y before and after PEC study (1 hour chronoamperometric i-t study at 0.05 V vs RHE) to study the stability of the photoelectrode.

The remarkable improvement in PEC activity and stability of the electrode led us to examine the PEC properties and interfacial resistance in detail. In this context, Electrochemical Impedance Spectroscopy (EIS) measurements were carried out.

All the samples showed either a single or two semicircular arcs which can be used to study the resistive and capacitive nature related to PEC activity. The diameter of the

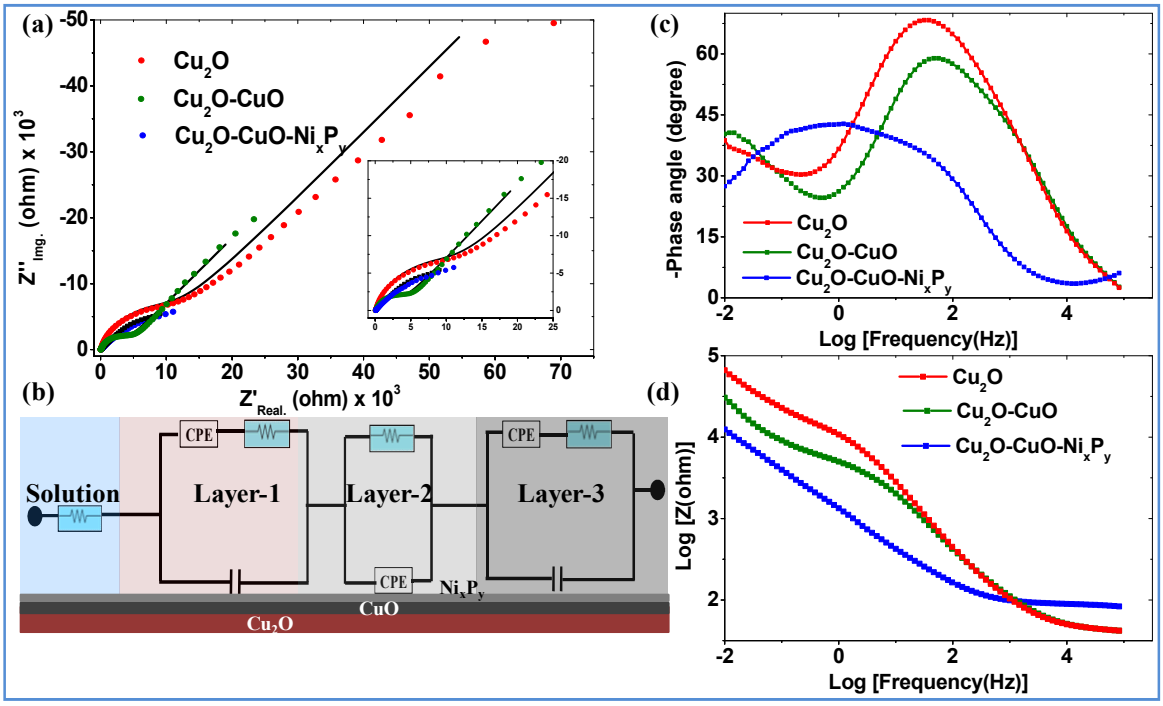

Figure 6.31: (a) Nyquist plots of the electrodes in 0.5 M Na_2SO_4 solution as an electrolyte under illumination. The inset shows a magnified view of the plot in the high frequency region. (b) Schematic representation of the equivalent circuit used to fit the electrochemical impedance spectroscopy data in the Nyquist plot. CPE is the constant phase electrode, and the resistance has its usual symbol. Complex impedance analysis of the photocathode film in 0.5 Na_2SO_4 solutions given by (c) phase angle vs. log frequency (f) and (d) showing log |Z| vs. log f.

semicircular arc gives the extent of the resistance experienced at the electrode electrolyte interface upon illumination, leading to successful hydrogen production. It can be unambiguously concluded that the introduction of the Ni_xP_y layer on Cu_2O–CuO promotes fast electron transfer to H^+ ions, the former being an excellent electrocatalytic HER catalyst (small semicircular arc diameter, **Figure 6.31**). The nature of the semicircular arcs was also confirmed from phase angle diagrams (**Figure 6.31c and d**). The decrease in charge transfer resistance might be due to an increased number of charge carriers accumulated at the electrode–electrolyte interface with varied composition at the surface, which is also evident from the Mott–Schottky (MS) analysis (**Figure 6.32**).

In addition, the lowest resistance observed in the case of Ni_xP_y is because of the ease of electron percolation down the energy level as explained in the band energy diagram (**Scheme 1**) and the superior electrocatalytic HER activity of Ni_xP_y which forms the external layer. **Figure 6.31c** shows the *phase angle vs. log f* plots. A broad phase angle around the frequency range

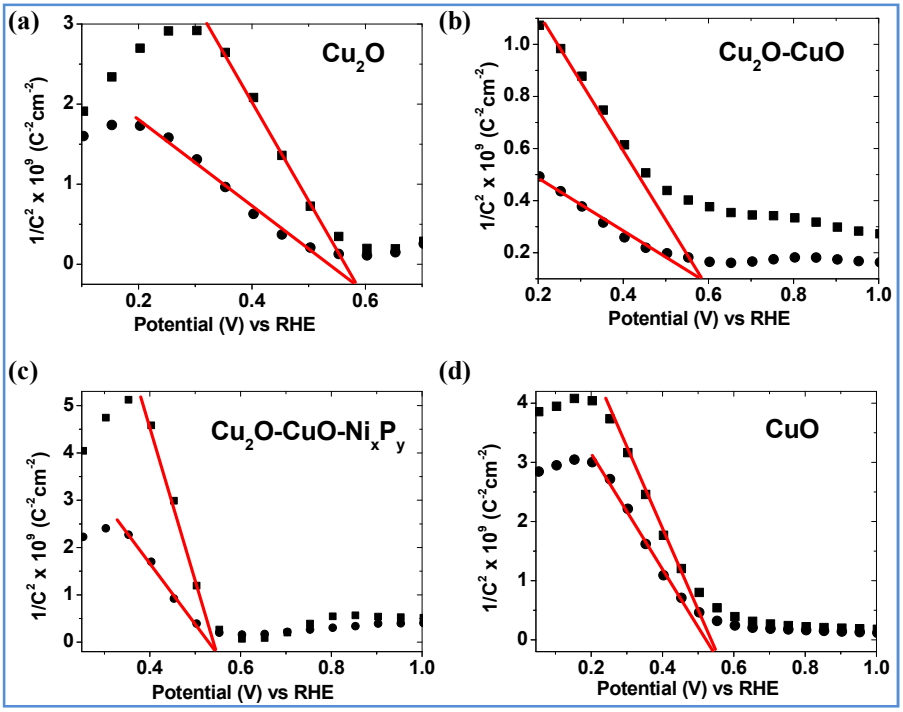

Figure 6.32: Mott–Schottky (MS) plots of (a) Cu_2O (b) Cu_2O–CuO (c) Cu_2O–CuO–Ni_xP_y (d) CuO measured in 0.5 M Na_2SO_4 (pH 7) at different AC frequencies (circle: 50 kHz, square: 75 Hz).

from 1 to 80 Hz was observed for the Ni_xP_y coated electrode, whereas for the Cu_2O and Cu_2O–CuO electrodes a fairly sharp phase angle change was observed. This broad semicircle observed for the Cu_2O–CuO– Ni_xP_y electrode indicates the catalytic surface for the hydrogen evaluation reaction.[53] The less negative phase angles for the Cu_2O–CuO–Ni_xP_y (42^o) in comparison to the other two Cu_2O–CuO (59^o) and Cu_2O (68^o) electrodes confirmed a lower charge mobility resistance at the electrolyte/electrode interface. The PEC behavior of the electrodes was further examined with the log |Z| vs. log frequency (f) plots in **Figure 6.31d**. |Z| has both the real (Z') and imaginary (Z'') components of impedance. The Ni_xP_y layer coated electrode shows minimum |Z| compared to the electrodes without Ni_xP_y indicating its higher activity.

In order to probe the effect of the cocatalyst, we used NiO as a replacement for Ni_xP_y and found that the PEC activity of the latter is superior (**Figure 32**). The values of the flat band potential (V_{fb}) estimated for each electrode are different and they are frequency-independent (**Figure 32**). This indicates that the nanoparticulate nature of the surface of the electrode has minimum effect on the MS analysis and hence the conclusions from MS analysis are valid.[30] The values of V_{fb} are most negative for the Cu_2O–CuO– Ni_xP_y and CuO indicating the efficient

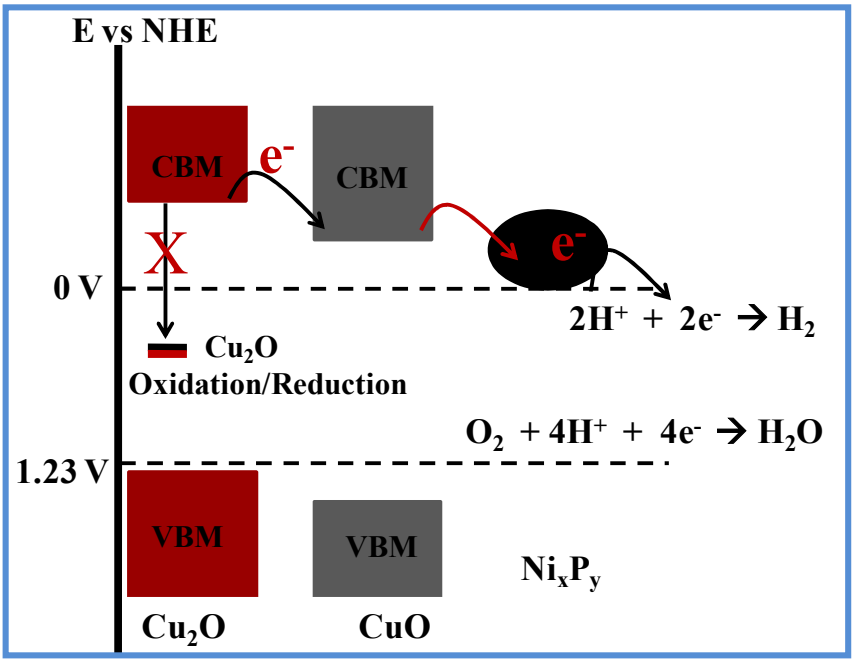

Scheme 1: Mechanism of PEC water splitting via unidirectional flow of photogenerated electrons avoiding photodegradation of Cu_2O and exhibiting hydrogen evolution by the introduction of electroactive Ni_xP_y as a HER catalyst.

PEC hydrogen evolution activity. This is also evident from the open circuit potential under illuminated conditions (**Figure 6.33**) and the values of V_{fb} are thus close to the Fermi level. The slopes at 50 kHz and 75 Hz are different for each electrode and hence addition of the HER catalyst layer affects the carrier density within the Cu_2O electrode, following the trend in PEC activity.

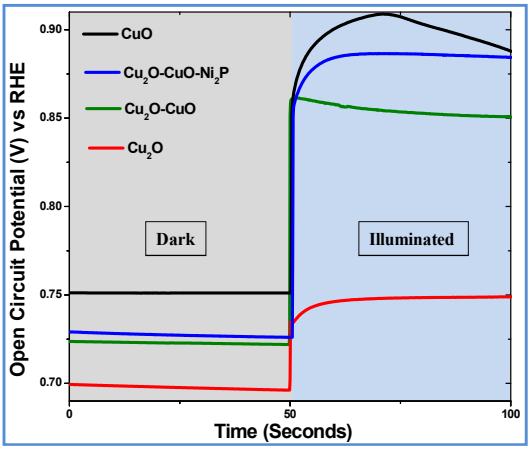

Figure 6.33: Open circuit potential vs time graph of the photocathodes in dark and illuminated conditions obtained by chopping of incident light.

The exact value of the surface carrier density was not calculated because the values of the dielectric constant and the real electrochemical surface area of the electrodes can vary

depending on the uniformity of the deposits, but the trend in PEC activity can be explained by the comparative analysis of the MS plots. With the conclusions drawn from EIS and MS analysis, we can explain the relative PEC activity trend and conclude that the introduction of protective layers of CuO and Ni_xP_y indeed helps in improving the photoactivity. The Cu_2O/CuO heterojunction shows not only enhanced photocurrent density but also superior photostability than Cu_2O, due to the prevention of photocorrosion and a unidirectional flow of photogenerated charges (charge carrier rachet). The appropriate band edge positions enable the photogenerated electrons on Cu_2O to transfer to the conduction band of CuO and the holes from CuO to transfer to the valence band of Cu_2O. The Cu_2O/CuO heterojunction thus enhances efficient charge separation, resulting in an improved PEC water splitting performance. Further improvements in photocurrent density and photostability occur by incorporating Ni_xP_y in the Cu_2O/CuO photocathode, resulting in the fast transfer of the photoinduced charge carriers (electrons) from the Cu_2O/CuO surface. This is because of the exceptional HER activity of Ni_xP_y.

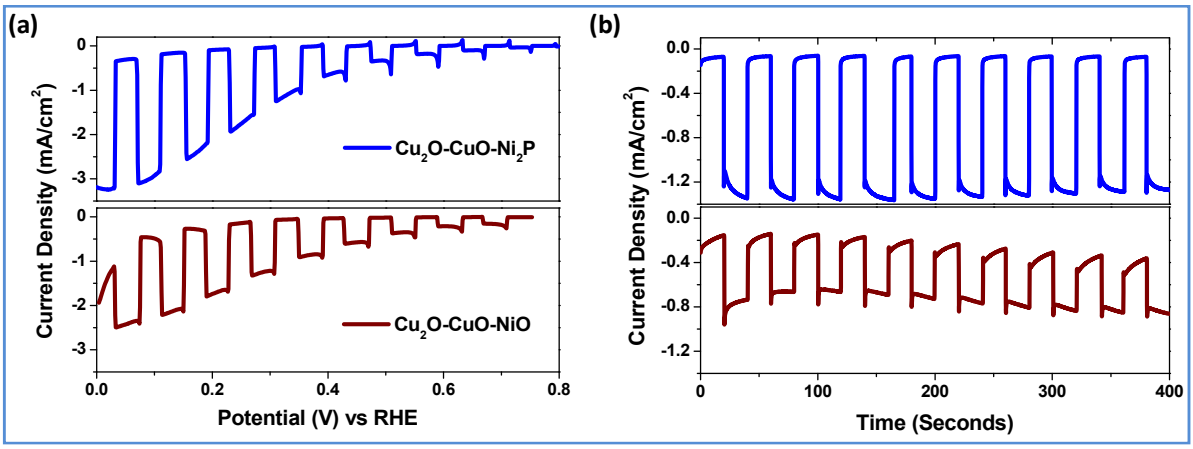

Figure 6.34: Comparison of PEC activity with NiO as cocatalyst: (a) LSV curve at same conditions as when Ni_xP_y is used as cocatalyst. (b) Transient photocurrent stability test for both the catalysts with NixPy and NiO as cocatalyst.

4.1. PEC H_2 evolution activity of Cu_2O-CuO-NiO: study of PEC activity with another cocatalyst:

A Cu_2O-CuO-NiO electrode was fabricated by the method used for the other electrodes in this study except for the last step. Pulse plating electrodeposition of $Ni(OH)_2$ was carried out from a solution of 0.5 M Nickel acetate in 5wt% NMF (without the phosphorous source). The electrodeposition parameters were the same. After deposition the film annealed at 400^{o}C for 30 mins (5^{o}C/min heating rate). The photocurrent study for hydrogen evolution with NiO as

cocatalyst suggests that Ni_xP_y is better for HER (**Figure 6.34**). This is obvious because of the superior electrochemical HER activity of Ni_xP_y than that of NiO.

In summary, the heterojunction electrodes are stable for the PEC hydrogen evolution because of facile charge transfer from the bulk of Cu_2O to the electrolyte via CuO and Ni_xP_y. The use of Ni_xP_y as the cocatalyst by us is the first report of higher photocurrent and better photostability relative to previous reports. The synthetic method adopted by us helps in the precise fabrication of the electrode besides being a simple low-cost technique. This work provides a different strategy for fabricating photostable electrodes and reveals the critical importance of composition/morphological changes of the surface in creating high stability photocathodes for photoelectrochemical and photocatalytic applications.

Part C: Sea Water Splitting

Photoelectrochemical Hydrogen Generation by Sea Water Splitting.

Taking into account the scarcity of fresh water on earth and the high cost of water treatment, it is important to use an abundant source of water without compromising with the efficiency of water splitting. Nearly 71% of the earth is covered with water out of which 97% is present in the oceans which are saline in nature. The possible use of seawater for generating hydrogen clearly is a worthy proposition. Direct electrolysis of seawater results in the evolution of hydrogen at the cathode and evolution of chlorine and hypochlorite at the anode. Evolution of chlorine and hypochlorite implies the competing nature of chloride oxidation with the oxidation of water. Oxidation of chloride ions is thermodynamically less favourable than that of water(redox potential considerations: 1.23 V (H_2O/O_2) vs 1.36 V Cl^-/Cl_2)), but the former is a two electron process and hence is kinetically more favourable (H_2O/O_2, being a 4 e^- process). Another issue with direct electrolysis or photoelectrolysis is the deactivation of active sites at cathode by the build-up of insoluble precipitates. Photoelectrochemical Splitting of sea water using semiconductor catalysts depends on the band structure of the semiconductor. The ions present in water can get oxidised or reduced by the photogenerated electrons or holes thereby competing with water oxidation and reduction. This greatly affects the efficiency of water splitting. We have also carried out photoelectrochemical water splitting using Cu_2O-CuO-Ni_xP_y and $BiVO_4$-MDH electrodes.

The activity of our electrodes towards sea water splitting was tested by photoelectrochemical (PEC) hydrogen evolution and oxygen evolution activity test. The PEC performance of the optimized electrodes of Cu_2O-CuO-Ni_xP_y and $BiVO_4$-MDH are shown in (**Figures 6.35 and 6.36**). The currents obtained in dark and light illumination conditions of the electrodes show that the photocurrent density of Cu_2O-CuO-Ni_xP_y are high even in sea water showing comparable activity with respect to the activity tested in Na_2SO_4 electrolyte which is devoid of numerous cations and anions affecting the PEC activity in various ways. Similarly for $BiVO_4$-MDH, we obtained a slightly lower PEC activity relative to Potassium phosphate buffer (KPi buffer solution, pH=7). These results are given in (**Figures 6.34 and 6.35**).

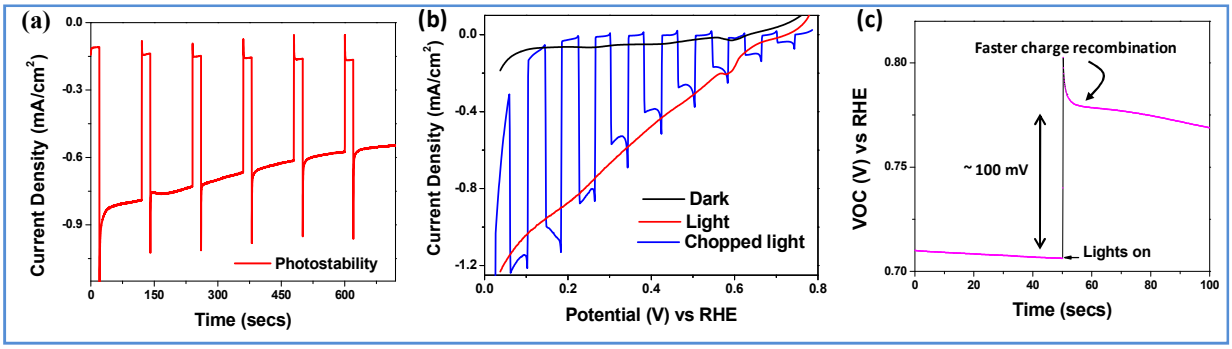

Figure 6.35: (a) Transient photocurrent study using chronoamperometric stability measurement biased at 0.05 V (vs RHE). (b) Current–Voltage (*J-V*) characteristics of a photocathode in dark, illuminated and chopped light illumination conditions. (c) Open circuit potential vs time graph of the photocathode in dark and illuminated conditions obtained by chopping the incident light. All measurements were carried out in pH-6.8 sea water.

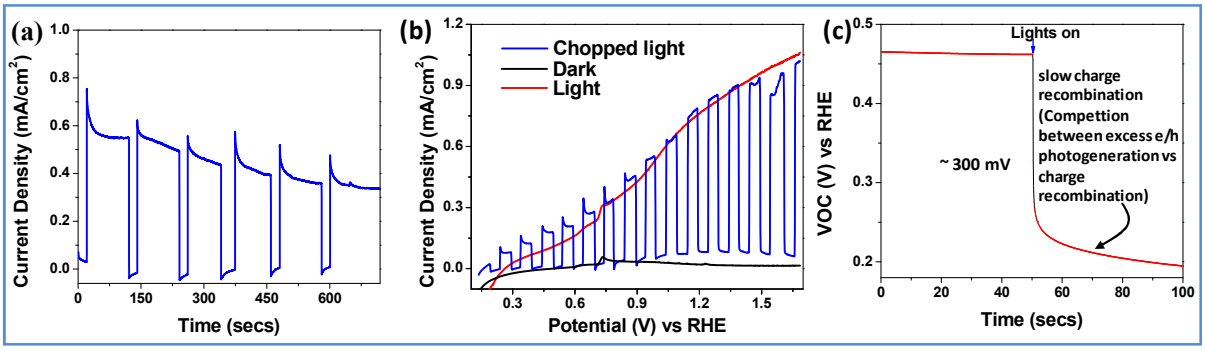

Figure 6.36: (a) Transient photocurrent study using chronoamperometric stability measurement biased at 0.3 V (vs RHE). (b) Current–Voltage (*J-V*) characteristics of a photoanode in dark, illuminated and chopped light illumination conditions. (c) Open circuit potential vs time graph of the photocathode in dark and illuminated conditions.

The photoelectrodes were examined before and after the water splitting in seawater to find the reason behind the decreased activity. SEM and EDAX measurements of the electrodes show the presence of Mg forming a flaky layer over the electrode material which could be seen as a change in colour of the electrode (**Figure 6.37**). Therefore, the slight decrease may have been arisen due to the accumulation of insoluble hydroxides of the metal (present in sea water) viz. $Mg(OH)_2$, $Ca(OH)_2$ etc or due to the formation of $Cu(OH)_2$ on the surface of the catalysts which then block the active sites. This is possible since during water splitting (hydrogen generation), the catholyte pH increases abruptly due to the utilization of the H_3O^+ ions. This can cause hydroxide formation (electrogeneration of base). We observed the sea water to be turbid after PEC activity test. We tested the composition of the turbid precipitates by collecting them (centrifugation) and using EDAX and ICP-OES as the elemental detection techniques.

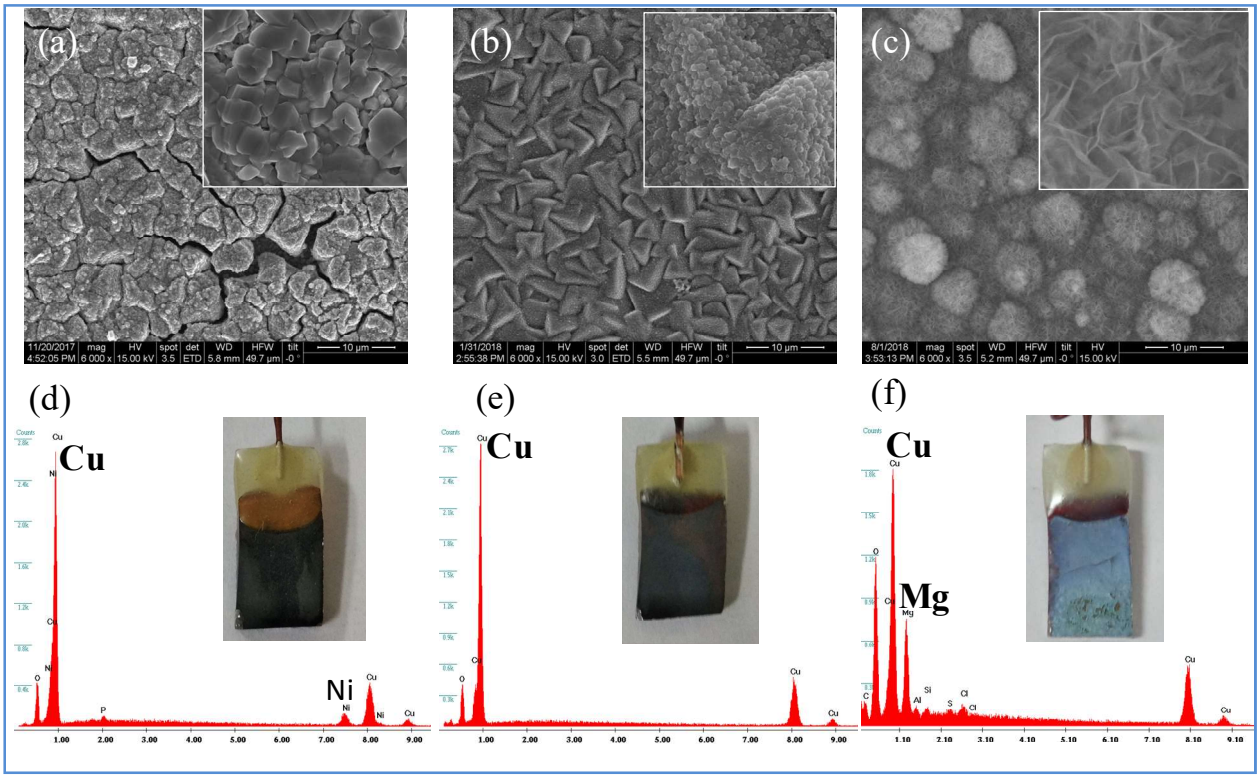

Figure 6.37: FESEM of Cu_2O-CuO-Ni_xP_y photocathode (a) before PEC study, (b) after PEC study in distilled water and (c) after PEC study in seawater. EDAX of Cu_2O-CuO-Ni_xP_y photocathode (d) before PEC study, (e) after PEC study in distilled water and (f) after PEC study in seawater (inset shows the colour of photocathode).

The precipitates were found to be $Mg(OH)_2$. Also, the activity tests in KPi buffer and Na_2SO_4 does not lead us to any such observation of turbidity of electrolyte confirming the effect of insoluble hydroxides in decreasing the PEC activity.

In two electrode configuration cathode (Cu_2O-CuO-Ni_xP_y) and anode ($BiVO_4$-MDH), we obtain a remarkable PEC activity and stability (**Figure 6.38**). Thus it can be concluded that the combination of Cu_2O and $BiVO_4$ based electrodes with appropriate modifications to counter the slight activity loss (as discussed) can lead to successful sea water splitting.

Furthermore, the open circuit potential (OCP) corresponds to the variation in Fermi levels between the photoactive material and the counter electrode. In the dark, both Cu_2O-CuO-Ni_xP_y and $BiVO_4$-MDH exhibits an initial OCP of 0.46 V and 0.705 V (vs RHE), which suggested an accumulation of electrons on the film electrode. When the light is illuminated, the majority of the excited photoelectrons are accumulated, resulting in the shift of the Fermi level

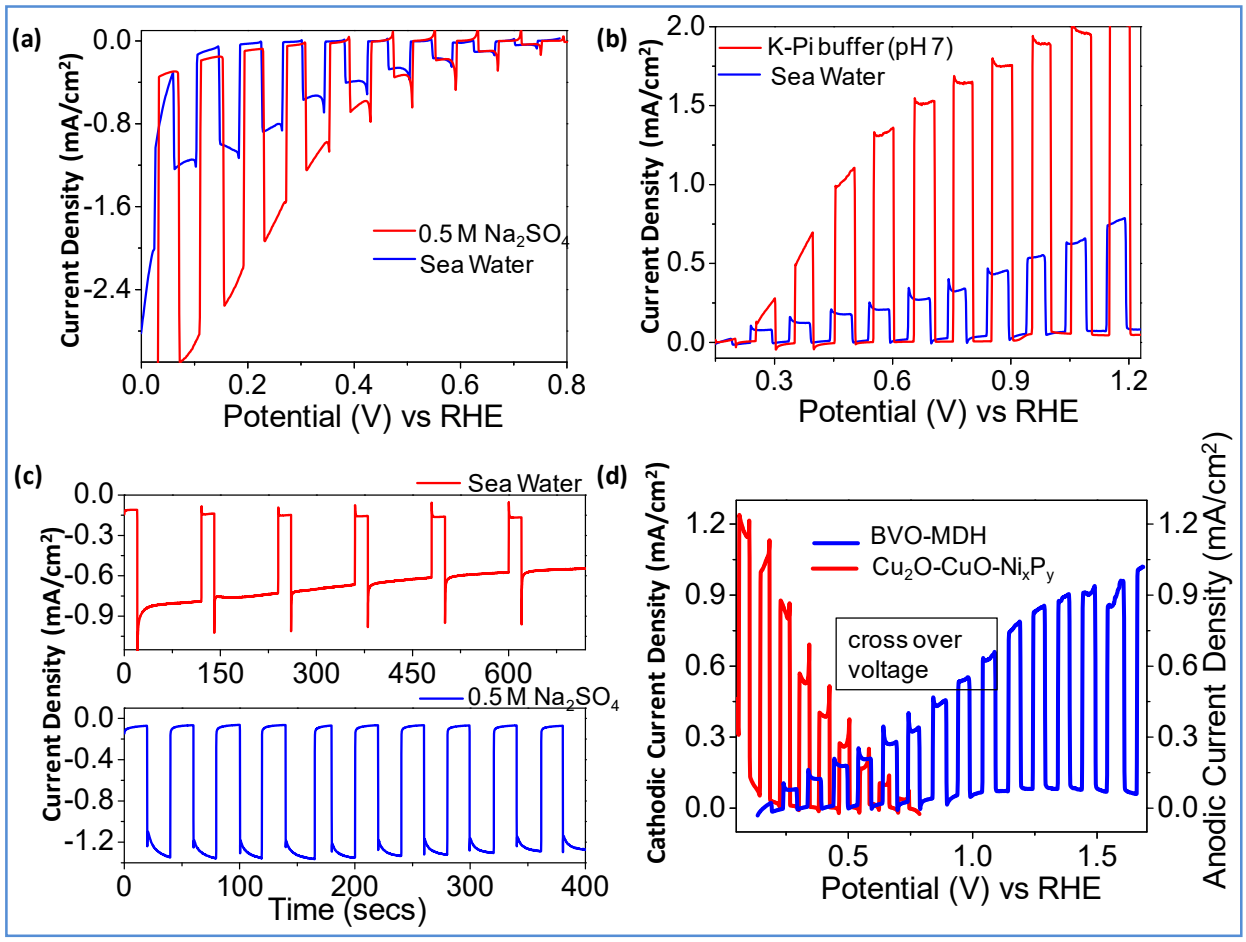

Figure 6.38: Comparison of PEC activity in sea water and pH-7 electrolyte. (a) and (b) Current–Voltage (I-V) characteristics of a photocathode in chopped light illumination conditions. (c) Transient photocurrent study of Cu_2O-CuO-Ni_xP_y using chronoamperometric stability measurement biased at 0.05 V (vs RHE). (d) selection of voltage for two electrode set-up PEC water splitting study with BVO-MDH as working electrode and Cu_2O-CuO-NixPy as counter electrode. The potential corresponding to cross over voltage was selected.

to a more negative/positive potential depending on the nature of semiconductor. For an n-type ($BiVO_4$), the OCP shifts to negative potential whereas for a p-type (Cu_2O) the shift is in positive potential. Competition between charge recombination and electron accumulation, the OCP approaches a stable state resulting from the increase of photo-induced electrons/holes under light irradiation. It is noteworthy that $BiVO_4$-MDH exhibits slow charge recombination in comparison to Cu_2O-CuO-Ni_xP_y as evident form (**Figures 6.35c and 6.36c**). Slow OCP decay under illumination is due to the efficient utilization of the light and the low recombination rate of the excited electron/hole pair. When these two electrodes were used as cathode or anode with Pt coil acting as their respective counter electrodes we obtained OCP of 100 mV (Cu_2O-

CuO-Ni_xP_y) and 300 mV ($BiVO_4$-MDH). However, in a two electrode setup when we used these two electrodes as cathode (Cu_2O-CuO-Ni_xP_y) and anode ($BiVO_4$-MDH), interestingly we obtained 600 mV OCP (**Figure 6.39**). This may be due to enhanced light utilization since both the electrodes are light absorbers.

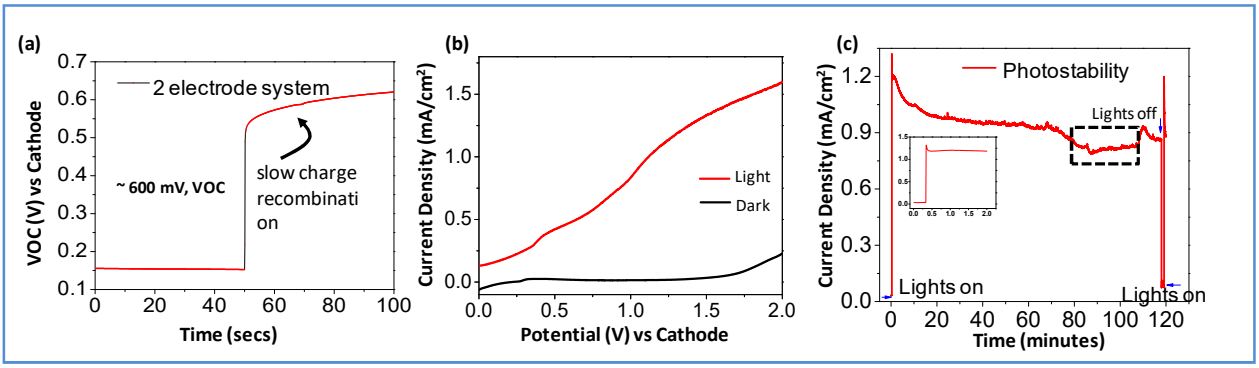

Figure 6.39: Two electrode set-up PEC water splitting study with BVO-MDH as anode and Cu_2O-CuO-NixPy as cathode. (a) Open circuit potential vs time graph of the photocathode in dark and illuminated conditions obtained by chopping the incident light. (b) Current–Voltage (I-V) characteristics of a photocathode in dark and illuminated conditions. (c) Transient photocurrent study using chronoamperometric stability measurement two electrodes biased at 1.23 V. All measurements were carried out in pH-6.8 sea water.

In summary the work described in this part provides a brief overview of utilization of sea water as the hydrogen source. The electrode fabrication method employed gives photostable electrodes and reveals the critical importance of composition/morphological changes of the surface in creating high stability photocathodes for photoelectrochemical and photocatalytic applications.

5. Conclusions

In this chapter, we have been able to improve the photostability of $BiVO_4$ and Cu_2O photo-anode/cathode film for PEC water splitting by appropriate co-catalyst or by engineering the interfacial band edge energetics by using Ni_xP_y as the cocatalyst. The maximum current density of -3.2 $mAcm^{-2}$ obtained from CuO–CuO–Ni_xP_y at 0 V (RHE) is doubly better than the current density reported for bare Cu_2O–CuO heterojunction systems. The pulse plating approach helps in attaining an advantageous $BiVO_4$/MDH interface to reduce photogenerated charge recombination and enhance their transport by controlling the grain size. PEC water oxidation reveals reduction in the onset potential by 0.53 V besides 33.4 times increment in J at a lower potential (0.6 V) achieved by $BiVO_4$/MDH. The increased amorphous nature of the MDH and modified interface of $BiVO_4$/OEC obtained by the present method helps in gaining better transient photostability and PEC activity. The charge-transfer resistance of $BiVO_4$ decreases by a few orders of magnitude with MDH deposition. Deposition of Co−$La(OH)_x$-based MDH not only enhances the ABPE of $BiVO_4$ significantly even at a lower potential but also provides a remarkable resistance against photocorrosion, establishing it as a promising candidate for photoelectrochemical water splitting. The synthetic method we employed can be extended to other metal hydroxide/oxide combinations.

6. References:

[1] Press, Roman J.; Santhanam, K. S. V.; Miri, Massoud J.; Bailey, Alla V.; Takacs, Gerald A. (2008). *Introduction to hydrogen Technology*. John Wiley & Sons

[2] T. W. Kim, K.-S. Choi, Science 2014, 343, 990.

[3] R. D. L. Smith, M. S. Prévot, R. D. Fagan, Z. Zhang, P. A. Sedach, M. K. J. Siu, S. Trudel, C. P. Berlinguette, Science 2013, 340, 60.

[4] W. Kim, T. Tachikawa, D. Monllor-Satoca, H.-i. Kim, T. Majima, W. Choi, Ener. Environ. Sci. 2013, 6, 3732.

[5] C. Li, T. Hisatomi, O. Watanabe, M. Nakabayashi, N. Shibata, K. Domen, J.-J. Delaunay, Ener. Environ. Sci. 2015, 8, 1493.

[6] H. Dotan, K. Sivula, M. Grätzel, A. Rothschild, S. C. Warren, Ener. Environ. Sci. 2011, 4, 958.

[7] J. Luo, L. Steier, M.-K. Son, M. Schreier, M. T. Mayer, M. Grätzel, Nano Lett. 2016, 16, 1848.

[8] A. Paracchino, V. Laporte, K. Sivula, M. Grätzel, E. Thimsen, Nat. Mater. 2011, 10, 456.

[9] T. W. Kim, K.-S. Choi, J. Phys. Chem. Lett. 2016, 7, 447.

[10] K.-H. Ye, Z. Chai, J. Gu, X. Yu, C. Zhao, Y. Zhang, W. Mai, Nano Energy 2015, 18, 222.

[11] S. Xie, T. Zhai, Y. Zhu, W. Li, R. Qiu, Y. Tong, X. Lu, Int. J. Hyd. Energy 2014, 39, 4820.
[12] L. Kuai, J. Geng, C. Chen, E. Kan, Y. Liu, Q. Wang, B. Geng, Angew. Chem. Int. Ed. 2014, 53, 7547.
[13] R. D. L. Smith, B. Sporinova, R. D. Fagan, S. Trudel, C. P. Berlinguette, Chem. Mater. 2014, 26, 1654.
[14] R. D. L. Smith, M. S. Prévot, R. D. Fagan, S. Trudel, C. P. Berlinguette, J. Am. Chem. Soc. 2013, 135, 11580.
[15] D. K. Zhong, D. R. Gamelin, J. Am. Chem. Soc. 2010, 132, 4202.
[16] M. Gong, Y. Li, H. Wang, Y. Liang, J. Z. Wu, J. Zhou, J. Wang, T. Regier, F. Wei, H. Dai, J. Am. Chem. Soc. 2013, 135, 8452.
[17] L. Trotochaud, S. L. Young, J. K. Ranney, S. W. Boettcher, J. Am. Chem. Soc. 2014, 136, 6744.
[18] M. W. Louie, A. T. Bell, J. Am. Chem. Soc. 2013, 135, 12329.
[19] Y. Q. Gao, X. Y. Liu, G. W. Yang, Nanoscale 2016, 8, 5015.
[20] H. Li, Y. Gao, C. Wang, G. Yang, Adv. Energy Mater. 2015, 5, 1401767.
[21] A. Shinde, D. Guevarra, G. Liu, I. D. Sharp, F. M. Toma, J. M. Gregoire, J. A. Haber, ACS Appl. Mater. Interfaces 2016, 8, 23696.
[22] A. Shinde, G. Li, L. Zhou, D. Guevarra, S. K. Suram, F. M. Toma, Q. Yan, J. A. Haber, J. B. Neaton, J. M. Gregoire, J. Mater. Chem. A 2016, 4, 14356.
[23] L. Wang, B. Li, X. Zhao, C. Chen, J. Cao, PloS One 2012, 7, e37781.
[24] A. J. Esswein, Y. Surendranath, S. Y. Reece, D. G. Nocera, Ener. Environ. Sci. 2011, 4, 499.
[25] D. K. Zhong, S. Choi, D. R. Gamelin, J. Am. Chem. Soc. 2011, 133, 18370.
[26] S. Chen, L.-W. Wang, Chem. Mater. 2012, 24, 3659.
[27] F. Du, Q.-Y. Chen, Y.-H. Wang, J. Phys. Chem. Solids 2017, 104, 139.
[28] E. J. Popczun, J. R. McKone, C. G. Read, A. J. Biacchi, A. M. Wiltrout, N. S. Lewis, R. E. Schaak, J. Am. Chem. Soc. 2013, 135, 9267.
[29] Z. Zhou, L. Wei, Y. Wang, H. E. Karahan, Z. Chen, Y. Lei, X. Chen, S. Zhai, X. Liao, Y. Chen, J. Mater. Chem. A 2017, 5, 20390.
[30] S. Jamali, A. Moshaii, Appl. Surf. Sci. 2017, 419, 269.
[31] Lanthanum. http://xpssimplified.com/elements/lanthanum.php
[32] N. S. McIntyre, M. G. Cook, Anal. Chem. 1975, 47, 2208.
[33] B.-K. Park, R.-H. Song, S.-B. Lee, T.-H. Lim, S.-J. Park, C.-O. Park, J.-W. Lee, J. Electrochem. Soc. 2015, 162, F1549.
[34] J. Yu, A. Kudo, Adv. Funct. Mater. 2006, 16, 2163.
[35] C. Li, P. Zhang, R. Lv, J. Lu, T. Wang, S. Wang, H. Wang, J. Gong, Small 2013, 9, 3951.
[36] L. Zhang, C.-Y. Lin, V. K. Valev, E. Reisner, U. Steiner, J. J. Baumberg, Small 2014, 10, 3970.
[37] F. Lin, B. F. Bachman, S. W. Boettcher, J. Phys. Chem. Lett. 2015, 6, 2427.
[38] F. Lin, S. W. Boettcher, Nat. Mater. 2013, 13, 81.
[39] R. Li, F. Zhang, D. Wang, J. Yang, M. Li, J. Zhu, X. Zhou, H. Han, C. Li, Nat. Commun. 2013, 4, 1432.
[40] X. Chang, T. Wang, P. Zhang, J. Zhang, A. Li, J. Gong, J. Am. Chem. Soc. 2015, 137, 8356.
[41] M. Zhong, T. Hisatomi, Y. Kuang, J. Zhao, M. Liu, A. Iwase, Q. Jia, H. Nishiyama, T. Minegishi, M. Nakabayashi, N. Shibata, R. Niishiro, C. Katayama, H. Shibano, M. Katayama, A. Kudo, T. Yamada, K. Domen, J. Am. Chem. Soc. 2015, 137, 5053.
[42] Q. Jia, K. Iwashina, A. Kudo, Proc. Natl. Acad. Sci. U.S.A 2012, 109, 11564.
[43] F. F. Abdi, R. van de Krol, J. Phys. Chem. C 2012, 116, 9398.
[44] Y. Tang, R. Wang, Y. Yang, D. Yan, X. Xiang, ACS Appl. Mater. Interfaces 2016, 8, 19446.
[45] J. A. Seabold, K.-S. Choi, J. Am. Chem. Soc. 2012, 134, 2186.
[46] W. He, R. Wang, L. Zhang, J. Zhu, X. Xiang, F. Li, J. Mater. Chem. A 2015, 3, 17977.
[47] J. P. Espinós, J. Morales, A. Barranco, A. Caballero, J. P. Holgado, A. R. González-Elipe, J. Phys. Chem. B 2002, 106, 6921.

[48] S. Poulston, P. M. Parlett, P. Stone, M. Bowker, Surf. Interface Anal. 1996, 24, 811.
[49] T. I. Korányi, Appl. Catal. A: General 2003, 239, 253.
[50] Y. Shi, Y. Xu, S. Zhuo, J. Zhang, B. Zhang, ACS Appl. Mater. Interfaces 2015, 7, 2376.
[51] Y.-F. Lim, C. S. Chua, C. J. J. Lee, D. Chi, Phys. Chem. Chem. Phys. 2014, 16, 25928.
[52] A. A. Dubale, C.-J. Pan, A. G. Tamirat, H.-M. Chen, W.-N. Su, C.-H. Chen, J. Rick, D. W. Ayele, B. A. Aragaw, J.-F. Lee, Y.-W. Yang, B.-J. Hwang, J. Mater. Chem. A 2015, 3, 12482.
[53] A. Mahmood, F. Tezcan, G. Kardaş, Int. J. Hydrog. Energy 2017, 42, 23268.
[54] T. Jafari, E. Moharreri, A. Amin, R. Miao, W. Song, S. Suib, Molecules 2016, 21, 900.

Epilogue

In this thesis, we have examined two important methods of hydrogen generation from water splitting. Each chapter addressed an important problem based on the system of study like enhancing activity of MoS_2, use of metal-free catalysts, new method of electrode fabrication method for higher current density and so on. We have succesfully achieved a low-cost metal-free electrocatalyst for electrochemical HER. $B_xC_yN_z$ with carbon rich composition and larger N:B ratio shows current densities beating many metal based electrocatalysts and comparable to that of Pt. The use of new electrode fabrication techique using sequential dual pulse platying afforded in obtaining very high current densities for hydrogen generation. The $Ni/Ni(OH)_2$/graphite electrode exhibited comparable activity to that of Pt electrodes.

In photoelectrochemical (PEC) water splitting, the introduction of better co-catalyst like mixed double hydroxide and Ni_xP_y by a new pulse plating electrodeposition method renders better charge transfer efficiencies and higher photocurrent density. The strategy to prevent the photocorrosion of Cu_2O has also been succesfully described.

An approach to split sea water keeping in mind its abundancy has been demonstrated using the photoelectrodes based on $BiVO_4$ and Cu_2O. Both the photoelectrodes successfuly exhibited sea water splittng.

*Before closing, it may be appropriate to briefly examine the status of this entire area of water splitting. The search for green fuel as an alternative to fossil fuel has paved the way for the emergence of hydrogen and fuel cell technologies especially in the power generation and transportation sectors. In fact the International Energy Agency has considered hydrogen as a flexible energy carrier with the potential for near-zero carbon emissions [1]. As discussed in the earlier chapters, in the long term, realizing the commercial hydrogen production (from water) will require low-cost, large-scale plants. Using sunlight as the input energy would require the semiconductor-based photo-electrochemical (PEC) cells and PV-Electrolyzer technologies. These two show greater potential but are also the most challenging processes. Laboratory scale demonstrations for PEC hydrogen production has been attained recently (**Figure 1**). From the perspective*

*of comparison between PEC water splitting and electrochemical water splitting driven by solar panels, various pros and cons can be analyzed. The deciding factor is the relation between efficiency, module price and balancing of system (BOS) costs [2]. For instance the price for PV-electricity is now around 0.03 $/kWh [3] which makes silicon based PV-electrolyzers more suitable for water splitting. The electrochemical water splitting has seen tremendous progress in terms of reduction in onset potential and higher current density. However the cost of catalysts has been the bottleneck for commercialization. So far metal-free catalysts have been the prime focus in this endeavor but no progress has been attained in successful demonstration of electrolyzers using them due to complicated electrode fabrication steps. However slightly cheaper than precious metal catalysts have been reported and demonstrated using a number of earth-abundant electrocatalysts, e.g. Ni_2P/NiO[4], $Ni/Ni(OH)_2$ and Ni–NiO/NiFe-LDH[5], that can operate at potentials as low as 1.5 V and are on the verge of commercial availability. In PEC water splitting, no single junction absorber has achieved STH greater than 10% yet. However in a tandem system with semiconductor/liquid junctions the best results that have been achieved are with $Cu_2O/BiVO_4$[6] and Cu_2O/WO_3[7] systems (but still below 1% STH). The state-of-the-art in particle-based and photoelectrode-based water splitting technologies research from leading groups in the field (NREL, EPFL, MIT, Stanford, Caltech, DOE labs) has been recently demonstrated in lab scale water splitting for the production of hydrogen (**Figure 2**).*

However, recently there has been contrasting views regarding PEC water splitting method to produce hydrogen as a viable process. In an opinion published in Energy Environ. Sci. in May 2018 it was argued that "with the rapid development of both PV-technology and earth-abundant electrocatalysis, it will be tremendously difficult, even in the best-case scenario, for a classical PEC water splitting device to compete with what PV-driven electrolysers can already do today"[2]. Given the pace at which the electrochemical water splitting has evolved in reporting activity of catalysts and the rate of advancements of the other alternatives of energy research (Battery, Solar Cells), it appears that PEC water splitting has a considerable slow development rate. Thus what seems to be needed now is demonstrating large-scale PEC Water splitting or PV-electrolyzer installations to establish the commercial viability of hydrogen production from water splitting.

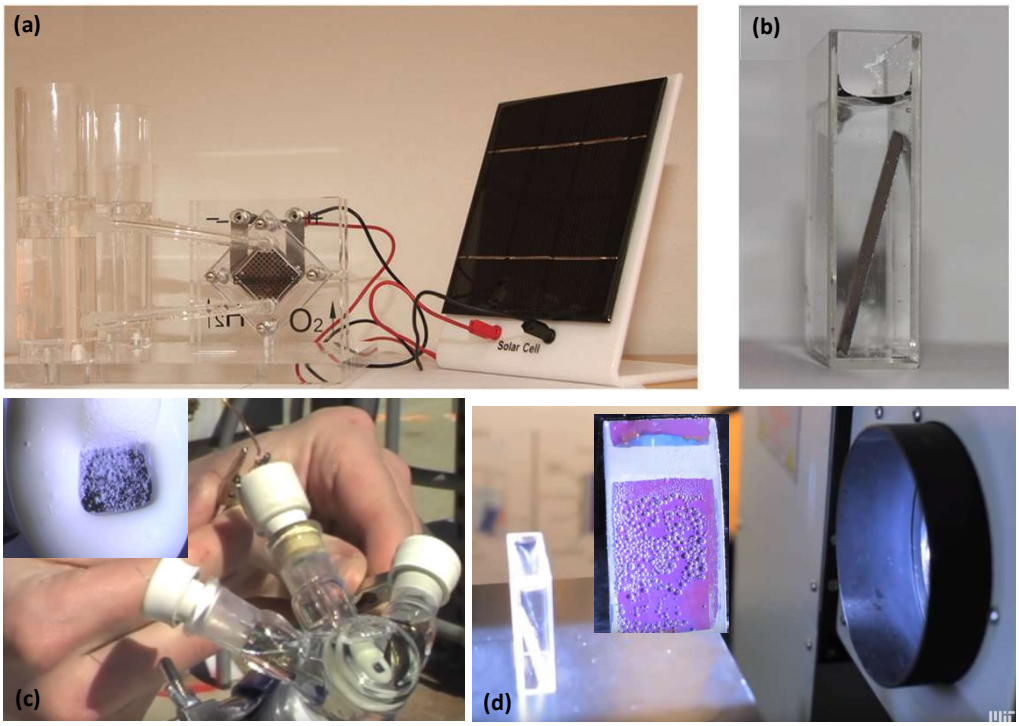

Figure 1: (a) – (d) Demonstrations of PEC water splitting and PV-Electrolyzers. Insets show the hydrogen evolution during the process. (a), (b) reproduced with permission[2], copyright 2018, The Royal Society of Chemistry. (c) Screeshot from (https://www.youtube.com/watch?v=6GT4Oiig1-8), NREL Research works (https://www.nrel.gov/). (d) Screenshot from (https://www.youtube.com/watch?v=LEEhxk-CiOQ), MIT research works, (http://news.mit.edu/2011/artificial-leaf-0930).

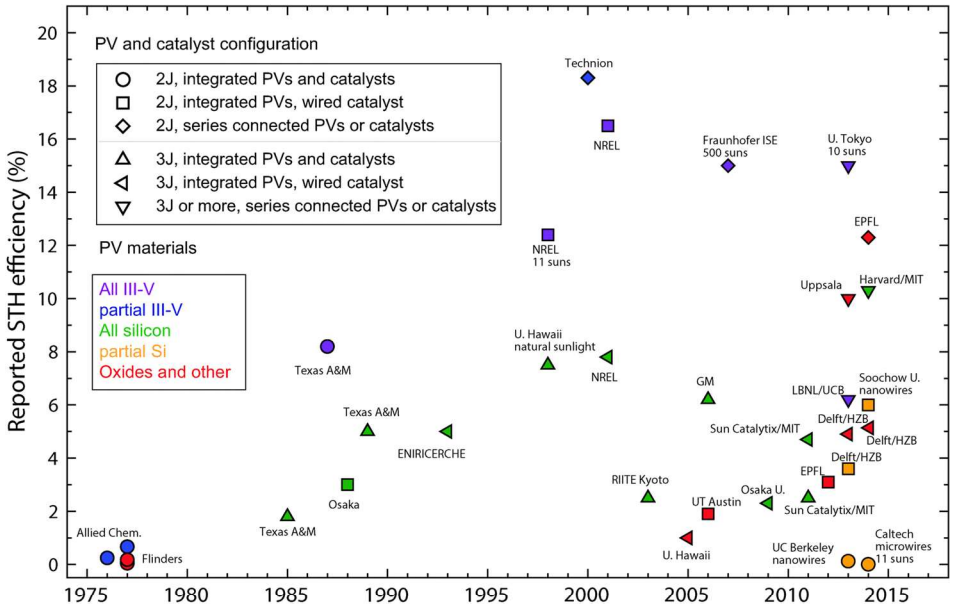

Figure 2: The reported solar to hydrogen (STH) conversion efficiencies as a function of year and sorted by the number of tandem photovoltaic junctions used (2 or 3). The fill colour represents the semiconductor materials used in the photovoltaic portion of the device. Reproduced with permission [8], copyright 2015, The Royal Society of Chemistry. Note: We have not included results from the laboratory since this figure shows the works up to 2015.

References:

[1] E. L. Miller, Energy Environ. Sci. 2015, 8, 2809.
[2] T. J. Jacobsson, Energy Environ. Sci. 2018, 11, 1977.
[3] E. Bellini, PV Magazine, 2017, https://www.pv-magazine.com/2017/10/06/interview-after-saudi-arabia-how-low-can-solarprices-go/.
[4] B. You, N. Jiang, M. Sheng, M. W. Bhushan, Y. Sun, ACS Catal. 2016, 6, 714.
[5] X. Liu, X. Wang, X. Yuan, W. Dong, F. Huang, J. Mater. Chem. A 2016, 4, 167.
[6] T. W. Kim, K.-S. Choi, J. Phys. Chem. Lett. 2016, 7, 447.
[7] J. Luo, L. Steier, M.-K. Son, M. Schreier, M. T. Mayer, M. Grätzel, Nano Lett. 2016, 16, 1848.
[8] J. W. Ager, M. R. Shaner, K. A. Walczak, I. D. Sharp, S. Ardo, Energy Environ. Sci., 2015, 8, 2811.